Experimental investigation of H_2O degassing in silicate melts during magma ascent: A closer look at decompression experiments

Dissertation

der Mathematisch-Naturwissenschaftlichen Fakultät

der Eberhard Karls Universität Tübingen

zur Erlangung des Grades eines

Doktors der Naturwissenschaften

(Dr. rer. nat.)

vorgelegt von

Holger Marxer

aus Miltenberg

Tübingen

2015

Gedruckt mit Genehmigung der Mathematisch-Naturwissenschaftlichen Fakultät der Eberhard Karls Universität Tübingen.

Tag der mündlichen Qualifikation:	13.11.2015
Dekan:	Prof. Dr. Wolfgang Rosenstiel
1. Berichterstatter:	Prof. Dr. Marcus Nowak
2. Berichterstatter:	Prof. Dr. Harald Behrens

Danksagung

Mein Dank gilt vor allem meinem Betreuer Marcus Nowak für seine permanente Diskussionsbereitschaft, die geschickte Platzierung von Denkanstößen und natürlich auch für das entspannte Arbeitsumfeld. Bei meinem zweiten Betreuer Harald Behrens möchte ich mich für die hilfreichen Ratschläge und Diskussionen bei unseren Treffen bedanken. Außerdem danke ich ihm für die Bereitschaft, sich trotz der Entfernung zwischen Tübingen und Hannover für meine Dissertation zu engagieren. Mein Dank gilt auch meinen zwei weiteren Prüfern Paul Bons und Thomas Wenzel im Rahmen der Disputation. Für die Mitarbeit im Projekt im Rahmen ihres Studiums bedanke ich mich bei Philipp Bellucci (Master-Arbeit), Sarah Ulmer (Bachelor-Arbeit), und Johannes Wolf (Bachelor-Arbeit). Großer Dank gilt dem Werkstatt-Team Norbert Walker, Barbara Maier und Marco Kahlfuss, die immer eine Lösung parat hatten oder entwickelten und fast jedes Teil reparieren oder neu bauen können. Für die Unterstützung bei Experimenten, in den Laboren und bei unzähligen Messungen am IR-Spektrometer danke ich Oliver Preuß, Daniel Russ und Annette Flicker. Alice Mahlbacher und Maximilian Klett danke ich für ihre HiWi-Tätigkeiten. Bei Thomas Wenzel möchte ich mich für die Betreuung an der Mikrosonde und bei Hartmut Schulz sowie Peter Fittkau für die Anleitung am SEM bedanken. Indra Gill-Kopp und Simone Schafflick danke ich für die Probenpräparation. Nicht zu vergessen sind natürlich meine Büro- und Fachkollegen Christopher Giehl, Oliver Preuß, Andreas Winterhalder und Richard Brooker, die immer den nötigen Pfiff in den Arbeitsalltag gebracht haben und mit denen ich meine Ergebnisse diskutieren konnte. Selbstverständlich bedanke ich mich auch bei allen anderen (ehemaligen) Doktoranden und Diplomanden im Haus (die Liste wird bald zu lang, man möge mir diese Verallgemeinerung verzeihen) für Rat und Tat, tolle Grillabende und gemeinschaftliche Feierabendrunden. Für die organisatorische Unterstützung danke ich unseren Sekretärinnen Beate Fritz, Claudia Jahn und Dagmar Dimitrovice. Besten Dank an Fabian Zeitvogel und Andreas Winterhalder für das Korrekturlesen der Dissertation. An dieser Stelle möchte ich mich auch noch einmal bei meinen Eltern bedanken, die mich während meines Studiums immer unterstützt haben.

List of publications

This doctoral thesis is an integrated accumulation of two publications and a submitted manuscript that are included in the appendix.

Marxer, H., Nowak, M. (2013). Micro-FTIR imaging: An advanced method for the determination of CO_2 and H_2O concentration gradients in silicate glasses. European Journal of Mineralogy, 25, 307-316. Appendix A of this thesis.

Marxer, H., Bellucci, P., Nowak, M. (2015). Degassing of H_2O in a phonolitic melt: A closer look at decompression experiments. Journal of Volcanology and Geothermal Research, 297, 109-124. Appendix B of this thesis.

Preuss, O., Marxer, H., Ulmer, S., Wolf, J., Nowak, M. (submitted manuscript). Degassing of hydrous trachytic Campi Flegrei and phonolitic Vesuvius melts: Experimental limitations and chances to study homogeneous bubble nucleation. American Mineralogist, paper 5480. Appendix C of this thesis.

Table of contents

Abbreviations and variables

BSD	bubble size distribution
BSE	back-scattered electron
CD	continuous decompression
CF	Campi Flegrei
CFDDP	Campi Flegrei deep drilling project
CI	Campanian Ignimbrite
EMP(A)	electron microprobe (analysis)
EOS	equation of state
FOV	field of view
FPA	focal plane array
FTIR	Fourier-transform infrared (spectroscopy)
HDAC	hydrothermal diamond anvil cell
IB	isobaric experiment/sample
(T)IHPV	(transparent) internally heated pressure vessel
MIR	mid-infrared
MORB	mid-ocean ridge basalt
MSD	multi-step decompression
NIR	near-infrared
NQ	normal quench
QFM	quartz-fayalite-magnetite (solid oxygen buffer)
REF	reference experiment/sample
RQ	rapid quench
S/N	signal-to-noise
SD	step-wise decompression
SE	single-element
SEM	scanning electron microscopy
SSD	single-step decompression
TLM	transmitted light microscopy
VAD79	phonolitic starting glass from the Vesuvius AD 79 eruption
WDS	wavelength-dispersive X-ray spectroscopy

A	absorption
α_4	defining parameter for the diffusion- or viscosity-controlled regime
B_s	shrinking factor of the bubble volume during cooling
C	total H_2O concentration expressed as molecular number
ΔF_c	free energy of formation for a bubble nucleus with critical radius
ΔP_{HeN}	supersaturation pressure for heterogeneous bubble nucleation
ΔP_{HoN}	supersaturation pressure for homogeneous bubble nucleation
ΔP_{ss}	supersaturation pressure of H_2O in the melt
D	diffusion coefficient (thesis text and Appendix A)
	diffusivity of total H_2O (Appendix C)
$dP \cdot dt^{-1}$	decompression rate
ε	molar extinction coefficient
η	viscosity
l	bubble diameter
λ	jump distance of a cation in the melt
$n(l)$	population density of bubbles with diameter l
N_C	number of quench crystal aggregates per unit volume of sample
N_V	number of bubbles per unit volume of sample, bubble number density
$N_V(n)$	number of bubbles per unit volume of pure melt or glass
$N_V(t)$	number of bubbles per total unit volume of sample ($V_{melt/glass} + V_b$)
ρ	density
P	pressure
P_e	hydrostatic exterior pressure in the melt around a bubble
P_{eq}	equilibration pressure
P_{final}	final pressure of decompression
P_i	interior bubble vapor pressure
P_{start}	starting pressure of decompression
P_W	H_2O saturation pressure in the melt
Q'	absorption quotient
r	bubble radius
σ	surface tension
t_{dec}	decompression time to P_{final}

t_{eq}	equilibration time prior to decompression
T	temperature
T_{eq}	equilibration temperature
T_f	fictive temperature of the melt where the bubble volume reduction stops
T_g	glass transition temperature
T_{rq}	run temperature prior to rapid quench
V_b	volume of the bubbles in a sample
v_{bubble}	ascent velocity of a bubble
V_{glass}	volume of the glass without bubbles
V_{melt}	volume of the melt without bubbles
V_m	molar volume (thesis text and Appendix B)
	volume of a H_2O molecule in the melt (Appendix C)
X_b	volume fraction of bubbles in a sample
X_{H2O}(fluid)	molar fraction of H_2O in the fluid

Zusammenfassung

Die Entgasung von Magmen während des Aufstiegs kann anhand von Dekompressionsexperimenten mit Volatil-haltigen Silikatschmelzen simuliert werden. Die dekompressionsinduzierte Volatil-Übersättigung in der Schmelze führt zur Nukleation und dem Wachstum von Blasen. Die Simulation dieser dynamischen Entgasungsprozesse erfordert optimierte Experimente, deren Ergebnisse hauptsächlich von der Dekompressionsrate abhängig sind. Diese Dissertation liefert wichtige Erkenntnisse über den Einfluss der in der Literatur beschriebenen Dekompressionsmethoden (kontinuierliche/stufenweise Dekompression, CD/SD) und Startmaterialien (Glaszylinder/-pulver) auf die homogene Blasennukleation und den Verlauf der H_2O-Entgasung. H_2O-haltige Silikatschmelzen wurden in einer intern beheizten Argon-Gasdruckanlage bei einer Temperatur von 1323 K oberhalb des Liquidus dekomprimiert. Die Dekompression startete bei einem Druck von 200 MPa und wurde mit nominellen Dekompressionsraten von 0.0028-1.7 $MPa \cdot s^{-1}$ durchgeführt. Bei Erreichen der Zieldrücke von 100-60 MPa wurden die Proben isobar abgeschreckt.

Die Experimente belegen, dass die Entgasung von Silikatschmelzen gegenüber dem experimentellen Protokoll höchst sensibel ist. Diese Dissertation offeriert auf Basis der Ergebnisse von optimierten Versuchen grundlegende Richtlinien für die Durchführung und die Interpretation von Entgasungsexperimenten. Ein fundamental wichtiger Aspekt ist die Berücksichtigung der Volumenreduktion der Blasen aufgrund des sinkenden molaren Volumens (V_m) des entgasten H_2O während der isobaren Abkühlung. Die Blasenvolumina und die Porosität in einer abgeschreckten Probe stimmen nicht mit dem Zustand vor dem Abkühlen überein. Das Blasenvolumen kann über einen Schrumpf-Faktor korrigiert werden. Dieser Faktor ist definiert über die V_m (H_2O) bei der Versuchstemperatur vor dem Abkühlen (T_{rq}) und bei einer fiktiven Temperatur (T_f), bei der weiteres Schrumpfen der Blasen durch die Viskosität der Schmelze verhindert wird. In erster Näherung kann die Glastransformations-Temperatur für T_f angenommen werden. Die korrigierte Porosität einer abgeschreckten Probe ist innerhalb eines relativen Fehlers von <10 % identisch zu der erwarteten Porosität bei T_{rq}, die anhand des residualen H_2O-Gehalts im Glas berechnet werden kann. Die Volumenreduktion der Blasen während der Abkühlung unter hohem Druck ist bei der Analyse und der Interpretation von Blasen-haltigen Proben bis heute nicht berücksichtigt worden.

Diffusives Blasenwachstum während der Dekompression kann zu Volatil-Konzentrationsgradienten in Richtung der Blasen führen. Die Evaluation der bildgebenden Mikro-FTIR-Spektroskopie mit einem „focal plane array"-Detektor als analytische Methode zur Untersuchung von CO_2- und H_2O-Diffusionsprozessen in Silikatschmelzen ist ebenfalls Teil dieser Dissertation. Gesamt-CO_2/H_2O-Diffusionskoeffizienten, die über das bildgebende Verfahren anhand von Konzentrations-Distanz-Profilen in Diffusionspaar-Proben ermittelt wurden, sind innerhalb des Fehlers identisch zu den Diffusionskoeffizienten, die über die klassische Einelement-Detektor-Analyse bestimmt wurden. Das bildgebende Verfahren ist besonders gut geeignet, um Diffusionsprozesse auf einem Maßstab weniger Mikrometer zu untersuchen. Allerdings ließen Messungen der gesamt-H_2O-Konzentration um Blasen in einer dekomprimierten Probe keine signifikanten Konzentrationsgradienten erkennen. Dies könnte auf den Transport von Schmelze während des Blasenschrumpfens zurückzuführen sein.

Der Vergleich zwischen CD und SD hat gezeigt, dass die Simulation von kontinuierlichem Magmenaufstieg CD-Experimente mit angemessenen Dekompressionsraten erfordert. SD führte zu umfangreicher Nukleation von Blasen, da die Diffusion von H_2O während der Dekompressionsschritte zeitlich limitiert war. CD mit Raten $\leq$0.024 MPa·s^{-1} ermöglichte eine kontinuierliche Reduktion der Übersättigung durch Diffusion von H_2O, nachdem sich erste Blasen gebildet hatten. Die Anzahldichten der Blasen (N_V) in Proben von CD-Experimenten mit geringen Dekompressionsraten sind mehrere Größenordnungen niedriger und die Blasen sind größer als in Proben von SD-Experimenten.

Entgasungsexperimente mit dem Fokus auf homogener Blasennukleation sollten mit blasenfreien Glaszylindern von ausreichender Größe durchgeführt werden. Im Gegensatz zu Glaszylindern verhinderte die Verwendung von Glaspulvern die homogene Nukleation von Blasen. Die eingeschlossene Luft im Porenraum des Glaspulvers führte wahrscheinlich zur Bildung von kleinsten, in der Schmelze verteilten H_2O-N_2-Blasen vor der Dekompression. Die Entgasung der Glaspulver-Proben wurde über das diffusive Wachstum dieser bereits vorhandenen Blasen bewerkstelligt. Dies belegen die im Vergleich zu den Glaszylinder-Proben höheren Porositäten und größeren Blasen, wobei die N_V in den Glaspulver-Proben um mehrere Größenordnungen geringer sind. Weiterhin erfordert die Untersuchung von homogener Blasennukleation einen kurzen Dekompressionszeitraum, um die Reduzierung der N_V durch Ostwald-Reifung und Koaleszenz von Blasen zu minimieren. Aufsteigende Blasen dürfen die homogene Nukleation nicht beeinflussen.

Anhand der N_V der Glaszylinder-Proben wurde die Anwendbarkeit eines Modells zur homogenen Blasennukleation in Abhängigkeit von der Dekompressionsrate (Toramaru, 2006) getestet. Die experimentell bestimmten N_V sind bis zu 5 Größenordnungen höher als die mit dem Modell berechneten Werte. Eine der Hauptursachen könnte die Verwendung der makroskopischen Oberflächenspannung im Modell zur Beschreibung der Blasennukleation auf molekularer Ebene sein. Die modellierten N_V stimmen am besten für eine um mehr als eine Größenordnung verminderte Oberflächenspannung von ~0.003 $N \cdot m^{-1}$ mit den experimentellen Werten überein. In Anbetracht der über optimierte Experimente neu bestimmten, hohen N_V ist es erforderlich, dass bestehende Modelle zur homogenen Blasennukleation während des Magmenaufstiegs an die neuen Datensätze angepasst werden. Dies wird dazu beitragen, die dynamischen Prozesse der Schmelzentgasung, die zu explosiven Vulkanausbrüchen führen kann, besser zu verstehen.

Abstract

Magma degassing during ascent can be simulated by decompression experiments with volatile-bearing silicate melts. Decompression-induced volatile supersaturation in the melt results in bubble nucleation and growth. The simulation of these dynamic degassing processes necessitates optimized experiments in which the results are primarily dependent on the decompression rate. This doctoral thesis reveals the influence of the decompression methods (continuous/step-wise decompression, CD/SD) and starting materials (glass cylinder/powder) reported in literature on homogeneous bubble nucleation and the course of H_2O degassing. H_2O-bearing silicate melts were decompressed at a super-liquidus temperature of 1323 K in an internally heated argon pressure vessel. Decompression started from a pressure of 200 MPa with nominal decompression rates of 0.0028-1.7 $MPa \cdot s^{-1}$. At final pressures of 100-60 MPa, the samples were quenched rapidly at isobaric conditions.

The experiments document that melt degassing is highly sensitive to the experimental protocol. Based on the results of optimized experiments, this thesis provides essential guidelines for the conduction and interpretation of degassing experiments. A fundamentally important aspect is the consideration of the bubble volume reduction due to decreasing molar volume (V_m) of the exsolved H_2O during isobaric rapid quench. The bubble volumes and the porosity of a vitrified sample do not correspond to the condition prior to cooling. The bubble volume can be corrected using a shrinking factor that is dependent on the V_m (H_2O) at run temperature prior to isobaric rapid quench (T_{rq}) and at a fictive temperature (T_f) where further shrinkage is prevented by melt viscosity. In first approximation, the glass transition temperature of the melt can be used for T_f. The corrected porosity of a quenched sample is within a relative error of <10 % equal to the expected porosity at T_{rq} that can be calculated from the residual H_2O content in the glass. To date, the volume reduction of bubbles during cooling under high pressure has not been considered in the analysis and interpretation of vesiculated samples.

Diffusive bubble growth during decompression can result in volatile concentration gradients towards bubbles. The evaluation of micro-FTIR imaging with a focal plane array detector as analytical method to study diffusion processes of CO_2 and H_2O in silicate melts is also part of this thesis. Bulk CO_2 and H_2O diffusivities derived from imaging of concentration-distance profiles in diffusion couple samples are within the error identical to the diffusivities derived from standard single-element detector analysis. The imaging technique is particularly

suited to study diffusion processes on a micrometer scale. However, imaging of the total H_2O concentration around a bubble in a decompressed sample did not reveal significant concentration gradients. This could be a result of melt transport around the bubbles during shrinkage.

The comparison between CD and SD has shown that the simulation of continuous magma ascent requires CD experiments with reasonable decompression rates. SD resulted in extensive bubble nucleation, because H_2O diffusion was limited in time during the decompression steps. CD with rates ≤ 0.024 MPa·s^{-1} facilitated continuous reduction of the supersaturation by diffusive bubble growth after bubble nucleation was triggered. The bubble number densities (N_V) in glass cylinder samples from CD experiments with low decompression rates are several orders of magnitude lower and the bubble diameters are bigger than in samples of SD experiments.

Degassing experiments with focus on homogeneous bubble nucleation should start from sufficiently sized, bubble-free glass cylinders. In contrast to glass cylinders, the use of glass powders prevented homogeneous bubble nucleation. The trapped air in the pore space of the glass powder probably led to the formation of tiny H_2O-N_2 bubbles throughout the melt prior to decompression. Degassing of the glass powder samples was facilitated by diffusive growth of these pre-existing bubbles. This is evidenced by higher porosities, bigger bubbles and several orders of magnitude lower N_V than in the glass cylinder samples. Furthermore, the investigation of homogeneous bubble nucleation necessitates a short decompression timescale to minimize the reduction of N_V due to Ostwald ripening and bubble coalescence and to prevent alteration of the nucleation record due to bubble ascent.

Based on the N_V of the glass cylinder samples, the applicability of a model for homogeneous bubble nucleation in dependence of the decompression rate (Toramaru, 2006) was tested. The experimentally determined N_V are up to 5 orders of magnitude higher than the values calculated with the model. This may be mainly attributed to the usage of the macroscopic surface tension in the model to describe the nucleation of bubbles at the molecular level. The modeled N_V match the experimental values best for a more than one order of magnitude reduced surface tension of ~0.003 N·m^{-1}. Considering the newly determined high N_V from optimized experiments, current models for homogeneous bubble nucleation during magma ascent have to be adjusted to the new data. This will contribute to a better understanding of the dynamic melt degassing processes that can trigger explosive volcanic eruptions.

1. Introduction

1.1. Magma ascent and melt degassing

The dynamic processes in the course of magma ascent through the crust are controlling parameters for volcanic activity. The exsolution of dissolved volatiles such as H_2O, CO_2 and sulphur compounds from the melt in a super-critical fluid phase (referred to as "degassing") at high pressure (P) and temperature (T) is the most important mechanism triggered during ascent, because it influences the physico-chemical evolution of a magma including the ascent rate and the eruptive style of a volcano (e.g. Sparks, 1978; Gonnermann and Manga, 2007). In most magmatic systems, H_2O is the dominant volatile component with up to several wt% H_2O dissolved in the melt. Its solubility is strongly dependent on P and to a lesser extent on the chemical composition of the melt (e.g. Duan, 2014). The ascent of magma is coupled with a decrease of P that lowers the solubility and ultimately leads to a supersaturation with volatiles in the melt (Sparks et al, 1994; Gonnermann and Manga, 2007). This supersaturation initiates bubble nucleation and growth in the melt that decrease the density of the ascending magma by increasing its porosity. The degassing process of H_2O can also result in decompression-induced crystallization due to increasing liquidus T (Hammer and Rutherford, 2002; Couch et al., 2003). Both degassing and crystallization influence the rheology of the ascending magma (Manga et al., 1998).

Bubbles can either nucleate homogeneously in the melt from an aggregation of H_2O molecules or heterogeneously on suitable nucleation sites such as small crystals (Sparks, 1978; Hurwitz and Navon, 1994). In both cases, the free energy of formation (ΔF_c) of a bubble nucleus with critical radius has to be overcome to create a new melt-fluid phase boundary. This energetic barrier is dependent on the supersaturation pressure (ΔP_{ss}, P difference between vapor P in the melt and exterior P) and on surface tension (σ) (Hirth et al., 1970; Hurwitz and Navon, 1994; Sparks et al., 1994). In case of heterogeneous nucleation on suitable crystals, ΔF_c can be lowered due to a decrease of surface tension that depends on crystal morphology and the wettability of the crystal surface (Hurwitz and Navon, 1994). With increasing ΔP_{ss} during magma ascent, the energetic barrier is reduced and the bubble nuclei start to grow by exceeding the critical radius (Hirth et al., 1970; Toramaru, 1989). The corresponding critical

supersaturation pressure for homogeneous nucleation (ΔP_{HoN}) is higher than for heterogeneous nucleation (ΔP_{HeN}). Typical ΔP_{HoN} reported for H_2O-bearing rhyolitic and phonolitc melts at different *P*-*T* conditions are ~60-120 MPa, whereas heterogeneous nucleation already occurs at ΔP_{HeN} of >5 MPa (e.g. Hurwtiz and Navon, 1994; Gardner et al., 1999; Mangan and Sisson, 2000, Gardner and Denis, 2004; Iacono Marziano et al, 2007). The newly formed bubbles in the ascending magma grow by volatile diffusion into the bubbles, coalescence and due to expansion of the exsolved volatile phase in the course of decompression. At the early stage of degassing, a small bubble can also be dissolved again in favor of a bigger bubble in close proximity. This Ostwald ripening process decreases the surface of the melt-fluid interface and therefore minimizes the free energy of the system (Voorhees, 1992; Higgins, 2006).

The degassing paths of the ascending melt in terms of dissolved volatile content against *P* can follow disequilibrium and/or equilibrium trends once the melt has become saturated (Mangan and Sisson, 2000; Gonnermann and Manga, 2005). Until the first bubbles nucleate and grow, the melt follows a disequilibrium trend due to increasing volatile supersaturation. After bubble nucleation, this supersaturation can be decreased by diffusive bubble growth. The early onset of heterogeneous bubble nucleation can lead to efficient equilibrium degassing (Mangan and Sisson, 2000). Homogeneous bubble nucleation delays degassing and the melt can become highly supersaturated, following a disequilibrium path. Further degassing of the melt is strongly dependent on the ascent rate of the magma, because it controls the timescale for diffusive bubble growth.

In return, the ascent rate of the magma is influenced by the growth of bubbles. Bubbles reduce the density and increase the buoyancy of the magma (Gonnermann and Manga, 2007). Persistent bubble growth therefore increases the ascent velocity and in positive feedback also ΔP_{ss} in the melt due to accelerated decompression. Magma ascent rates are additionally dependent on reservoir depth, crystal content and conduit diameter (Rutherford, 2008). Typical ascent rates for felsic and intermediate magmas through the crust are 0.001-0.015 $m \cdot s^{-1}$. Mid-ocean ridge basalt (MORB) magmas can already reach ascent velocities of 0.1-10 $m \cdot s^{-1}$ during effusive eruptions. The highest ascent rates with more than 200 $m \cdot s^{-1}$ are reported for kimberlitic magmas and other explosive eruptions (Paonita and Martelli, 2006; Sparks et al., 2006; Rutherford, 2008; Misiti et al., 2011).

The interaction of the growing bubbles during magma ascent is crucial for the eruptive style of a volcanic system. Bubbles can stay isolated without interconnections until the magma reaches a shallow level. The volatile phase cannot escape the system. Close to the surface, the decrease of *P* leads to rapid expansion of the bubbles. This closed-system degassing can result in magma fragmentation and explosive volcanism (Gaonac'h et al., 2003). In case of open-system degassing, the bubbles can rise in the magma body towards the surface if the ascent rate is slow enough or the bubbles interconnect by rupture of the bubble wall (Gonnermann and Manga, 2007). Bubble coalescence can be triggered by bubble wall stretching and inter-bubble *P* gradients of neighbored bubbles (Castro et al., 2012). The extent of bubble coalescence is strongly dependent on melt viscosity, timescale of magma ascent and the inter-bubble distance (Gardner, 2007). The lower the viscosity of a system, the easier bubbles can get interconnected or rise towards the surface. Extensive coalescence of bubbles generates magma permeability and facilitates volatile discharge from the magmatic system that also controls the fumarolic activity of a volcanic system. Low viscosity magmas such as MORBs are more likely to erupt effusively due to an efficient degassing network, whereas highly silicic magmas with increased viscosity and lacking interconnection of bubbles to enable gas permeability bear the potential for explosive eruptions (Sparks et al., 1994). The strain rate due to rapid volatile expansion in a highly vesiculated melt during accelerated magma ascent can increase rapidly and prevent melt relaxation by viscous flow. As a result, the magma starts to fragment by brittle failure (Dingwell and Webb, 1989; 1990; Alidibirov and Dingwell, 1996). This process can also lead to pyroclast formation at low *T*.

1.2. Decompression experiments

The concealed processes of bubble nucleation, growth and coalescence in ascending magmas below the fragmentation level can be simulated by decompression experiments in H*P*-H*T* setups with volatile-bearing melts. The experiments were mostly performed in a cold seal pressure vessel or an internally heated pressure vessel (IHPV) with H_2O or argon (+H_2) as pressure medium and the possibility for a rapid quench (RQ) of the sample (e.g. Huwitz & Navon, 1994; Iacono Marziano et al., 2007; Pichavant et al., 2013). Due to its importance and for simplification, the majority of the decompression experiments was conducted with H_2O as single volatile component in the melt in order to investigate the principal degassing

mechanisms. In case of homogeneous bubble nucleation and growth in melts, the corresponding experiments should be performed at super-liquidus conditions to avoid the energetically favored heterogeneous bubble nucleation on crystals. A few in situ degassing studies were also conducted in a transparent IHPV with sapphire windows (Gondé et al., 2011) and in Bassett-type diamond or moissanite anvil cells (Martel and Bureau, 2001; Masotta et al., 2014). However, these setups are either limited in the *T* range in case of the transparent IHPV or non-isothermal during decompression, because (uncontrolled) *P* decrease is facilitated by rapid cooling of the anvil cells.

Due to technical limitations, a step-wise decompression (SD) technique was used in most of the previous experimental simulations of magma ascent in high pressure vessels. The *P* was released by a single- or a multi-step decompression (SSD or MSD) method (e.g. Hurwitz and Navon, 1994; Gardner et al., 1999; Larsen and Gardner, 2004; Mastrolorenzo and Pappalardo, 2006; Iacono Marziano et al., 2007). At SSD only one decompression step is performed to reach the final pressure (P_{final}) and at MSD the sample is decompressed by sequential *P* drops of equal height. In both cases, the *P* decrease is followed by an isobaric annealing period over a certain amount of time (Appendix B). Commonly, a nominal decompression rate was interpolated from the onset of each *P* decrease to the endpoint of the annealing period (e.g. Gardner et al., 2000; Hammer and Rutherford, 2002; Gardner, 2007, Iacono Marziano et al., 2007). The actual decompression rate of 2.5-10 $MPa \cdot s^{-1}$ during each *P* drop was sometimes orders of magnitude higher than the calculated nominal decompression rate, because the *P* decrease was usually facilitated by manually opening and closing a conventional H*P* needle valve that is connected to the autoclave. The resulting decompression rates correspond to extreme magma ascent rates of 93-370 $m \cdot s^{-1}$ (Appendix B). Such high magma ascent velocities only occur during kimberlitic volcanism and lead to immediate eruption of the magma. Due to the annealing period at SSD after the fast decompression step, this method does not represent a natural magma ascent scenario. Explosive eruptions and pyroclast formation can be simulated in shock-tube experiments (e.g. Alidibirov and Dingwell, 1996). The MSD technique can be used to simulate complex natural magma ascent paths with periods of ascent followed by temporary storage throughout the volcanic feeding system, but the previous studies that involved MSD were not performed to investigate the effect of complex magma ascent paths (Brugger and Hammer, 2010).

Up to now, only few experimental studies of magma ascent below the fragmentation level were conducted with realistic continuous decompression (CD) rates. Mangan and Sisson (2000) found that delayed disequilibrium degassing during continuous decompression of rhyolitic melts can lead to a supersaturation of H_2O within the melt of about two times the equilibrium content. The study of Brugger and Hammer (2010) on decompression-induced crystallization in rhyodacitic magmas revealed that MSD and CD paths with identical nominal decompression rates lead to differences in plagioclase crystal textures due to diverging growth regimes. In order to investigate the effect of the decompression method on melt degassing, Nowak et al. (2011) performed a single set of decompression experiments with a hydrous rhyodacitic melt at SSD, MSD and CD at an identical nominal decompression rate of 0.28 $MPa \cdot s^{-1}$. It could be demonstrated that SD enhances bubble nucleation due to sudden supersaturation, whereas the degassing at CD is mainly achieved by bubble growth. Pichavant et al. (2013) simulated basaltic magma degassing with the CD method and were able to generate CO_2-supersaturated melts that could give insights to explosive basaltic volcanism.

1.3. Starting materials of the experiments

The decompression experiments to date were either performed with glass cylinders or glass powders as starting material. The material was pre-saturated or the capsules were loaded with the nominally dry glass and additional H_2O (e.g. Gardner et al., 1999; Iacono Marziano et al., 2007). Glass powder can be used to shorten the equilibration time (t_{eq}) for the dissolution of the H_2O in the melt prior to decompression due to shorter diffusion distances corresponding to the grain sizes. Many experiments were conducted with glass powder and additional H_2O in excess to solubility prior to decompression (e.g. Gardner et al., 1999; Larsen and Gardner, 2004). This method results in so-called hydration bubbles that develop during equilibration in the former pore spaces filled with the residual H_2O which could not be dissolved in the melt (Gardner et al., 1999). These pre-existing bubbles throughout the melt influence melt degassing in their H_2O drainage zone, because diffusive growth of pre-existing bubbles is energetically favored to bubble nucleation. The radius of the spherical drainage zone is controlled by the decompression rate that governs ΔP_{ss} and the time available for H_2O diffusion (Larsen and Gardner, 2000; Iacono-Marziano et al., 2007). The use of glass cylinders and additional H_2O is less critical, because all the H_2O is at first located at the capsule-melt interface. Only the amount

that matches H_2O solubility will diffuse into the initially volatile-free melt cylinder. The excess H_2O will remain in one or a few big fluid bubbles at the capsule-melt interface that are barely able to influence melt degassing in the center of sufficiently sized samples.

A further problem related to glass powder as starting material is the trapped air (or simplified N_2) in the pore space during capsule preparation. Nominally H_2O-undersaturated starting conditions using glass powder are suggested to produce N_2 bubbles throughout the melt prior to decompression (Simakin et al., 1999; Mourtada-Bonnefoi and Laporte, 2002). Besides typical volatile components such as H_2O, CO_2 and S-species, silicate melts can also dissolve several hundred ppm N_2 dependent on P (e.g. Carroll and Webster, 1994). The solubility of a volatile component in the melt is also influenced by the activity in the coexisting fluid (e.g. Duan, 2014). In case of a mixed volatile phase consisting of several wt% H_2O and only few hundred ppm N_2 in the capsules at the beginning of the experiments, the activity and therefore the solubility of N_2 is greatly reduced (Appendix C). It can therefore be expected that after equilibration, the bubbles consist of a mixed H_2O-N_2 fluid with a high molar fraction of H_2O (X_{H2O}). The problem of pre-existing H_2O-N_2 bubbles throughout the melt and its critical impact on the simulation of melt degassing can be avoided by using bubble-free glass cylinders. The glass cylinders can sometimes also contain air-filled bubbles due to fusing of the starting material in the atmospheric furnace from powder. However, the porosity and the corresponding amount of N_2 in the bubbles of a synthesized glass batch are usually very low compared to the glass powder mixture (Appendix C).

1.4. Bubble size distributions and number densities

The decompressed and partially degassed samples can be analyzed for the number of nucleated bubbles per unit volume (N_V) and the bubble size distribution (BSD). Size distributions were initially introduced for crystallization processes (Randolph and Larson, 1971; Marsh, 1988). They can give insights into nucleation and growth rates of crystals (Marsh, 1988; Higgins, 2006). The basic theory is also applicable to bubbles (e.g. Mourtada-Bonnefoi and Laporte, 2004; Shea et al., 2010b). BSDs are commonly expressed as the natural logarithm of the population density in dependence of bubble size ln $n(l)$, because nucleation and growth of bubbles (or crystals) over time follow exponential functions (e.g. Blower et al., 2002; Hammer,

2008). The population density is the number of bubbles per unit volume within a confined size interval and the sum of the bubbles of every size class is equal to N_V. The sample analysis is either based on 2D or 3D imaging information (Appendix B). BSDs and N_V-values of experimental samples can be compared to natural volcanic eruption products to obtain information about onset of degassing (depth), nucleation mechanism (heterogeneous and/or homogeneous) and magma ascent velocity. It is also possible to infer non-linear magma ascent due to changes in the conduit or multiple nucleation and growth events (e.g. Shea et al., 2010a, b). In this context it is important to normalize the derived number densities per total unit volume of the sample (volume of melt and bubbles) N_V(t) to pure melt volume N_V(n) in order to correct N_V for the individual porosity of a sample (Appendix B).

1.5. Bubble shrinkage and other quench effects

Unless the degassing experiments are performed with in-situ methods, the partially degassed melts have to be quenched at P_{final} of decompression to vesiculated, volatile-bearing glasses in order to analyze the samples for their BSD and porosity. A rapid quench of melt samples can prevent crystallization during cooling. Above the glass transition, the viscosity of the melt and the speciation of dissolved H_2O is not quenchable (Dingwell and Webb, 1990; Nowak and Behrens, 2001). The density of the melt also increases with decreasing T (Ochs and Lange, 1999). Two degassing studies casually mentioned that the size of H_2O-filled bubbles decreases during quench. Hurwitz and Navon (1994) presumed that cooling reduced the bubble volumes in their samples, because they observed unstable wetting angles of ~90° between necked bubbles and microlites. Simakin et al. (1999) also mention the shrinkage of bubbles during quench and a relation to melt viscosity, but both publications do not go into any further details. Further experimental studies did not consider this volume reduction of bubbles during quench in the interpretation of porosities and BSDs determined from vitrified experimental samples. Therefore, the reported porosities and BSDs in the vitrified samples probably do not correspond to the conditions prior to rapid quench of the melts. The shrinkage of bubbles also increases the N_V(t)-value of a sample during cooling. Only the N_V(n)-value (normalized to the respective porosity in the melt and the glass) remains constant.

McIntosh et al. (2014) lately attributed the decrease of the bubble volumes to resorption of H_2O by diffusion into the melt during quench due to a possible increase of H_2O solubility with decreasing *T*. Such a dependence of H_2O solubility on *T* was shown by Holtz et al. (1995) for a rhyolitic and Schmidt and Behrens (2008) for a phonolitic melt at $P \leq 400$ MPa. However, this effect might be strongly dependent on melt composition and the few experimental data for the phonolitic melt only document the solubility >1123 K. McIntosh et al. (2014) calculated a mass reduction of ~40 % of the exsolved H_2O in a bubble due to quench resorption, which would significantly decrease sample porosity and shift the BSD towards lower diameters during cooling. The basis for their interpretation and calculation are increased total H_2O concentrations around the bubbles. Such total H_2O concentration-distance profiles are a quenchable feature in experiments with silicate melts (e.g. Nowak and Behrens, 1997). However, these concentration gradients are only valuable if mass transport in the melt during quench does not interfere with the profile.

1.6. Micro-FTIR imaging of H_2O and CO_2 concentration gradients in glasses

The growth of bubbles in ascending magmas is greatly affected by volatile diffusivity, because it influences the amount and the timescale of supersaturation in the melt once bubbles have nucleated (e.g. Sparks et al., 1994). The quantification of H_2O and CO_2 diffusion processes is therefore essential to investigate the dynamics of diffusive bubble growth. Volatile concentration-distance profiles in silicate glasses in the direction of diffusion can be used to determine the diffusion coefficients (*D*) of the volatile species in the melt (e.g. Nowak and Behrens, 1997; Sierralta et al., 2002). The *D*-values are a measure for volatile mobility and can be obtained from diffusion couple experiments. In this method, a volatile-bearing and a nominally volatile-free glass cylinder are sealed in plane contact in a capsule and annealed at H*P*-H*T*, enabling unidirectional diffusion into the nominally volatile-free cylinder (Lapham et al., 1984). After a specific run time, the diffusion couple is quenched rapidly and the resulting concentration-distance profile in the glass is usually obtained by Fourier transform infrared (FTIR) spectroscopy in case of H_2O and CO_2. The corresponding *D*-values can be derived from a modified Boltzman-Matano analysis or from least-square fits of an applied error function (Nowak and Behrens, 1997; Nowak et al., 2004). Diffusion couple experiments have e.g. shown that volatile mobility increases with *T*. Furthermore, the diffusivity of total H_2O strongly

increases with total H_2O content in the melt, whereas the mobility of bulk CO_2 is independent of CO_2 concentration (e.g. Nowak and Behrens, 1997; Spickenbom et al., 2010).

The previous diffusion couple studies mostly involved spatially resolved FTIR transmission measurements with a standard single-element (SE) detector mounted on an infrared microscope to monitor the concentration-distance profiles (e.g. Sierralta et al., 2002). The measurements (mid- or near-infrared, MIR or NIR) were performed in 10-100 µm steps using a knife-edge aperture to narrow the field of view (FOV) in the direction of diffusion. Each measurement provides the averaged sample information of the FOV in a single spectrum. This method results in a single concentration-distance profile (Appendix A). FTIR microscopes can also be equipped with a focal plane array (FPA) detector to enable micro-FTIR imaging in a single measurement. In contrast to the SE detector, the FPA combines multiple detector elements (pixels) and facilitates simultaneous recording of individual spectra within one measurement (Lewis et al., 1995). Micro-FTIR imaging is meanwhile an established application to visualize H_2O and CO_2 concentrations in earth materials and enables measurements at high spatial resolution on a micrometer scale (Della Ventura et al., 2010; Appendix A). This method is therefore also applicable for imaging of H_2O and CO_2 concentration gradients in silicate glasses, especially in diffusion couples. A single sample measurement with the FPA detector results in multiple parallel concentration-distance profiles (Appendix A). Volatile concentration gradients are also expected around bubbles in partially degassed samples due to diffusive growth (e.g. Proussevitch and Sahagian, 1996). Micro-FTIR imaging is a promising method for the verification of such bubble growth models by monitoring total H_2O concentrations around bubbles.

1.7. Objectives of this thesis

A first objective is to compare micro-FTIR imaging to conventional SE detector analysis for the determination of total CO_2 and total H_2O diffusion coefficients from diffusion couple samples to highlight advantages of the FPA detector. The Micro-FTIR imaging technique is also tested on a partially degassed sample of a decompression experiment to visualize the concentration of total H_2O in the glass matrix around bubbles (Appendix A) in order to obtain information on diffusive bubble growth.

The degassing study of Nowak et al. (2011) comparing SSD, MSD and CD in hydrous rhyodacitic melts was based on a single set of experiments with a fixed decompression rate and a relatively high step size of 50 MPa at MSD. One aim of this study is to verify the differences in degassing behavior of H_2O at SD and CD for a less silicic, alkali-rich phonolitic melt composition from Vesuvius at different nominal decompression rates and a smaller step size during MSD (Appendix B). The most important objective is the quantification of bubble shrinkage during isobaric rapid quench due to cooling of the exsolved H_2O in the bubbles (Appendix B). This process has to be considered for proper interpretation of the porosity and the BSD that is determined from a partially degassed, virtrified sample. Based on the quantification of the bubble volume reduction, a correction method for the porosity and the BSD of a vitrified sample is provided in this study.

A further aim is to investigate the influence of the starting material (glass cylinder vs. glass powder) on H_2O degassing during decompression of hydrous phonolitic and trachytic melts (Appendix C). The experimentally determined N_V(n) are compared to calculated N_V(n) of the bubble number density decompression rate meter of Toramaru (2006) for homogeneous bubble nucleation at a constant decompression rate (Appendix C). Experimental limitations (e.g. degassing timescale) are outlined and will contribute to improve the investigation of homogeneous bubble nucleation in silicate melts.

1.8. Experimental and analytical strategy

At first, Micro-FTIR imaging with a 64x64 pixels FPA detector was compared to standard SE detector analysis on four pre-existing samples of CO_2 diffusion couple experiments (Appendix A). The double-sided ground and polished glass slabs of rhyolitic to hawaiitic composition were monitored in MIR transmission mode for total CO_2 (and total H_2O) concentration-distance profiles in the direction of diffusion. The SE detector profiles were determined in steps of 10 µm with a knife-edge aperture of 170x15 µm. The total length of the profiles was ~1 mm. The FOV of the FPA detector is 170x170 µm. The measurements were conducted with maximum FPA resolution as well binned resolutions (4x4 and 16x16 pixels) by seamless sample mapping (Appendix A). The different FPA detector resolutions correspond to nominal lateral resolutions of ~2.7-42.5 µm in the direction of diffusion. The resulting parallel

concentration-distance profiles were averaged to a single profile and compared to SE detector analysis.

All degassing-related experiments were performed in a vertically operated IHPV with argon as pressure medium. The IHPV is equipped with a piezo-actuator-controlled decompression valve facilitating both SD and CD (Nowak et al., 2011). The decompression valve was improved with a retaining spring that drives the valve needle out of the valve seat if the coupled piezo-ceramic is shortened. Furthermore, the valve was upgraded with a digital micrometer for more precise manual positioning of the needle together with the force-fit connected piezo-actuator. The IHPV is equipped with a RQ device that enables a maximum sample cooling rate of approximately 150 $K \cdot s^{-1}$ (Berndt et al., 2002).

The main experimental parameters for the comparison of SD and CD (Appendix B) were adopted from the decompression experiments of Iacono Marziano et al. (2007). The phonolitic starting glass VAD79 was synthesized from mostly dried oxide and carbonate powders at 1873 K in several steps. Cylinders of 6-7 mm length and 2.5 and 5 mm diameter were drilled out and loaded into either Pt or $Au_{80}Pd_{20}$ capsules with deionized water. The bigger sample diameter was chosen to minimize the effect of early degassing at the capsule-melt interface (Mangan and Sisson, 2000; Iacono-Marziano et al., 2007). Reference samples (REF) with variable H_2O content in the melt were generated for FTIR and EMP analysis. The starting conditions for all decompression experiments were 200 MPa and 1323 K. The equilibration time (t_{eq}) at these *P-T* conditions for the H_2O to distribute homogeneously in the 2.5 or 5 mm cylinders was either 72 or 96 h. The solubility of the VAD79 melt was found to be ~5.6 wt% prior to decompression (Appendix B). The 2.5 mm glass cylinders were sealed with H_2O in excess in capsules with flat-crimped headspaces. The 5 mm glass cylinders were loaded into capsules with a lid at the bottom and a star-crimped headspace at the top to force the volumetric expansion of the sample during decompression in a single direction. These samples were sealed with ~5 wt% H_2O, resulting in nominally H_2O-undersaturated conditions at the beginning of decompression to avoid the presence of a big fluid bubble in the capsule. After equilibration, decompression was conducted isothermally with nominal rates from 0.0028 to 1.7 $MPa \cdot s^{-1}$ in sets of each SSD, MSD and CD. The samples were quenched rapidly at isobaric conditions at a P_{final} of mostly 75 MPa. The vesiculated glasses were analyzed for residual H_2O contents. The stereological

conversion method of Higgins (2000) to obtain 3D data from limited 2D sample information was positively tested for the application on bubbles and mainly used to determine BSDs, volume fraction of bubbles (X_b) and N_V-values in suitable samples (Appendix B). Additionally, Micro-FTIR imaging was applied to a partially degassed sample that was prepared as a double-sided polished glass slab for transmission measurements (Appendix A). The thickness of the slab was decreased to a level where the bubbles in the slab are cut at both top and bottom to avoid apparent total H_2O concentration gradients due to sample thinning at the curved bubble wall (Appendix A).

Further sets of CD experiments starting from nominally H_2O-undersaturated conditions were conducted with moderate decompression rates of 0.024 and 0.17 MPa·s^{-1} down to a P_{final} of 100 MPa with glass cylinders (5 mm) and glass powders as starting material (Appendix C). Capsule geometry of the glass powder experiments was identical to the glass cylinder experiments and the initial H_2O contents in the melts were within the error ~4.7 wt%. The samples in Appendix C were equilibrated at a T_{eq} of 1573 K to eliminate former grain boundaries of the glass powder that could serve as possible nucleation sites and to speed up dissolution of H_2O into the massive glass cylinders. Equilibration times (t_{eq}) for glass powder experiments were either 24 or 96 h. After t_{eq}, the T was decreased to 1323 K prior to decompression. The effect of different starting materials on H_2O degassing was also investigated for a trachytic melt composition (Campanian Ignimbrite, CI) of Campi Flegrei (Appendix C). Isobaric experiments (IB) with the CI composition were performed to document the conditions after equilibration and prior to decompression. One IB sample was quenched with a moderate cooling rate of ~150 K·min^{-1} (referred to as normal quench, NQ) to verify the formation of quench crystals in the CI experiments. Further CD experiments with hydrous CI melts were performed down to a P_{final} of 75 and 60 MPa. The vesiculated samples in Appendix C were additionally analyzed using transmitted light microscopy (TLM) to determine N_V-values of bubbles with diameters on a micrometer scale.

1.9. Contributions to this thesis

A first test of the micro-FTIR imaging method on a single CO_2 diffusion couple was performed by Marxer (2009). Basic insights into the comparison of CD vs. MSD in experiments with 2.5 mm VAD79 glass cylinders and H_2O in excess in the capsules down to a P_{final} of 75 MPa were reported in Marxer (2011). Some of the H_2O-bearing reference samples were also generated in the course of Marxer (2011). The applicability of the stereological conversion method of Higgins (2000) on bubbles was verified by Bellucci (2013). A part of the H_2O-undersaturated experiments with 5 mm cylinders for the comparison of CD vs. SD was conducted and analyzed by Bellucci (2013). The comparison of different starting materials for the degassing experiments with hydrous trachytic melts and the discussion of homogeneous bubble nucleation (Appendix C) are part of the CFDDP (Campi Flegrei Deep Drilling Project) that is conducted by Oliver Preuß under supervision of Prof. Dr. Marcus Nowak. In this case, the author of this thesis conceived and performed experiments with hydrous phonolitic Vesuvius melts that were integrated in Appendix C. First experiments and analyses for the comparison between glass cylinder and glass powder with the VAD79 melt composition were performed and analyzed by Wolf (2014). A part of the experiments and analyses for the comparison glass cylinder vs. glass powder with the trachytic melt composition was conducted by Ulmer (2013). All experiments and analyses of Bellucci (2013) and Wolf (2014) were co-supervised by the author of this thesis under general supervision of Prof. Dr. Marcus Nowak in the course of this experimental degassing study. The basic results of the listed student theses were combined in the publications and the manuscript provided in Appendix A-C together with further substantial experimental and analytical data from the author. Appendix C is used together with Oliver Preuß. The interpretation and discussion of the individual results were interlinked and extended, especially with respect to bubble shrinkage and correction of this quench effect as well as the influence of the starting material and the discussion of homogeneous bubble nucleation. All authors listed above are acknowledged as co-authors of the publications and the manuscript. Specific personal contributions of the author of this doctoral thesis are presented on the first page of each appendix.

2. Results and discussion

2.1. Micro-FTIR imaging

FPA detector measurements at a resolution of 64x64 pixels enabled detailed imaging of sample features such as cracks or bubbles in the diffusion couple samples (Appendix A). The spatial resolution is nonetheless limited the by the wavelength-dependent diffraction of light (Ippolito et al., 2005), geometric sample effects and the confocal beam path of the microscope. Increasing FPA detector resolution decreased the signal-to-noise ratio (S/N) of the recorded MIR spectra and resulted in scattering of the determined absorption band areas that were used as basis for the concentration-distance profiles (Appendix A). Nevertheless, averaging of the multiple parallel profiles reduced this scatter to the level of SE detector analysis, which are based on the averaged sample information from the FOV confined by the knife edge aperture (Appendix A). The timescale of FPA sample mapping at maximum resolution was similar to standard SE detector analysis at identical profile length and the diffusion couple could be easily monitored for interfering melt convection due to the resulting multiple parallel profiles.

The concentration-distance profiles had to be corrected in length for cracks in the diffusion couples and crack-related data points had to be deleted. Micro-FTIR imaging at maximum resolution allowed precise correction of these features. Despite a different lateral resolution in the direction of diffusion, the SE detector concentration-distance profile and the averaged profiles obtained by FPA mapping are almost congruent. The profile shapes with a length of more than 1 mm are barely influenced by averaging sample information over ~2.7 or ~42.5 µm in the direction of volatile diffusion. However, the influence of lateral resolution in the direction of diffusion is crucial for shorter concentration-distance profiles. The error function fits of the profiles also display matching trends (Appendix A). The derived bulk CO_2 and H_2O diffusivities from measurements with different FPA detector resolutions range from log D = -11.03 to -11.33 (D in $m^2 \cdot s^{-1}$) at 500 MPa and 1523-1623 K and are within the error identical to SE detector analysis.

Micro-FTIR imaging was also used to visualize total H_2O concentration around bubbles in a decompressed and partially degassed sample (Appendix A). Within error, concentration

gradients towards the bubble wall could not be detected. The readjustment of thermodynamic equilibrium prior to rapid quench could have eliminated the expected spherical H_2O concentration gradients around the bubble in this confined sample volume. Nevertheless, the spatial resolution of this technique in thin samples is sufficient to investigate diffusion processes on a micrometer scale. Recently, McIntosh et al. (2014) applied this imaging technique to partially degassed samples and in contrast to our results, they monitored total H_2O concentration-distance gradients in the glass around bubbles with profile lengths of several dozen micrometers. However, there are no data on the H_2O solubility of the VAD79 melt around the glass transition temperature (T_g) to verify their suggestion of H_2O resorption into the melt.

2.2. Bubble shrinkage during isobaric rapid quench

The headspaces of the capsules from the degassing experiments are usually widened due to expansion of the sample during decompression. The bubbles are often deformed and some samples show large- and small-scale flow textures (Appendix B). Flow textures in and around bubble indentions that document melt transport at high viscosity are direct evidence for bubble volume reduction during isobaric rapid quench of the samples. The interpretations of bubble deformation mechanisms by Castro et al. (2012) and McIntosh et al. (2014) due to bubble wall-stretching during coalescence and quench resorption of H_2O are not considered for the samples. The deformed bubbles are often too isolated in the sample and significant total H_2O concentration gradients around the bubbles could not be detected (Appendix A). Besides, the interpretation of McIntosh et al. (2014) is based on measurements of total H_2O distribution in several year old samples. This timescale could have led to alteration of the samples by H_2O incorporation in the vitrified state. Indicators for this consideration are the increasing total H_2O concentrations towards cracks in the glasses and the H_2O species concentration-distance profiles obtained by micro-FTIR imaging around formerly H_2O-filled bubbles. Their measured species concentrations suggest an increase of molecular H_2O in the melt. However, the speciation of dissolved H_2O (OH^- and molecular H_2O) in the melt is not quenchable above T_g (e.g. Dingwell and Webb, 1990; Nowak and Behrens, 2001). Quench resorption of molecular H_2O above T_g would affect the concentration of both species at the bubble rim in case of profile B-B' (Fig. 6d in McIntosh et al., 2014), because equilibrium speciation is regained (e.g. Nowak

and Behrens, 2001). It is unlikely that the maximum measured OH^- concentration in this profile is linked to the lowest measured molecular H_2O content if the total H_2O concentration change occurred above T_g.

The volume reduction of bubbles in the partially degassed samples was the consequence of the decrease in molar volume (V_m) of the exsolved H_2O inside the bubbles with decreasing T during isobaric rapid quench (Duan and Zhang, 2006; Appendix B). The resulting difference between interior vapor pressure in the bubble (P_i) and the constant exterior P during isobaric rapid quench in the autoclave was equilibrated by reduction of the bubble volume. From the onset of cooling until the glass transition, the melt reacted to shear forces by viscous flow (e.g. Dingwell and Webb, 1990). The viscosity of the melt increased with decreasing T during quench. Bubble volume reduction proceeded during isobaric cooling until the melt was too viscous to relax at a fictive temperature (T_f). In a first approximation, T_g (log η ~ 10; η in Pa·s) was used as T_f to quantify the extent of bubble shrinkage (Appendix B). During isobaric cooling the volume of a bubble decreases by a shrinking factor B_s that is dependent on P_{final} and T:

$$B_s = \frac{V_m(\mathrm{H_2O})\ [P_{final}, T_{rq}]}{V_m(\mathrm{H_2O})\ [P_{final}, T_f]} \qquad \textbf{(1)}$$

where T_{rq} is the run temperature prior to isobaric rapid quench. For a quench with ~150 $K \cdot s^{-1}$ at a P_{final} of 75 MPa, T_{rq} of 1323 K and a uniform residual H_2O content of ~3 wt% in the partially degassed VAD79 melt, B_s is ~2.5 using a T_g of ~840 K (Dingwell and Webb, 1990; Giordano et al., 2008; Appendix B). This calculation is a scenario for maximum shrinkage. The termination of volume reduction due to a "viscosity quench" at e.g. 10^9 Pa·s (Thomas et al., 1994; Barclay et al., 1995) would decrease B_s to ~2.2. This difference in B_s is considered to be within the uncertainty of the approximation for bubble shrinkage. Furthermore, B_s is considered constant for all bubbles in the decompressed samples. The effect of bubble size on P_i (and therefore on V_m of the exsolved H_2O) is negligible for the observed bubble diameters in the vitrified samples (Appendix B). T_g is dependent on the residual H_2O content in the melt and on the cooling rate (e.g. Dingwell and Webb, 1990; Giordano et al., 2005). Applying the principles of the hydrous species geospeedometer of Zhang et al. (2000), the decompressed samples do

not provide any evidence for variable quench rates of the melt from capsule center towards the rim that would result in different T_g over the sample profile.

The reduction of the bubble volumes in the samples was achieved by isometrical shrinkage and/or deformation of the bubbles (ellipsoids/indentations). This depended on the location of the bubble in the capsule as well as on the bubble shape before shrinkage was initiated. The collapse of big fluid bubbles (e.g. in decompression experiments with H_2O in excess) in the cooling melt resulted in a directed melt flow in the capsules that affected the bubble texture and possibly also the capsule geometry (Appendix B). Excess fluid prior to decompression should therefore be avoided. The effect of bubble shrinkage can also be observed in the reference samples that were loaded with H_2O in excess (Fig. 1). After a few days of equilibration time, the big H_2O-filled bubbles in the capsule should be spherically rounded, at least on the side facing the capsule center in order to achieve minimum surface energy. However, the bubbles are massively deformed and dented due to the volume reduction during isobaric rapid quench. This observation in the un-degassed reference samples is a further proof that the deformation of the bubbles does not arise because of bubble interactions.

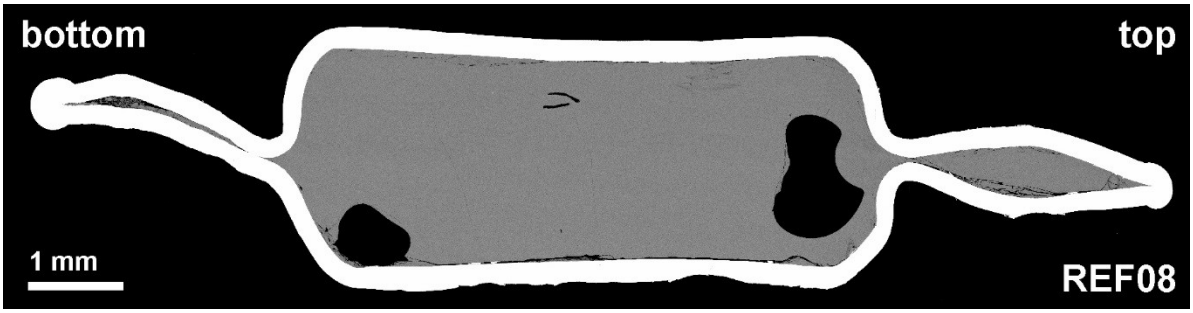

Fig. 1: Back-scattered electron (BSE) image of REF08. The capsule (white) was loaded with a 2.5 mm glass cylinder and H_2O in excess. Equilibration time was 72 h at 75 MPa and 1323 K. The experiment was performed in a vertically operated IHPV. Capsule orientation is provided in the image. The two big excess H_2O bubbles (black) in the glass (grey) are deformed due to volume reduction of the bubbles during isobaric rapid quench of the melt.

The melt transport during rapid quench can also interfere with possible total H_2O concentration gradients that could have formed towards bubbles due to diffusive growth during decompression. This could be the explanation for the lack of total H_2O concentration gradients

in the decompressed sample that was monitored by micro-FTIR imaging (Appendix A). If concentration gradients due to diffusive bubble growth are partly preserved and still detectable in a vitrified sample, the derived concentration-distance profiles have to be corrected for the disturbance due to the melt transport. The investigation of diffusive bubble growth based on information collected from quenched samples (e.g. by micro-FTIR imaging) has become extremely complex due to the shrinkage of the bubbles in the melt during isobaric rapid quench.

2.3. Correction of BSDs and porosities

Due to the bubble volume reduction, the BSD in a vitrified sample does not correspond to the size distribution in the melt prior to rapid quench. The determined BSD can be easily corrected after deformed bubbles have been transformed to spherical bubbles of identical volume (Appendix B). Afterwards, the bubbles of each size class in the BSD of the spheres can be corrected for the volumetric loss by inflation with the respective B_s (Eq. 1), shifting the new BSD towards bigger diameters and lower $n(l)$-values. The decrease of the bubble volumes during isobaric rapid quench also reduces the porosity of a partially degassed sample. In order to correct the volume fraction of bubbles in the vitrified sample, the volumes of the bubble-free melt and glass are considered to be equal. The volume fraction of bubbles in the melt prior to quench can be calculated from the volume fraction of bubbles in the glass considering B_s. The volume fraction of bubbles in the glass is defined as:

$$X_b(\text{glass}) = \frac{V_b(\text{glass})}{V_b(\text{glass}) + V_{glass}} \quad \textbf{(2)}$$

where V_b is the volume of the bubbles in a sample and V_{glass} is the volume of the glass without bubbles. It is assumed that the volume of the melt without bubbles at T_{rq} (V_{melt}) is equal to V_{glass} of the vitrified sample. V_{melt} can then be expressed as:

$$V_{melt} = V_{glass} = \frac{V_b(\text{glass})}{X_b(\text{glass})} - V_b(\text{glass}) \quad \textbf{(3)}$$

by rearrangement of Eq. 2. At T_{rq}, the total volume of the bubbles in the melt is:

$$V_b(\text{melt}) = B_s \cdot V_b(\text{glass}) \quad \textbf{(4)}$$

because the individual bubble volumes are inflated with the shrinking factor. In analogy to Eq. 2, the volume fraction of bubbles in the sample prior to rapid quench is calculated by:

$$X_b(\text{melt}) = \frac{V_b(\text{melt})}{V_b(\text{melt}) + V_{melt}} \quad \textbf{(5)}$$

and can be re-written as:

$$X_b(\text{melt}) = \frac{B_s \cdot V_b(\text{glass})}{B_s \cdot V_b(\text{glass}) + \frac{V_b(\text{glass})}{X_b(\text{glass})} - V_b(\text{glass})} \quad \textbf{(5)}$$

by substitution of V_{melt} and V_b(melt) using Eq. 3 and 4. Factorization of V_b(glass) in the denominator of Eq. 5 results in:

$$X_b(\text{melt}) = \frac{B_s \cdot V_b(\text{glass})}{V_b(\text{glass}) \cdot \left[B_s + \frac{1}{X_b(\text{glass})} - 1\right]} = \frac{B_s}{B_s + \frac{1}{X_b(\text{glass})} - 1} \quad \textbf{(6)}$$

and enables the reduction of V_b(glass) from the general fraction. In order to remove the sub-fraction in the denominator of Eq. 6, the general fraction can be expanded by X_b(glass) to:

$$X_b(\text{melt}) = \frac{B_s \cdot X_b(\text{glass})}{B_s \cdot X_b(\text{glass}) + 1 - X_b(\text{glass})} = \frac{B_s \cdot X_b(\text{glass})}{1 + \{X_b(\text{glass}) \cdot [B_s - 1]\}} \quad \textbf{(7)}$$

for final simplification. This correction of X_b is an approximation, because it depends e.g. on a uniform residual H_2O content in the sample that controls T_f. The 2D phase proportions of bubbles were used for this correction, because the calculated 3D data are sometimes error-prone due to a limited number of analyzed bubbles and problems with the stereological conversion of deformed objects (Appendix B).

The corrected porosities can now be compared to the expected porosities in the melt based on the residual H_2O content in the glass (Gardner et al., 1999). For a P_{final} of 75 MPa, the corrected porosities of the vesiculated VAD79 glasses (22-35 %) are close to the expected porosities in the melt that range from 24-31% (Appendix B). The correction of bubble shrinkage is also applicable to higher P_{final} of 150 and 100 MPa after adjustment of B_s to the respective H_2O content and P_{final}. For samples with minor bubble deformation and a high number of analyzed bubble intersections, the correction results in a relative error <10 % between expected and corrected porosity.

2.4. Application of bubble shrinkage to other studies

Simakin et al. (1999) assumed that the relatively high visocosity of their partially degassed rhyolitic melts at 1023 K and 3 wt% equilibrium H_2O content at a P_{final} of 40 MPa (log η ~ 6.8; using Giordano et al., 2008) prevented bubble shrinkage during quench. Nevertheless, Hurwitz and Navon (1994) most likely observed bubble shrinkage in a rhyolitic melt at similar conditions with an even higher T_g due to their faster quench rate. In first approximation, the bubble volumes in Simakin et al. (1999) could still be reduced by a maximum B_s of ~1.9 during quench (Table 1).

Table 1: Estimations of B_s for decompressed rhyolitic and basaltic samples in literature.

	P_{final} [MPa]	T_{rq} [K]	$c(H_2O)$ melt [wt%]	T_g[a] [K]	B_s
rhyolite (Simakin et al., 1999)	40	1023	2.8	~775	~1.9
basalt (Pichavant et al., 2013)	50	1423	1.5	~860	~2.1[b]
rhyolite (Gardner et al., 1999)	75	1098	3.7	~820	~2.1

[a]: T_g was calculated after Giordano et al. (2008) and Dingwell and Webb (1990).

[b]: Pichavant et al. (2013) used a H_2O-CO_2 fluid. A molar fraction of CO_2 of 0.1 in the bubble fluid was assumed for the EOS program of Duan and Zhang (2006) for the calculation of an exemplary B_s.

The approximation for shrinkage during quench can also be used for bubbles with mixed volatile components if the V_m of the fluid as a function of T is known. Pichavant et al. (2013) conducted decompression experiments with basaltic melts and H_2O-CO_2 fluids. The V_m of a H_2O-CO_2 fluid is also computable using Duan and Zhang (2006). However, low molar fractions of CO_2 in the fluid phase have barely any influence on V_m of the mixture compared to pure H_2O. The addition of CO_2 nevertheless reduces H_2O solubility in the melt and therefore results in higher T_g (Morizet et al., 2007).

Larsen and Gardner (2000) excluded bubble shrinkage in the decompressed and quenched rhyolitic samples of Gardner et al. (1999). They attributed bubble elongation of small bubbles in the vicinity of big hydration bubbles as indicators for the growth of these bubbles during degassing, instead of their shrinkage during quench. They substantiated this consideration by the good correspondence of expected porosities in the melt and the measured porosities in the glasses in decompression experiments starting with glass cylinders. In contrast to this observation, the estimated B_s for a sample quenched at a P_{final} of 75 MPa is quite significant with a value of ~2.1 (Table 1). It is possible that the extent of bubble shrinkage is influenced by the viscosity of the melt at the onset of cooling, but without further experimental data this is just a consideration.

2.5. Continuous vs. step-wise decompression

The reference samples document that decompression of the VAD79 samples started from a homogeneous melt (Appendix B). In the decompressed samples, bubbles at the capsule walls are often bigger than the bubbles in the center. Many specimens show a bubble-free zone between capsule wall and vesiculated sample center that resulted from early degassing at the melt-capsule interface due to heterogeneous bubble nucleation. This process most probably prevented homogenous bubble nucleation in the 2.5 mm CD samples with the lowest decompression rate, because the supersaturation in the melt could be reduced by H_2O diffusion towards the sample rim. This effect is less pronounced in the 5 mm samples, because the diffusion distance is doubled. The H_2O content in the center of 5 mm samples is not measurably affected.

For a P_{final} of 75 MPa, the N_V(n)-values of CD and MSD samples increase with nominal decompression rate, whereas the average bubble diameter decreases (Appendix B). The N_V(n)-values of the SSD samples are generally higher than those in the samples of MSD and CD experiments. At low nominal decompression rates, the basic results of Nowak et al. (2011) could be verified. In contrast to CD, SD led to higher population densities of bubbles with smaller diameters in the BSDs of the vitrified samples. SD resulted in up to several orders of magnitude higher N_V(n)-values. At a CD rate of 0.024 MPa·s^{-1}, ΔP_{ss} increased only slowly. After the first bubbles nucleated and started to grow, further degassing of the melt was primarily facilitated by H_2O diffusion into existing bubbles. This is evidenced by more or less constant N_V(n)-values of the 2.5 mm CD samples decompressed with 0.024 MPa·s^{-1} to different P_{final}. These CD experiments suggest a ΔP_{HoN} <50 MPa for the VAD79 melt. The P drop during SSD led to sudden supersaturation in the melt and caused extensive homogeneous nucleation due to the rapid decrease of the energetic barrier for bubble nucleation (Hirth et al., 1970). MSD samples with low nominal rates can display features of both SSD and CD. Decompression was performed with extreme decompression rates and followed by annealing periods that enabled diffusive bubble growth. It could be demonstrated that the SD technique is not suitable to simulate the degassing processes during CD of a hydrous melt with low, reasonable decompression rates. MSD can be used to simulate periods of magmatic ascent and storage in the volcanic feeding system, but only with reasonable decompression rates during P decrease.

The measured residual H_2O contents in the glasses slightly increase with nominal decompression rate (Appendix B). This observation is perhaps due to the decreasing timescale for diffusion-controlled melt degassing. On the other hand, this increase could result from the measurement of H_2O-filled bubbles in the analyzed sample volume due to a narrow bubble spacing on a micrometer scale. The differences between CD and SD decreased with increasing nominal decompression rate, because actual and nominal decompression rates aligned. The rapidly increasing ΔP_{ss} triggered massive bubble nucleation that shortened the diffusion distances for H_2O towards bubbles. SSD always resulted in the highest N_V(n)-values in the decompressed samples in the order of ~10^5 mm^{-3} after P drop, because the induced supersaturation with H_2O in the melt was always identical for all nominal decompression rates and higher than necessary for homogeneous bubble nucleation. Only for the lowest nominal

decompression rate, the measured N_V(n)-value is significantly decreased, because the extreme annealing period facilitated extensive bubble coalescence and ascent in the capsule.

2.6. Reproducibility of VAD79 decompression results

The reproducibility of results from CD experiments with high decompression rates, 2.5 mm cylinders and a P_{final} of 75 MPa is very good in terms of bubble size and N_V(n)-values (Appendix B). The minor differences in experiments with lower CD rates may be attributed to sectioning effects during sample preparation or capsule width during decompression that would influence H_2O diffusion distances. Significant differences in N_V(n)-values and bubble sizes in samples of repeated experiments can be observed for MSD with low nominal decompression rates. The poor reproducibility can be attributed to the method of decompression. Variations in the onset of bubble nucleation due to P drop uncertainties caused by the fast actual decompression rate could have influenced the available timescale for diffusive bubble growth and coalescence and would result in different bubble sizes and N_V(n)-values. The bubbles in the initially H_2O-undersaturated experiments with 5 mm glass cylinders and P_{final} of 75 MPa are usually bigger than in the corresponding 2.5 mm samples with H_2O in excess. This could be an effect of the bigger sample diameter that prevented significant H_2O loss towards the capsule walls in the 5 mm samples.

The decompressed 2.5 mm samples can be compared to specimens of Iacono Marziano et al. (2007) and reveal significant differences (Appendix B). The experiments were performed with nearly identical parameters. The quench rates in both studies were comparable. Differences due to diverging shrinking factors are therefore unlikely. Iacono Marziano et al. (2007) did not observe homogeneous bubble nucleation in MSD experiments with decompression rates of 0.0028-0.17 MPa·s^{-1}. The reported ΔP_{HoN} of ~100 MPa for a fast decompression rate in Iacono Marziano et al. (2007) is higher than the experiments with a low CD rate in Appendix B suggest (CD10, CD11). The residual H_2O contents reported by Iacono Marziano et al. (2007) are therefore higher and porosities are significantly lower than in this study. The early onset of degassing reported in Appendix B is probably related to the presence of pre-existing bubbles prior to decompression as discussed in Appendix C.

2.7. Glass cylinder vs. glass powder as starting material

The samples of isobaric CI experiments with the highest H_2O contents contain crystal aggregates with number densities (N_C) in the same order of magnitude (~10^5 mm^{-3}) as the number densities of the bubbles in the CI cylinder samples decompressed to a P_{final} of 100 MPa (Appendix C). However, these crystals most likely formed after homogeneous bubble nucleation during quench of the vesiculated sample and did not trigger melt degassing. In any case, the occurrence of heterogeneous bubble nucleation on the quench crystals during quench in the CI glass cylinder samples would not interfere with the principal observations for the comparison of glass cylinder vs. glass powder as starting material in experiments decompressed to a P_{final} of 100 MPa.

Although all decompression experiments reported in Appendix C started from the same nominally H_2O-undersaturated conditions with ~4.7 wt% H_2O in the melt, the glass powder samples with a t_{eq} of 24 h degassed more efficiently than the corresponding glass cylinder and glass powder experiments with a t_{eq} of 96 h for both the CI and VAD79 composition as well as for both applied decompression rates. The glass powder samples with a t_{eq} of 24 h are characterized by lower residual H_2O contents in the glass, higher porosities and bigger bubbles with N_V(n) <550 mm^{-3} that are orders of magnitude lower than in the decompressed glass cylinder or glass powder samples with a t_{eq} of 96 h (N_V (n) ~1-5·10^5 mm^{-3}, bubble diameters <5 µm). Near-equilibrium degassing of the glass powder samples equilibrated for only 24 h started with the onset of decompression and was facilitated by growth of tiny pre-existing H_2O-N_2 bubbles with a high X_{H2O}(fluid) of ~0.9 (Appendix C). These pre-existing bubbles formed throughout the melt, because the amount of trapped N_2 in the pore space of glass powder samples was higher than N_2 solubility at experimental conditions. The glass cylinder samples were initially free of bubbles in the melt prior to decompression. Therefore, a significant ΔP_{SS} had to build up to trigger homogeneous bubble nucleation at a later stage during decompression. Considering the H_2O saturation pressure for both compositions, ΔP_{HoN} can be estimated as <76 MPa for the CI and <70 MPa for the VAD79 melt. Due to this delayed onset of degassing, the cylinder samples feature a high residual H_2O concentration in the glass close to the initial H_2O content in combination with very low porosities and bubble diameters on a micrometer scale. The decompressed glass powder samples with a significantly longer t_{eq} of 96 h show a

very similar degassing behavior. This is probably due to the increased timescale for Ostwald ripening, coalescence and ascent of the pre-existing H_2O-N_2 bubbles in the powder samples to the top of the capsules prior to decompression, resulting in a bubble-free melt (Appendix C). The use of glass powder in decompression experiments to simulate homogeneous bubble nucleation is therefore not of advantage, because t_{eq} must be extended to remove pre-existing bubbles in the melt by growth and ascent. This problem would be even more pronounced for melts with higher viscosity due to decreasing bubble ascent velocity.

2.8. Effects of decreasing P_{final} on the record of bubble nucleation

Further decompression experiments with the hydrous CI melt starting from glass cylinders were conducted down to a P_{final} of 75 and 60 MPa (Appendix C). Decreasing P_{final} at a certain decompression rate increases the degassing timescale (time from the onset of homogeneous bubble nucleation to P_{final}). This can enhance Ostwald ripening and bubble coalescence, which both decrease the N_V(n) in a sample and would suggest a less extensive bubble nucleation. The N_V(n) in the trachytic samples decompressed to a P_{final} of 75 MPa (Appendix C) are slightly decreased compared to the samples quenched at 100 MPa. This documents that the first bubble nucleation event was completed. It is likely that extensive ripening and coalescence of bubbles would occur if the samples were decompressed to P_{final} <60 MPa. The timescale for extensive coalescence is suggested to be in the order of seconds in case of high N_V(n) combined with short inter-bubble distances in hydrous melts with a low viscosity (Appendix C).

At the lowest decompression rates, the reduction of P_{final} aggravated the problem of diffusional H_2O loss from the melt to the heterogeneously nucleated bubbles at the capsule-melt interface. These bubbles detached and ascended from the bottom of the capsule during decompression due to increasing buoyancy force. The detached bubbles grew by volatile expansion and H_2O diffusion from the supersaturated melt into the bubbles. The latter led to depletion of H_2O on the whole ascent track (Appendix C). This reduction of supersaturation could prevent homogeneous bubble nucleation in the bubble tracks. If these bubbles ascended through clouds of homogeneously nucleated small bubbles, they could also grow by Ostwald ripening and coalescence at the expense of the small bubbles and delete the record of their nucleation. Further decompression and the corresponding increase of ΔP_{ss} may be sufficient to trigger a second

homogeneous bubble nucleation event in the formerly depleted ascend tracks and suggest a ΔP_{HoN} that is much higher than for the first bubble population.

2.9. Comparison of determined N_V(n) to the model of Toramaru (2006)

Toramaru (2006) developed a model for homogeneous bubble nucleation and growth at a constant decompression rate in the diffusion-controlled regime. It can be used to calculate the N_V(n) of a completed single nucleation event in dependence of the decompression rate considering the surface tension of the melt as well as the diffusivity and concentration of total H_2O (Appendix C). The model is valid for homogeneous bubble nucleation in a single-phase melt free of pre-existing bubbles during super-liquidus isothermal decompression. A further pre-requisite is the absence of Ostwald ripening and coalescence. Therefore, the applicability of the model was tested for the glass cylinder samples with the highest P_{final} of 100 MPa (Appendix C). The calculated values are several orders of magnitude lower than the experimentally determined N_V(n). This difference presumably arises due the use of a macroscopic surface tension and effects of H_2O speciation on H_2O molecule concentration and diffusivity. Bubble nucleation is a process on a molecular scale, where the application of macroscopic physical descriptions may fail and lowered surface tensions have to be considered (e.g. Gonnermann and Manga, 2013). A significant decrease of the macroscopic σ (~0.133 $N \cdot m^{-1}$) to a value of ~0.003 $N \cdot m^{-1}$ would be necessary to describe the new experimental data (Appendix C). It is also conceivable that bubble nucleation is influenced by the comparably low diffusivity of silicate network components that may control the clustering of the H_2O molecules in the melt (Navon and Lyakhovsky, 1998).

At identical decompression rates, the VAD79 CD samples with a P_{final} of 75 MPa reported in Appendix B have much lower N_V(n) than the corresponding CI and VAD79 samples with P_{final} of 100, 75 and 60 MPa that are documented in Appendix C. Their N_V(n) are within the error close to the values calculated with the model using a macroscopic surface tension (Appendix C). However, the initial H_2O contents in these samples were higher and the extended degassing timescale due to earlier onset of bubble nucleation and lower P_{final} probably led to extensive bubble interactions (Ostwald ripening and coalescence) that reduced the N_V(n). Toramaru (2006) adjusted the model parameters considering experimentally determined N_V(n)

of selected decompressed samples from previous degassing studies (e.g. Mangan and Sisson, 2000; Mourtada-Bonnefoi and Laporte, 2002). Some of these samples were probably subject to significant bubble interactions that reduced the N_V(n) during further decompression. This is evident from N_V(n) that decrease with increasing degassing timescale in experimental sets with similar decompression rates (Appendix C). It is probably necessary to improve current models for homogeneous bubble nucleation with data from new experiments that are not affected by Ostwald ripening and bubble coalescence.

3. Implications and limitations for future degassing studies

The results of this thesis will help to improve future experimental studies of homogeneous bubble nucleation and melt degassing to a point where the results of decompression experiments are only controlled by the decompression rate as single variable under otherwise identical conditions. Homogeneous bubble nucleation necessitates a single-phase melt prior to decompression. Bubble-free glass cylinders should be used as starting material. Depending on the timescale of decompression, the sample size must be sufficient to guarantee a melt pool that is not affected by volatile loss to heterogeneously nucleated bubbles at the capsule-melt interface. The ascent and growth of these bubbles narrows down the experimental window for decompression. In order to simulate continuous magma ascent, a continuous decompression rate corresponding to reasonable ascent rates has to be applied. For a more accurate determination of ΔP_{HoN}, the P_{final} has to be as close to the terminus of the nucleation event as possible (until the bubbles are detectable). Finally, the volume reduction of bubbles during quench has to be considered. High porosities in the samples prior to quench will force massive melt transport during cooling of the exsolved fluid and destroy the bubble texture. The bubble sizes and porosities determined from the vitrified samples have to be corrected for this quench effect.

4. Unresolved issues and outlook

The approximation for the bubble shrinkage factor can be refined to apply to variable H_2O contents around bubbles in the melt that influence T_f. Experiments with different melt compositions should be performed to investigate possible influences of melt viscosity prior to cooling on the extent of the volume reduction. The viscosity limit for shrinkage that corresponds to T_f could be narrowed down by isobaric in-situ cooling experiments of bubble-bearing melts at high P. The shrinking effect extremely complicates the investigation of diffusive bubble growth. However, if volatile concentration gradients around bubbles are detectable at some point, a precise knowledge of the melt flow around bubbles (e.g. by modeling) could enable the correction of the measured volatile concentration-distance profiles in the glass to the condition prior to rapid quench.

Simakin et al. (1999) stated that the expansion of welded capsules during decompression may provoke a nucleation event due to the mechanical perturbation. This could be true if the crimped headspaces suddenly expand due to a high preserved overpressure in the capsule compared to the ambient P in the autoclave. The timescale of capsule expansion is unknown, but it is unlikely that the walls or crimped headspaces of the precious metal sample container are very rigid at high T or that the welded seal is able to hold a significant overpressure of e.g. 5 MPa before leakage occurs. Nevertheless, the effects of sample container geometry (e.g. length of the crimped headspaces) and sealing method (lid vs. crimped headspace at identical sample diameter) have to be investigated in a forthcoming study. Significant overpressure in the capsules would delay bubble nucleation and degassing. The differences in the derived maximum ΔP_{HoN} for the VAD79 melt in this study and in Iacono Marziano et al. (2007) could be linked to this effect. However, it is also conceivable that a difference in porosity (and therefore also in the amount of initially trapped N_2) of the VAD79 glass cylinders is the reason for a low apparent ΔP_{HoN} for H_2O in Appendix B, because the presence of a few pre-existing H_2O-N_2 bubbles could have prevented homogeneous nucleation of H_2O bubbles at low CD rates. The initial porosity of the VAD79 glass cylinders was not determined for every sample. Considering the high $N_V(n)$ in the samples of the experiments with low decompression rates reported in Appendix C and the comparably high $N_V(n)$ in some samples of experiments with orders of magnitude higher decompression rates documented in Appendix B, it is conceivable

that the amount of initially nucleated bubbles is independent of the decompression rate. Only after bubble nucleation, the decompression rate (in combination with P_{final}) could become the controlling parameter for the evolution of the bubble population by defining the timescale available for the reduction of the N_V(n) by Ostwald ripening and bubble coalescence. It is also possible that the comparably low N_V(n) in the samples of CD experiments with low decompression rates reported in Appendix B could be a result from ascent of heterogeneously nucleated bubbles from the capsule-melt interface due to the increased degassing timescale. On the other hand, the effect of differences in the initial H_2O content in the melt on bubble nucleation are up to now barely constrained by experiments. Further CD experiments with different melt compositions and a wider range of decompression rates are necessary to investigate the onset of homogeneous bubble nucleation in greater detail. These experiments should be quenched at decreasing P_{final} in small P intervals to gaplessly document the influence of the degassing timescale. Additional CD experiments have to be performed with mixed volatiles such as H_2O-CO_2 fluids to approach the natural system. Differences in the fluid composition could influence ΔP_{HoN} and therefore the timescale available for degassing during magma ascent. Furthermore, sub-liquidus CD experiments will allow the combined study of homogeneous bubble nucleation in melts and heterogeneous nucleation on crystals as nucleation sites. The resulting datasets can be used to improve models for bubble nucleation and growth in ascending magmas that help to retrace the ascent and eruption dynamics of natural vesiculated samples.

References

Alidibirov, M. and Dingwell, D.B., 1996. Magma fragmentation by rapid decompression. Nature, 380(6570): 146-148.

Barclay, J., Riley, D.S. and Sparks, R.S.J., 1995. Analytical models for bubble growth during decompression of high viscosity magmas. Bulletin of Volcanology, 57(6): 422-431.

Bellucci, P., 2013. Decompression of magmas: Experimental and analytical optimization. Master thesis. University of Tübingen, 136 pp.

Berndt, J., Liebske, C., Holtz, F., Freise, M., Nowak, M., Ziegenbein, D., Hurkuck, W. and Koepke, J., 2002. A combined rapid-quench and H_2-membrane setup for internally heated pressure vessels: Description and application for water solubility in basaltic melts. American Mineralogist, 87(11-12): 1717-1726.

Blower, J.D., Keating, J.P., Mader, H.M. and Phillips, J.C., 2002. The evolution of bubble size distributions in volcanic eruptions. Journal of Volcanology and Geothermal Research, 120(1-2): 1-23.

Brugger, C.R. and Hammer, J.E., 2010. Crystallization kinetics in continuous decompression experiments: Implications for interpreting natural magma ascent processes. Journal of Petrology, 51(9): 1941-1965.

Carroll, M.R. and Webster, J.D., 1994. Solubilities of sulfur, noble gases, nitrogen, chlorine and fluorine in magmas. Reviews in Mineralogy, 30: 231-279.

Castro, J.M., Burgisser, A., Schipper, C.I. and Mancini, S., 2012. Mechanisms of bubble coalescence in silicic magmas. Bulletin of Volcanology, 74(10): 2339-2352.

Couch, S., Sparks, R.S.J. and Carroll, M.R., 2003. The kinetics of degassing-induced crystallization at Soufriere Hills volcano, Montserrat. Journal of Petrology, 44(8): 1477-1502.

Della Ventura, G., Bellatreccia, F., Marcelli, A., Guidi, M.C., Piccinini, M., Cavallo, A. and Piochi, M., 2010. Application of micro-FTIR imaging in the earth sciences. Analytical and Bioanalytical Chemistry, 397(6): 2039-2049.

Dingwell, D.B. and Webb, S.L., 1989. Structural relaxation in silicate melts and non-Newtonian melt rheology in geologic processes. Physics and Chemistry of Minerals, 16(5): 508-516.

Dingwell, D.B. and Webb, S.L., 1990. Relaxation in silicate melts. European Journal of Mineralogy, 2(4): 427-449.

Duan, X.Z., 2014. A general model for predicting the solubility behavior of H_2O-CO_2 fluids in silicate melts over a wide range of pressure, temperature and compositions. Geochimica et Cosmochimica Acta, 125: 582-609.

Duan, Z.H. and Zhang, Z.G., 2006. Equation of state of the H_2O, CO_2, and H_2O-CO_2 systems up to 10 GPa and 2573.15 K: Molecular dynamics simulations with ab initio potential surface. Geochimica et Cosmochimica Acta, 70(9): 2311-2324.

Gaonac'h, H., Lovejoy, S. and Schertzer, D., 2003. Percolating magmas and explosive volcanism. Geophysical Research Letters, 30(11).

Gardner, J.E., 2007. Bubble coalescence in rhyolitic melts during decompression from high pressure. Journal of Volcanology and Geothermal Research, 166(3-4): 161-176.

Gardner, J.E. and Denis, M.H., 2004. Heterogeneous bubble nucleation on Fe-Ti oxide crystals in high-silica rhyolitic melts. Geochimica et Cosmochimica Acta, 68(17): 3587-3597.

Gardner, J.E., Hilton, M. and Carroll, M.R., 1999. Experimental constraints on degassing of magma: Isothermal bubble growth during continuous decompression from high pressure. Earth and Planetary Science Letters, 168(1-2): 201-218.

Gardner, J.E., Hilton, M. and Carroll, M.R., 2000. Bubble growth in highly viscous silicate melts during continuous decompression from high pressure. Geochimica et Cosmochimica Acta, 64(8): 1473-1483.

Giordano, D., Nichols, A.R.L. and Dingwell, D.B., 2005. Glass transition temperatures of natural hydrous melts: A relationship with shear viscosity and implications for the welding process. Journal of Volcanology and Geothermal Research, 142(1-2): 105-118.

Giordano, D., Russell, J.K. and Dingwell, D.B., 2008. Viscosity of magmatic liquids: A model. Earth and Planetary Science Letters, 271: 123-134.

Gondé, C., Martel, C., Pichavant, M. and Bureau, H., 2011. In situ bubble vesiculation in silicic magmas. American Mineralogist, 96(1): 111-124.

Gonnermann, H.M. and Gardner, J.E., 2013. Homogeneous bubble nucleation in rhyolitic melt: Experiments and nonclassical theory. Geochemistry Geophysics Geosystems, 14(11): 4758-4773.

Gonnermann, H.M. and Manga, M., 2005. Nonequilibrium magma degassing: Results from modeling of the ca.1340 AD eruption of Mono Craters, California. Earth and Planetary Science Letters, 238(1-2): 1-16.

Gonnermann, H.M. and Manga, M., 2007. The fluid mechanics inside a volcano. Annual Review of Fluid Mechanics, 39: 321-356.

Hammer, J.E., 2008. Experimental studies of the kinetics and energetics of magma crystallization. Reviews in Mineralogy & Geochemistry, 69: 9-59.

Hammer, J.E. and Rutherford, M.J., 2002. An experimental study of the kinetics of decompression-induced crystallization in silicic melt. Journal of Geophysical Research - Solid Earth, 107(B1): 1-24.

Higgins, M.D., 2000. Measurement of crystal size distributions. American Mineralogist, 85(9): 1105-1116.

Higgins, M.D., 2006. Quantitative textural measurements in igneous and metamorphic petrology. Cambridge University Press, New York, 265 pp.

Hirth, J.P., Pound, G.M. and St. Pierre, G.R., 1970. Bubble nucleation. Metallurgical Transactions, 1(4): 939-945.

Holtz, F., Behrens, H., Dingwell, D.B. and Johannes, W., 1995. H_2O solubility in haplogranitic melts: Compositional, pressure and temperature dependence. American Mineralogist, 80(1-2): 94-108.

Hurwitz, S. and Navon, O., 1994. Bubble nucleation in rhyolitic melts: Experiments at high pressure, temperature and water content. Earth and Planetary Science Letters, 122(3-4): 267-280.

Iacono Marziano, G., Schmidt, B.C. and Dolfi, D., 2007. Equilibrium and disequilibrium degassing of a phonolitic melt (Vesuvius AD 79 "white pumice") simulated by decompression experiments. Journal of Volcanology and Geothermal Research, 161(3): 151-164.

Ippolito, S.B., Goldberg, B.B. and Unlu, M.S., 2005. Theoretical analysis of numerical aperture increasing lens microscopy. Journal of Applied Physics, 97(5).

Lapham, K.E., Holloway, J.R. and Delanay, J.R., 1984. Diffusion of H_2O and D_2O in obsidian at elevated temperatures and pressures. Journal of Non-Crystalline Solids, 67: 179-191.

Larsen, J.F. and Gardner, J.E., 2000. Experimental constraints on bubble interactions in rhyolite melts: Implications for vesicle size distributions. Earth and Planetary Science Letters, 180(1-2): 201-214.

Larsen, J.F. and Gardner, J.E., 2004. Experimental study of water degassing from phonolite melts: Implications for volatile oversaturation during magmatic ascent. Journal of Volcanology and Geothermal Research, 134(1-2): 109-124.

Lewis, E.N., Treado, P.J., Reeder, R.C., Story, G.M., Dowrey, A.E., Marcott, C. and Levin, I.W., 1995. Fourier-transform spectroscopic imaging using an infrared focal-plane array detector. Analytical Chemistry, 67(19): 3377-3381.

Manga, M., Castro, J., Cashman, K.V. and Loewenberg, M., 1998. Rheology of bubble-bearing magmas. Journal of Volcanology and Geothermal Research, 87(1-4): 15-28.

Mangan, M. and Sisson, T., 2000. Delayed, disequilibrium degassing in rhyolite magma: Decompression experiments and implications for explosive volcanism. Earth and Planetary Science Letters, 183: 441-455.

Marsh, B.D., 1988. Crystal Size Distribution (CSD) in rocks and the kinetics and dynamics of crystallization. 1. Theory. Contributions to Mineralogy and Petrology, 99(3): 277-291.

Martel, C. and Bureau, H., 2001. In situ high-pressure and high-temperature bubble growth in silicic melts. Earth and Planetary Science Letters, 191(1-2): 115-127.

Marxer, H., 2009. FT-IR-Messungen von CO_2-Konzentrationsprofilen in Rhyolith mit dem Focal-Plane-Array(FPA)-Detektor. Student research project. University of Tübingen, 38 pp.

Marxer, H., 2011. Entgasung von Magmen: Ein neuer experimenteller Ansatz. Diploma thesis. University of Tübingen, 122 pp.

Masotta, M., Ni, H. and Keppler, H., 2014. In situ observations of bubble growth in basaltic, andesitic and rhyodacitic melts. Contributions to Mineralogy and Petrology, 167(2).

Mastrolorenzo, G. and Pappalardo, L., 2006. Magma degassing and crystallization processes during eruptions of high-risk Neapolitan-volcanoes: Evidence of common equilibrium rising processes in alkaline magmas. Earth and Planetary Science Letters, 250(1-2): 164-181.

McIntosh, I.M., Llewellin, E.W., Humphreys, M.C.S., Nichols, A.R.L., Burgisser, A., Schipper, C.I. and Larsen, J.F., 2014. Distribution of dissolved water in magmatic glass records growth and resorption of bubbles. Earth and Planetary Science Letters, 401: 1-11.

Misiti, V., Vetere, F., Freda, C., Scarlato, P., Behrens, H., Mangiacapra, A. and Dingwell, D.B., 2011. A general viscosity model of Campi Flegrei (Italy) melts. Chemical Geology, 290: 50-59.

Morizet, Y., Nichols, A.R.L., Kohn, S.C., Brooker, R.A. and Dingwell, D.B., 2007. The influence of H_2O and CO_2 on the glass transition temperature: Insights into the effects of volatiles on magma viscosity. European Journal of Mineralogy, 19(5): 657-669.

Mourtada-Bonnefoi, C.C. and Laporte, D., 2002. Homogeneous bubble nucleation in rhyolitic magmas: An experimental study of the effect of H_2O and CO_2. Journal of Geophysical Research - Solid Earth, 107(B4).

Mourtada-Bonnefoi, C.C. and Laporte, D., 2004. Kinetics of bubble nucleation in a rhyolitic melt: An experimental study of the effect of ascent rate. Earth and Planetary Science Letters, 218(3-4): 521-537.

Navon, O. and Lyakhovsky, V., 1998. Vesiculation processes in silicic magmas. In: J.S. Gilbert and R.S.J. Sparks (Editors), The physics of explosive volcanic eruptions. Geological Society, London, Special Publications, 145: 27-50.

Nowak, M. and Behrens, H., 1997. An experimental investigation on diffusion of water in haplogranitic melts. Contributions to Mineralogy and Petrology, 126(4): 365-376.

Nowak, M. and Behrens, H., 2001. Water in rhyolitic magmas: Getting a grip on a slippery problem. Earth and Planetary Science Letters, 184(2): 515-522.

Nowak, M., Cichy, S.B., Botcharnikov, R.E., Walker, N. and Hurkuck, W., 2011. A new type of high-pressure low-flow metering valve for continuous decompression: First experimental results on degassing of rhyodacitic melts. American Mineralogist, 96: 1373-1380.

Nowak, M., Schreen, D. and Spickenbom, K., 2004. Argon and CO_2 on the race track in silicate melts: A tool for the development of a CO_2 speciation and diffusion model. Geochimica et Cosmochimica Acta, 68(24): 5127-5138.

Ochs, F.A. and Lange, R.A., 1999. The density of hydrous magmatic liquids. Science, 283(5406): 1314-1317.

Paonita, A. and Martelli, M., 2006. Magma dynamics at mid-ocean ridges by noble gas kinetic fractionation: Assessment of magmatic ascent rates. Earth and Planetary Science Letters, 241(1-2): 138-158.

Pichavant, M., Di Carlo, I., Rotolo, S.G., Scaillet, B., Burgisser, A., Le Gall, N. and Martel, C., 2013. Generation of CO_2-rich melts during basalt magma ascent and degassing. Contributions to Mineralogy and Petrology, 166(2): 545-561.

Proussevitch, A.A. and Sahagian, D.L., 1996. Dynamics of coupled diffusive and decompressive bubble growth in magmatic systems. Journal of Geophysical Research - Solid Earth, 101(B8): 17447-17455.

Randolph, A.D. and Larson, M.A., 1971. Theory of particulate processes. Academic Press, New York, 251 pp.

Rutherford, M.J., 2008. Magma Ascent Rates. Reviews in Mineralogy & Geochemistry, 69: 241-271.

Schmidt, B.C. and Behrens, H., 2008. Water solubility in phonolite melts: Influence of melt composition and temperature. Chemical Geology, 256(3-4): 259-268.

Shea, T., Gurioli, L., Larsen, J.F., Houghton, B.F., Hammer, J.E. and Cashman, K.V., 2010a. Linking experimental and natural vesicle textures in Vesuvius 79AD white pumice. Journal of Volcanology and Geothermal Research, 192(1-2): 69-84.

Shea, T., Houghton, B.F., Gurioli, L., Cashman, K.V., Hammer, J.E. and Hobden, B.J., 2010b. Textural studies of vesicles in volcanic rocks: An integrated methodology. Journal of Volcanology and Geothermal Research, 190(3-4): 271-289.

Sierralta, M., Nowak, M. and Keppler, H., 2002. The influence of bulk composition on the diffusivity of carbon dioxide in Na aluminosilicate melts. American Mineralogist, 87(11-12): 1710-1716.

Simakin, A.G., Armienti, P. and Epel'baum, M.B., 1999. Coupled degassing and crystallization: Experimental study at continuous pressure drop, with application to volcanic bombs. Bulletin of Volcanology, 61(5): 275-287.

Sparks, R.S.J., 1978. The dynamics of bubble formation and growth in magmas: A review and analysis. Journal of Volcanology and Geothermal Research, 3(1-2): 1-37.

Sparks, R.S.J., Baker, L., Brown, R.J., Field, M., Schumacher, J., Stripp, G. and Walters, A., 2006. Dynamical constraints on kimberlite volcanism. Journal of Volcanology and Geothermal Research, 155(1-2): 18-48.

Sparks, R.S.J., Barclay, J., Jaupart, C., Mader, H.M. and Phillips, J.C., 1994. Physical aspects of magmatic degassing. 1. Experimental and theoretical constraints on vesiculation. Reviews in Mineralogy, 30: 413-445.

Spickenbom, K., Sierralta, M. and Nowak, M., 2010. Carbon dioxide and argon diffusion in silicate melts: Insights into the CO_2 speciation in magmas. Geochimica et Cosmochimica Acta, 74(22): 6541-6564.

Thomas, N., Jaupart, C. and Vergniolle, S., 1994. On the vesicularity of pumice. Journal of Geophysical Research - Solid Earth, 99(B8): 15633-15644.

Toramaru, A., 1989. Vesiculation Process and Bubble Size Distributions in Ascending Magmas with Constant Velocities. Journal of Geophysical Research - Solid Earth, 94(B12): 17523-17542.

Toramaru, A., 2006. BND (bubble number density) decompression rate meter for explosive volcanic eruptions. Journal of Volcanology and Geothermal Research, 154(3-4): 303-316.

Ulmer, S., 2013. Entgasung eines trachytischen Campi Flegrei Magmas: Experimentelle Untersuchung der Auswirkungen des Ausgangsmaterials und der Abkühlungsgeschwindigkeit auf die H_2O-Entgasung einer trachytischen Schmelze. Bachelor thesis. University of Tübingen, 88 pp.

Voorhees, P.W., 1992. Ostwald ripening of 2-phase mixtures. Annual Review of Materials Science, 22: 197-215.

Wolf, J., 2014. Glaszylinder vs. Glaspulver als Ausgangsmaterial für die experimentelle Untersuchung der Entgasung von H_2O in einer phonolithischen Schmelze. Bachelor thesis. University of Tübingen, 80 pp.

Appendix A

Title

Micro-FTIR imaging: An advanced method for the determination of CO_2 and H_2O concentration gradients in silicate glasses

Authors

Holger Marxer, Marcus Nowak

Status

Published, 2013, European Journal of Mineralogy 25(3): 307-316
DOI: 10.1127/0935-1221/2013/0025-2299
Accepted author manuscript included with permission from Schweizerbart

Reviewers

Fabio Bellatreccia and an anonymous reviewer

Contributions of the candidate

Scientific ideas: 60 %
Data generation: 80 %
Analysis and interpretation: 80 %
Paper writing: 95 %

Micro-FTIR imaging: An advanced method for the determination of CO_2 and H_2O concentration gradients in silicate glasses

Holger Marxer* and Marcus Nowak

Department of Geosciences, University of Tübingen, Wilhelmstraße 56, 72074 Tübingen, Germany

*Corresponding author, e-mail: holger.marxer@uni-tuebingen.de

Abstract

Glass samples of diffusion couple experiments with rhyolitic to hawaiitic melts were analyzed by FTIR microscopy with a common single element and a 64x64 element focal plane array detector to obtain total CO_2 and H_2O concentration distance profiles. In contrast to the single element detector, the array detector facilitates mid-infrared spectral imaging with a resolution on a micrometer scale. The imaged sample information was converted to multiple parallel concentration distance profiles, using the absorption band areas of the dissolved volatile species. The bulk CO_2 and H_2O diffusivities from measurements with different array resolutions range from log D = -11.03 to -11.33 (D in $m^2 \cdot s^{-1}$) at 500 MPa and 1523-1623 K. All determined diffusion coefficients are within the error identical to single element detector analysis. Further test measurements were performed on a partially degassed, vesiculated phonolite in order to visualize the concentration of H_2O around bubbles. Both applications confirm that FTIR imaging is a convenient tool to investigate the spatial distribution of CO_2 and H_2O in silicate glasses, especially in terms of diffusion-related studies.

Key-words: FTIR microscopy, spectral imaging, FPA, CO_2, H_2O, diffusion, bubbles, silicate melt

1. Introduction

The detection of concentration gradients of volatiles such as H_2O and CO_2 in silicate glasses is essential for the quantification of diffusion processes in corresponding melts. Fourier-transform infrared (FTIR) microscopy in combination with the focal plane array (FPA) detector technology is an advanced tool for measurements of high spatial resolution. Multiple detector elements (pixel) allow the simultaneous recording of individual spectra within one measurement (frame). The employment of different detector materials enables either near-infrared (NIR) or mid-infrared (MIR) imaging in the range of 10000-500 cm^{-1}, corresponding to wavelengths of 1-20 µm (Lewis *et al.*, 1995). In most cases, commercially accessible arrays are multi-channel mid-infrared Mercury-Cadmium-Telluride (MCT) detectors for a spectral range of 4000-1000 cm^{-1}. The spectral range includes the fundamental OH-stretching vibration and the H_2O-bending vibration as well as the absorption bands of molecular CO_2 and CO_3^{2-} (Fine & Stolper, 1986; Davis & Tomozawa, 1996). Hence, this method can provide detailed information on the spatial distribution of H_2O and CO_2 in the sample.

There are already several studies in geosciences applying micro-FTIR imaging techniques. Most of these applications comprise imaging of CO_2 and H_2O distributions in different geologic materials. Della Ventura *et al.* (2010) compiled a review on new applications published so far and employed FPA imaging to visualize the kinetics of leucite dehydration with increasing temperature. Several studies involve the investigation of melt inclusions (MIs). Wysoczanski & Tani (2006) analyzed H_2O species concentration and distribution in volcanic glasses and in MIs within plagioclase crystals. Furthermore, Nichols & Wysoczanski (2007) determined CO_2 and H_2O concentrations in unexposed MIs hosted in olivine crystals. Qualitative and quantitative imaging of H-C-O groups in olivine-hosted MIs was applied by Mormone *et al.* (2011). Other FPA applications focus on the distribution of CO_2 and H_2O in single crystals from natural samples such as sodalite-group minerals (Balassone *et al.*, 2012), pollucite (Bellatreccia *et al.*, 2012) and cordierite (Della Ventura *et al.*, 2009, 2012). Ito & Nakashima (2002) detected liquid-like H_2O in polycrystalline quartz grains and finally, Prechtel & Stalder (2010, 2012) employed FPA imaging to locate OH-defects in synthetic enstatite.

With this study we want to propagate the use of micro-FTIR imaging in experimental petrology, especially for the investigation of CO_2 and H_2O diffusion. The first application is focused on the detection of one-dimensional concentration gradients of CO_2 and H_2O in synthetic silicate glasses to determine total CO_2 and H_2O diffusion coefficients in corresponding silicate melts. FPA imaging is compared with conventional single element (SE) detector micro-FTIR analysis to highlight the advantages. The second objective is to test FTIR imaging as a method for the visualization of H_2O concentration around vesicles in a quenched, hydrous phonolitic melt that was decompressed experimentally.

2. Sample characterization

FTIR measurements with a standard SE and a FPA detector were carried out on four samples of CO_2 diffusion couple experiments conducted by Sierralta *et al.* (2002) and Nowak *et al.* (2004). The diffusion couple technique facilitates investigation of unidirectional diffusion processes (Lapham *et al.*, 1984). The analyzed diffusion couples are of synthetic rhyolitc to hawaiitic composition (Table 1). The CO_2-free glass cylinders with a nominally dry composition (AbNa2, Rhyolite and Hawaiite) contain ~400-600 ppm of H_2O due to the incorporation of H_2O from the atmosphere during glass synthesis in the furnace. In the CO_2-bearing glass cylinders, the use of hygroscopic silver-oxalate as CO_2 source (Sierralta *et al.*,

2002; Nowak *et al.*, 2004) resulted in up to ~600 ppm of additional H_2O content, depending on the H_2O contamination level of the silver-oxalate (Table 1). Therefore, H_2O concentration distance profiles can be obtained after the CO_2 diffusion experiments if the difference in H_2O content within a diffusion couple is sufficiently high. The experiments were performed in an internally heated pressure vessel (IHPV) at 500 MPa and 1523 or 1623 K with an effective diffusion time (Nowak & Behrens, 1997) of about 1 h. The measured samples are double-sided ground and polished glass slabs prepared parallel to the diffusion direction of CO_2 with a thickness of 100 µm, containing no crystals and only few bubbles and cracks. The slabs are glued on slotted glass slides for infrared analysis in transmission mode. The samples were already analyzed with a SE detector for the determination of total CO_2 diffusion profiles (Sierralta *et al.*, 2002; Nowak *et al.*, 2004).

Additional FPA images were obtained from a vesiculated, phonolitic glass. A hydrous melt (containing 5.6 wt% H_2O) was synthesized in an IHPV at 200 MPa and 1323 K. Subsequently, the melt was isothermally decompressed to a final *P* of 75 MPa with a nominal decompression rate of 0.17 $MPa \cdot s^{-1}$, applying the multistep decompression technique provided by Iacono Marziano *et al.* (2007). At final *P*, the partially degassed melt was quenched rapidly to a crystal-free glass. The equilibrium H_2O-content in the residual melt at 75 MPa and 1323 K is ~3 wt% for this phonolitic composition (Iacono Marziano *et al.*, 2007). The vesiculated glass was double-sided ground and polished to a thickness of ~50 µm.

3. Analytical technique

3.1. FTIR spectroscopy

All MIR absorption spectra were acquired in transmission mode with a Bruker Vertex 80v vacuum FTIR spectrometer coupled with a Hyperion 3000 infrared microscope for spatially resolved measurements, using a globar light source and a KBr beamsplitter. Spectra were collected with 32 scans from 3950-950 cm^{-1} at a spectral resolution of 4 cm^{-1}. The spectrometer was evacuated and the microscope was flushed continuously with dried air to minimize the influence of atmospheric H_2O and CO_2. The microscope is equipped with both a SE-MCT detector, coupled with a knife-edge aperture in the beam path, and a FPA detector consisting of 64x64 MCT detector elements. Both detectors were used with a 15x Cassegrain objective.

The FPA detector facilitates fast micro-FTIR imaging by simultaneous acquisition of 4096 MIR spectra within less than 60 s at 32 scans, a spectral resolution of 4 cm^{-1} and a mirror

velocity of 5 kHz. In combination with the 15x objective, the array detector has a field of view (FOV) of 170x170 µm in the focal plane. Each pixel therefore maps a sample area of ~2.7x2.7 µm. Nevertheless, true maximum lateral resolution is limited by the wavelength-dependent diffraction of light (Ippolito *et al.*, 2005). The resolution of FPA detector measurements can be decreased by a pixel binning function with the Bruker OPUS spectroscopy software (version 7.0). Square pixel clusters with a side length of 2, 4, 8 or 16 detector elements are generated and the sample information across all binned detector elements is averaged. A digitally controlled, motorized sample stage facilitates automated mapping of large sample areas by gapless concatenation of multiple frames.

3.2. Band assignment

Background corrected spectra of the four CO_2-bearing glasses recorded with the SE detector are shown in Fig. 1. The references for background subtraction were taken from the CO_2-free part of the samples. All spectra show sinusoidal modulations due to partial internal reflection of the beam between the plane-parallel surfaces of the polished glass slabs, causing interference fringes (Tamic *et al.*, 2001). The spectra of the diffusion couples Rhyolite, Ab0.7H_2O and AbNa2 expose a distinct absorption band at ~2350 cm^{-1}, resulting from the ν_3 antisymmetric stretching vibration of dissolved molecular CO_2 (Fogel & Rutherford, 1990; Blank & Brooker, 1994). Due to the change in bulk composition towards the hawaiitic glass, the speciation of dissolved total CO_2 successively shifts from molecular CO_2 towards CO_3^{2-} (Fine & Stolper, 1986; Fogel & Rutherford, 1990; Sierralta *et al.*, 2002). The spectrum of the depolymerized Hawaiite only displays the absorption band doublet due to the ν_3 antisymmetric stretch vibration of distorted CO_3^{2-} in the range of 1750-1300 cm^{-1} (Fine & Stolper, 1986; Nowak *et al.*, 2004).

The broad absorption band at ~3570 cm^{-1} due to the fundamental OH stretching vibration (Davis & Tomozawa, 1996) in the spectra of the diffusion couples Rhyolite and AbNa2 also reveals the difference in total H_2O concentration (~300 and ~600 ppm) between the CO_2-bearing glass cylinder and the CO_2-free reference (Table 1). The concentration of OH is expressed as $c(H_2O)$ in wt% (Nowak & Behrens, 1995). Background subtraction with identical concentrations of OH in both reference and sample would have eliminated the OH absorption band, as evident from the spectra of the diffusion couples Ab0.7H_2O and Hawaiite. The spectra of AbNa2 and Rhyolite do not reflect the actual H_2O content within these samples.

However, the relative values of H_2O concentration, used as basis for the determination of the total H_2O diffusion coefficient, are not affected by this background subtraction.

3.3. Determination of concentration distance profiles

In order to validate the comparability of SE and FPA detector results to the previous measurements by Sierralta *et al.* (2002) and Nowak *et al.* (2004), total CO_2 and H_2O concentration distance profiles were at first determined with the conventional SE detector method. Single absorption spectra were collected using a knife-edge aperture of 15x170 µm with the short side length parallel to the volatile diffusion direction (Fig. 2). Each recorded spectrum displays the averaged information of the analyzed sample volume. Background measurements were programmed after every 10th measurement to minimize the effect of changes in the concentration of atmospheric H_2O and CO_2 and to avoid influence of instrumental drift. Analyses were performed in increments of 10 µm parallel to the diffusion direction, resulting in an overlap of 5 µm for consecutive measurements (Fig. 2). The fixed increments were adjusted by the motorized sample stage. All SE measurements result in a single concentration distance profile for each sample. Profiles range from maximum to zero CO_2 concentration on a length of 1.5-2.5 mm. The mere analytical time for obtaining a single concentration distance profile with the SE detector is around 30-40 minutes.

FPA mapping was applied to the identical sample volume using the maximum detector resolution of 64x64 pixel as well as binned resolutions of 16x16 and 4x4 pixel clusters for each 170x170 µm frame. Every pixel or cluster records an individual spectrum with the averaged sample information of the corresponding volume. The mapping was restricted to the direction of diffusion and reference spectra were recorded prior to each measured frame. Analytical times for FPA sample mapping are comparable to conventional SE detector analysis at the described settings, but the resulting data density is many times higher. In contrast to the SE detector method, FPA mapping at maximum resolution results in 64 parallel, gapless profiles. The recorded spectra are sorted by column across all FPA frames (Fig. 2). Measurements with binned resolutions correspondingly contain 16 or 4 parallel profiles at chosen mapping parameters. The pixel binning function was applied to test the influence of lateral resolution in the direction of diffusion on the concentration distance profile.

For both the SE and the FPA method, the peak areas of either the molecular CO_2 (Rhyolite & Ab0.7H_2O) or the CO_3^{2-} absorption band (AbNa2 & Hawaiite) were used to obtain

total CO_2 concentration distance profiles (Nowak *et al.*, 2004; Spickenbom *et al.*, 2010). The peak areas were determined by integration, applying a tangential linear baseline correction provided by the OPUS spectroscopy software. H_2O concentration distance profiles on the basis of the OH fundamental stretching mode (Fig. 1) could be obtained from AbNa2. The spectrum of the Rhyolite also reveals a small H_2O concentration difference of ~300 ppm between the CO_2-bearing and the CO_2-free glass cylinder. However, the corresponding OH concentration distance profiles in this sample were very inhomogeneous. These profiles were excluded from further analysis.

Exported OPUS output data had to be converted from relative sample coordinates to absolute diffusion distances. Cracks within the glass slabs artificially extend the length of the obtained concentration distance profiles of H_2O or CO_2 (Fig. 3). To avoid influences of crack-related data points on the determination of the diffusion coefficients, all affected values were cut out of each profile. The widths of the cracks in the direction of diffusion were measured by optical microscopy. The profile lengths were then corrected for this displacement. For each FPA resolution, the mean values of all data points at the same diffusion distance in the parallel profiles were calculated to create a single concentration distance profile. The corresponding total CO_2 and H_2O diffusion coefficients D_{CO2}^{total} and D_{H2O}^{total} for both SE and averaged FPA profiles were derived from least-square fits of an applied error function (Nowak *et al.*, 2004). Considering the concentration-dependent diffusion of H_2O, D_{H2O}^{total} can be derived by a modified Boltzmann-Matano analysis, utilizing Fick's second law (Nowak & Behrens, 1997). However, since the total concentrations and the concentration difference of incorporated H_2O in the diffusion couple AbNa2 are in the range of several hundred ppm (Table 1), H_2O diffusion is presumed to be independent of concentration. Therefore, the same error function used for the determination of D_{CO2}^{total} is applied in a first approximation to calculate D_{H2O}^{total}. For this approximation, concentration distance profiles based on the relative values of H_2O concentration are sufficient. The derived D_{H2O}^{total} for AbNa2 are only valid for the specific H_2O contents and *P*-*T* conditions listed in Table 1.

3.4. Imaging of H_2O concentration around vesicles in a silicate glass

Further single frame FPA test measurements were performed on the experimentally decompressed, quenched phonolitic melt. MIR spectra were recorded at a FPA resolution of 64x64 pixel, using air as reference for background subtraction. The concentration of H_2O is

imaged as peak area of the OH absorption band at ~3600 cm^{-1}. The OH peak areas were determined applying a tangential linear baseline correction, provided by the OPUS software.

4. Results and discussion

4.1. Geometric effects

FPA measurements with a resolution of 64x64 pixel enable detailed imaging of sample features like cracks or bubbles inside the glass (Fig. 4a, b). Data points related to the crack in the rhyolitic sample can be clearly assigned by the breakdown in peak area of molecular CO_2. The transmitted light image displays a width of ~25 µm in the un-forked part of the crack (Fig. 4a). Nevertheless, the determined peak areas are affected to a lateral extent of more than 50 µm (Fig. 4b). The difference to the measured width in the transmitted light image can be attributed to the crack geometry within the sample. For most samples, the crack surfaces do not run parallel to the beam path. In the affected sample volume, the MIR signal passes through two offset, superimposed glass wedges (Fig. 5a). The beam therefore travels through a reduced sample thickness and crosses non-plane-parallel surfaces. This leads to partial reflection as well as refraction of the beam and causes blurring of the crack edges. Thinning of the glass wedges (Fig. 5a) also results in imaging of apparent concentration gradients towards the crack (Fig. 4b), because the absorption is dependent on sample thickness. Due to these distorting geometric effects, all affected data points were deleted during profile length correction. However, the length of the profiles was only corrected for the actual width of the crack. This resulted in data gaps, but the fitting procedure with the error function is stable enough despite missing data points.

Similar geometric effects have to be considered if FPA imaging is used for the partially degassed, vesiculated phonolite. The analyzed sample volume contains a completely closed vesicle (Fig. 5b, A) and a bubble cut at both top and bottom (Fig. 5b, B). Assuming spherical vesicle growth, FPA transmittance analysis will provide the most detailed information on H_2O distribution if applied on a very thin section with a bubble cut at both sides. The curvature of the bubble wall and of possible spherical diffusion fronts around the bubble is reduced to a nearly planar excerpt, situated plane-parallel to the beam path. In contrast to an enclosed vesicle, the analyzed glass volume with variable thickness is minimized (Fig. 5b).

4.2. Concentration distance profiles and diffusion coefficients

For each diffusion couple, the comparison of the resulting total CO_2 (and H_2O) concentration distance profiles of the SE and the FPA method displays the same trend. The profiles of the rhyolitic sample were chosen as representative examples (6a-d). The three sets of multiple parallel profiles obtained by FPA mapping and the SE detector profile reveal identical concentration gradients. All profiles display the crack in the glass. The difference in the breakdown of peak area in the FPA profiles due to the crack is a consequence of applied detector resolution. Depending on the binning factor, each data point corresponds to a profile segment of 42.5, ~10.6 or ~2.7 µm. The crack, affecting a volume with a width of ~50 µm (Fig. 5a), is therefore only imaged roughly with a high pixel binning factor.

Increasing FPA resolution intensifies scattering of the determined peak areas (Fig. 6a-c). This effect can be attributed to the quality of the recorded MIR spectra. The signal-to-noise (S/N) ratio of the individual spectra increases with the number of binned detector elements (Fig. 7). The energy information collected by each detector element is used to create an averaged spectrum for each pixel cluster, resulting in reduced spectral noise. A low S/N ratio randomly influences the peak areas, especially for low IR-active species concentrations or broad absorption bands (e.g. OH-band at ~3570 cm^{-1}). Automated peak area determination also contributes to the observed scattering. The erratically distributed noise patterns in the spectra interfere with the fixed limits of integration at specific wavenumbers. The slope of the applied baseline, and therefore the peak area of the absorption band, varies for the individual spectra. This effect could be minimized by manual peak area determination. The SE detector spectra display the highest signal to noise (S/N) ratios due to the recording of a single, averaged spectrum for a FOV of 15x170 µm. Nevertheless, the variations in determined peak areas (Fig. 6d) are comparable to FPA measurements with 16x16 pixel (~10.6x10.6 µm, Fig. 6b). This can be attributed to a similar lateral resolution in the direction of CO_2 diffusion.

Despite different S/N ratios of the individual spectra and variable resolutions in the direction of diffusion, the SE concentration distance profile and the averaged profiles obtained by FPA mapping are almost congruent (Fig. 8a). The number of recorded spectra and the advantage to average over multiple parallel profiles at highest FPA resolution reduces the scattering of the peak areas to a minimum. Likewise, the error function fits of the averaged profiles display matching trends (Fig. 8b).

For each diffusion couple and every applied method, the derived total CO_2 diffusion coefficients (Table 2; D in [$m^2 \cdot s^{-1}$]) are identical within the error of ~0.15 log units of the former SE detector analysis by Sierralta *et al.* (2002) and Nowak *et al.* (2004). At 1623 K and 500 MPa the determined log D_{CO2}^{total} range from -11.10 to -11.22 for the Rhyolite and from -11.17 to -11.21 for the Hawaiite. SE and FPA analysis of the diffusion couples Ab0.7H_2O and AbNa2 result in log D_{CO2}^{total} from -11.18 to -11.33 at 1523 K.

The obtained OH concentration distance profile for AbNa2 displays the same gradient as the corresponding CO_3^{2-} profile (Fig. 8c). In comparison to the peak areas of CO_3^{2-} at the highest FPA resolution, the scattering of the averaged OH peak areas is more pronounced due to the described effect of a broad absorption band at a low S/N ratio. Nevertheless, the fitted profiles at FPA mapping with 64x64 pixel are still congruent (Fig. 8d). The derived log D_{H2O}^{total} for the SE and the FPA method range from -11.03 to -11.29 for the specific H_2O concentrations in the diffusion couple (Table 1). Considering the small concentration difference (about 600 ppm), the symmetrical total H_2O concentration distance profile implies in first approximation concentration-independent H_2O diffusion. The application of an error function to calculate D_{H2O}^{total} is therefore considered to be convenient for such low H_2O concentration differences. The derived diffusivities of total H_2O and CO_2 for AbNa2 are within the error identical at 1523 K and 500 MPa.

The application of different FPA resolutions within each diffusion couple does not affect the reproducibility of the derived diffusion coefficients. The obtained concentration distance profiles with a length of more than 1 mm are barely influenced by averaging the sample information over ~2.7 or 42.5 µm in the direction of volatile diffusion. All glasses are nearly free of cracks and bubbles within the concentration gradients. The correction of diffusion distances and the elimination of affected data points also barely influenced the determined diffusion coefficients. However, the influence of lateral resolution in the direction of diffusion will become crucial for shorter concentration distance profiles.

4.3. H_2O concentration around vesicles in a silicate glass

The comparison of the transmitted light image (Fig. 9a) with the OH concentration image (Fig. 9b) reveals nearly homogeneous concentration of H_2O around the bubbles in the quenched, decompressed phonolitic melt. The vesicle in the lower left part of the frame (Fig. 9a, A) is completely surrounded by glass. Despite the small dimension of ~10 µm of the

vesicle in the direction of the IR beam (determined by optical microscopy in combination with the z-drive of the motorized sample stage), the outline is still visible in the OH concentration image due to the described geometric effects. The glass thickness around the vesicle varies and the beam path is altered by non-plane-parallel surfaces (Fig. 5b, A). On the contrary, the OH concentration image of the big vesicle (Fig. 9a, B) cut at both top and bottom in the center of the frame is decisively sharper (Fig. 9b, B). The dark rim around the bubble in the transmitted light image corresponds to a concentration gradient in the OH concentration image. In consideration of the homogeneous H_2O distribution in the rest of the sample, this feature is interpreted as an apparent concentration gradient due to the thinning of the glass slab caused by the remaining curvature of the bubble wall (Fig. 5b, B). At a nominal decompression rate 0.17 $MPa \cdot s^{-1}$, the readjustment of thermodynamic equilibrium prior to rapid quench could have eliminated the expected spherical H_2O concentration gradients around the bubble.

5. Conclusion and outlook

Due to the simultaneous acquisition of multiple parallel concentration distance profiles, FTIR imaging is particularly suited to study diffusion processes of CO_2 and H_2O in silicate melts. In comparison to conventional SE detector analysis, FPA imaging is proven to yield reliable diffusion data with a high data density on a micrometer scale in a short time. Nevertheless, transmission measurements for the investigation of diffusion processes should be considered with caution if the diffusion front in the sample is not plane-parallel to the beam path. Concentration gradients in the direction of the beam path cannot be displayed.

Future objectives are the elucidation of diffusive H_2O and CO_2 bubble growth and to study the fractionation of these volatiles in ascending magmas by analyzing the quenched melts of continuous decompression experiments (Nowak *et al.*, 2011). FPA test measurements on partially crystallized samples are in progress to investigate H_2O distribution and possible concentration gradients in the glass matrix around crystals.

Acknowledgements

This project was funded by the Deutsche Forschungsgemeinschaft (NO378/5-1). We thank Daniel Russ for programming a VBA tool for easy re-ordering and further processing of OPUS output data and Dr. Gernot Höhne from Bruker Optics GmbH for additional information related to the FPA detector. Thanks to Ph.D. Fabio Bellatreccia and an anonymous reviewer for their competent and helpful comments.

References

Balassone, G., Bellatreccia, F., Mormone, A., Biagioni, C., Pasero, M., Petti, C., Mondillo, N., Fameli, G. (2012): Sodalite-group minerals from the Somma-Vesuvius volcanic complex, Italy: A case study of K-feldspar-rich xenoliths. *Mineral. Mag.* **76**, 191-212.

Bellatreccia, F., Della Ventura, G., Gatta, G.D., Guidi, M.C., Harley, S. (2012): Carbon dioxide in pollucite, a feldspathoid with the ideal composition $(Cs,Na)_{16}Al_{16}Si_{32}O_{96}\cdot nH_2O$. *Mineral. Mag.* **76**, 903-911.

Blank, J.G. & Brooker, R.A. (1994): Experimental studies of carbon dioxide in silicate melts: Solubility, speciation, and stable carbon isotope behavior. *Rev. Mineral.*, **30**, 157-186.

Davis, K.M. & Tomozawa, M. (1996): An infrared spectroscopic study of water-related species in silica glasses. *J. Non-Cryst. Solids*, **201**, 177-198.

Della Ventura, G., Bellatreccia, F., Cesare, B., Harley, S., Piccinini, M. (2009): FTIR microspectroscopy and SIMS study of water-poor cordierite from El Hoyazo, Spain: Application to mineral and melt devolatilization. *Lithos*, **113**, 498-506.

Della Ventura, G., Bellatreccia, F., Marcelli, A., Guidi, M.C., Piccinini, M., Cavallo, A., Piochi, M. (2010): Application of micro-FTIR imaging in the earth sciences. *Anal. Bioanal. Chem.*, **397**, 2039-2049.

Della Ventura, G., Radica, F., Bellatreccia, F., Cavallo, A., Capitelli, F., Harley, S. (2012): Quantitative analysis of H_2O and CO_2 in cordierite using polarized FTIR spectroscopy. *Contrib. Mineral. Petrol.*, **164**, 881-894.

Fine, G. & Stolper, E. (1986): Dissolved carbon-dioxide in basaltic glasses: Concentrations and speciation. *Earth Planet. Sci. Lett.*, **76**, 263-278.

Fogel, R.A. & Rutherford, M.J. (1990): The solubility of carbon dioxide in rhyolitic melts: A quantitative FTIR study. *Am. Mineral.*, **75**, 1311-1326.

Ippolito, S.B., Goldberg, B.B., Unlu, M.S. (2005): Theoretical analysis of numerical aperture increasing lens microscopy. *J. Appl. Phys.*, **97**, 053105.

Ito, Y. & Nakashima, S. (2002): Water distribution in low-grade siliceous metamorphic rocks by micro-FTIR and its relation to grain size: A case from the Kanto Mountain region, Japan. *Chem. Geol.*, **189**, 1-18.

Lapham, K.E., Holloway, J.R., Delanay, J.R. (1984): Diffusion of H_2O and D_2O in obsidian at elevated temperatures and pressures. *J. Non-Cryst. Solids*, **67**, 179-191.

Lewis, E.N., Treado, P.J., Reeder, R.C., Story, G.M., Dowrey, A.E., Marcott, C., Levin, I.W. (1995): Fourier-transform spectroscopic imaging using an infrared focal-plane array detector. *Anal. Chem.*, **67**, 3377-3381.

Iacono Marziano, G., Schmidt, B.C., Dolfi, D. (2007): Equilibrium and disequilibrium degassing of a phonolitic melt (Vesuvius AD 79 "white pumice") simulated by decompression experiments. *J. Volc. Geotherm. Res.*, **161**, 151-164.

Mormone, A., Piochi, M., Bellatreccia, F., De Astis, G., Moretti, R., Della Ventura, G., Cavallo, A., Mangiacapra, A. (2011): A CO_2-rich magma source beneath the Phlegraean Volcanic District (Southern Italy): Evidence from a melt inclusion study. *Chem. Geol.*, **287**, 66-80.

Nichols, A.R.L. & Wysoczanski, R.J. (2007): Using micro-FTIR spectroscopy to measure volatile contents in small and unexposed inclusions hosted in olivine crystals. *Chem. Geol.*, **242**, 371-384.

Nowak, M. & Behrens, H. (1995): The speciation of water in haplogranitic glasses and melts determined by in situ near-infrared spectroscopy. *Geochim. Cosmochim. Acta*, **59**, 3445-3450.

Nowak, M. & Behrens, H. (1997): An experimental investigation on diffusion of water in haplogranitic melts. *Contrib. Mineral. Petrol.*, **126**, 365-376.

Nowak, M., Schreen, D., Spickenbom, K. (2004): Argon and CO_2 on the race track in silicate melts: A tool for the development of a CO_2 speciation and diffusion model. *Geochim. Cosmochim. Acta*, **68**, 5127-5138.

Nowak, M., Cichy, S.B., Botcharnikov, R.E., Walker, N., Hurkuck, W. (2011): A new type of high-pressure low-flow metering valve for continuous decompression: First experimental results on degassing of rhyodacitic melts. *Am. Mineral.*, **96**, 1373-1380.

Prechtel, F. & Stalder, R. (2010): FTIR spectroscopy with a focal plane array detector: A novel tool to monitor the spatial OH-defect distribution in single crystals applied to synthetic enstatite. *Am. Mineral.*, **95**, 888-891.

Prechtel, F. & Stalder, R. (2012): OH-defects in Al- and Cr- doped synthetic enstatites and defect geobarometry on natural orthopyroxenes from the earth's mantle. *Eur. J. Mineral.*, **24**, 471-481.

Sierralta, M., Nowak, M., Keppler, H. (2002): The influence of bulk composition on the diffusivity of carbon dioxide in Na aluminosilicate melts. *Am. Mineral.*, **87**, 1710-1716.

Spickenbom, K., Sierralta, M., Nowak, M. (2010): Carbon dioxide and argon diffusion in silicate melts: Insights into the CO_2 speciation in magmas. *Geochim. Cosmochim. Acta*, **74**, 6541-6564.

Tamic, N., Behrens, H., Holtz, F. (2001): The solubility of H_2O and CO_2 in rhyolitic melts in equilibrium with a mixed CO_2-H_2O fluid phase. *Chem. Geol.*, **174,** 333-347.

Wysoczanski, R. & Tani, K. (2006): Spectroscopic FTIR imaging of water species in silicic volcanic glasses and melt inclusions: An example from the lzu-Bonin arc. *J. Volc. Geotherm. Res.*, **156**, 302-314.

Tables

Table 1: Experimental parameters and characterization of the analyzed diffusion couple samples.

	AbNa2[1]	Ab0.7H_2O[1]	Rhyolite[2]	Hawaiite[2]
***P* [MPa]**	500	500	500	500
***T* [°K]**	1523	1523	1623	1623
***c* (CO_2) [wt%]**	0.20	0.20	0.20	0.20
***c* (H_2O) [wt%][3]**	0.11/0.05	0.73/0.73	0.07/0.04[4]	0.06/0.06[4]
$t_{effective}$[5] **[s]**	3770	3770	3798	3798

Notes: For further details see [1]Sierralta *et al.* (2002) and [2]Nowak *et al.* (2004). Ab0.7H_2O = albitic composition with additional 0.7 wt% H_2O (original exp. no. D38), AbNa2 = albite with 2 wt% Na_2O in excess (original exp. no. D25). The rhyolitic and hawaiitic composition are simplified and iron-free (original run no. Rh01-CO2 and Ha01-CO2). [3]The concentration of H_2O in the CO_2-doped/CO_2-free glass cylinders can be different. [4]The H_2O contents in the CO_2-free rhyolitic and hawaiitic glass cylinders were not determined explicitly by Nowak *et al.* (2004). For this study, the H_2O concentrations were determined following the same method, using the peak heights of the OH-absorption band from MIR measurements with air as reference. *c*(OH) is expressed as *c*(H_2O) in wt% (Nowak & Behrens, 1995). [5]$t_{effective}$ = effective diffusion time (Nowak & Behrens, 1997).

Table 2: Comparison of the derived logarithmic diffusion coefficients log D_{CO2}^{total} and log D_{H2O}^{total} (D in [$m^2 \cdot s^{-1}$]).

	analyzed species	SE (2002/2004)	SE (current)	FPA 4x4 pixel	FPA 16x16 pixel	FPA 64x64 pixel
AbNa2	CO_3^{2-}	-11.22[1]	-11.26	-11.33	-11.33	-11.30
	OH	n.d.	-11.17	-11.03	-11.07	-11.29
Ab0.7H$_2$O	CO_2 (mol.)	-11.33[1]	-11.29	-11.18	-11.29	-11.28
Rhyolite	CO_2 (mol.)	-11.10[2]	-11.10	-11.13	-11.15	-11.22
Hawaiite	CO_3^{2-}	-11.18[2]	-11.19	-11.20	-11.17	-11.21

Notes: [1]Sierralta *et al.* (2002) and [2]Nowak *et al.* (2004). Ab0.7H_2O = albitic composition with additional 0.7 wt% H_2O, AbNa2 = albite with 2 wt% Na_2O in excess. The error is estimated to be ~0.15 log units for total CO_2 (Nowak *et al.*, 2004). The error for log D_{H2O}^{total} was not determined, but is expected to be slightly higher than for log D_{CO2}^{total} due to the low S/N ratio of the broad OH absorption band.

Figure captions

Fig. 1: Background subtracted MIR SE detector spectra of measurements in the CO_2 (H_2O)-bearing cylinder half of the diffusion couples, using reference spectra collected in the CO_2-free part of the samples. Ab0.7H_2O = albitic composition with additional 0.7 wt% H_2O, AbNa2 = albite with 2 wt% Na_2O in excess. Further diffusion couple details are provided in Table 1. Spectra are shifted for clarity.

Fig. 2: Comparison of measurements with the SE (left) and the FPA detector (right). Sample mapping with the SE detector was performed with an aperture of 15x170 µm in increments of 10 µm, resulting in one spectrum for each aperture frame and a single concentration distance profile. The illustrated FPA measurement represents a detector resolution of 64x64 pixel. Each detector element is assigned an individual spectrum obtained with a FOV of ~2.7x2.7 µm. Column-wise data handling results in 64 parallel concentration distance profiles.

Fig. 3: FPA mapping of the rhyolitic sample consisting of 10 frames (170x170 µm each frame) in the direction of diffusion at a resolution of 64x64 pixel, resulting in 4096 individual spectra each frame. The displayed peak areas of the CO_2^{mol} absorption band are assembled in 64 parallel concentration distance profiles. The crack in the transmitted light image in the bottom of the plot is clearly imaged by the breakdown of the determined peak areas.

Fig. 4: (a) Transmitted light image of the crack in the Rhyolite. The width of the crack is ~25 µm in the un-forked part. The black frame (170x170 µm) confines the glass volume of a single frame FPA measurement. The sample thickness is 100 µm. (b) Corresponding CO_2^{mol} concentration image, derived from a FPA measurement at 64x64 pixel. The peak areas around the crack are affected to a lateral extent of more than 50 µm and display an apparent concentration gradient due to the crack geometry within the sample (Fig. 5a).

Fig. 5: (a) Schematic section parallel to the beam path through the un-forked part of the crack in the Rhyolite. In the affected sample volume the IR beam passes a variable glass thickness and non-plane-parallel surfaces. Decreasing sample thickness can lead to imaging of apparent concentration gradients. (b) Schematic section parallel to beam path through two bubbles in the partially degassed phonolite. Bubble A is closed and completely surrounded by glass, bubble B is cut at top and bottom. Assuming spherical concentration gradients around the bubbles, transmittance measurements for the determination of spatial volatile distribution in the glass around a bubble will provide the most detailed information for a thin sample and a cut bubble. The curvature of the bubble wall and of concentration gradients towards the bubble is minimized and bubble-glass transitions of the IR beam are reduced to a small sample volume. In both schematic sections the beam path was simplified for graphical reasons.

Fig. 6: CO_2^{mol} concentration distance profiles of the rhyolitic sample for FPA mapping with 10 frames (170x170 µm each frame) in the direction of diffusion at (a) 4x4 pixel (4 parallel profiles), (b) 16x16 pixel (16 parallel profiles) and (c) 64x64 pixel (64 parallel profiles). (d) CO_2^{mol} concentration distance profile determined by SE detector analysis. The breakdown in CO_2^{mol} peak area corresponds to the crack in the glass.

Fig. 7: Comparison of individual spectra from the Rhyolite for SE and FPA measurements. The S/N ratio of the spectra decreases with increasing FPA resolution. Spectra are shifted for clarity.

Fig. 8: (a) Length-corrected CO_2^{mol} concentration distance profiles of the Rhyolite. The parallel profiles obtained by FPA mapping were averaged to a single profile for each FPA resolution. Profiles are shifted for clarity. (b) The corrected profiles of the Rhyolite were fitted with an error function. Total CO_2 concentration is normalized from 1 (max. *c*) to 0 (min. *c*). (c) Length-corrected and averaged CO_3^{2-} and OH concentration distance profiles of sample AbNa2, determined by FPA mapping at 64x64 pixel. AbNa2 = albite with 2 wt% Na_2O in excess. Profiles are shifted for clarity. (d) Fitted error functions for AbNa2. Total CO_2 and H_2O concentration is normalized from 1 (max. *c*) to 0 (max. *c*).

Fig. 9: (a) Transmitted light image of a closed vesicle surrounded by glass (A) and a bubble cut at top and bottom (B) in the experimentally decompressed phonolite. The black frame (170x170 µm) confines the glass volume of a single frame FPA measurement. The sample thickness is about 50 µm. (b) Corresponding OH concentration image, derived from a FPA measurement at 64x64 pixel. The outlines of the enclosed vesicle (A) are blurred, whereas the cut bubble (B) is imaged sharply. The concentration gradient corresponding to the black rim in the transmitted light image is probably due to the decreasing glass thickness at the bubble wall, as illustrated in Fig. 5b.

Figures

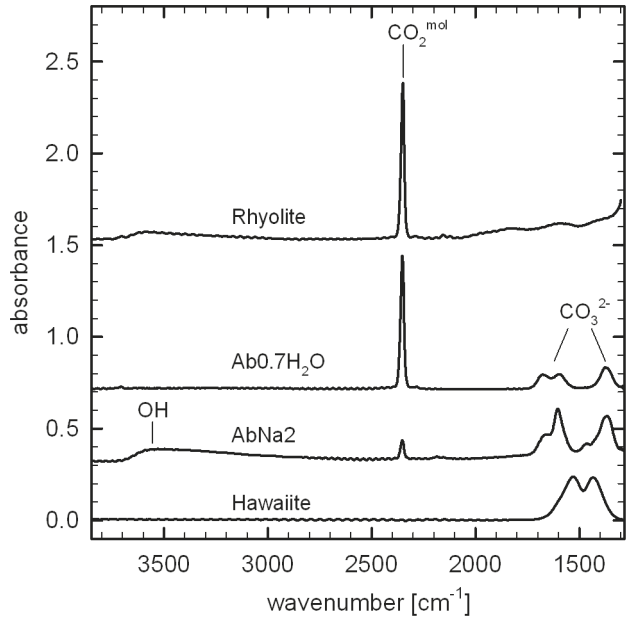

Fig. 1

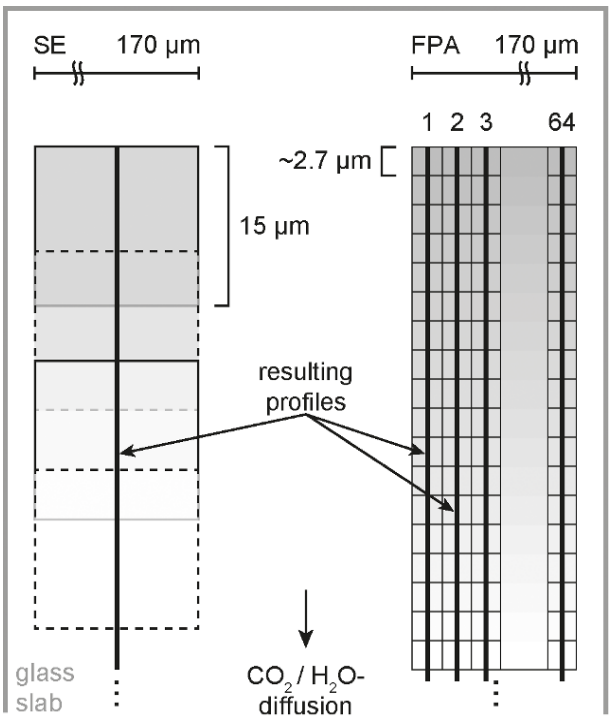

Fig. 2

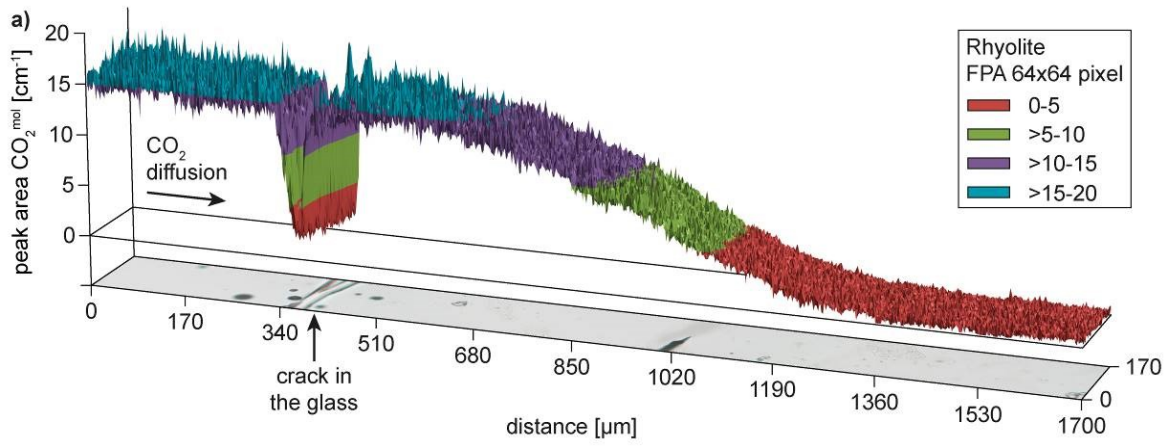
a)
peak area CO_2^{mol} [cm^{-1}]
20
15
10
5
0
CO_2 diffusion
Rhyolite
FPA 64x64 pixel
0-5
>5-10
>10-15
>15-20
0
170
340
510
680
850
1020
1190
1360
1530
1700
crack in the glass
distance [µm]
170
0

Fig. 3

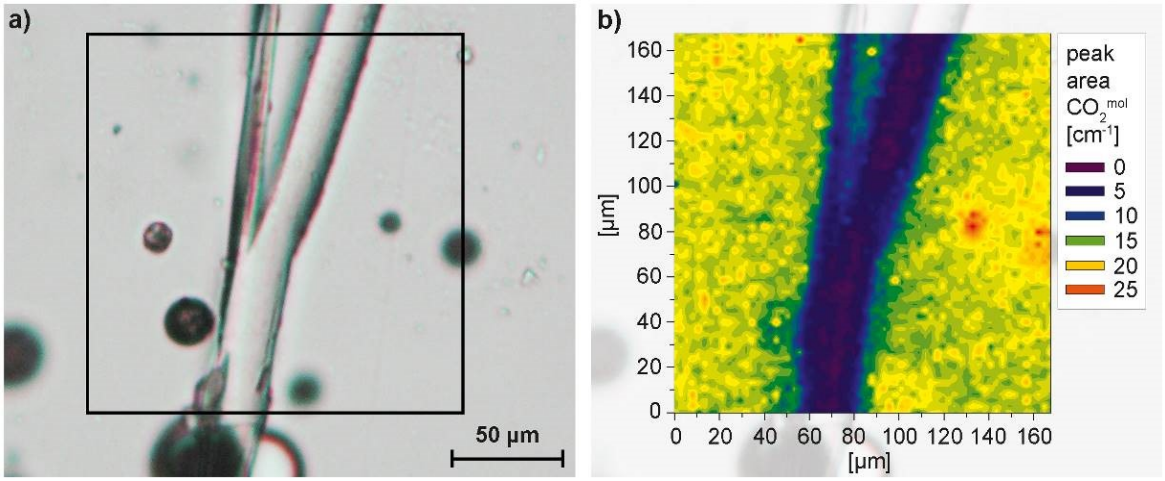
a)
50 µm
b)
[µm]
0
20
40
60
80
100
120
140
160
peak area CO_2^{mol} [cm^{-1}]
0
5
10
15
20
25

Fig. 4a, b

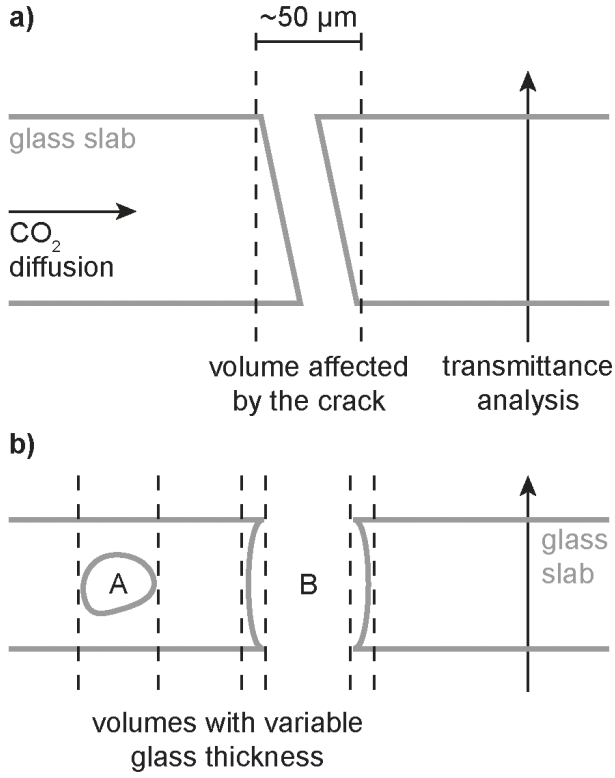
a)
~50 µm
glass slab
CO2
diffusion
volume affected
by the crack
transmittance
analysis
b)
A
B
glass
slab
volumes with variable
glass thickness

Fig. 5a, b

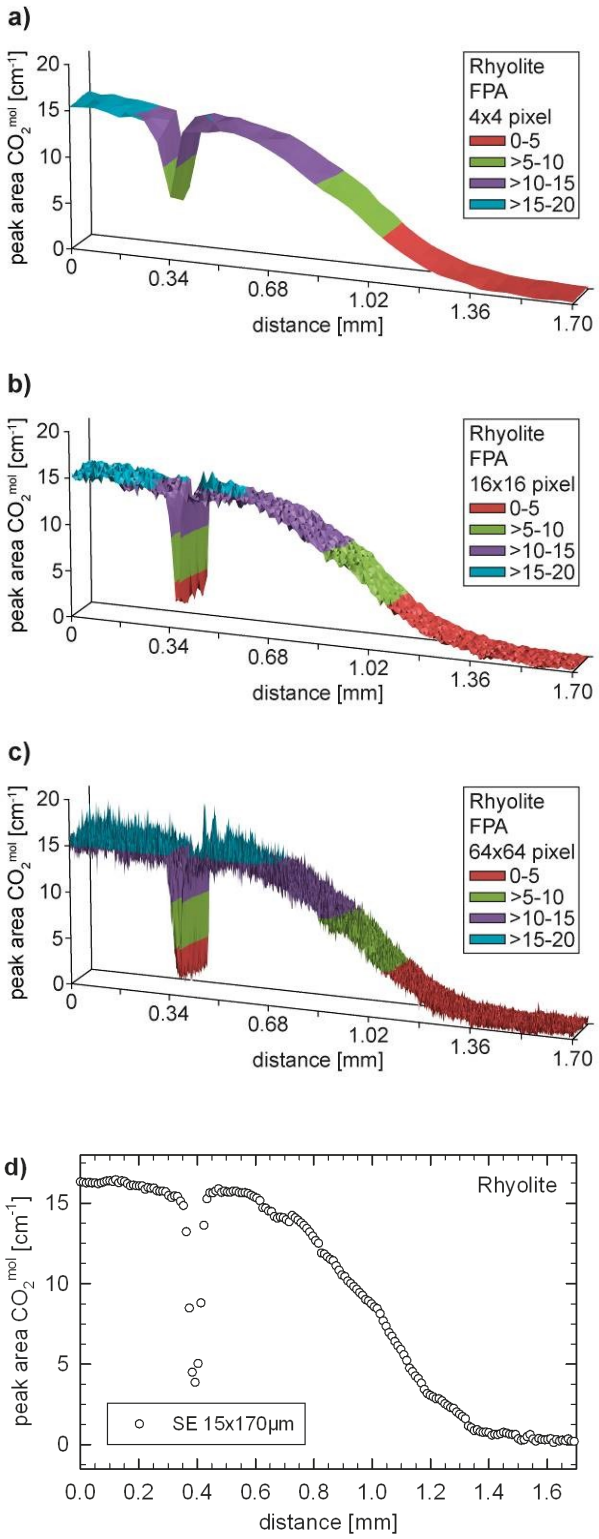
a)
peak area CO_2^{mol} [cm^{-1}]
Rhyolite
FPA
4x4 pixel
0-5
>5-10
>10-15
>15-20
distance [mm]
b)
Rhyolite
FPA
16x16 pixel
c)
Rhyolite
FPA
64x64 pixel
d)
Rhyolite
SE 15x170µm

Fig. 6a-d

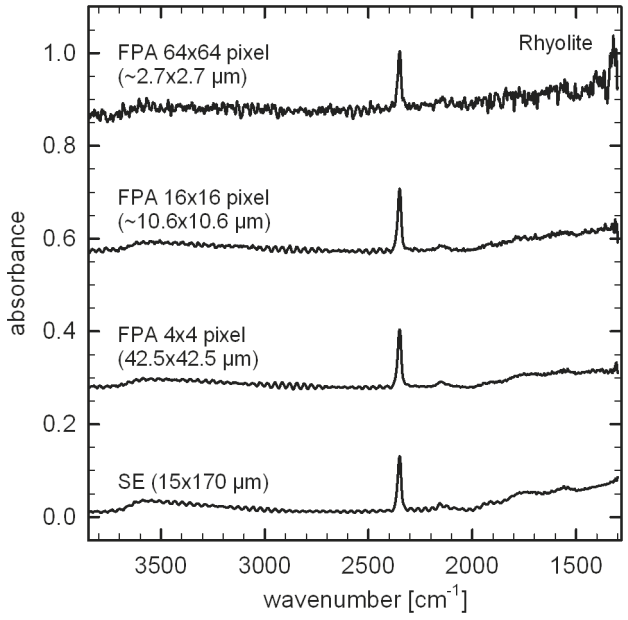
Rhyolite
FPA 64x64 pixel
(~2.7x2.7 µm)
FPA 16x16 pixel
(~10.6x10.6 µm)
FPA 4x4 pixel
(42.5x42.5 µm)
SE (15x170 µm)
absorbance
1.0
0.8
0.6
0.4
0.2
0.0
3500
3000
2500
2000
1500
wavenumber [cm-1]

Fig. 7

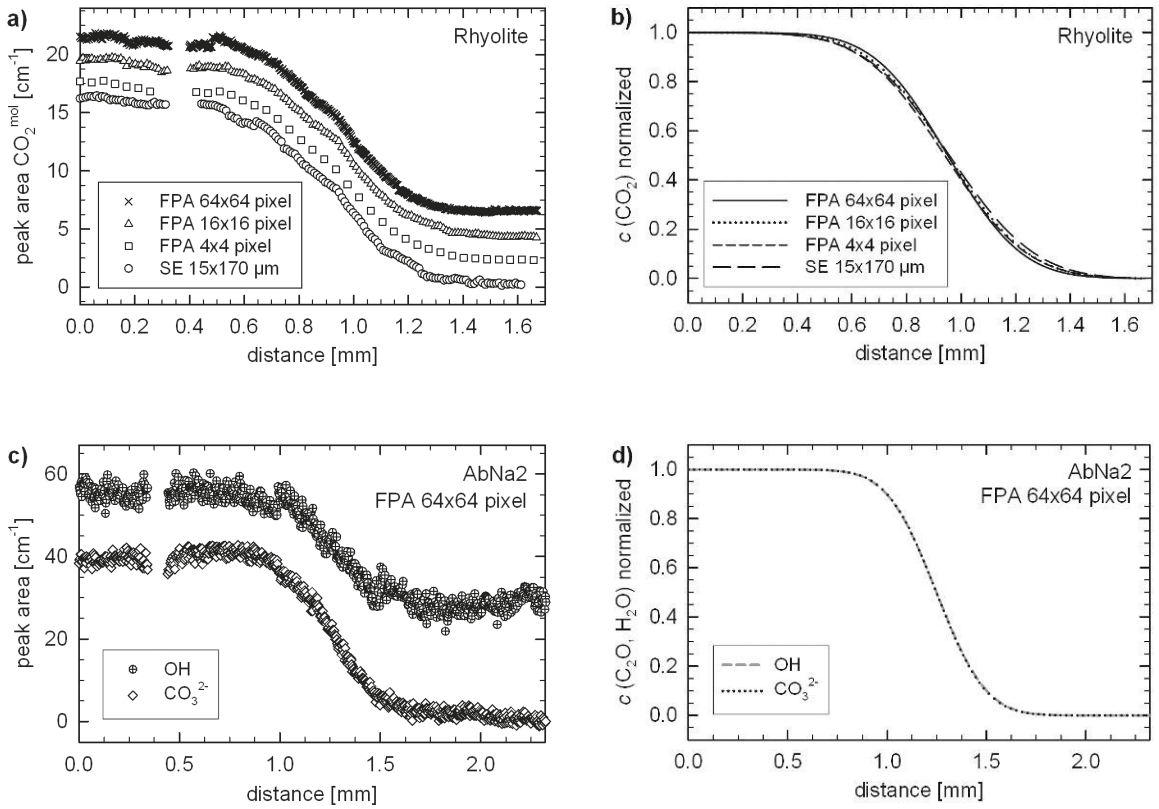

Fig. 8a-d

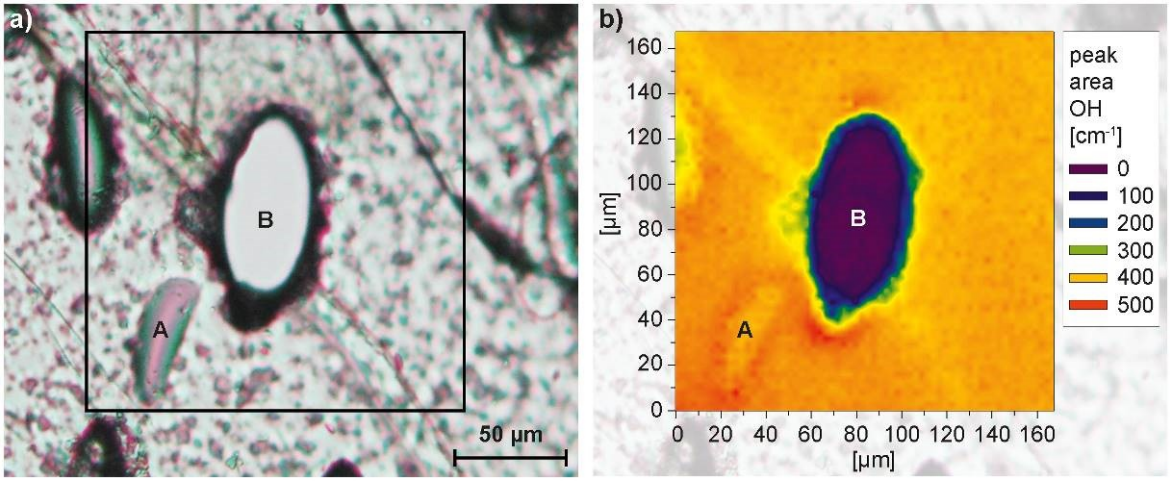

Fig. 9a, b

Appendix B

Title

Degassing of H_2O in a phonolitic melt: A closer look at decompression experiments

Authors

Holger Marxer, Philipp Bellucci, Marcus Nowak

Status

Published, 2015, Journal of Volcanology and Geothermal Research 297: 109-124

DOI: 10.1016/j.jvolgeores.2014.11.017

Reviewers

Madeleine Humphreys and an anonymous reviewer

Contributions of the candidate

Scientific ideas: 75 %

Experimental work: 50 %

Data generation: 50 %

Analysis and interpretation: 80 %

Paper writing: 90 %

Journal of Volcanology and Geothermal Research 297 (2015) 109–124

Contents lists available at ScienceDirect

Journal of Volcanology and Geothermal Research

journal homepage: www.elsevier.com/locate/jvolgeores

Degassing of H_2O in a phonolitic melt: A closer look at decompression experiments

Holger Marxer *, Philipp Bellucci, Marcus Nowak

Department of Geosciences, University of Tübingen, Wilhelmstraße 56, 72074 Tübingen, Germany

ARTICLE INFO

Article history:
Received 14 April 2014
Accepted 14 November 2014
Available online 17 February 2015

Keywords:
Decompression experiment
H_2O
Phonolitic melt
Degassing
Bubble

ABSTRACT

Melt degassing during magma ascent is controlled by the decompression rate and can be simulated in decompression experiments. H_2O-bearing phonolitic melts were decompressed at a super-liquidus T of 1323 K in an internally heated argon pressure vessel, applying continuous decompression (CD) as well as to date commonly used step-wise decompression (SD) techniques to investigate the effect of decompression method on melt degassing. The hydrous melts were decompressed from 200 MPa at nominal decompression rates of 0.0028–1.7 MPa·s^{-1}. At final pressure (P_{final}), the samples were quenched rapidly at isobaric conditions with ~150 K·s^{-1}. The bubbles in the quenched samples are often deformed and dented. Flow textures in the glass indicate melt transport at high viscosity. We suggest that this observation is due to bubble shrinkage during quench. This general problem was mostly overlooked in the interpretation of experimentally degassed samples to date. Bubble shrinkage due to decreasing molar volume (V_m) of the exsolved H_2O in the bubbles occurs during isobaric rapid quench until the melt is too viscous too relax. The decrease of $V_m(H_2O)$ during cooling at P_{final} of the experiments results in a decrease of the bubble volume by a shrinking factor B_s:

$$B_s = \frac{V_m(H_2O)\left[P_{final}, T_{rq}\right]}{V_m(H_2O)\left[P_{final}, T_f\right]}$$

where T_{rq} is the run temperature of the sample prior to isobaric rapid quench and T_f is the fictive temperature where the bubbles stop to shrink. In a first approximation, the glass transition temperature (T_g) of the melt can be used for T_f. At a P_{final} of 75 MPa and a T_g of ~840 K in our experiments, the bubble volume decreases by a B_s of ~2.5. Thus, bubble textures, size distributions and porosities derived from the vitrified samples do not correspond to the conditions prior to isobaric rapid quench. Nevertheless, the volume fraction of bubbles (X_b) in the melt can be calculated by:

$$X_b(\text{melt}) = \frac{B_s \cdot X_b(\text{glass})}{1 + [B_s \cdot X_b(\text{glass})] - X_b(\text{glass})}$$

using the measured volume fraction of bubbles in the glass in consideration of B_s. The corrected porosities are within a relative error of <10% equal to the expected porosities at T_{rq} that can be easily calculated from the residual H_2O content in the glass.

At nominal decompression rates >0.17 MPa·s^{-1} and a P_{final} of 75 MPa, the decompression method has only minor influence on melt degassing. SD and CD result in high bubble number densities of 10^4–10^5 mm^{-3}. Fast P drop leads to immediate supersaturation with H_2O in the melt. At such high nominal decompression rates, the diffusional transport of H_2O is limited and therefore bubble nucleation is the predominant degassing process. The residual H_2O contents in the melts decompressed to 75 MPa increase with nominal decompression rate. After homogeneous nucleation is triggered, CD rates ≤0.024 MPa·s^{-1} facilitate continuous reduction of the supersaturation by H_2O diffusion into previously nucleated bubbles. Bubble number densities of CD samples with low nominal decompression rates are several orders of magnitude lower than for SD experiments and the bubble diameters are larger. The reproducibility of MSD experiments with low nominal decompression rates is worse than for CD runs. Commonly used SD techniques are therefore not suitable to simulate melt degassing during continuous magma ascent with low ascent rates.

* Corresponding author. Tel.: +49 7071 29 76097.
E-mail address: holger.marxer@uni-tuebingen.de (H. Marxer).

http://dx.doi.org/10.1016/j.jvolgeores.2014.11.017
0377-0273/

1. Introduction

Melt degassing is the jet propulsion of magma ascent. Decompression of magma induces supersaturation with dissolved volatiles such as H_2O, CO_2 and sulfur compounds in the melt and results in nucleation and growth of bubbles (Sparks, 1978; Gonnermann and Manga, 2007). Volatile exsolution primarily controls magma ascent velocity and the eruptive style of a volcano (e.g., Eichelberger et al., 1986; Woods and Koyaguchi, 1994; Mangan et al., 2004; Gonnermann and Manga, 2007). Open or closed system degassing is influenced by viscosity of the magma, volatile diffusivity as well as bubble interconnectivity and set terms for explosive or effusive volcanism. The concealed processes of homogeneous bubble nucleation and growth during magma ascent can be investigated by decompression experiments with volatile-bearing melts. A crucial parameter for these experiments is the decompression rate, which is directly proportional to magma ascent velocity. Natural ascent rates cover a wide range, from 0.001 to 0.015 $m \cdot s^{-1}$ for felsic and intermediate magmas in the crust, 0.1–10 $m \cdot s^{-1}$ for effusive MORBs and more than 200 $m \cdot s^{-1}$ for kimberlites and explosive eruptions (e.g., Paonita and Martelli, 2006; Sparks et al., 2006; Rutherford, 2008; Misiti et al., 2011).

Due to technical limitations, a step-wise decompression (SD) method was used in most previous experimental studies for the simulation of continuous magma ascent. The pressure was either released by single- or multi-step decompression (SSD/MSD) with decompression rates of 2.5–10 $MPa \cdot s^{-1}$ for the decompression steps (e.g., Hurwitz and Navon, 1994; Lyakhovsky et al., 1996; Larsen and Gardner, 2004; Gardner, 2007). After *P* drop, the sample was annealed for a certain amount of time at lower pressure. Nominal continuous decompression (CD) rates were interpolated between the onset of a decompression step and the endpoint of the subsequent annealing period (e.g., Gardner et al., 1999; 2000; Hammer and Rutherford, 2002; Larsen et al., 2004; Gardner, 2007; Iacono Marziano et al., 2007). These nominal decompression rates are sometimes orders of magnitude lower than the rate of the actual decompression step. Assuming an average bulk rock density of 2.7 $g \cdot cm^{-3}$, the rapid decompression steps correspond to extreme ascent velocities of 93–370 $m \cdot s^{-1}$, realized in nature only during kimberlitic volcanism. To date, only few decompression experiments were performed using CD with reasonable decompression rates (e.g., Mangan and Sisson, 2000; Brugger and Hammer, 2010; Pichavant et al., 2013). The SD technique was therefore compared to true, continuous decompression by Nowak et al. (2011) to determine the influence of decompression path on melt degassing. A hydrous, rhyodacitic melt was decompressed at a nominal decompression rate of 0.28 $MPa \cdot s^{-1}$ with SSD, MSD and CD. SD resulted in enhanced bubble nucleation due to sudden supersaturation of H_2O within the melt, whereas CD favored bubble growth as predominant degassing mechanism.

Besides the method of decompression, further problems arise during quenching of the vesiculated sample. Hurwitz and Navon (1994) already presumed that the volume of H_2O-filled bubbles in the melt decreases during cooling, but did not go into further details. However, the consideration of bubble shrinkage is important for the interpretation of data (such as porosities, bubble diameters etc.) that are derived from vitrified samples of decompression experiments. Nevertheless, the consequences of bubble shrinkage during quench were not taken into account in further experimental studies. A first quantification of the actual volumetric loss of a bubble during isobaric rapid quench due to cooling of the exsolved H_2O was presented by Marxer et al. (2013). Recently, McIntosh et al. (2014) additionally reported on decreasing bubble volumes during quench due to resorption of H_2O from fluid into the melt. It is essential to realize and investigate such quench effects for a critical evaluation of experimental data.

One aim of this study is to compare the H_2O degassing behavior of a phonolitic melt at SSD, MSD and CD at different decompression rates to verify the basic results of the single set of decompression experiments from Nowak et al. (2011) for a less silicic melt composition from Vesuvius and a smaller step-size at MSD. The main experimental parameters were adopted from the decompression experiments of Iacono Marziano et al. (2007). A further objective is to demonstrate major experimental and analytical problems. Especially bubble shrinkage during quench due to cooling of the exsolved H_2O was mostly not considered in the interpretation of experimental data to date and is now quantified in this study.

2. Experimental and analytical methods

2.1. Starting material and capsule preparation

Batches of phonolitic glass (Table 1) were synthesized on the basis of the EMP analysis from Iacono Marziano et al. (2007) of the "white pumice" from the Vesuvius AD79 (VAD79) eruption. A mixture of dried oxide (SiO_2, TiO_2, Al_2O_3, FeO, MnO, MgO) and carbonate ($CaCO_3$, Na_2CO_3, K_2CO_3) powders was ground up for 30 min in a ball mill. Phosphorus was added as $(NH_3)_2HPO_4$. The powder mixture was slowly decarbonized in a furnace at 1 atm and finally fused at 1873 K for 6 h in a $Pt_{90}Rh_{10}$ crucible. After the melt was quenched rapidly in water, the shattered glass was ground up again for 20 min for final homogenization and re-melted at 1873 K for 1 h. This melt was air-cooled to produce a crack-less glass. The quench rate was sufficient to prevent crystallization during cooling. 6–7 mm long cylinders with diameters of 2.5 and 5 mm were drilled out of the glass. The different cylinder diameters were used to investigate the effects of sample size in the decompression experiments. The edges of the glass cylinders were ground to prevent cutting of the capsule material during pressurization in the autoclave prior to heating.

The glass cylinders with 2.5 mm diameter were sealed in Pt-capsules with an outer diameter of 3 mm and a wall thickness of 0.25 mm (initial tube length 15–17 mm). Deionized water was loaded at the bottom of the capsules. The Pt-capsules were closed by crimping the ends together with flat-nose pliers and the seams were welded shut. The glass cylinders with 5 mm diameter were sealed in $Au_{80}Pd_{20}$-capsules with an outer diameter of 5.4 mm and a wall thickness of 0.2 mm (initial tube length 13 mm). The bottoms of the AuPd-capsules were closed with fitting inner lids and the top was crimped using a drill chuck, resulting in a three-armed star. After welding, all capsules were checked for leaks by heating (1 h at 383 K in the compartment dryer) and subsequent re-weighing.

Table 1
Chemical composition of the synthesized VAD79 glass by EMPA.

	[wt.%][a]	1σ[b]
SiO_2	57.53	0.63
TiO_2	0.29	0.02
Al_2O_3	20.73	0.18
FeO[c]	2.71	0.19
MnO	0.14	0.03
MgO	0.38	0.03
CaO	3.32	0.11
Na_2O	5.28	0.17
K_2O	9.53	0.21
P_2O_5	0.10	0.03
Σ	100.00	

A total number of 17 analyses distributed over several pieces of glass was used for the determination of the chemical composition of the starting material.
[a] Averaged chemical composition, normalized to 100 wt.%.
[b] 1σ is the standard deviation of the mean value.
[c] Total Fe as FeO.

2.2. Isobaric experiments

All experiments were performed in a vertically operated internally heated argon pressure vessel (IHPV) with a rapid quench setup (Berndt et al., 2002). The isobaric experiments were conducted to determine H_2O solubilities and to produce reference glasses for electron microprobe (EMP) and Fourier transform infrared (FTIR) analysis. Six Pt-capsules were loaded with 2.5 mm glass cylinders and increasing weighed portions of ~2–6 wt.% H_2O (Table 2). These samples were equilibrated at super-liquidus conditions of 200 MPa and 1323 K to generate homogeneous, H_2O-bearing melts. One solubility experiment with a 2.5 mm cylinder was performed at 75 MPa and 1323 K. A minimum equilibration time (t_{eq}) of 72 h was derived from the time series experiments of Iacono Marziano et al. (2007). Another experiment was conducted with a 5 mm cylinder and ~5 wt.% H_2O at 200 MPa and 1323 K. A t_{eq} of 96 h was sufficient for the diffusion and homogeneous distribution of the H_2O into the melt cylinder (Table 2). After equilibration, the samples were quenched rapidly with ~150 $K \cdot s^{-1}$ at isobaric conditions. The quench rate was reported in Berndt et al. (2002).

2.3. Decompression experiments

The IHPV is equipped with a special high-*P* valve construction (Nowak et al., 2011), facilitating both CD and SD. The super-liquidus starting conditions of 200 MPa and 1323 K as well as the range of nominal decompression rates from 0.0028 to 1.7 $MPa \cdot s^{-1}$ were adopted from Iacono Marziano et al. (2007). The solubility of H_2O at starting conditions prior to decompression was found to be 5.6 wt.% (Table 2). The 2.5 mm glass cylinders were sealed in Pt-capsules with ~6 wt.% deionized H_2O to ensure a H_2O-saturated melt coexisting with a free fluid phase prior to decompression (Iacono Marziano et al., 2007). The AuPd-capsules were loaded with ~5 wt.% H_2O for slightly fluid-undersaturated conditions. All decompression experiments were carried out in two steps. The samples were equilibrated for 72 h (2.5 mm cylinders) or 96 h (5 mm cylinders) at 200 MPa and 1323 K. The required equilibration periods for homogeneous H_2O distribution in the melt were adopted from the synthesis of the reference glasses (Table 2). Subsequently after equilibration, the samples were decompressed isothermally using SSD, MSD and CD (Table 3). MSD was performed in steps of approximately 10 MPa (Fig. 1). The decompression rate for the actual decompression steps at SD was ~10 $MPa \cdot s^{-1}$. This rate corresponds to a magma ascent velocity of 370 $m \cdot s^{-1}$. The CD rates compare to ascent velocities of 0.1–63 $m \cdot s^{-1}$. Due to the fast decompression rate during SD, the error of the *P* drop during the decompression steps is up to 1.5 MPa. A final pressure (P_{final}) of 75 MPa was chosen for the comparison of SD and CD run products. Two additional CD experiments were decompressed to 150 and 100 MPa to determine a minimum *P* for the onset of bubble nucleation and growth. At P_{final} the samples were quenched rapidly with ~150 $K \cdot s^{-1}$ at isobaric conditions.

Table 2
Synthesis of the H_2O-bearing reference glasses.

Exp. #	Cylinder diameter [mm]	P_{eq} [MPa]	t_{eq} [h]	Weighed portion of H_2O in capsule [wt.%][a]	Total H_2O content in glass by FTIR [wt.%][b]
REF02	2.5	200	96	1.98(0.22)[c]	2.20(0.01)
REF03	2.5	200	96	3.00(0.23)[c]	3.10(0.01)
REF04	2.5	200	96	3.88(0.20)[c]	4.10(0.06)
REF05	2.5	200	96	5.04(0.23)[c]	5.15(0.05)
REF06	2.5	200	96	5.68(0.20)[d]	5.60(0.10)
REF09	2.5	200	72	6.14(0.18)[d]	5.63(0.07)
REF08	2.5	75	96	3.74(0.20)[d]	3.01(0.04)
REF12	5.0	200	96	4.86(0.05)[c]	4.89(0.12)

Equilibration temperature (T_{eq}) was 1323 K for all experiments. Equilibration pressure (P_{eq}) and time (t_{eq}) varied.
The extinction coefficients (ε) and the density (ρ) of the glasses for the calculation of the H_2O content were adopted from Iacono Marziano et al. (2007): $\varepsilon(4470\ cm^{-1}) = 1.14 \pm 0.09$ and $\varepsilon(5210\ cm^{-1}) = 1.18 \pm 0.09$ [$l \cdot mol^{-1} \cdot cm^{-1}$]; $\rho = 2.47 - (0.013$ wt.% $H_2O)$ [$g \cdot cm^{-3}$].
[a] Weighing error in brackets.
[b] Means of at least 10 individual measurements over the whole sample ($\pm 1\sigma$ in brackets).
[c] H_2O-undersaturated.
[d] H_2O in excess.

2.4. Sample preparation

The samples were weighed after the experiments to check for leaks. Most of the capsules were deformed after the decompression experiments. Many of these show an inflexion of the walls around the middle of the capsule and inflated headspaces. The specimens were cut in half lengthwise along the cylinder axis, mostly through the maximum deformation. One half was directly embedded (sample enclosed by the noble metal container) with the cut surface upside. This surface was ground and polished on for scanning electron microscopy (SEM) and EMP analysis. The other cylinder half was carefully peeled out of the capsule and also embedded with the cut surface upside. These glasses were double-sided ground parallel to the cut surface down to a thickness of 125–500 μm (depending on the porosity of the specimen) and polished for FTIR transmission measurements. The FTIR samples were mostly ground on the side opposing the cut surface to obtain a maximum sample area.

2.5. EMP analysis and SEM images

The glass composition was analyzed by WDS measurements with a JEOL JXA 8900 R EMP at an acceleration voltage of 15 kV and a beam current of 4 nA. All samples were measured with a defocused beam of 20 μm diameter. The peak counting times were set to 10 s (Na), 16 s (K, Si, Ca, Al, Mg and Fe) and 30 s (Mn, Ti and P). The residual total H_2O content in the glass of some highly vesiculated samples was determined using the by-difference method (Devine et al., 1995). The nominally dry VAD79 starting glass and the synthesized H_2O-bearing glasses (REF02-06, Table 2) were used as reference samples. At least 10 measurements were performed on each of those references.

For some of their decompressed samples, Mangan and Sisson (2000) and Iacono Marziano et al. (2007) already demonstrated decreasing H_2O concentrations from the center of the glass cylinders to the side wall of the capsules. This was explained by H_2O diffusion towards the heterogeneously nucleated bubbles at the capsule-melt interface during decompression. The residual total H_2O contents (also those by FTIR) of the decompressed samples in this study were therefore determined parallel to the cylinder axis in the center area of the specimens on the basis of at least 10 individual measurements. The determination of the residual H_2O content in the glass with the by-difference technique in extremely vesiculated samples is difficult. In general, this method has a comparably low accuracy and precision (>0.5 wt.%; Devine et al., 1995). This is most probably the main reason for the relatively high standard deviations of the means of the H_2O contents determined with this technique in the fast decompression experiments (Table 3). Bubbles just beneath the polished surface in or very close to the excitation volume could additionally result in infrequent overestimation of the residual H_2O content in the glass, especially in highly vesiculated samples with bubble interstices on a micrometer scale.

Back-scattered electron (BSE) images were recorded with a LEO 1450 VP SEM at a resolution of 1024 × 768 pixel. The magnification was adjusted to resolve the smallest bubbles in each sample. The bisected capsules were completely mapped with up to 60 single BSE images. These images were stitched together and corrected for differences in tonal value.

Table 3
Synopsis of the decompression experiments and the main results.

Exp. #	Cylinder diameter [mm]	Nominal decomp. rate $\Delta P \cdot \Delta t^{-1}$ [MPa·s^{-1}]	P_{final} [MPa]	SSD/MSD decomp. step [MPa]	Total H_2O content dissolved in melt at P_{start} [wt.%][a]	Excess total H_2O in capsule at P_{start} [wt.%][b]	Residual total H_2O content in the glass by FTIR/*by-diff.* [wt.%][c]	Number of analyzed bubble intersections	X_b(glass) · 100;2D porosity (glass) by ImageJ [area%][d]	3D porosity (glass) from BSD [vol%]	Expected porosity (melt) [vol%][e]	X_b(melt) · 100;corrected 2D porosity (melt) [vol%][f]	N_V(t) (glass) [mm^{-3}][g]	N_V(n) [mm^{-3}][h]
CD06	2.5	0.0028	75	–	5.63(0.07)	0.60	3.24(0.05)	–	n.d.	n.d.	n.d.	n.d.	4[i]	5[i]
MSD06	2.5	0.0028	75	10	5.63(0.07)	0.40	2.97(0.11)	59	5.9	7.6(2.7)	n.d.	n.d.	153	166
SSD03	2.5	0.0028	75	125	5.63(0.07)	0.44	3.02(0.04)	148	13.4	18.8(5.4)	n.d.	n.d.	709	873
CD07	2.5	0.024	75	–	5.63(0.07)	0.54	3.23(0.03)	–	n.d.	n.d.	n.d.	n.d.	16[i]	20[i]
CD08	2.5	0.024	75	–	5.63(0.07)	0.50	3.20(0.08)	104	17.6	19.2(3.7)	30.6	34.7	143	177
MSD02	2.5	0.024	75	10	5.63(0.07)	0.46	3.34(0.31)	57	12.7	16.8(5.3)	29.4	26.5	64	77
MSD07	2.5	0.024	75	10	5.63(0.07)	0.40	3.29(0.22)	540	15.2	18.6(3.1)	29.8	30.9	3090	3796
SSD04	2.5	0.024	75	125	5.63(0.07)	0.48	n.d.[j]	1033	16.0	18.5(1.5)	n.d.	n.d.	90,600	111,166
CD10	2.5	0.024	150	–	5.63(0.07)	0.47	5.02(0.07)	73	2.6	3.3(0.7)	5.4	6.3	429	444
CD11	2.5	0.024	100	–	5.63(0.07)	0.46	3.55(0.14)	85	8.5	10.9(2.5)	22.1	20.6	370	415
CD03	2.5	0.17	75	–	5.63(0.07)	0.41	3.18(0.03)	212	14.9	19.6(2.7)	30.8	30.3	1440	1791
MSD03	2.5	0.17	75	10	5.63(0.07)	0.47	3.61(0.34)	128	12.6	14.5(3.2)	26.8	26.4	927	1084
SSD05	2.5	0.17	75	125	5.63(0.07)	0.53	n.d.[j]	843	13.9	16.5(1.5)	n.d.	n.d.	68,900	82,515
CD04	2.5	1.7	75	–	5.63(0.07)	0.47	*2.96(0.48)*[j]	406	12.1	15.8(1.7)	n.d.	n.d.	17,000	20,190
CD09	2.5	1.7	75	–	5.63(0.07)	0.51	3.84(0.24)[i]	488	14.5	16.9(1.6)	n.d.	n.d.	20,900	25,150
MSD04	2.5	1.7	75	10	5.63(0.07)	0.39	*3.67(0.94)*[j]	471	12.9	16.0(1.8)	n.d.	n.d.	30,100	35,833
SSD06	2.5	1.7	75	125	5.63(0.07)	0.60	n.d.[j]	1023	16.8	20.7(1.8)	n.d.	n.d.	128,000	161,412
CD20	5.0	0.0028	75	–	5.32(0.05)	–	3.27(0.07)	–	n.d.	n.d.	n.d.	n.d.	3[i]	4[i]
CD19	5.0	0.024	75	–	5.23(0.05)	–	3.23(0.15)	72	17.7	17.5(4.9)	26.6	34.8	13[i]	16[i]
MSD08	5.0	0.024	75	10	4.96(0.05)	–	3.18(0.05)	109	15.3	19.5(4.5)	24.4	31.1	23	30
SSD07	5.0	0.024	75	125	5.03(0.05)	–	3.83(0.21)[j]	1110	13.8	16.1(1.2)	n.d.	n.d.	26,800	31,943
CD18	5.0	0.17	75	–	5.22(0.05)	–	3.41(0.09)	221	13.9	15.3(2.3)	24.7	28.6	108	128
CD21	5.0	1.7	75	–	5.16(0.05)	–	3.43(0.17)	870	10.4	12.4(1.1)	23.9	22.4	11,200	12,785

The starting conditions for all decompression experiments were 200 MPa and 1373 K.
n.d.: not determined.

[a] H_2O content prior to decompression at H_2O-saturated conditions on the basis of REF09 (Table 2), the other values correspond to the weighed portions of H_2O (weighing error in brackets).

[b] Excess H_2O displayed as difference between weighed portion of H_2O and solubility of H_2O at starting conditions.

[c] Means of at least 10 individual measurements in the center area of the samples ($\pm 1\sigma$ in brackets). The values for CD04 and MSD04 provided in *italic* characters were determined with the EMP by-difference method.

[d] X_b(glass) · 100; porosity of the vitrified sample determined with ImageJ from a representative excerpt in the sample center (see 2.7). Porosities for the samples from experiments with a nominal decompression rate of 0.0028 MPa·s^{-1} are not provided, because of massive bubble coalescence and ascend of bubbles towards the top of the capsules.

[e] Expected porosity of the melt after decompression prior to rapid quench. Calculated from Eq. (5) in Gardner et al. (1999).

[f] X_b(melt) · 100; porosity prior to quench. Calculated from Eq. (4) using a shrinking factor B_s of ~2.5 (P_{final} = 75 MPa, T_g ~840 K) and the 2D porosity determined with ImageJ as basis. Due to different P_{final}, the B_s used for CD10 and CD11 were ~2.6 (T_g ~770 K) and ~2.8 (T_g ~810 K), respectively.

[g] N_V(t) is the number of bubbles per total unit volume ($V_{glass} + V_{bubbles}$).

[h] N_V(n) is the number of bubbles normalized to the bubble-free volume of only glass or melt (see Eq. (1)).

[i] Derived from optical microscopy.

[j] Bubble number density too high and spacing between bubbles too narrow for reliable H_2O analysis. For extremely vesiculated samples no measurements are available.

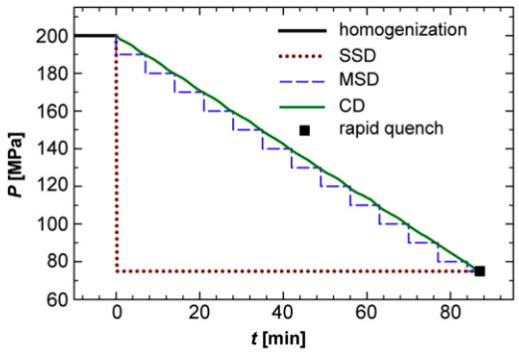

Fig. 1. *P–t* diagram for a set of SSD, MSD and CD experiments that were isothermally decompressed from 200 to 75 MPa with a nominal decompression rate of 0.024 MPa·s^{-1} at 1323 K. After the homogenization period, the decompression methods differ significantly despite an identical nominal decompression rate. Errors for the *P* drop during the decompression steps of MSD and SSD are up to 1.5 MPa. The CD path is an actual *P–t* log of CD08 (Table 3). At P_{final} the samples were quenched rapidly.

2.6. Fourier transform infrared spectroscopy

Near infrared (NIR) absorption spectra of the glasses were recorded in transmission mode using a Bruker Vertex 80v vacuum FTIR spectrometer with a CaF_2 beam splitter and a halogen light source. The spectrometer is connected to a Hyperion 3000 microscope with an In–Sb single element detector and a motorized sample stage for spatially resolved measurements. The microscope was used in combination with a 15× Cassegrain objective and a knife-edge aperture. The spectra were recorded with 32–120 scans at a spectral resolution of 4 cm^{-1} using air as reference. The microscope was flushed continuously with dried air to avoid influence of atmospheric H_2O and CO_2. Depending on the spacing between the bubbles in the glass and the thickness of each sample, the knife-edge aperture was adjusted to a square of 10–90 μm side length. It was taken care to avoid bubbles in the confined sample volume by focusing through the glass slab. The spacing between the bubbles in highly vesiculated samples is extremely narrow over the whole sample thickness. It is most likely that the measurements in these specimens included parts or even whole H_2O-filled bubbles due to the confocal beam path of the microscope. In this case, the determined total H_2O contents are higher than the residual contents in the glass. In principle, this problem could be minimized by reducing the sample thickness, but the preparation of highly vesiculated glasses to double-sided polished slices of <100 μm resulted in the destruction of some of the samples.

Total H_2O contents were determined following the method of Behrens et al. (1996). The peak heights of the OH-absorption band at ~4470 cm^{-1} and the absorption band of molecular H_2O at ~5210 cm^{-1} were used for the calculation of the species concentration after linear-tangential background correction of the spectra. The sample thickness was measured with an error of 2–3 μm using a Mitutoyo digital micrometer. The density of the phonolitic glass and the molar absorption coefficients were adopted from Iacono Marziano et al. (2007). The reference glasses with variable H_2O content were analyzed at first to verify the application of the adopted data (Table 2). At least 10 individual measurements were performed parallel to the cylinder axis in the center area of the decompressed samples. Additional concentration distance profiles were measured perpendicular to the cylinder axis in the middle of the glass slabs to monitor a decrease of H_2O content towards the capsule walls.

2.7. Quantitative image analysis

Bubble size distributions (BSDs) and bubble number densities (N_V) of the partially degassed phonolitic melts were determined for qualitative comparison of bubble nucleation and growth during decompression. The application of size distributions to characterize vesiculated samples was initially adopted from Marsh (1988), who used crystal size distributions (CSDs) to derive information about nucleation density as well as nucleation and growth rates. The size distributions can be generated by direct 3D measurement or stereological transformation of 2D information from cut sections (Jerram and Higgins, 2007). 3D methods involve e.g., serial sectioning (Mock and Jerram, 2005) or X-ray micro-tomography (Polacci et al., 2006; Baker et al., 2012). Gardner et al. (1999) directly measured the diameters of spherical bubbles within a confined volume under a transmitted light microscope. 2D techniques require stereological models (e.g., Saltikov, 1967) combined with corrections for the intersection probability and the cut section effect (Peterson, 1996; Sahagian and Proussevitch, 1998; Higgins, 2006). User-friendly, semi-automated software can be used to calculate 3D size distributions and number densities from image analysis (e.g., Higgins, 2000; Shea et al., 2010).

The BSDs and N_V of most samples in this study were determined on the basis of the BSE images using the program CSDCorrections 1.40 (Higgins, 2000), because this software includes an option to correct for ellipsoidal (deformed) bubbles. CSDCorrections was already used e.g., by Mastrolorenzo and Pappalardo (2006) for the calculation of BSDs. Nevertheless, a simplified modeling experiment was performed to verify the usability of this crystal size distribution program in terms of bubbles. Therefore, cubes (representing melt batches) containing randomly arranged spheres (bubbles) with up to three different diameters were modeled with a CAD software (Fig. 2a). The dimensions of all objects are known. Different slice planes through the cubes were processed with the program ImageJ 1.47 (Schneider et al., 2012). The intersections of the spheres in these planes (Fig. 2b) were fit with ellipses and their axes were measured. The axes lengths were imported to CSDCorrections for BSD and N_V calculation of the model. The roundness factor and the aspect ratios of the axes were set to 1 for spheres. The option to correct for voids/bubbles cannot be used in the specific case of calculating BSDs with this program, because the population densities and the volumetric phase proportions of all size intervals would be massively overestimated. The bubbles must be treated like a crystalline phase. As a result, the bubble number density is calculated per total unit volume of glass and bubbles (N_V(t)). The determined BSD size intervals match true sphere diameters in the 3D models best for not less than 150–250 measured intersections of spheres within the slice planes. This number is similar to a result of the detailed study from Mock and Jerram (2005), where CSDs were determined from 3D reconstruction. It was demonstrated, that a sample size of at least ~200 individual particles is sufficient to determine size distributions with appropriate reproducibility. N_V(t) and the volumetric phase proportions of spheres in the cubes (porosities of the models) could be reproduced with a relative error of <10%. The application of this method on highly vesiculated samples from this study should result in a better accuracy, because the number of analyzed bubble intersections is higher than in the 3D models. The error is therefore sufficiently small for the comparative purpose of BSDs and N_V in this study.

The BSDs of most vesiculated glasses were determined on the basis of the BSE images by analyzing a representative orthogonal excerpt from center of the samples (along the cylinder axis of the capsule) where the bubbles are mostly least deformed. The intersections of the bubbles were manually redrawn and colored in a second image layer over the BSE images with the help of an image processing program to maximize posterization (Fig. 3). This layer was imported into ImageJ and all intersections were fitted and measured. 2D porosities (phase proportion of bubble intersections in the sample excerpt) could be determined from these data. The deformation of former spherical bubbles to ellipsoids in some samples was taken into account by adjusting the aspect ratios of the 3 axes in CSDCorrections. The aspect ratios were determined from the double-sided polished glass slabs with a transmitted light microscope and a digitally controlled sample stage.

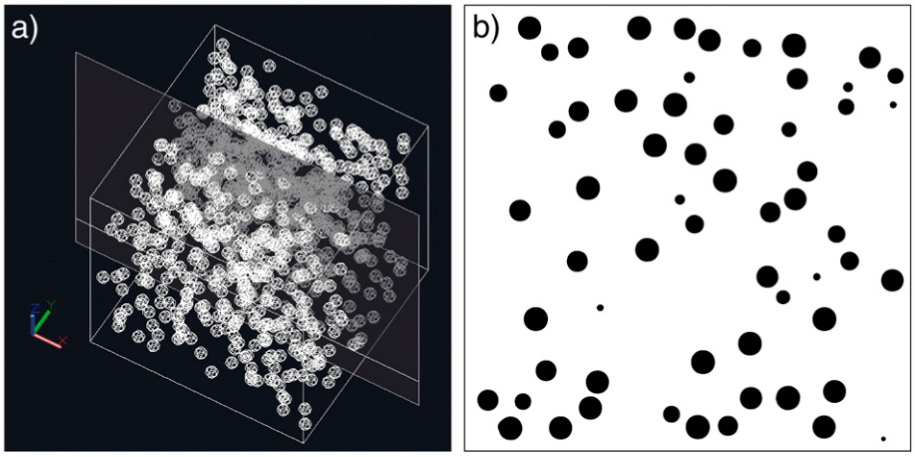

Fig. 2. (a) 3D model of a cubic sample with randomly arranged bubbles. The models were generated to test the usability of the stereological conversion method. The slice plane in the cube above is located parallel to a face in the center of this cube. In this example, all bubbles have the same diameter. (b) The intersections of the bubbles with equal diameter have different sizes in the slice plane. All intersections were colored in black, fitted/measured with ImageJ and the resulting dataset was processed with CSDCorrections.

In some of the samples the aspect ratios of the measured ellipsoidal bubbles are scattered randomly. The aspect ratios were then set to $1{:}[(1+c)/2]{:}c$, where c corresponds to the longest axis. This adjustment resulted in the best match between 2D and calculated 3D porosities. The lengths of the major axes of the fit ellipses from ImageJ were used as basis for the generation of the BSDs. A logarithmic base 10 size scale with 5 bins per decade was chosen. After processing with CSDCorrections, the calculated $N_V(\mathrm{t})$-values have to be normalized to the bubble-free melt (or glass) volume:

$$N_V(\mathrm{n}) = \frac{N_V(t)}{(1-X_b)} \quad (1)$$

where $N_V(\mathrm{n})$ is the number of bubbles per melt (or glass) volume and X_b is the volume fraction of bubbles. The normalization of $N_V(\mathrm{t})$ is essential, because only $N_V(\mathrm{n})$ is independent of bubble growth (Proussevitch et al., 2007). Samples with the same number of bubbles and an identical bubble-free melt volume, but with different porosities (due to different average diameter of the bubbles) will have contrasting $N_V(\mathrm{t})$-values. However, the $N_V(\mathrm{n})$-values of these samples are equal. In the absence of Ostwald ripening or bubble coalescence, this can reveal similarities in the nucleation behavior. The $N_V(\mathrm{n})$-values of samples with very few bubbles were derived from transmitted light microscopy of the double-sided polished glass slabs in combination with the BSE images of these samples.

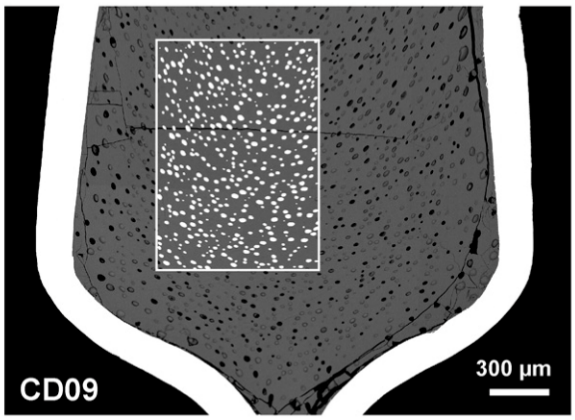

Fig. 3. BSE image of the vesiculated sample CD09 with a second image layer containing the manually colored intersections of the bubbles (white ellipses) in a representative part from the center of the sample. The redrawn bubble intersections were used to determine the BSD and N_V of the specimen. In this sample, 488 intersections were analyzed.

If the BSD and N_V of a deformed sample is exclusively based on BSE images or similar 2D information, it has to be noticed that sample preparation can influence the result of the stereological conversion. Assuming that a sample has ellipsoidal bubbles whose major axes are all parallel to the cylinder axis of the capsule and the capsule is prepared perpendicular to the cylinder axis, there is a chance that the intersections of the bubbles in the slice plane are perfectly circular. This could lead to the assumption that the bubbles in the specimen are spherical. In this case, the calculated individual bubble volumes would be significantly lower.

3. Results

3.1. Starting material

The reference sample REF09 (Table 2), which was quenched at the starting conditions of the H_2O-saturated decompression experiments with the 2.5 mm cylinders, reveals a homogeneous and crystal-free glass. It is almost completely free of small bubbles (Fig. 4a). It has to be noticed that the addition of ~0.5 wt.% H_2O in excess inevitably led to the formation of a big fluid bubble in the capsule. This fluid bubble in REF09 was simply not cut during sample preparation. In the corresponding slightly H_2O-undersaturated 5 mm sample (REF12), the glass does not contain any visible bubbles or other inhomogeneities (Fig. 4b).

3.2. Comparison of the decompression experiments

Decompression led to nucleation and growth of bubbles in the samples (Fig. 5). The complete BSE images of all decompressed samples are provided in the electronic appendix (eFig. 1–10). Bubbles at or close to the capsule walls are often bigger than the bubbles in the center and many samples show the bubble-free zone between capsule wall and vesiculated sample center that was already described by Iacono Marziano et al. (2007). The initially crimped headspaces of the capsules are usually widened and filled with melt and the bubbles in the samples are at least partially deformed (Fig. 6a, b). The big fluid bubble due to initial excess H_2O in the capsules with the 2.5 mm cylinders (H_2O-saturated starting conditions) is always present, but was not always sectioned during sample preparation.

The BSE images of the samples from the experiments with a low nominal decompression rate of 0.024 MPa·s^{-1} and a P_{final} of 75 MPa reveal evident differences in degassing behavior (Fig. 7a, c). In the center of the samples, the bubbles are distributed homogeneously in the glass. In contrast to CD, both MSD and SSD result in higher population

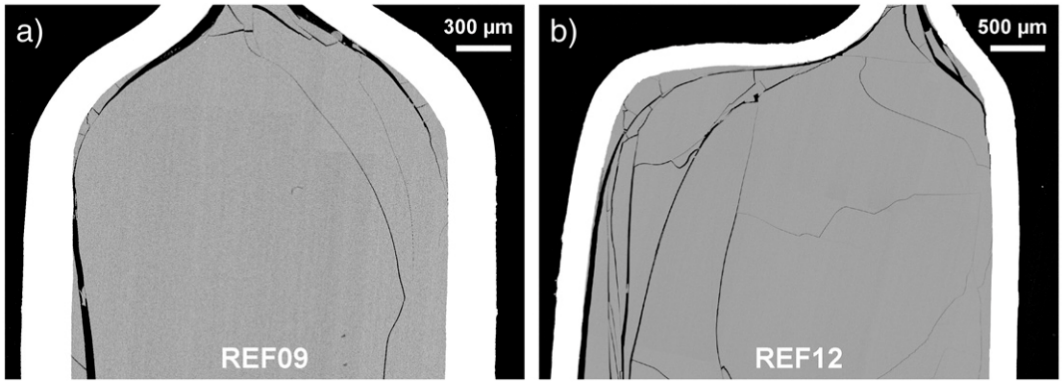

Fig. 4. BSE images of the reference samples REF09 (a) and REF12 (b) quenched at 200 MPa (details in Table 2). The glasses (gray) are homogeneous and crystal-free. Only REF09 contains a few, very small bubbles. REF09 was equilibrated with H_2O in excess in the capsule, REF12 is slightly H_2O-undersaturated. The black lines in both glasses are tension cracks that formed during quench in the glassy state.

densities of bubbles with smaller diameters in the quenched samples (Fig. 7b, d). The MSD and CD samples have broader BSDs than the extremely vesiculated SSD specimens. The bubble diameters in the 5 mm CD and MSD sample are generally bigger and the population densities are lower than in the corresponding 2.5 mm specimens (Fig. 7b, d). The BSDs of the 2.5 and 5 mm SSD samples are comparable. At a fast nominal decompression rate of 1.7 MPa·s^{-1}, the differences in degassing behavior between SD and CD are less pronounced (Fig. 7e). The BSDs of the CD and MSD sample are shifted towards smaller bubble diameters and higher population densities, but the peak bubble diameter is still bigger than in the SSD sample (Fig. 7f). In comparison to the results of a nominal decompression rate of 0.024 MPa·s^{-1}, the BSD of the SSD sample barely changed.

For a fixed P_{final} of 75 MPa, the $N_V(n)$-values of CD and MSD samples increase with nominal decompression rate, whereas the average bubble diameter decreases (Fig. 8, 9). At low rates, MSD can result in an up to two orders of magnitude higher $N_V(n)$ than CD. These differences gradually align with increasing nominal decompression rate. The $N_V(n)$-values of the SSD samples are generally higher than those in

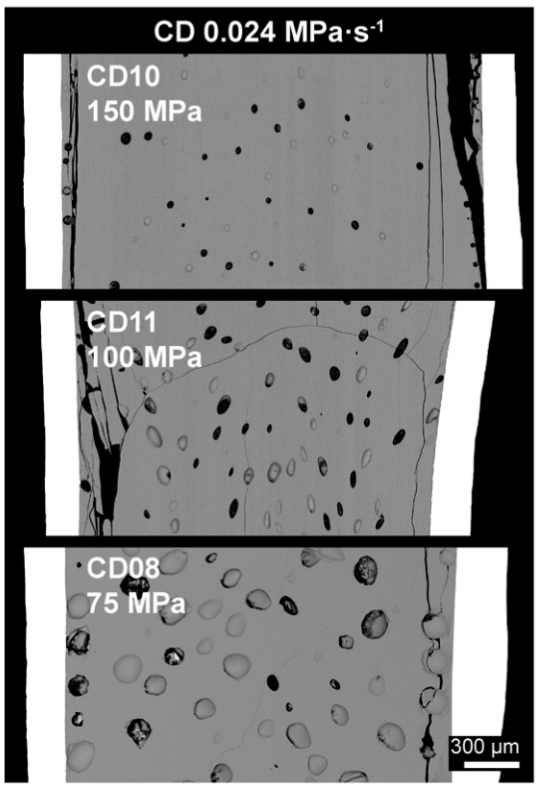

Fig. 5. BSE images of CD samples (2.5 mm cylinders, H_2O-saturated starting conditions) after decompression with a rate of 0.024 MPa·s^{-1} at a P_{final} of 150, 100 and 75 MPa.

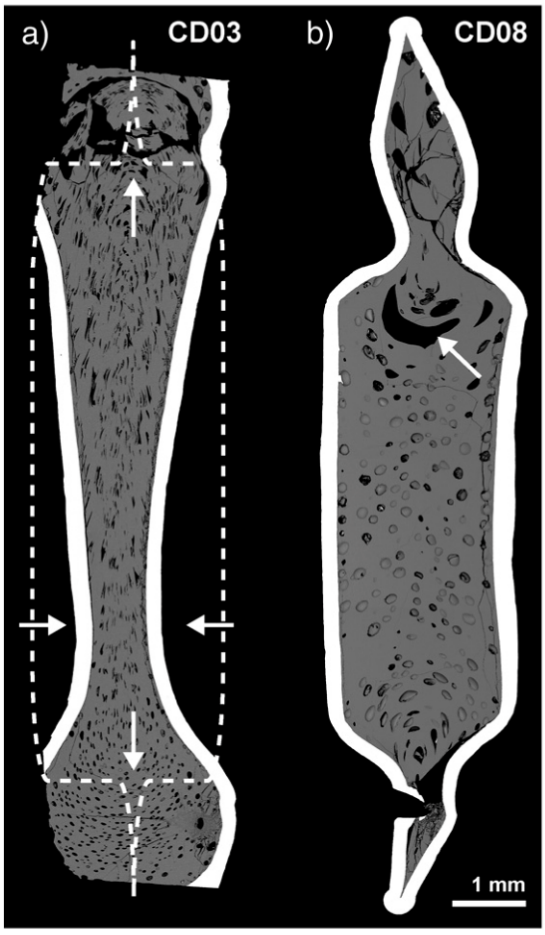

Fig. 6. BSE images of CD03 (a) and CD08 (b) after decompression (2.5 mm cylinders, H_2O-saturated starting conditions). CD03 was decompressed with 0.17 MPa·s^{-1} and CD08 was decompressed with 0.024 MPa·s^{-1} to a P_{final} of 75 MPa. The capsules were cut in half parallel to the cylinder axis, CD03 was bisected through the maximum deformation. Different amounts of melt migrated in to the initially crimped headspaces. The side walls of CD03 are massively inflexed. The capsule ends of this sample were lost during preparation. The dashed line indicates the capsule outline prior to the experiment. Both samples display deformed bubbles at least in some parts of the capsule. The big bubble at the top of CD08 (marked with the white arrow) was initially formed due to excess H_2O in the capsule prior to decompression.

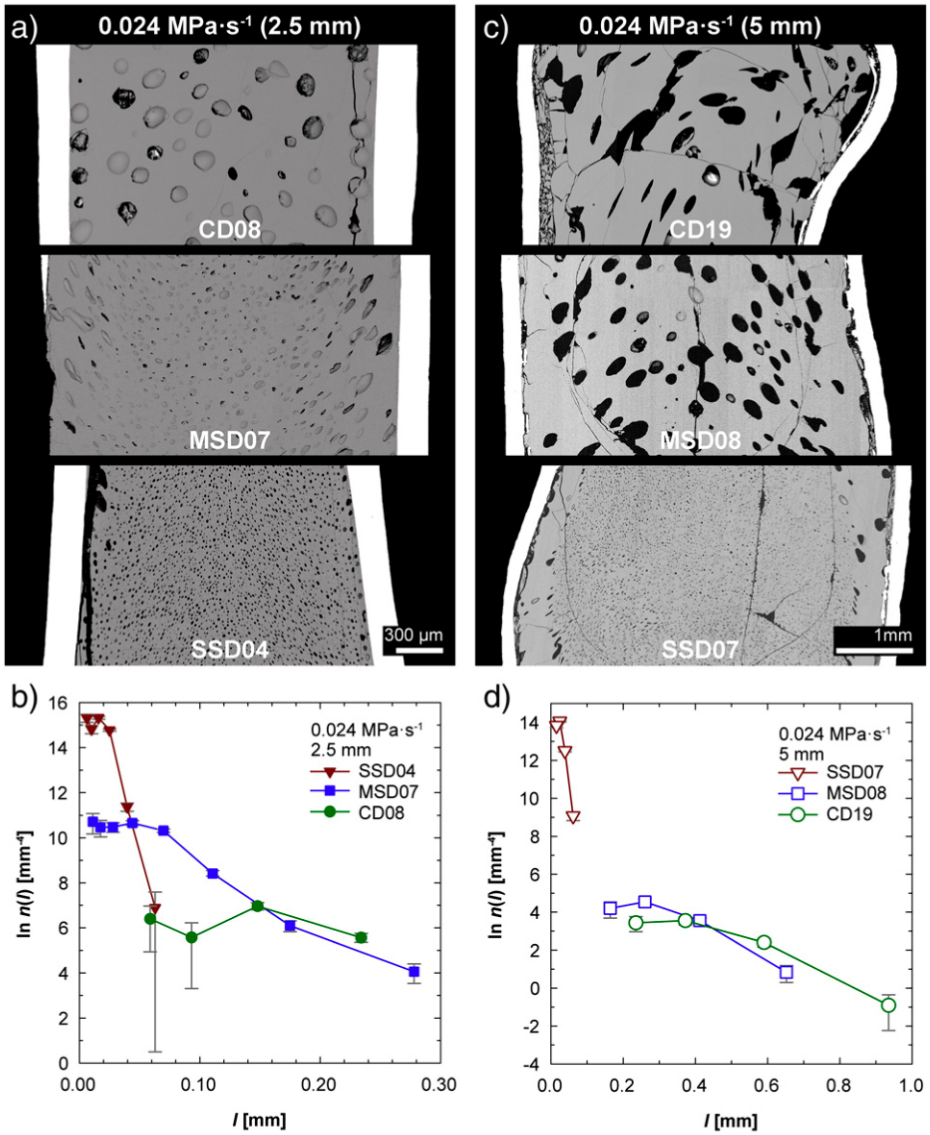

Fig. 7. Comparison of the BSE images and the BSDs of selected samples decompressed with CD, MSD and SSD at the same nominal decompression rate. (a, b) 0.024 MPa·s^{-1} with 2.5 mm cylinders at H_2O-saturated starting conditions. (c, d) 0.024 MPa·s^{-1} with 5 mm cylinders at slightly H_2O-undersaturated starting conditions. (e, f) 1.7 MPa·s^{-1} with 2.5 mm cylinders at H_2O-saturated starting conditions. P_{final} was 75 MPa for all experiments. The BSDs show the population density $n(l)$ as a function of the diameter (l) of the bubbles in the quenched sample. The diameter corresponds to the major axis of the bubble-ellipsoid. Due to graphical reasons, the excerpts of the BSE images do not directly correspond to the BSDs. The 2D images that were used as basis for the BSDs are deposited in the electronic appendix.

the samples of MSD and CD experiments (Table 3). For SSD at nominal decompression rates ≥0.024 MPa·s^{-1}, N_V(n) is in the order of ~10^5 mm^{-3} and then drops about nearly two orders of magnitude at the lowest rate (Fig. 8). The N_V(n)-values of the 2.5 mm CD samples with a decompression rate of 0.024 MPa·s^{-1} that were quenched at different P_{final} are all within the same order of magnitude (Table 3, Fig. 5). The bubble diameter increases with decreasing P_{final}.

The residual H_2O contents in the samples with a P_{final} of 75 MPa are displayed in Fig. 10. At CD and MSD with low nominal decompression rates ≤0.024 MPa·s^{-1}, the H_2O concentration is within the error in the range of the solubility of H_2O at P_{final} (~3 wt.%). This is also valid for the single analyzed 2.5 mm SSD sample at a nominal decompression rate of 0.0028 MPa·s^{-1}. Faster decompression results in an increase of about 0.5 wt.% for MSD samples and a slightly lower increase for the 5 mm CD samples. The error bars that correspond to the standard deviations of the plotted means also increase with decompression rate. H_2O concentration distance profiles perpendicular to the cylinder axis of the 5 mm CD samples decompressed with 0.17 MPa·s^{-1} and 1.7 MPa·s^{-1} do not reveal severe concentration gradients from sample center towards the former capsule-melt interface (Fig. 11). The residual H_2O concentration of the 2.5 mm CD sample with a decompression rate of 0.024 MPa·s^{-1} that was quenched at a P_{final} of 100 MPa (Table 3, Fig. 5) is within the error equal to the corresponding equilibrium H_2O content determined by Iacono Marziano et al. (2007). The sample quenched at a P_{final} of 150 MPa has a ~0.5 wt.% higher concentration than the equilibrium H_2O content.

4. Discussion

4.1. Experimental and analytical problems

4.1.1. Bubble shrinkage during rapid quench

Burgisser and Gardner (2005) already mentioned a migration of melt into the initially crimped headspaces of their capsules due to the volumetric expansion during degassing, because of the nucleation and growth of fluid bubbles. This deformation is also observed in almost all of the decompression experiments with the 2.5 mm cylinders (H_2O in excess in the capsule) to varying degrees (Fig. 6a, b). The

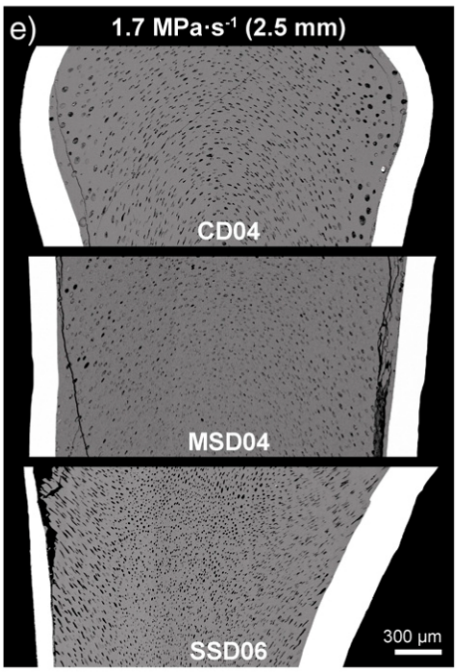

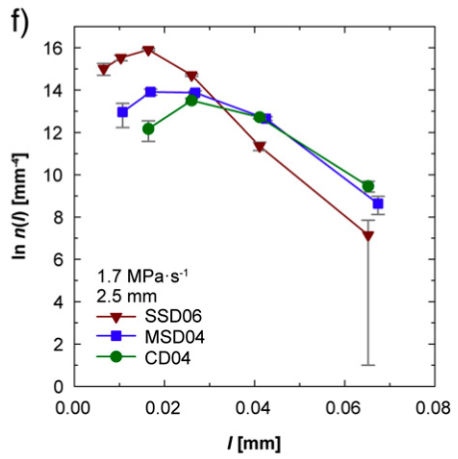

Fig. 7 (*continued*).

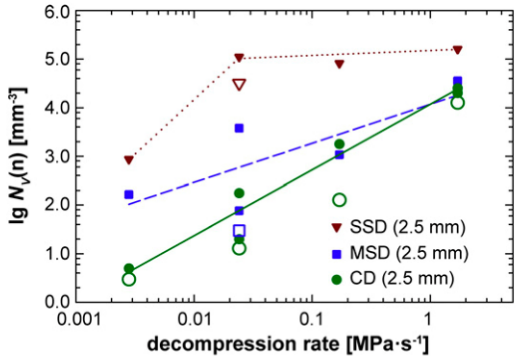

Fig. 8. Normalized bubble number densities (N_V(n), logarithmic) of the samples as a function of nominal decompression rate. The data points with solid symbols are derived from experiments with 2.5 mm cylinders at H_2O-saturated starting conditions. Open symbols correspond to the 5 mm samples (slightly H_2O-undersaturated starting conditions). P_{final} was 75 MPa for all experiments. The solid green line and the dashed blue line are linear regressions of the data points from the 2.5 mm CD and MSD experiments. The N_V(n)-values of the 5 mm samples were excluded from regression due to lower initial H_2O content prior to decompression. The red dotted line is only a non-committal trend for the 2.5 mm SSD specimens.

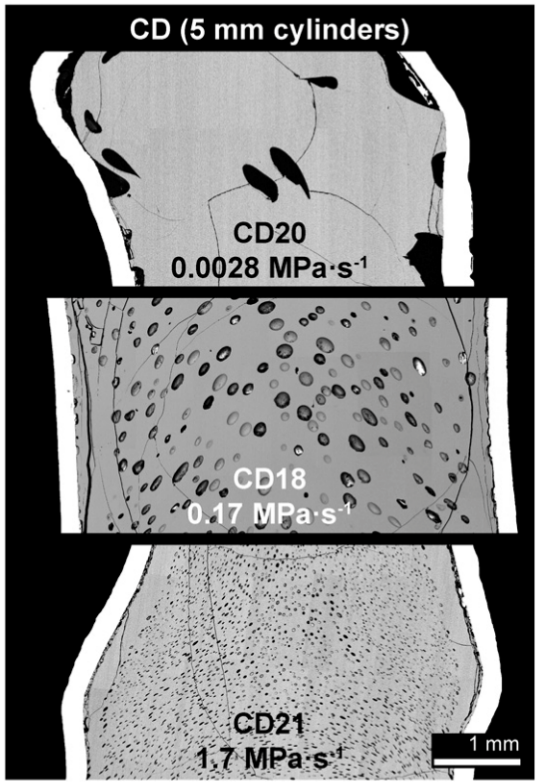

Fig. 9. BSE image excerpts of 5 mm CD samples decompressed with rates of 0.0028–1.7 MPa·s^{-1}. With increasing decompression rate, the bubble diameters decrease and the N_V(n)-values increase. At the lowest rate, the sample center is nearly completely free of bubbles. Larger void spaces can be found at the capsule-melt interface.

bubbles in these samples are also partially deformed. This could be due the movement of the vesiculated melt into the headspaces during decompression and expansion. On the other hand, the bubbles would target spherical shape in a short time after deformation at a low melt viscosity in order to lower the surface energy. The precise point of time during decompression where the crimped headspaces open up is unknown. In addition, the timescale of this capsule deformation (slow process or instantaneous event) is obscure. Nevertheless, this capsule deformation definitely occurs before rapid quench is initiated and the resulting bubble deformation is therefore unlikely to be preserved in a low viscosity melt, especially in experiments with a low nominal decompression rate and a correspondingly high time interval

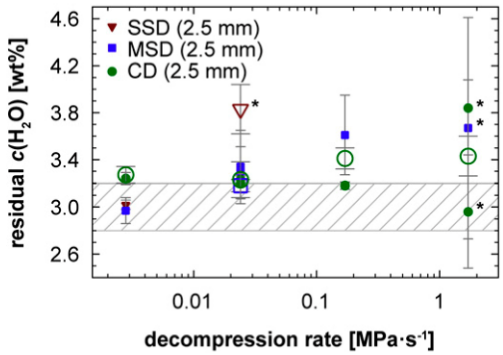

Fig. 10. Residual H_2O contents of the samples decompressed to a P_{final} of 75 MPa. The shaded area corresponds to the solubility at P_{final} (± analytical error). The solid symbols correspond to experiments with 2.5 mm cylinders at H_2O-saturated starting conditions. The open symbols correspond to the 5 mm samples (slightly H_2O-undersaturated starting conditions). The data points are the means of at least 10 individual measurements in the center area of the samples (error bars ±1σ). The data points marked with a star are means from samples with high N_V(n)-values and very narrow spacing between the bubbles. Explicit data and further details are listed in Table 3.

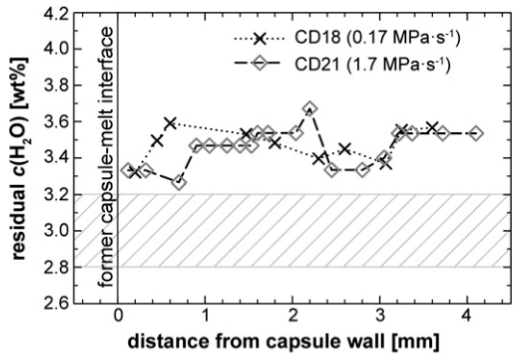

Fig. 11. H_2O concentration distance profiles determined by FTIR measurements perpendicular to the cylinder axis over the complete width of two CD experiments with 5 mm cylinders. Deformation of the samples can reduce the sample diameter. The decompression rates were 0.17 MPa·s^{-1} and 1.7 MPa·s^{-1} at a P_{final} of 75 MPa. The shaded area corresponds to the solubility at P_{final} (± analytical error).

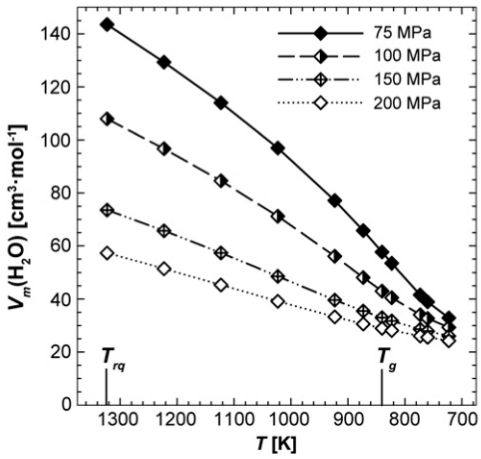

Fig. 13. V_m of the exsolved H_2O within the bubbles decreases with T during isobaric rapid quench. This effect is enhanced by decreasing P_{final} (legend) of the decompression experiment. All data points were generated with the EOS program of Duan and Zhang (2006). The run temperature prior to rapid quench (T_{rq}) was 1323 K for all experiments. The marked glass transition temperature (T_g) of ~840 K corresponds to a VAD79 melt with ~3 wt.% H_2O that is quenched rapidly at ~150 K·s^{-1}.

for bubble re-shaping. Bubble deformation was also observed in the experimental study of Mongrain et al. (2008) and attributed to local melt shearing due to expansion and interconnection of bubbles during decompression. In many natural pumices, the deformation of bubbles can be explained by increasing interconnectivity between bubbles with associated gas escape from the melt (Gardner et al., 1996). Castro et al. (2012) attributed bubble deformation to bubble wall stretching. Thinning bubble walls in combination with inter-bubble P gradients were identified as a cause for dimpled bubbles in the course of coalescence. McIntosh et al. (2014) re-interpreted buckled bubble walls as evidence for bubble shrinkage due to quench resorption of H_2O.

In the course of sample preparation, a closer look at the bubbles on the side wall of a 5 mm glass cylinder revealed dented bubbles as well as flow textures within the indentations (Fig. 12) and the surrounding glass matrix. Due to the isolated location of the big bubble in the center of Fig. 12, bubble wall thinning and coalescence (Castro et al., 2012) is not considered as cause for the indentation. Considerable total H_2O concentration gradients around the bubbles as reported by McIntosh et al. (2014) could not be detected (Marxer and Nowak, 2013). We suggest that the observed bubble deformation in our case is mostly due to a severe decrease of the molar volume (V_m) of the exsolved and the excess H_2O in the capsule during rapid quench. Throughout the onset of cooling until the glass transition, the melt is able to react to shear forces by viscous flow (e.g., Dingwell and Webb, 1990). In contrast to

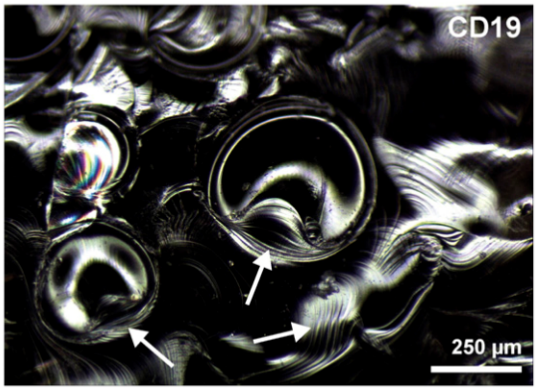

Fig. 12. Microscope image of the side wall of the vesiculated glass cylinder from sample CD19. The visible surface was in contact to the capsule wall. The heterogeneously nucleated bubbles are dented and the white arrows indicate flow textures around the bubbles and within the indentations.

V_m(melt), V_m of the exsolved H_2O is strongly dependent on the P–T conditions. It can e.g., be calculated using the equation of state (EOS) program for H_2O, CO_2 and the H_2O–CO_2 system from Duan and Zhang (2006). For exsolved pure H_2O, V_m continuously decreases with T for a fixed P_{final} (Fig. 13). The lower the quench P in the range of 200–75 MPa, the higher is the effect of cooling on $V_m(H_2O)$. The interior fluid P of the bubbles in the melt diminishes while the exterior argon P in the autoclave remains constant. This difference in P is counterbalanced by a reduction of the bubble volumes during cooling until the melt is too viscous to relax and the bubbles stop to shrink at a fictive temperature (T_f). As a first approximation, the volumetric loss of a H_2O-filled bubble is quantified for the case that the bubble is able to shrink until the glass transition temperature (T_g) is reached ($T_f = T_g$). For the determination of T_g, it is assumed that the residual H_2O content in the melt has reached equilibrium prior to rapid quench. At a P_{final} of 75 MPa, the solubility of H_2O in the VAD79 melt is ~3 wt.% (Table 2). For a moderate quench rate of ~150 K·min^{-1}, T_g (corresponding to the maximum of the c_p-peak with a viscosity of log η ~ 10 Pa·s) of this H_2O-bearing phonolitic melt is ~760 K (Giordano et al., 2008). A rapid quench with a cooling rate that is 60 times faster (from K·min^{-1} to K·s^{-1}) results in an increase of T_g of about 80 K for a rhyolitic melt with 3 wt.% H_2O (Dingwell and Webb, 1990). If a similar effect is assigned to the phonolite, T_g is reached at approximately 840 K for a rapid quench rate of 150 K·s^{-1}. During an isobaric rapid quench at a P_{final} of 75 MPa, $V_m(H_2O)$ decreases from ~144 cm^3·mol^{-1} at 1323 K to ~58 cm^3·mol^{-1} at T_g (Fig. 13). Assuming that the amount of the exsolved H_2O in the bubble remains constant, the decrease of $V_m(H_2O)$ results in a decrease of the bubble volume by a shrinking factor B_s that corresponds to the ratio of $V_m(H_2O)$ before and after rapid quench:

$$B_s = \frac{V_m(H_2O)\left[P_{final}, T_{rq}\right]}{V_m(H_2O)\left[P_{final}, T_f\right]} \quad (2)$$

where T_{rq} is the run temperature of the sample prior to rapid quench. For a quench at 75 MPa, 1323 K and a H_2O content of ~3 wt.% in the VAD79 melt, B_s is ~2.5, if we assume in first approximation that the bubbles are able to shrink until T_g is reached.

It is conceivable that B_s is dependent on bubble size. Due to the surface tension (σ) there is a positive P difference between the interior vapor pressure (P_i) in the bubble and the hydrostatic exterior pressure

in the melt (P_e). This relation is generally described by the Young–Laplace equation. The P difference across the melt-vapor interface can be calculated by:

$$(P_i - P_e) = \frac{2 \cdot \sigma}{r} \quad (3)$$

where r is the radius of a spherical bubble (Hirth et al., 1970; Toramaru, 1989). This relation shows that P_i is dependent on the size of the bubbles. Therefore, V_m of the exsolved H_2O at a certain P_{final} and T_f additionally depends on the bubble radius (Toramaru, 1989). With decreasing radius the P difference ($P_i - P_e$) increases exponentially (Eq. (3)). For an observed minimum bubble radius of 1.5 μm in the vitrified samples (that corresponds to r at T_f), this P difference is only ~0.2 MPa, assuming a surface tension of ~0.16 $N \cdot m^{-1}$ for the VAD79 melt with ~3 wt.% H_2O at a P_{final} of 75 MPa and a T_f of ~840 K. The σ-value was derived starting from a surface tension of ~0.08 $N \cdot m^{-1}$ for the hydrous VAD79 melt at 200 MPa and 1323 K (Gardner, 2012) and considering an increase of σ by a factor of 2 due the decreased H_2O content in the melt at a P_{final} of 75 MPa and the decrease of T_{rq} to T_f (Bagdassarov et al., 2000; Mangan and Sisson, 2005; Gardner et al., 2013). This small P difference has negligible influence on V_m of the exsolved H_2O (Duan and Zhang, 2006). Thus, in the approximation for bubble shrinkage (Eq. (2)) B_s can be considered as constant for the observed bubble sizes. Furthermore, bubbles with a radius ≤1.5 μm in our samples do not significantly contribute to the measured porosity.

The calculation of B_s is a scenario for maximum shrinkage, because the cooling melt will possibly prevent bubble shrinkage at a higher T_f due to increasing viscosity. The studies of Thomas et al. (1994) and Barclay et al. (1995) suggested a 'viscosity quench' of bubble size at melt viscosities ≥10^9 Pa·s. Isothermal expansion of the bubbles due to external P decrease is assumed to be minimized or negligible at such high viscosities and fast decompression rates. The viscosity limit of 10^9 Pa·s could also be applicable for the shrinkage of bubbles. Based on this limit, the corresponding T_f of a VAD79 melt with 3 wt.% H_2O would be ~40 K higher than for a viscosity of 10^{10} Pa·s (Giordano et al., 2008). The corresponding B_s for a P_{final} of 75 MPa would be ~2.2 (instead of ~2.5 for a viscosity limit of 10^{10} Pa·s). This minor difference is considered to be within the uncertainty of our approximation for bubble shrinkage. The viscosity of a melt is influenced by the concentration of dissolved H_2O (e.g., Giordano et al., 2005). Differences in the residual H_2O content within the melt therefore influence T_f and the residual bubble volume. For the approximation of the volumetric loss of bubbles across the sample, the H_2O-content of the melt was considered to be constant at the level of equilibrium solubility prior to rapid quench in order to determine a fixed value for T_g. Differences in the quench rate of the melt inside the capsule from the wall to the center of the cylindrical sample could also affect T_g (Dingwell and Webb, 1990). The hydrous species geospeedometer of Zhang et al. (2000) in rhyolite can be used in first approximation for a qualitative comparison of the quench rate across the sample. Therefore, NIR measurements in the center and close to the capsule wall (Fig. 14) were performed in one of the partially degassed 5 mm samples. The total residual H_2O contents in the glass are identical within the analytical error. The quotient $Q' = (A_{4470})^2/A_{5210}$ was determined following Zhang et al. (2000) using the peak heights of the absorption bands of OH^- (A_{4470}) and molecular H_2O (A_{5210}) from the NIR absorption spectra. Within the relative uncertainty of 2% both determined Q'-values (sample rim: 0.223 and sample center: 0.221) are identical. Following Zhang et al. (2000), the respective quench rates for the rim and the center of the sample can be considered as equal in first approximation. Variations of T_g due to differences in the quench rate across the samples are therefore not taken into account.

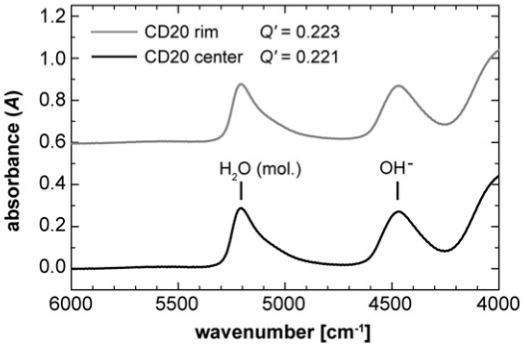

Fig. 14. NIR absorption spectra of measurements close to the capsule wall and in the center of CD20. The spectra are normalized to a sample thickness of 1 mm and shifted for clarity. The absorption bands at ~5210 and ~4470 cm^{-1} correspond to molecular H_2O and OH^-, respectively. The residual total H_2O contents are equal. The quotient $Q' = (A_{4470})^2/A_{5210}$ is dependent on the quench rate (Zhang et al., 2000) and within the error of 2% identical for the rim and the center of the sample.

In decompression experiments with hydrous silicate melts in *HP–HT* autoclaves, V_m of the exsolved H_2O in the fluid phase is a non-quenchable parameter. The bubble sizes (and therefore the porosity) will decrease with T during isobaric quench, until melt relaxation is negligible. This implies that $N_V(t)$ of a sample increases during cooling until T_f is reached, because the total V decreases. The viscosity of the melt as well as the speciation of H_2O (OH^- or molecular H_2O) that is dissolved in the melt are also not quenchable above the glass transition (e.g., Dingwell and Webb, 1990; Nowak and Behrens, 2001). The V_m of a hydrous silicate melt (and therefore the melt density) is affected by P, T and the amount of dissolved H_2O (Ochs and Lange, 1999), but the effect of T on V_m(melt) is negligible compared to the effect on V_m of the exsolved H_2O. For the VAD79 composition with 3 wt.% dissolved H_2O at 75 MPa, the density of the melt increases only ~5% from 2.28 to 2.37 $g \cdot cm^{-3}$ during cooling from 1323 to 840 K (Ochs and Lange, 1999). A quenchable feature in experiments with hydrous silicate melts are total H_2O concentration-distance profiles caused by diffusion (e.g., Nowak and Behrens, 1997). Furthermore, the $N_V(n)$-values (Eq. (1)) of a vesiculated sample before (melt) and after rapid quench (glass) are identical, because the $N_V(t)$-values have to be normalized to the respective porosity. A comparison of our results to melt degassing experiments of other authors should be possible, because the vesiculated samples of fellow experimentalists were most likely subjects to similar bubble shrinking processes during isobaric rapid quench at high P in their autoclaves.

4.1.2. Influence of bubble shrinkage on the sample texture

The cooling, H_2O-filled bubbles can either contract isometrically due to multi-directional melt transport around the bubble or they shrink asymmetrically and get deformed near T_f. The size of the bubbles and the location in the capsule influences the shrinking process. Bigger bubbles close to the capsule-melt interface are more likely to get deformed than small bubbles in the center of the capsule, because multi-directional melt transport close to the capsule wall is limited. The observed flow textures in the dented bubbles at the capsule wall (Fig. 12) are inferred to result from bubble shrinkage at a high viscosity during rapid quench. The cooling melt was sucked inwards due to the decreasing fluid P inside the bubble. The transport of melt towards or around shrinking bubbles may also be an explanation for the lack of H_2O concentration gradients in the glass matrix around bubbles in sample MSD03 with a nominal decompression rate of 0.17 MPa·s^{-1}, as evident from micro-FTIR imaging (Marxer and Nowak, 2013). H_2O concentration gradients, resulting from diffusive bubble growth during decompression, could be distorted or leveled.

The shrinkage of big bubbles in the capsules affected the whole sample texture. The 3 mm Pt-capsules were loaded with ~0.5 wt.% H_2O in excess (Table 3), resulting in a big fluid bubble in the capsule prior to decompression, which is usually located in the top part of the sample (Fig. 6b, 15a). During decompression, these excess fluid bubbles grew substantially because of diffusive bubble growth and expansion due to

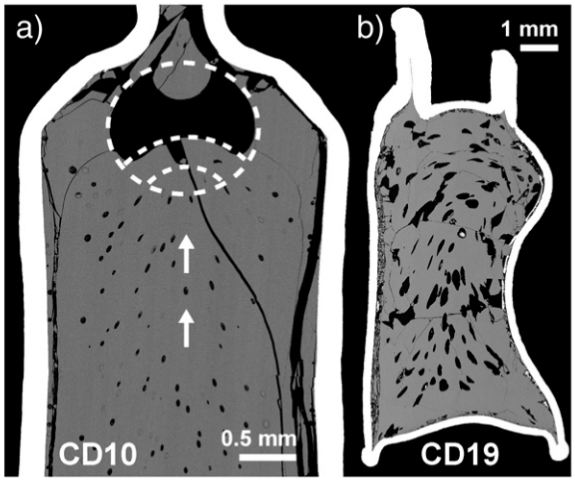

Fig. 15. BSE images of CD10 (a) and CD19 (b) after decompression. The big bubble at the top of CD10 was initially formed due to excess H_2O in the capsule. During rapid quench this bubble collapsed and was dented on the side facing the sample center. This shrinkage caused melt movement in the capsule. Smaller bubbles were entrained and elongated. Despite initially slightly H_2O-undersaturated conditions and the lack of a big fluid bubble in the top of CD19, the bubbles are still deformed. It is likely that any capsule deformation prior to rapid quench is intensified during volume reduction of the sample due to bubble shrinkage. Such a directed capsule deformation during cooling may result in deformed bubbles as observed in CD19.

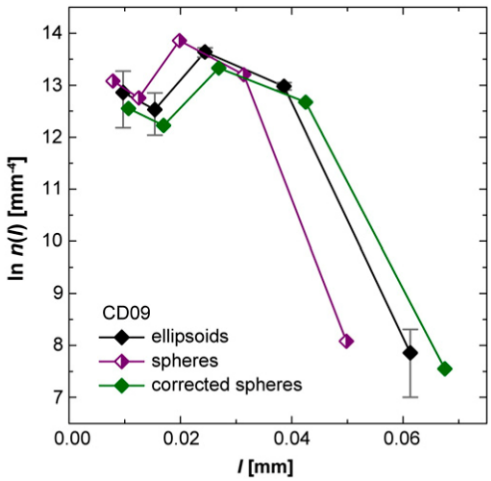

Fig. 16. BSD correction of sample CD09 for a B_s of ~2.5. The ellipsoids were transformed to spheres of equivalent volume to correct the deformation and then the diameters of the spheres were expanded to match the size of the bubbles prior to rapid quench. $N_V(n)$ is identical for all displayed BSDs.

decreasing exterior *P*. The volumetric collapse of these bubbles during rapid quench was associated with extensive melt transport in the capsule. The vesiculated melt was drawn towards the collapsing bubble and the smaller bubbles were entrained and deformed in combination with their own shrinkage (Fig. 15a). This can lead to elongation of spherical bubbles in the sample center (Fig. 15a). Some of the big bubbles collapsed on the side facing the crimped headspace (Fig. 6b). The bubbles in the sample center were then probably not entrained and deformed due to the melt movement that is triggered by the collapse of the big bubble. In this case, bubbles could keep their spherical shape by isometrical shrinkage. The AuPd-capsule setup with the 5 mm glass cylinder, ~5 wt.% initial H_2O content and the lid at the bottom was inter alia chosen to prevent excess H_2O in the capsules prior to decompression. The other aim was to force the volumetric expansion in the course of decompression in one preferred direction to avoid thinning of the sample as it was observed for some of the 2.5 mm samples (Fig. 6a). However, some of the big capsules are also inflexed (Fig. 15b, eFig. 5, 6). The inflexions may be attributed in part to melt migration into the headspace prior to rapid quench. Moreover, it is conceivable that these inflexions result from the reduction of the sample volume due to shrinkage of bubbles during cooling. A directed contraction of the capsule by inflexion of the side wall during quench can lead to the observed deformation of the bubbles to ellipsoids (Fig. 15b). Other capsules (independent of material) and the bubbles inside appear to be quite un-deformed (eFig. 1–10) after decompression, but it is not known, if e.g., the capsules were barrel-like inflated prior to rapid quench.

4.1.3. Correction of BSDs and porosities

The derived BSDs in the vesiculated glass samples do not correspond to the actual size distributions in the melt, because the bubbles shrink during quench and the associated melt transport in the capsule can lead to bubble deformation. The BSDs can be corrected in two steps. The deformation can be taken into account by transforming the bubble ellipsoids of each size interval of the BSD to bubble spheres of equivalent volume. The porosity of the sample does not change by this transformation. $N_V(n)$ and the number of size classes are also identical. The individual volume of the ellipsoids in a size class can be calculated using the aspect ratios of the ellipsoids' axes. The diameter of the corresponding spheres can then be derived from this calculated volume. The resulting BSD of the spheres is shifted towards smaller diameters and slightly higher population densities (Fig. 16), because the BSD of the vesiculated glass was initially calculated on the basis of the major axis of the ellipses (see 2.7). The BSD of the spheres can then be corrected for the volumetric loss of the bubbles during cooling. Therefore, the bubbles of each size class are inflated by the shrinking factor (Eq. (2)), whereas $N_V(n)$ is kept constant again. In comparison to the initial BSD in the glass, the corrected BSD is shifted towards bigger diameters and lower population densities (Fig. 16). The interval widths of the corresponding size intervals in each plot change due to the correction from ellipsoids to spheres to corrected spheres. Because of the constant number of bubbles in the corresponding size intervals of the three BSDs in Fig. 16, the population densities also change (Higgins, 2006).

The BSDs of this study are calculated from limited 2D information and therefore error-prone. Derived values like the porosity and $N_V(n)$ have to be considered carefully. As evident from Table 3, the 2D porosities measured with ImageJ and the calculated 3D phase proportion of bubbles in the glasses with CSDCorrections often differ significantly (e.g., for MSD02 and SSD03). This might be due to the fact that fixed aspect ratios of the bubble ellipsoids were used for each sample, whereas the individual bubbles feature a whole range of aspect ratios (e.g., Fig. 6a, 15b). In this context, the use of the major axis of the ellipses as basis for the stereological transformation of all intersections (see 2.7) can also contribute to the error. In some samples, the total amount of bubbles that were intersected and analyzed was below the recommended number of particles for a realistic 3D calculation. A few big bubbles in the analyzed 2D sample area can already have a great effect on the calculated 3D phase proportion, because their individual volume is already high. These effects are even worse for samples with very deformed bubbles such as CD19 (Fig. 15b). The 2D phase proportion of bubbles is therefore more reliable than the calculated 3D information for these samples.

The shrinkage of bubbles during isobaric rapid quench results in a decrease of porosity in the sample. The volume of the bubble-free melt is considered to be identical to the bubble-free glass. The volume fraction of bubbles (X_b) in the melt at the endpoint of decompression can be calculated from the measured volume fraction of bubbles in the vesiculated glass, considering the ratio of $V_m(H_2O)$ before and after bubble shrinkage at P_{final}:

$$X_b(\text{melt}) = \frac{B_s \cdot X_b(\text{glass})}{1 + [B_s \cdot X_b(\text{glass})] - X_b(\text{glass})} \quad (4)$$

where B_s is the shrinking factor of the bubbles (Eq. (2)). This calculation is again only an approximation on the basis of a uniform B_s, a constant H_2O concentration in the melt and thus a constant T_f over the analyzed sample area. The corrected porosities of suitable samples with a P_{final} of 75 MPa (H_2O content near 3 wt.%, limited bubble coalescence and ascent, sample center appears not to be influenced by degassing at the capsule-melt interface) range from 22 to 35% and are significantly higher than the porosities measured in the glasses (Table 3). These corrected porosities were calculated with a B_s of ~2.5. The 2D phase proportions (determined with ImageJ) were used for X_b(glass). This correction is of course also valid for reliable 3D data for X_b(glass). Another possibility to calculate X_b(melt) is directly from a corrected BSD. The determination of a volumetric phase proportion from a size distribution is described in Higgins (2002).

The expected porosity in the melt prior to rapid quench can be calculated using the H_2O content in the melt at starting conditions of decompression and the residual H_2O content in the glass (Eq. (5) in Gardner et al., 1999). The excess H_2O in the capsules of the decompression experiments with the 2.5 mm cylinders is expected not to contribute to the porosity that is derived from the bubbles in the sample center. Significant proportions of small preexisting bubbles in the melt prior to decompression as shown in Gardner et al. (2000) could not be found at starting conditions of the experiments (Fig. 4a), because the excess H_2O is concentrated in a big bubble (e.g., Fig. 15a). The corrected porosities of the glasses (22–35%) are close to the expected porosities in the melt that range from 24 to 31% (Table 3). The correction of bubble shrinkage can also be applied to the two 2.5 mm samples quenched at a higher P_{final} of 150 and 100 MPa (CD10 and CD11). Adjusting T_g and B_s to the respective H_2O content and P_{final}, the corrected porosities and the expected melt porosities agree very well (Table 3). Small differences between corrected and expected values can generally arise, because the correction is based on assumptions for viscosity and H_2O content in the melt to determine T_f. Additionally, the corrected porosities are only calculated from limited 2D information of mostly deformed objects. For samples with minor bubble deformation and a high number of analyzed bubble intersections, the correction results in a relative error <10% between expected and corrected porosity. This comparison is a further confirmation for the shrinkage of bubbles during isobaric rapid quench as well as the applicability of the correction. Bubble shrinking could also be an explanation for the difference between measured and expected porosity in some of the samples from the decompression experiments described in Gardner (2012).

4.2. CD vs. SD

Decompression from H_2O-saturated conditions leads to increasing supersaturation with H_2O in the melt. The resulting supersaturation P (ΔP_{ss}, difference between vapor P in the melt and exterior P) is a controlling parameter for bubble nucleation. At the beginning of decompression, homogeneous nucleation of bubbles is energetically inhibited. The free energy of formation (ΔF_c):

$$\Delta F_c = \frac{16\pi\sigma^3}{3\Delta P_{ss}^{\ 2}} \quad (5)$$

for a nucleus with critical radius is dependent on the surface tension and on ΔP_{ss} (Hirth et al., 1970). With increasing ΔP_{ss}, this energetic barrier is lowered until the critical supersaturation P for homogeneous bubble nucleation (ΔP_{HoN}) is reached and the first bubbles start to grow by exceeding the critical bubble embryo radius (Sparks, 1978). Further degassing of the melt is facilitated by diffusion of H_2O molecules into these existing bubbles (bubble growth) as well as nucleation and growth of new bubbles. The energetic barrier for nucleation can be lowered by surfactants such as crystals. In case of heterogeneous nucleation, ΔF_c is reduced by a dimensionless factor that is dependent on the wetting behavior of melt and vapor phase with respect to the nucleation surface (Sparks, 1978; Hurwitz and Navon, 1994; Sparks et al., 1994). In decompression experiments, early degassing of the sample due to heterogeneous bubble nucleation and growth at the capsule-melt interface is able to prevent homogeneous nucleation in the sample center, if the nominal decompression rate is low enough (Mangan and Sisson, 2000; Iacono Marziano et al., 2007).

The difference between the degassing behavior of the VAD79 samples decompressed with CD, MSD and SSD at a nominal rate of 0.024 MPa·s^{-1} is analogous to the results of Nowak et al. (2011) for their experiments with a rhyodacitic melt composition. Although the experiments with the 5 mm cylinders were conducted at slightly H_2O-undersaturated starting conditions, the results are similar to the observations made for the 2.5 mm samples (Fig. 7a, c). The effect of H_2O-undersaturated starting conditions is that ΔP_{HoN} is reached at a later stage during decompression, because the P has to decrease below equilibrium conditions for the respective H_2O-content at first in order to generate supersaturation. In this case, the total P decrease is always higher than ΔP_{ss}. The same applies to samples where H_2O diffused from the sample center towards heterogeneously nucleated bubbles at the capsule-melt interface, thus reducing the H_2O content in the melt (Mangan and Sisson, 2000). SSD down to 75 MPa at a nominal decompression rate of 0.024 MPa·s^{-1} results in a sudden high ΔP_{ss}, because the total P drop of 125 MPa is facilitated in less than 13 s. The energetic barrier for bubble nucleation is massively decreased (Eq. (5)), resulting in extremely high N_V(n)-values (Fig. 8). H_2O diffusion towards heterogeneously nucleated bubbles at the capsule-melt interface does not affect H_2O concentration in the center of the SSD samples during the decompression step. Only a thin rim close to the interface is bubble-free or decorated with bigger bubbles (Fig. 7a, c). In contrast to Nowak et al. (2011), the residual H_2O content in SSD07 is higher (~0.5 wt.%) than in the CD and MSD samples (Fig. 10). This is probably only an analytical problem (see 2.6), because the annealing period of >1 h after the decompression step is sufficient to regain fluid-melt equilibrium, because the diffusion distances are very short in such a highly vesiculated melt (<50 μm). At a CD rate of 0.024 MPa·s^{-1}, ΔP_{ss} increases only slowly (partially due to H_2O diffusion towards the capsule-melt interface). The nucleation of bubbles in the sample center is energetically inhibited until ΔP_{HoN} is exceeded. After the first bubbles start to grow, further degassing of the melt is primarily facilitated by H_2O diffusion into existing bubbles due to the moderate increase of ΔP_{ss} with time. This is evidenced by more or less constant N_V(n)-values of the CD samples decompressed with 0.024 MPa·s^{-1} to different P_{final} (Table 3, Fig. 5). ΔP_{HoN} is <50 MPa in the H_2O-saturated CD experiments at 0.024 MPa·s^{-1}, which is less than half of the P interval determined by Iacono Marziano et al. (2007) for the VAD79 composition. Heterogeneous nucleation of the bubbles on surfactants such as small crystals in CD10 (Fig. 5) is improbable, because the experiments were performed at super-liquidus conditions. Inhomogeneities in the melt could not be detected either in CD10 or at starting conditions of our experiments (REF09, Fig. 4a). There were very few, small bubbles in the melt prior to decompression (REF09) of the 2.5 mm samples, but these pre-existing bubbles are certainly not as homogeneously distributed in the melt as the bubbles in CD10 (Fig. 5). Bubble ascent during decompression from the interface at the capsule bottom is not considered due to the small size of the bubbles. Nevertheless, this does not interfere with the principal observation that bubble growth is the favored degassing mechanism at low CD rates. Although the N_V(n)-values of the CD series decompressed with 0.024 MPa · s^{-1} are below 500 mm^{-3} (Table 3), the residual H_2O contents are within the error equal to the equilibrium solubilities determined by Iacono Marziano et al. (2007), except for the sample with the highest P_{final} of 150 MPa (CD10). The slight measured supersaturation in this sample is probably the residue of the initial supersaturation that was necessary to trigger homogeneous bubble nucleation. After ΔP_{HoN} was reached, the supersaturation could be slowly decreased by diffusive bubble growth until it was degraded at the latest around a P of 100 MPa (CD11). CD at low

decompression rates therefore seems to enable equilibrium degassing, once the nucleation and growth of bubbles has started. MSD at 0.024 MPa·s^{-1} can display features of both SSD and CD (Fig. 7a). The decompression steps were performed with the same extreme decompression rate as for SSD, resulting in a sudden increase of ΔP_{ss} in the melt during each P drop. After the first nucleation event, degassing is facilitated by both nucleation of new bubbles as well as growth of existing bubbles due to the annealing intervals of ~7 min after each decompression step. These repeated changes in ΔP_{ss} result in N_V(n)-values and bubble diameters that are located between the SSD and CD samples (Fig. 7a, b; 8).

The 2.5 mm samples that were decompressed with a nominal decompression rate of 0.0028 MPa·s^{-1} to a P_{final} of 75 MPa show similar differences in the degassing behavior between CD and SD, but are also subject to the long nominal decompression time of more than 12 h. Many bubbles in CD06 and MSD06 have ascended and form a big void/bubble in the top part of the sample (eFig. 1). Homogeneous bubble nucleation in CD06 could have even been prevented, because the low ΔP_{ss} in combination with the time available for H_2O diffusion at this decompression rate probably resulted in degassing by heterogeneous bubble nucleation and growth at the capsule-melt interface. Due to the low level of supersaturation at CD and the available time for H_2O diffusion during the annealing periods at SD, the residual H_2O concentrations are all at equilibrium content at P_{final} (Fig. 10). The extreme annealing interval is also the reason for the decrease in N_V(n) of SSD03 compared to other SSD samples at higher decompression rates (Fig. 8). The initial total P drop with a rate of 10 MPa·s^{-1} is equal for all SSD experiments. Only the annealing periods increase with decreasing nominal decompression rate. Therefore, the N_V(n)-values in the melt are identical in all SSD samples immediately after the single decompression step. At the lowest nominal decompression rate, the annealing period is high enough to enable processes such as Ostwald ripening and bubble coalescence (eFig. 1). This results in the observed drop of N_V(n) of about two orders of magnitude.

With increasing nominal decompression rate, the differences in degassing behavior between CD and SD gradually decrease due to the effect of a fast P drop that results in a sudden high ΔP_{ss} in the melt. At the highest nominal decompression rate of 1.7 MPa·s^{-1}, there are barely any differences in the BSDs and N_V(n)-values between CD and MSD (Fig. 7e, f; 8). The CD rate of 1.7 MPa·s^{-1} is already close the actual rate of 10 MPa·s^{-1} during the decompression steps at SD. Diffusive bubble growth is extremely limited due to the short nominal decompression time of only ~1 min. Bubble nucleation is therefore the predominant degassing process at high nominal decompression rates as evident from the high N_V(n)-values for all decompression methods (Fig. 8). Despite the short time interval for H_2O diffusion during decompression, the melt already degassed significantly throughout the whole sample (Fig. 10, 11) due to the high N_V(n)-values in combination with short diffusion distances. This supports the results of other studies that a phonolitc melt can degas very efficiently after bubble growth has started (e.g., Mongrain et al., 2008).

4.3. Reproducibility of the decompression experiments

Some of the 2.5 mm experiments were performed in duplicate with identical nominal parameters. The reproducibility of the CD experiments at a high decompression rate (CD04, CD09) is good. The N_V(n)-values and porosities are within an acceptable range (Fig. 8, Table 3) and the bubble sizes are comparable (eFig. 8). At a low CD rate (CD07, CD08), N_V(n) differs slightly by one order of magnitude at a low level and the BSE images reveal that the bubbles in CD08 are smaller than the more heterogeneously distributed bubbles in CD07 (Fig. 8, eFig. 9). This could be due to differences in the capsule geometry during decompression. The initially crimped capsule headspaces open during decompression due to the increase of sample volume. It may be that different amounts of melt migrated into the capsule headspaces, thus changing

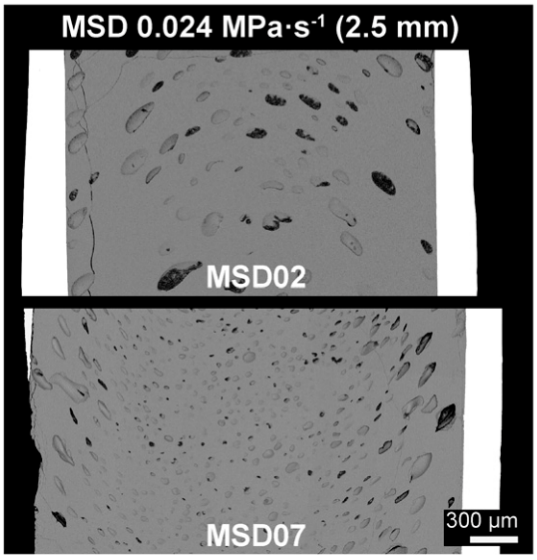

Fig. 17. BSE images of two MSD samples (2.5 mm cylinders, H_2O-saturated starting conditions) after decompression with a rate of 0.024 MPa·s^{-1} at a P_{final} of 75 MPa. Despite identical experimental protocol, the resulting bubble diameters, sample texture and N_V(n)-values are extremely different.

the H_2O diffusion distances towards the capsule-melt interface. On the other hand, cut effects from sample preparation can also contribute to diverging results, if the analysis is mainly based on 2D information. This applies especially to samples with only few big bubbles. Extreme differences occur during MSD at low nominal decompression rates. N_V(n) of MSD07 is three orders of magnitude higher than of MSD02 and the bubbles are clearly smaller (Table 3, Fig. 17). These contrasting results are most likely due to the step-wise method of decompression. The error of the P drop is about 1.5 MPa due to the fast decompression rate. In a first experiment ΔP_{HoN} can be exceeded already e.g., during the fourth P drop, by exceeding the nominal decompression steps of 10 MPa, if we assume a ΔP_{HoN} of 41 MPa for this consideration. In a second experiment, the nominal P drops are not overstepped during decompression. The supersaturation of H_2O that is achieved during the fourth step in this second run is therefore just below the limit for homogeneous bubble nucleation. The bubbles in the first experiment have time to grow by H_2O diffusion or even coalescence throughout the annealing period after the fourth decompression step (Fig. 1), whereas the bubbles in the second experiment did not even nucleate yet. The timescale of the annealing periods is up to ~1 h for the lowest nominal decompression rate (MSD06). The onset of bubble nucleation in MSD experiments with low nominal decompression rates could greatly differ and the variations in total time that is available for bubble growth will result in different N_V(n) and bubble sizes.

Despite lower initial H_2O-content at slightly H_2O-undersaturated starting conditions of the decompression experiments, the bubbles in the 5 mm specimens decompressed with 0.024 MPa·s^{-1} are clearly bigger than in the corresponding 2.5 mm samples (Fig. 7a–d). Due to the doubled cylinder diameter, the H_2O content in the center of the 5 mm samples is less affected by early degassing at the capsule-melt interface and the results are expected to be more reliable. The total amount of H_2O that degassed by homogeneous bubble nucleation and growth could have been higher than in the 2.5 mm samples, but without further CD experiments with 5 mm cylinders that are quenched at higher P_{final} to verify ΔP_{HoN}, this remains unclear.

Some of our decompressed samples can be compared to run products from the experiments of Iacono Marziano et al. (2007) and reveal significant differences. In contrast to Iacono Marziano et al. (2007), our glass cylinders were 100 µm wider in diameter and sometimes ~1 mm longer and we used a synthetic starting material. The chemical

composition of our VAD79 glass (Table 1) is within 1σ equal to the natural composition (Iacono Marziano et al., 2007), except for the weight fraction of Al_2O_3 (−0.61 wt.%). On the other hand, the weight fraction of SiO_2 is slightly higher (+0.38 wt.%) in our starting material and as both Si^{4+} and Al^{3+} are network forming cations, the contrasting differences should not significantly influence controlling parameters such as viscosity and T_g. The quench rates in both studies are comparable. Differences due to diverging shrinking factors are therefore unlikely. The samples B64, B76 and B75 in Iacono Marziano et al. (2007) correspond to the MSD experiments with decompression rates of 0.0028–0.17 MPa·s^{-1}. Iacono Marziano et al. (2007) reported that they did not observe homogeneous bubble nucleation in these samples and the measured residual H_2O contents are higher than in our corresponding MSD specimens (Table 3 in Iacono Marziano et al., 2007 vs. Table 3). Even the results of their CD experiment with a high decompression rate of 1.7 MPa·s^{-1} (sample B74) differ from our observations for CD04 and CD09. The uncorrected porosity of B74 is only 5% (vs. 14.5% for CD09), although it was decompressed to a slightly lower P_{final} of 70 MPa. The bubble number density of B74 is ~20 times higher than N_V(n) of our corresponding CD samples and the bubbles are much smaller (Fig. 5c in Iacono Marziano et al., 2007 vs. Fig. 7e). This is probably due the lower nucleation P of <50 MPa observed in this study (Fig. 5) compared to the reported ΔP_{HoN} of ~100 MPa in Iacono Marziano et al. (2007). Consequently, bubbles nucleated earlier in our runs and the timescale for growth and/or coalescence was larger. Marginal bulk compositional variations are unlikely to result in a more than twice as high value for ΔP_{HoN}. Heterogeneous nucleation on surfactants (such as small crystals below the detection limit) as described by Hurwitz and Navon (1994) is also improbable, because the experiments were conducted at super-liquidus conditions. A change of sample geometry due to melt migration into the capsule headspace during decompression could also influence the H_2O diffusion distance towards the capsule wall, thus affecting the level of H_2O supersaturation in the melt (especially in experiments with a low nominal decompression rate and small capsule diameters). Influences of parameters such as capsule length (including the crimped headspaces), sealing method and resulting rigidity of the sample container are conceivable, but have to be investigated in detail in a forthcoming study.

5. Conclusions and outlook

The basic results of Nowak et al. (2011) in terms of degassing behavior at different decompression methods could be verified for a H_2O-bearing phonolitic melt at nominal decompression rates of ≤0.024 MPa·s^{-1}. SD favors the nucleation of bubbles due to sudden supersaturation with H_2O in the melt within a limited period of time. At CD, the supersaturation resulting from moderate P decrease is continuously reduced by diffusive bubble growth after the first bubbles nucleated in the melt. With increasing nominal decompression rate, the differences between the three decompression methods gradually decrease due to the effect of fast P drop. Despite smaller decompression steps at MSD (10 instead of 50 MPa) and lower total P decrease (125 instead of 250 MPa) than in the study of Nowak et al. (2011), the SD technique is still not suitable to simulate the degassing processes during CD of a hydrated melt with low, reasonable decompression rates. Modified MSD experiments could be used for the simulation of melt degassing behavior during magma ascent with subsequent storage at higher crustal levels, but only if the decompression steps are realized with suitable CD rates.

The BSDs and the porosities in all our vitrified experimental samples do not correspond to the actual bubble sizes at P_{final} prior to isobaric rapid quench. The shrinkage of bubbles due to decreasing $V_m(H_2O)$ during quench initiates melt transport in the capsule. These effects have to be considered if such experimental samples are e.g., compared to natural specimens in terms of their porosities and BSDs or if models for diffusive bubble growth are derived from the H_2O concentration around bubbles. Direct comparison of quenched samples from different experimental setups can also be problematic, if quench parameters are varying. The comparison of experimental samples with different P_{final} is difficult, because the decrease of $V_m(H_2O)$ with T is dependent on P. The BSDs and porosities can be corrected in first approximation, but these calculations are based on assumptions for important influence parameters (viscosity limit, uniform residual H_2O content in the sample etc.) at the moment. For an accurate correction, 3D in situ measurements of bubble sizes in the whole samples during CD and isobaric cooling would have to be performed at HP–HT conditions to absolutely quantify the effect of bubble shrinkage. Only in case of a non-isobaric quench, where the external P of the pressure medium decreases by the same amount as the internal fluid P in the bubbles, the bubble volumes would remain constant. The effect of bubble shrinkage should be considered in future melt degasing studies.

The results of this study can be used to optimize decompression experiments for the simulation of continuous magma ascent. The experimental protocol must not negatively influence the degassing processes. Decompression has to be performed continuously. The diameter of the sample container must be maximized to exclude any influence on nucleation and growth processes in the sample center due to early degassing at the capsule-melt interface. Initial excess H_2O in the capsules prior to decompression should be avoided. The shrinkage of bubbles must be corrected in order to determine the porosity of the melt prior to rapid quench. Besides further improvement of the experimental setup and protocol, current decompression experiments involve the degassing processes during CD of the VAD79 melt with mixed H_2O–CO_2 fluids to continuously approach the natural system.

Supplementary data to this article can be found online at http://dx.doi.org/10.1016/j.jvolgeores.2014.11.017.

Acknowledgments

This project was funded by the “Deutsche Forschungsgemeinschaft” (DFG, NO378/5-1). We thank Dr. Kai-Uwe Hess from the LMU Munich for the calculation of T_g for the phonolitic melt at 150 K·min^{-1}. Special thanks to Indra Gill-Kopp for careful sample preparation, Annette Flicker for numerous NIR measurements, Sarah Ulmer for experimental assistance and PD Dr. Thomas Wenzel for support at the EMP. Many thanks to Norbert Walker and Barbara Maier from the workshop for keeping the decompression valve operational at all times. We also thank Dr. Madeleine Humphreys and an anonymous reviewer as well as the Editor-in-Chief Dr. Margaret T. Mangan for their very useful comments and suggestions that helped to greatly improve the manuscript.

References

Bagdassarov, N., Dorfman, A., Dingwell, D.B., 2000. Effect of alkalis, phosphorus and water on the surface tension of haplogranite melt. Am. Mineral. 85, 33–40.

Baker, D.R., Mancini, L., Polacci, M., Higgins, M.D., Gualda, G.A.R., Hill, R.J., Rivers, M.L., 2012. An introduction to the application of X-ray microtomography to the three-dimensional study of igneous rocks. Lithos 148, 262–276.

Barclay, J., Riley, D.S., Sparks, R.S.J., 1995. Analytical models for bubble growth during decompression of high viscosity magmas. Bull. Volcanol. 57, 422–431.

Behrens, H., Romano, C., Nowak, M., Holtz, F., Dingwell, D.B., 1996. Near-infrared spectroscopic determination of water species in glasses of system $MAlSi_3O_8$ (M = Li, Na, K): an interlaboratory study. Chem. Geol. 128, 41–63.

Berndt, J., Liebske, C., Holtz, F., Freise, M., Nowak, M., Ziegenbein, D., Hurkuck, W., Koepke, J., 2002. A combined rapid-quench and H_2-membrane setup for internally heated pressure vessels: description and application for water solubility in basaltic melts. Am. Mineral. 87, 1717–1726.

Brugger, C.R., Hammer, J.E., 2010. Crystallization kinetics in continuous decompression experiments: implications for interpreting natural magma ascent processes. J. Petrol. 51, 1941–1965.

Burgisser, A., Gardner, J.E., 2005. Experimental constraints on degassing and permeability in volcanic conduit flow. Bull. Volcanol. 67, 42–56.

Castro, J.M., Burgisser, A., Schipper, C.I., Mancini, S., 2012. Mechanisms of bubble coalescence in silicic magmas. Bull. Volcanol. 74, 2339–2352.

Devine, J.D., Gardner, J.E., Brack, H.P., Layne, G.D., Rutherford, M.J., 1995. Comparison of micro-analytical methods for estimating H_2O contents of silicic volcanic glasses. Am. Mineral. 80, 319–328.

Dingwell, D.B., Webb, S.L., 1990. Relaxation in silicate melts. Eur. J. Mineral. 2, 427–449.

Duan, Z.H., Zhang, Z.G., 2006. Equation of state of the H_2O, CO_2, and H_2O–CO_2 systems up to 10 GPa and 2573.15 K: molecular dynamics simulations with ab initio potential surface. Geochim. Cosmochim. Acta 70, 2311–2324.
Eichelberger, J.C., Carrigan, C.R., Westrich, H.R., Price, R.H., 1986. Non-explosive silicic volcanism. Nature 323, 598–602.
Gardner, J.E., 2007. Bubble coalescence in rhyolitic melts during decompression from high pressure. J. Volcanol. Geotherm. Res. 166, 161–176.
Gardner, J.E., 2012. Surface tension and bubble nucleation in phonolite magmas. Geochim. Cosmochim. Acta 76, 93–102.
Gardner, J.E., Thomas, R.M.E., Jaupart, C., Tait, S., 1996. Fragmentation of magma during Plinian volcanic eruptions. Bull. Volcanol. 58, 144–162.
Gardner, J.E., Hilton, M., Carroll, M.R., 1999. Experimental constraints on degassing of magma: Isothermal bubble growth during continuous decompression from high pressure. Earth Planet. Sci. Lett. 168, 201–218.
Gardner, J.E., Hilton, M., Carroll, M.R., 2000. Bubble growth in highly viscous silicate melts during continuous decompression from high pressure. Geochim. Cosmochim. Acta 64, 1473–1483.
Gardner, J.E., Ketcham, R.A., Moore, G., 2013. Surface tension of hydrous silicate melts: constraints on the impact of melt composition. J. Volcanol. Geotherm. Res. 267, 68–74.
Giordano, D., Nichols, A.R.L., Dingwell, D.B., 2005. Glass transition temperatures of natural hydrous melts: a relationship with shear viscosity and implications for the welding process. J. Volcanol. Geotherm. Res. 142, 105–118.
Giordano, D., Russell, J.K., Dingwell, D.B., 2008. Viscosity of magmatic liquids: a model. Earth Planet. Sci. Lett. 271, 123–134.
Gonnermann, H.M., Manga, M., 2007. The fluid mechanics inside a volcano. Annu. Rev. Fluid Mech. 39, 321–356.
Hammer, J.E., Rutherford, M.J., 2002. An experimental study of the kinetics of decompression-induced crystallization in silicic melt. J. Geophys. Res. 107, 1–24.
Higgins, M.D., 2000. Measurement of crystal size distributions. Am. Mineral. 85, 1105–1116.
Higgins, M.D., 2002. Closure in crystal size distributions (CSD), verification of CSD calculations and the significance of CSD fans. Am. Mineral. 87, 171–175.
Higgins, M.D., 2006. Quantitative Textural Measurements in Igneous and Metamorphic Petrology. Cambridge University Press, New York (265 pp.).
Hirth, J.P., Pound, G.M., St. Pierre, G.R., 1970. Bubble nucleation. Metall. Trans. 1, 939–945.
Hurwitz, S., Navon, O., 1994. Bubble nucleation in rhyolitic melts: experiments at high pressure, temperature and water content. Earth Planet. Sci. Lett. 122, 267–280.
Iacono Marziano, G., Schmidt, B.C., Dolfi, D., 2007. Equilibrium and disequilibrium degassing of a phonolitic melt (Vesuvius AD 79 "white pumice") simulated by decompression experiments. J. Volcanol. Geotherm. Res. 161, 151–164.
Jerram, D.A., Higgins, M.D., 2007. 3D analysis of rock textures: quantifying igneous microstructures. Elements 3, 239–245.
Larsen, J.F., Denis, M.H., Gardner, J.E., 2004. Experimental study of bubble coalescence in rhyolitic and phonolitic melts. Geochim. Cosmochim. Acta 68, 333–344.
Larsen, J.F., Gardner, J.E., 2004. Experimental study of water degassing from phonolite melts: implications for volatile oversaturation during magmatic ascent. J. Volcanol. Geotherm. Res. 134, 109–124.
Lyakhovsky, V., Hurwitz, S., Navon, O., 1996. Bubble growth in rhyolitic melts: experimental and numerical investigation. Bull. Volcanol. 58, 19–32.
Mangan, M., Sisson, T., 2000. Delayed, disequilibrium degassing in rhyolite magma: decompression experiments and implications for explosive volcanism. Earth Planet. Sci. Lett. 183, 441–455.
Mangan, M., Sisson, T., 2005. Evolution of melt-vapor surface tension in silicic volcanic systems: experiments with hydrous melts. J. Geophys. Res. 110 (B01202).
Mangan, M.T., Sisson, T., Hankins, W.B., 2004. Decompression experiments identify kinetic controls on explosive silicic eruptions. Geophys. Res. Lett. 31 (L08605).
Marsh, B.D., 1988. Crystal size distribution (CSD) in rocks and the kinetics and dynamics of crystallization. 1. Theory. Contrib. Mineral. Petrol. 99, 277–291.
Marxer, H., Nowak, M., 2013. Micro-FTIR imaging: an advanced method for the determination of CO_2 and H_2O concentration gradients in silicate glasses. Eur. J. Mineral. 25, 307–316.
Marxer, H., Bellucci, P., Ulmer, S., Nowak, M., 2013. Experimental magma degassing: the revenge of the deformed bubbles. Abstract V23E-02 Presented at 2013 Fall Meeting, AGU, San Francisco, Calif., 9–13 Dec.
Mastrolorenzo, G., Pappalardo, L., 2006. Magma degassing and crystallization processes during eruptions of high-risk Neapolitan-volcanoes: evidence of common equilibrium rising processes in alkaline magmas. Earth Planet. Sci. Lett. 250, 164–181.
McIntosh, I.M., Llewellin, E.W., Humphreys, M.C.S., Nichols, A.R.L., Burgisser, A., Schipper, C.I., Larsen, J.F., 2014. Distribution of dissolved water in magmatic glass records growth and resorption of bubbles. Earth Planet. Sci. Lett. 401, 1–11.
Misiti, V., Vetere, F., Freda, C., Scarlato, P., Behrens, H., Mangiacapra, A., Dingwell, D.B., 2011. A general viscosity model of Campi Flegrei (Italy) melts. Chem. Geol. 290, 50–59.
Mock, A., Jerram, D.A., 2005. Crystal size distributions (CSD) in three dimensions: insights from the 3D reconstruction of a highly porphyritic rhyolite. J. Petrol. 46, 1525–1541.
Mongrain, J., Larsen, J.F., King, P.L., 2008. Rapid water exsolution, degassing and bubble collapse observed experimentally in K-phonolite melts. J. Volcanol. Geotherm. Res. 173, 178–184.
Nowak, M., Behrens, H., 1997. An experimental investigation on diffusion of water in haplogranitic melts. Contrib. Mineral. Petrol. 126, 365–376.
Nowak, M., Behrens, H., 2001. Water in rhyolitic magmas: getting a grip on a slippery problem. Earth Planet. Sci. Lett. 184, 515–522.
Nowak, M., Cichy, S.B., Botcharnikov, R.E., Walker, N., Hurkuck, W., 2011. A new type of high-pressure low-flow metering valve for continuous decompression: first experimental results on degassing of rhyodacitic melts. Am. Mineral. 96, 1373–1380.
Ochs, F.A., Lange, R.A., 1999. The density of hydrous magmatic liquids. Science 283, 1314–1317.
Paonita, A., Martelli, M., 2006. Magma dynamics at mid-ocean ridges by noble gas kinetic fractionation: assessment of magmatic ascent rates. Earth Planet. Sci. Lett. 241, 138–158.
Peterson, T.D., 1996. A refined technique for measuring crystal size distributions in thin section. Contrib. Mineral. Petrol. 124, 395–405.
Pichavant, M., Di Carlo, I., Rotolo, S.G., Scaillet, B., Burgisser, A., Le Gall, N., Martel, C., 2013. Generation of CO_2-rich melts during basalt magma ascent and degassing. Contrib. Mineral. Petrol. 166, 545–561.
Polacci, M., Baker, D.R., Mancini, L., Tromba, G., Zanini, F., 2006. Three-dimensional investigation of volcanic textures by X-ray microtomography and implications for conduit processes. Geophys. Res. Lett. 33 L13312.
Proussevitch, A.A., Sahagian, D.L., Tsentalovich, E.P., 2007. Statistical analysis of bubble and crystal size distributions: formulations and procedures. J. Volcanol. Geotherm. Res. 164, 95–111.
Rutherford, M.J., 2008. Magma ascent rates. Rev. Mineral. Geochem. 69, 241–271.
Sahagian, D.L., Proussevitch, A.A., 1998. 3D particle size distributions from 2D observations: stereology for natural applications. J. Volcanol. Geotherm. Res. 84, 173–196.
Saltikov, S.A., 1967. The determination of the size distribution of particles in an opaque material from a measurement of the size distribution of their sections. In: Elias, H. (Ed.), Stereology. Springer Berlin, Heidelberg, pp. 163–173.
Schneider, C.A., Rasband, W.S., Eliceiri, K.W., 2012. NIH Image to ImageJ: 25 years of image analysis. Nat. Methods 9, 671–675.
Shea, T., Houghton, B.F., Gurioli, L., Cashman, K.V., Hammer, J.E., Hobden, B.J., 2010. Textural studies of vesicles in volcanic rocks: an integrated methodology. J. Volcanol. Geotherm. Res. 190, 271–289.
Sparks, R.S.J., 1978. The dynamics of bubble formation and growth in magmas: a review and analysis. J. Volcanol. Geotherm. Res. 3, 1–37.
Sparks, R.S.J., Barclay, J., Jaupart, C., Mader, H.M., Phillips, J.C., 1994. Physical aspects of magmatic degassing. 1. Experimental and theoretical constraints on vesiculation. Rev. Mineral. Geochem. 30, 413–445.
Sparks, R.S.J., Baker, L., Brown, R.J., Field, M., Schumacher, J., Stripp, G., Walters, A., 2006. Dynamical constraints on kimberlite volcanism. J. Volcanol. Geotherm. Res. 155, 18–48.
Thomas, N., Jaupart, C., Vergniolle, S., 1994. On the vesicularity of pumice. J. Geophys. Res. 99, 15633–15644.
Toramaru, A., 1989. Vesiculation process and bubble size distributions in ascending magmas with constant velocities. J. Geophys. Res. 94, 17523–17542.
Woods, A.W., Koyaguchi, T., 1994. Transitions between explosive and effusive eruptions of silicic magmas. Nature 370, 641–644.
Zhang, Y.X., Xu, Z.J., Behrens, H., 2000. Hydrous species geospeedometer in rhyolite: improved calibration and application. Geochim. Cosmochim. Acta 64, 3347–3355.

eFigure captions

eFig. 1: BSE images of CD06 (a), MSD06 (b) and SSD03 (c) decompressed to a P_{final} of 75 MPa with a nominal decompression rate of 0.0028 MPa·s^{-1} (2.5 mm cylinders, H_2O-saturated starting conditions). The headspaces of CD06 and MSD06 were lost during sample preparation.

eFig. 2: BSE images of CD08 (a), MSD07 (b) and SSD04 (c) decompressed to a P_{final} of 75 MPa with a nominal decompression rate of 0.024 MPa·s^{-1} (2.5 mm cylinders, H_2O-saturated starting conditions). The excerpts with the redrawn bubble intersections in white color were used for the generation of the BSDs in Fig. 7b.

eFig. 3: BSE images of CD03 (a), MSD03 (b) and SSD05 (c) decompressed to a P_{final} of 75 MPa with a nominal decompression rate of 0.17 MPa·s^{-1} (2.5 mm cylinders, H_2O-saturated starting conditions). The headspaces of CD03 and MSD03 were lost during sample preparation.

eFig. 4: BSE images of CD04 (a), MSD04 (b) and SSD06 (c) decompressed to a P_{final} of 75 MPa with a nominal decompression rate of 1.7 MPa·s^{-1} (2.5 mm cylinders, H_2O-saturated starting conditions). The excerpts with the redrawn bubble intersections in white color were used for the generation of the BSDs in Fig. 7f. The headspaces of CD04 and MSD04 were lost during sample preparation.

eFig. 5: BSE images of CD19 (a), MSD08 (b) and SSD07 (c) decompressed to a P_{final} of 75 MPa with a nominal decompression rate of 0.024 MPa·s^{-1} (5 mm cylinders, slightly H_2O-undersaturated starting conditions). The excerpts with the redrawn bubble intersections in white color were used for the generation of the BSDs in Fig. 7d.

eFig. 6: BSE images of CD samples (5 mm cylinders, slightly H_2O-undersaturated starting conditions) decompressed to a P_{final} of 75 MPa with decompression rates of 0.0028 MPa·s^{-1} (a), 0.024 MPa·s^{-1} (b), 0.17 MPa·s^{-1} (c) and 1.7 MPa·s^{-1} (d).

eFig. 7: BSE images of CD samples (2.5 mm cylinders, H_2O-saturated starting conditions) decompressed with 0.024 MPa·s^{-1} to different P_{final} of 150 MPa (a), 100 MPa (b) and 75 MPa (c). One headspace of CD11 was lost during sample preparation.

eFig. 8: BSE images of two CD samples (2.5 mm cylinders, H_2O-saturated starting conditions) decompressed to a P_{final} of 75 MPa with 1.7 MPa·s^{-1}: CD04 (a) and CD09 (b). The headspaces of CD04 were lost during sample preparation.

eFig. 9: BSE images of two CD samples (2.5 mm cylinders, H_2O-saturated starting conditions) decompressed to a P_{final} of 75 MPa with 0.024 MPa·s^{-1}: CD07 (a) and CD08 (b). The headspaces of CD07 were lost during sample preparation.

eFig. 10: BSE images of two MSD samples (2.5 mm cylinders, H_2O-saturated starting conditions) decompressed to a P_{final} of 75 MPa with a nominal decompression rate 0.024 MPa·s^{-1}: MSD02 (a) and MSD07 (b). The headspaces of MSD02 were lost during sample preparation.

eFigures

eFig. 1a-c

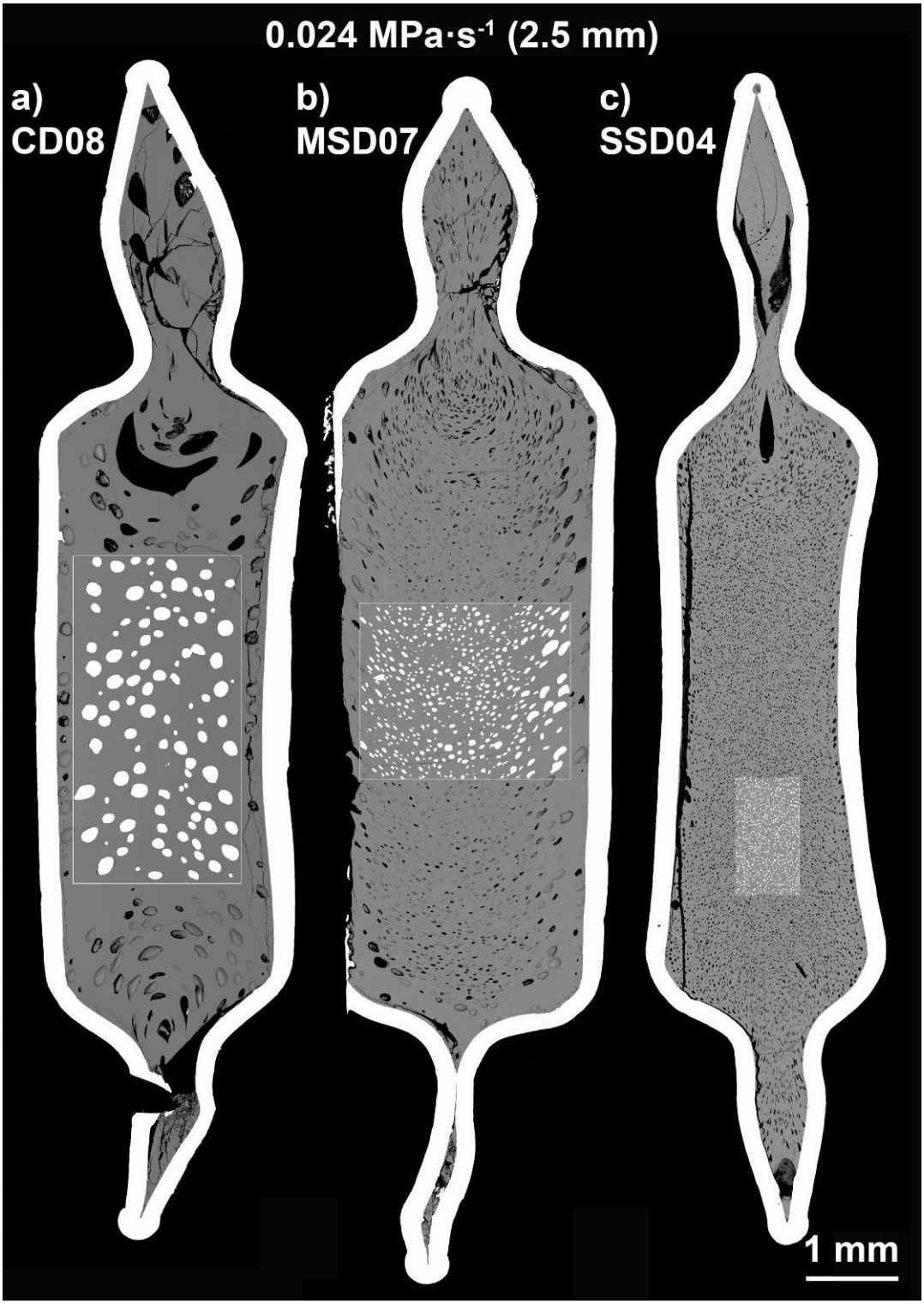

eFig. 2a-c

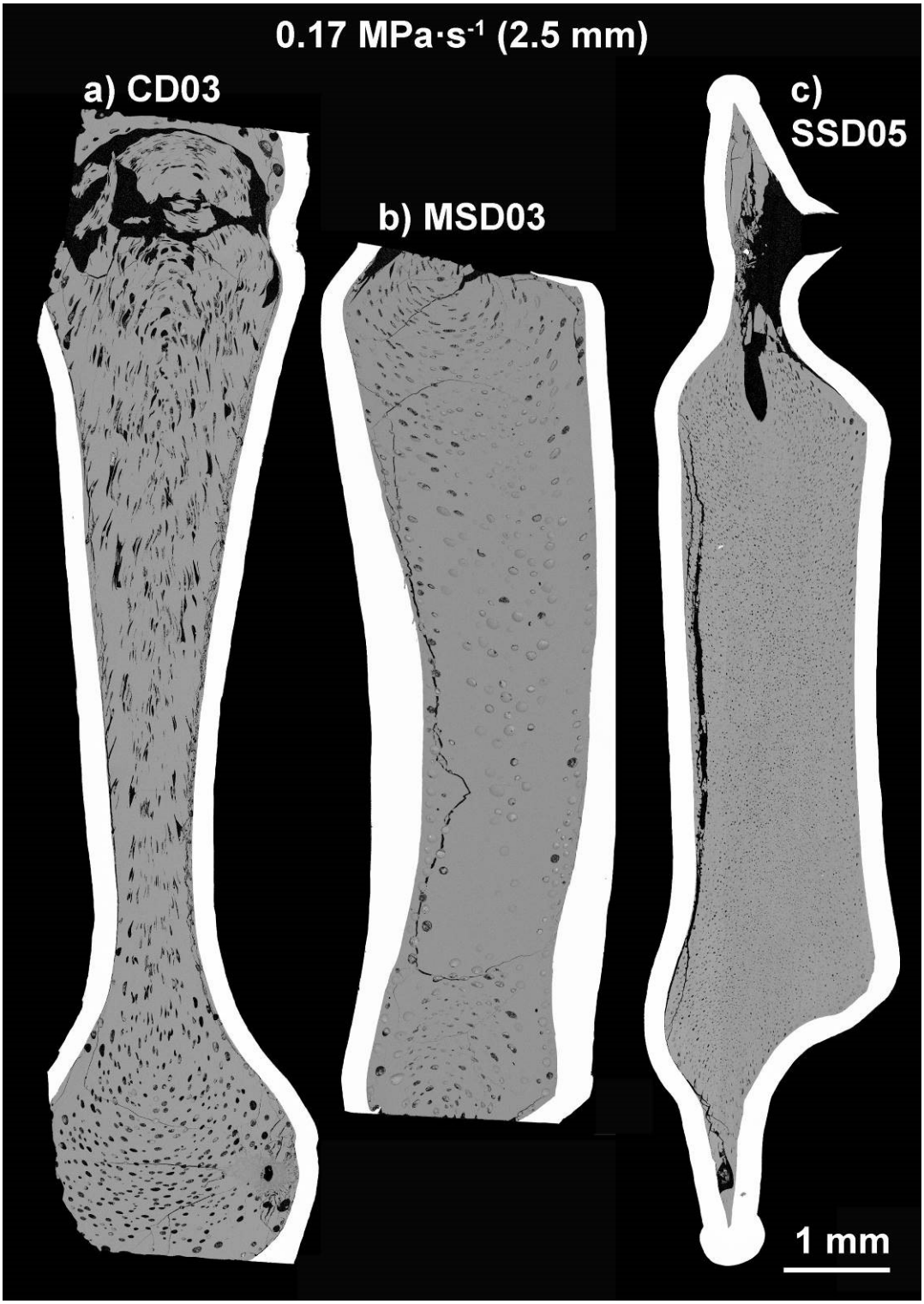

eFig. 3a-c

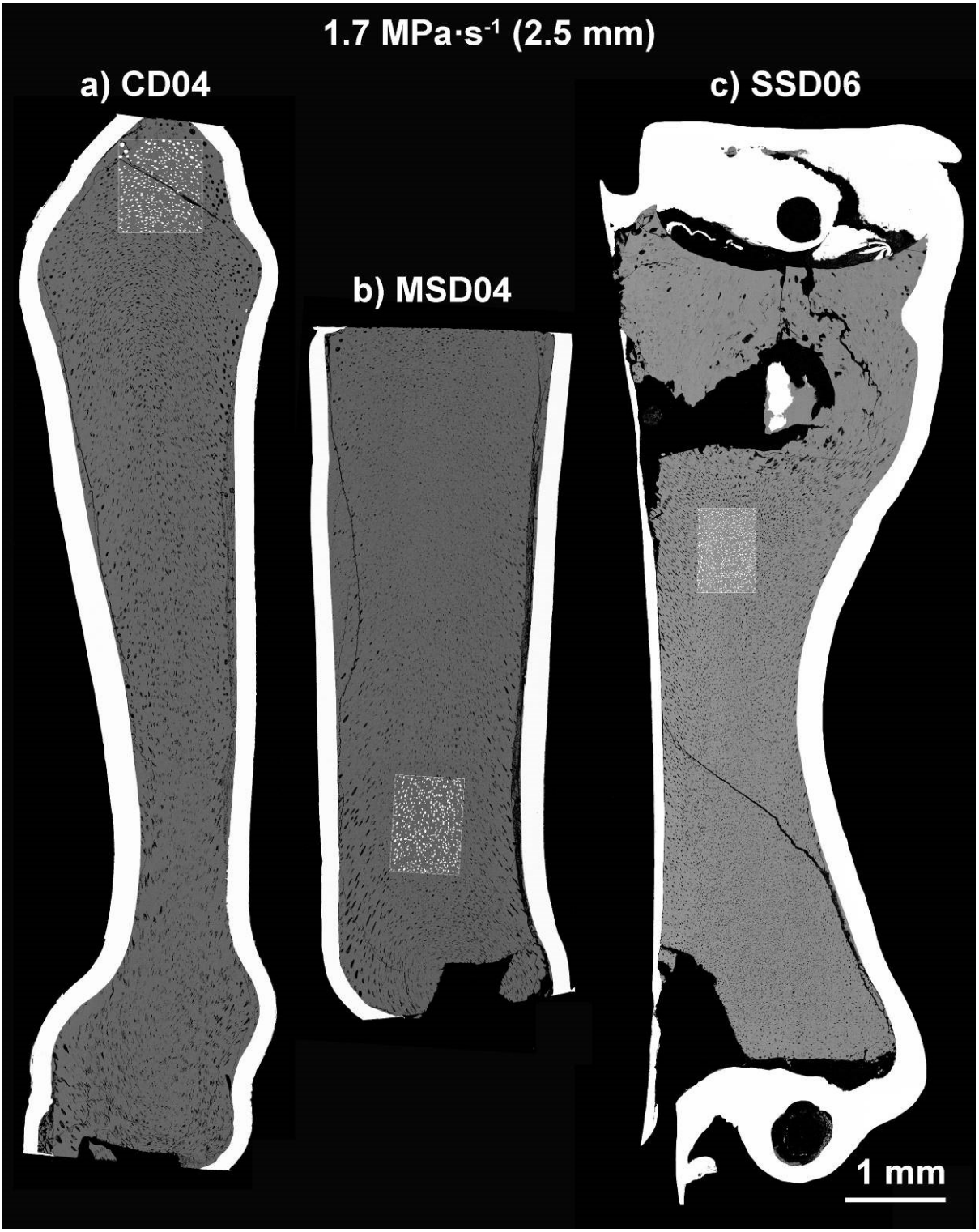

eFig. 4a-c

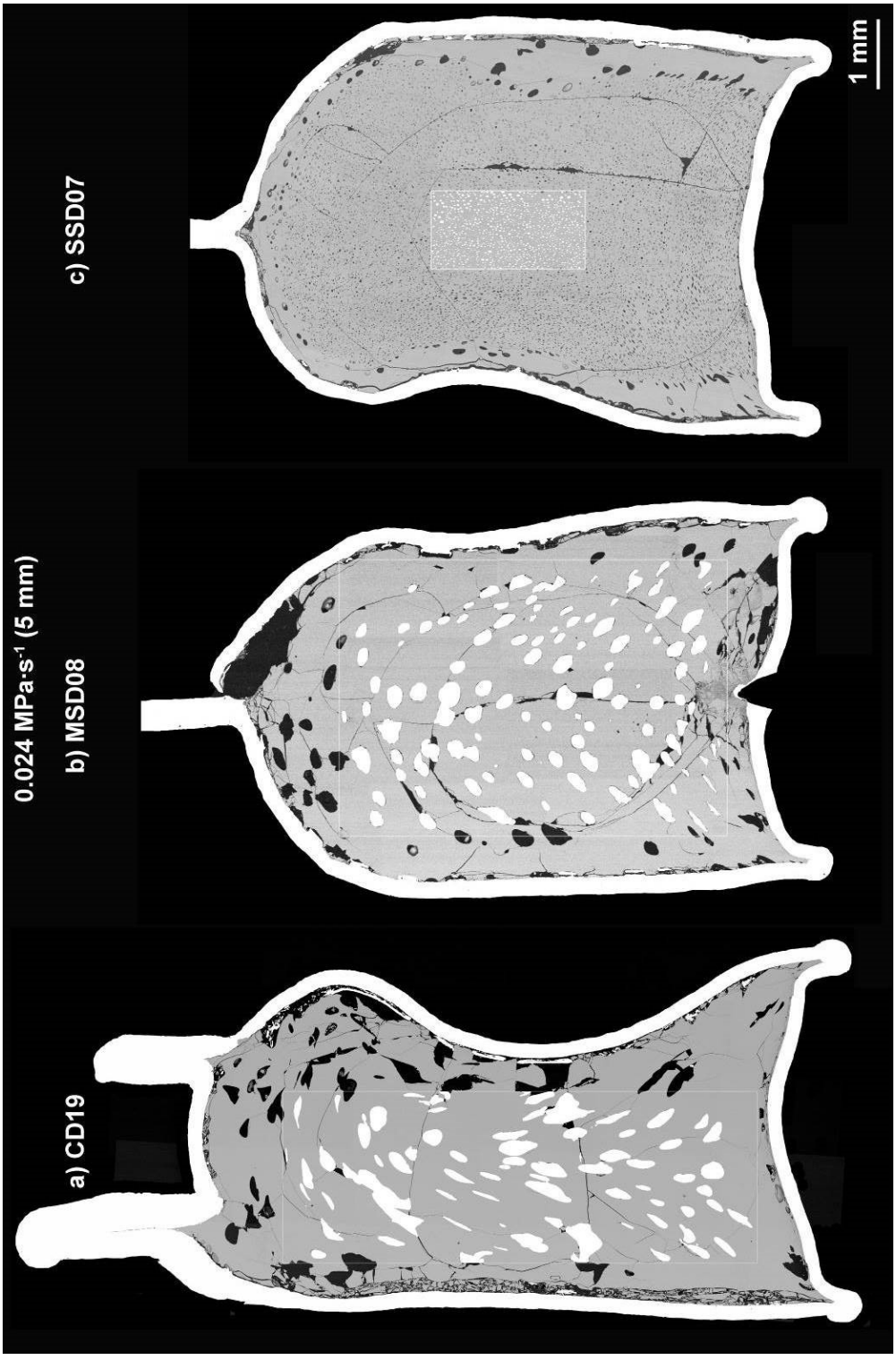

eFig. 5a-c

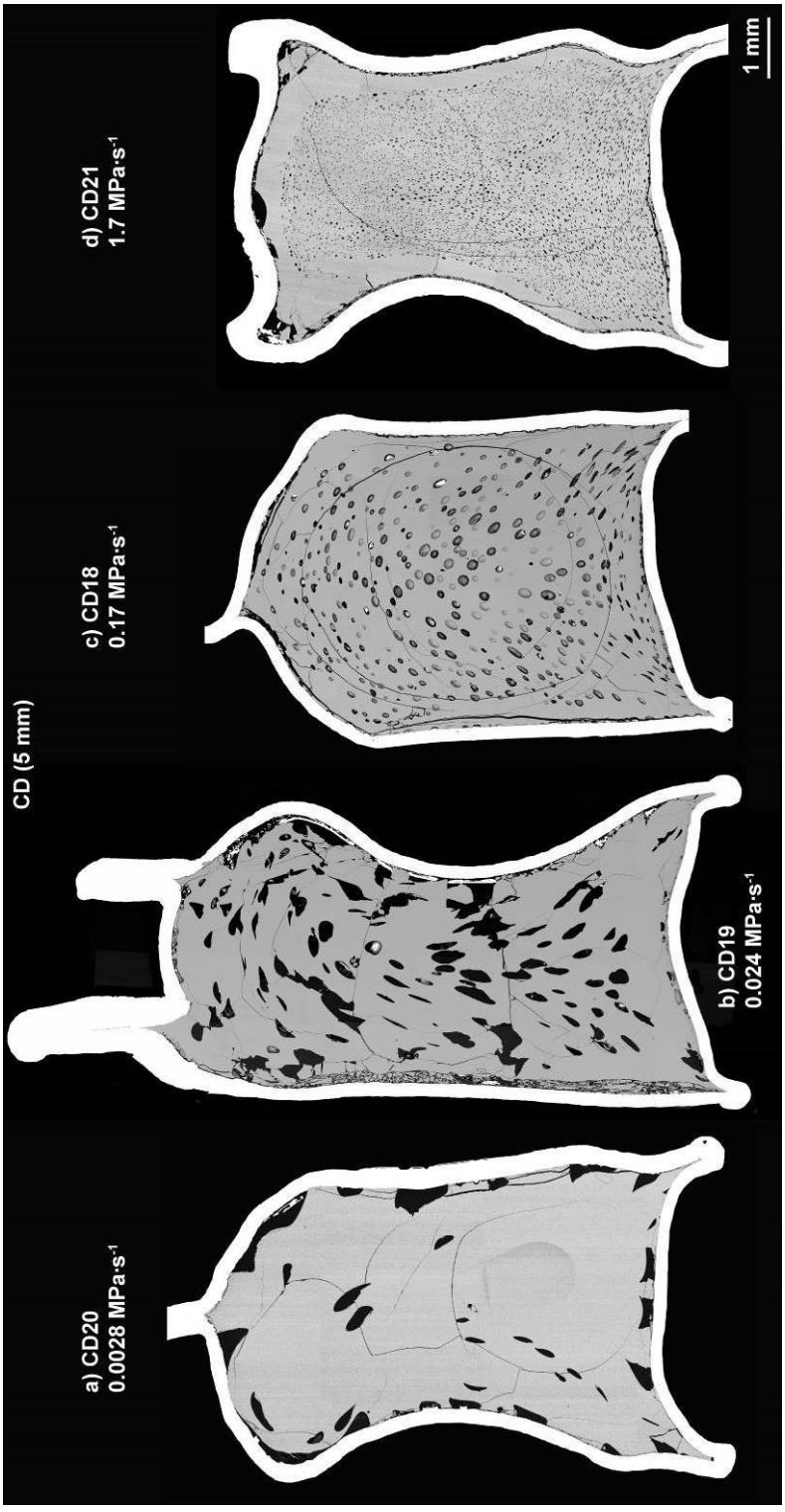
a) CD20
0.0028 MPa·s-1
b) CD19
0.024 MPa·s-1
CD (5 mm)
c) CD18
0.17 MPa·s-1
d) CD21
1.7 MPa·s-1
1 mm

eFig. 6a-d

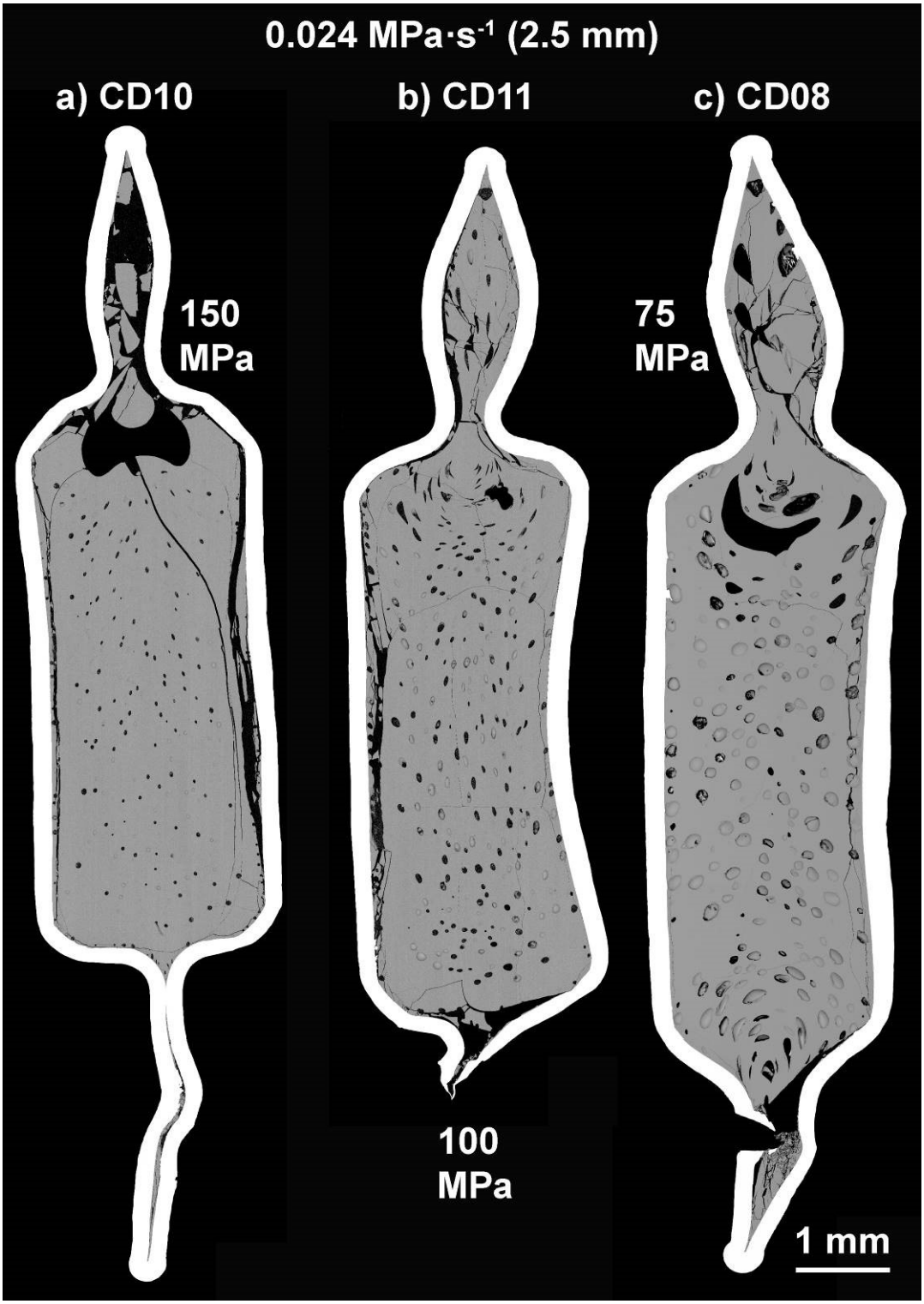

eFig. 7a-c

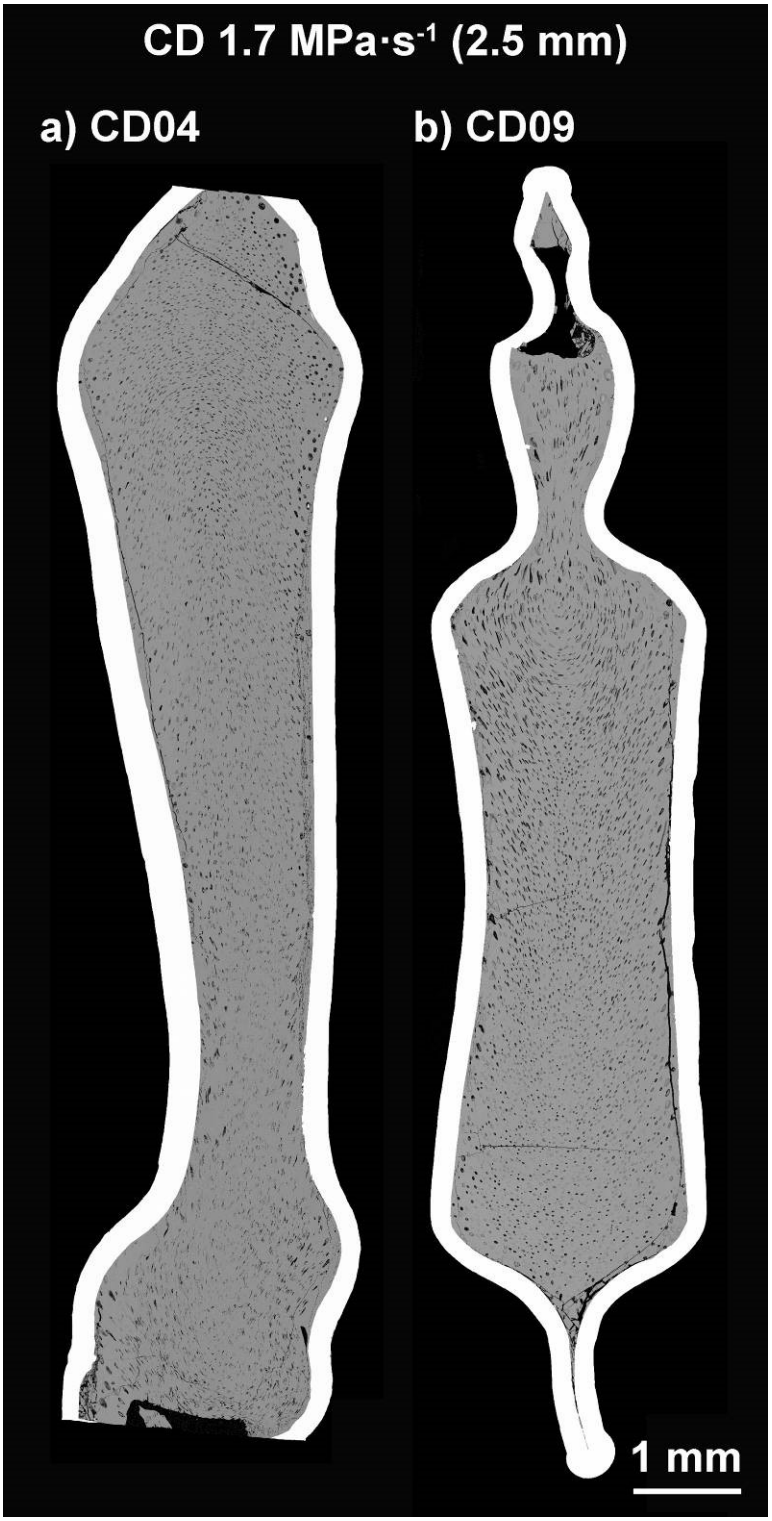

eFig. 8a, b

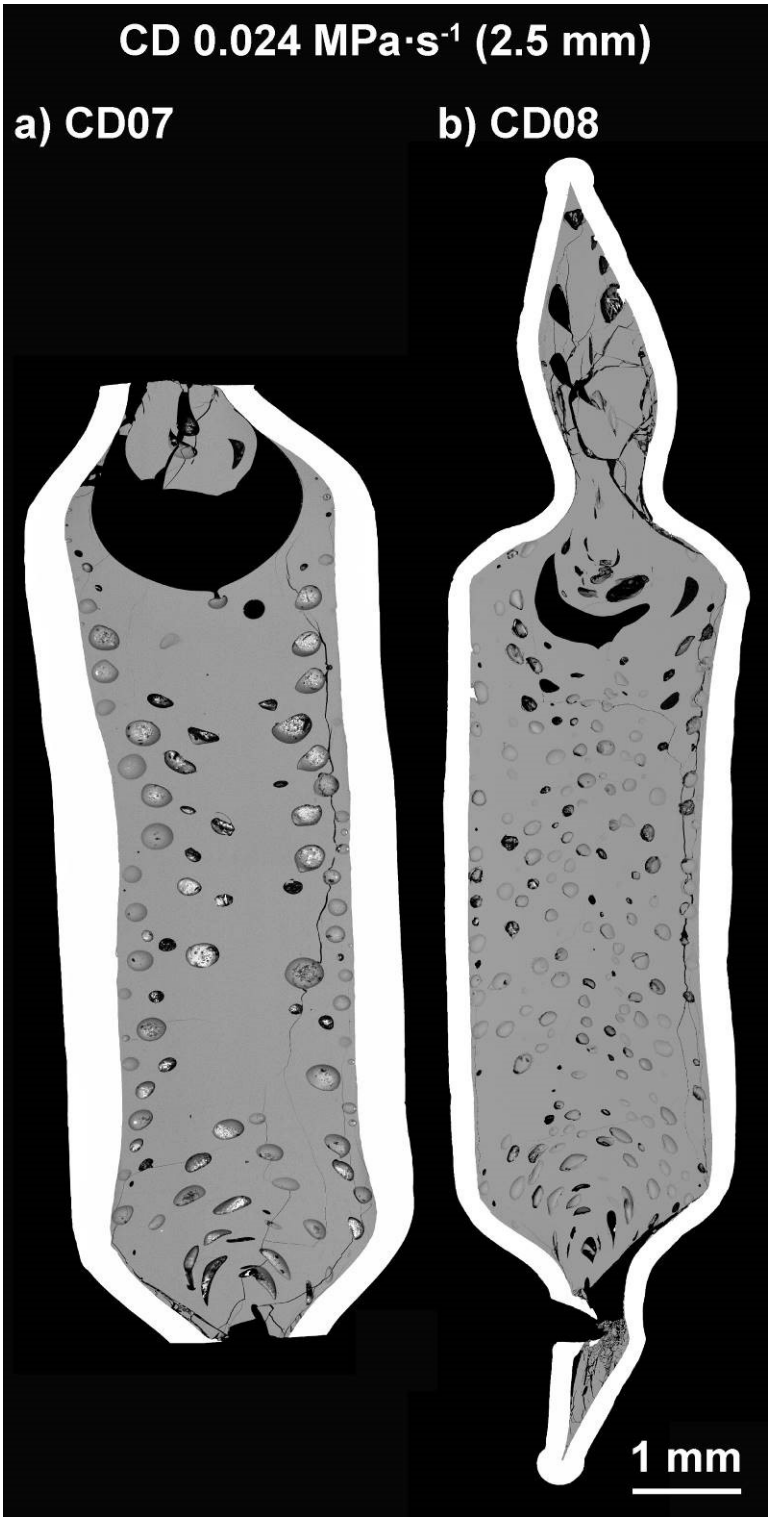

eFig. 9a, b

eFig. 10a, b

Appendix C

Title

Degassing of hydrous trachytic Campi Flegrei and phonolitic Vesuvius melts: Experimental limitations and chances to study homogeneous bubble nucleation

Authors

Oliver Preuß, Holger Marxer, Sarah Ulmer, Johannes Wolf, Marcus Nowak

Status

Submitted to American Mineralogist, paper 5480

Contributions of the candidate

Scientific ideas: 40 %

Experimental work: 20 %

Data generation: 20 %

Analysis and interpretation: 40 %

Paper writing: 40 %

Degassing of hydrous trachytic Campi Flegrei and phonolitic Vesuvius melts: Experimental limitations and chances to study homogeneous bubble nucleation

Oliver Preuss*, Holger Marxer[1], Sarah Ulmer[1,2], Johannes Wolf[1], Marcus Nowak*[1]

[1]Department of Geosciences, University of Tübingen, Wilhelmstraße 56, 72074 Tübingen, Germany

[2]Institue for Materials Science, University of Stuttgart, Heisenbergstraße 3, 70568 Stuttgart, Germany

*corresponding authors

postal: Department of Geosciences,
University of Tübingen,
Wilhelmstraße 56,
72074 Tübingen, Germany

e-mail: oliver.preuss@uni-tuebingen.de
marcus.nowak@uni-tuebingen.de

phone: +49 7071 29 72648

Abstract

Melt degassing by bubble nucleation and growth is a driving mechanism of magma ascent. Decompression experiments with hydrous silicate melts can be used to investigate the onset and the dynamics of H_2O degassing. Nominally H_2O-undersaturated trachytic Campi Flegrei and phonolitic Vesuvius melts were decompressed at a super-liquidus T of 1050 °C from 200 MPa to final pressures (P_{final}) of 100, 75 and 60 MPa using continuous decompression rates of 0.024 and 0.17 MPa·s^{-1}. Experiments started from either massive glass cylinders or glass powder to demonstrate the influence of the starting material on melt degassing. Glass (or natural rock) powder can be used to shorten the equilibration time (t_{eq}) prior to decompression for dissolution of H_2O in the melt. The decompressed samples were quenched and compared in terms of bubble number density (N_V), porosity and residual H_2O content in the melt.

Decompression of all glass cylinder samples led to homogeneous bubble nucleation with high N_V of ~10^5 mm^{-3}. With decreasing P_{final}, the residual H_2O concentrations in the glass decrease from values close to the initial content (P_{final} = 100 MPa) in direction of the equilibrium H_2O concentration (P_{final} = 60 MPa). The supersaturation pressures for homogeneous bubble nucleation can be estimated to be <76 MPa for the trachytic and <70 MPa for the phonolitic melt. In contrast to glass cylinders, the usage of glass powder prevented homogeneous bubble nucleation in the melt. We suggest that trapped air in the powder pore space resulted in the formation of tiny H_2O-N_2 bubbles throughout the samples prior to decompression. Degassing of the glass powder samples was facilitated by diffusive growth of these pre-existing bubbles and did not require significant supersaturation with H_2O in the melt. This is evidenced by several orders of magnitude lower N_V and lower residual H_2O contents at correspondingly higher porosities than in the glass cylinder samples. However, significant extension of t_{eq} in the glass powder experiments led to degassing results comparable to the glass cylinder samples. This effect is probably due to Ostwald ripening, coalescence and the ascent of the pre-existing bubbles during the extended equilibration time prior to decompression.

The N_V of the glass cylinder samples were used to test the applicability of the vesiculation model provided by Toramaru (2006). For the applied decompression rates, the experimental N_V are up to 5 orders of magnitude higher than the values predicted by the model. This may be mainly attributed to the usage of a macroscopic surface tension in the model to describe the molecular process of bubble nucleation. A significantly lowered surface tension of ~0.003 N·m^{-1} would be necessary to describe our results with the model of Toramaru (2006).

Our study has shown that the investigation of homogeneous bubble nucleation necessitates decompression experiments, where the derived data are mainly dependent on the applied decompression rate. We strongly recommend to perform experiments with massive glass cylinders as starting material. The timescale of decompression is a limiting parameter and must be short enough to minimize the opportunity for a reduction of N_V due to Ostwald ripening and bubble coalescence. Considering our comparably high N_V, the samples of many previous experimental studies that were used to calibrate models for homogeneous bubble nucleation were probably subject to significant bubble interactions. Newly derived data from optimized experiments will require improved models for homogeneous bubble nucleation during magma ascent.

Keywords

Homogeneous bubble nucleation, decompression experiment, magma ascent, Campi Flegrei, H_2O degassing, bubble number density

Introduction

The Campi Flegrei (CF) are an active volcanic field in the Campanian plain close to the highly populated area of Naples (Italy). The CF volcanism is characterized by mainly explosive activity with both magmatic and hydromagmatic episodes (e.g. Mastrolorenzo and Pappalardo, 2006). The main structural feature is a nested caldera that formed during two main collapses (Orsi et al., 1992) related to catastrophic eruptions: the 39 ka Campanian Ignimbrite (CI) and the 14 ka Neapolitan Yellow Tuff events. During the CI super-eruption 150-200 km^3 dense rock equivalent of magma were emitted and spread as ignimbrites over 30000 km^2 (De Vivo et al., 2010; Rolandi et al., 2003). A geophysical anomaly beneath the whole Neapolitan area suggests a huge and long-lived deep magma chamber shared by the CF and the Vesuvius stratovolcano, which is in direct neighborhood to the city of Naples (Pappalardo and Mastrolorenzo, 2012). The present bradyseism in the CF indicates magmatic activity that could lead to potentially catastrophic eruptions that threaten millions of people in this highly populated area (De Vivo et al., 2010). Such eruptions are driven by violent magmatic ‘degassing’. This term is used to describe the exsolution of a super-critical fluid phase from the ascending magma due to decreasing volatile solubility in the silicate melt. The driving degassing process is the exsolution of H_2O from the melt as main volatile component in most magmatic systems (Sparks, 1978).

However, these dynamic degassing processes beneath volcanic systems cannot be observed directly in nature. Therefore, the simulation of magma ascent by decompression experiments with volatile-bearing silicate melts is essential to understand these processes.

Pressure (*P*) decrease during magma ascent results in volatile supersaturation in the melt that initiates nucleation and growth of fluid bubbles. These processes cause a substantial density decrease and influence the viscosity of the ascending magma (e.g. Gonnermann and Manga, 2007). Therefore, melt degassing is the driving force for increased ascent rates. In volatile-saturated magmas, degassing during decompression can be facilitated by growth of pre-existing bubbles. Increasing supersaturation during magma ascent may trigger heterogeneous and/or homogeneous bubble nucleation and growth, depending on the presence of nucleation sites such as crystals. In case of heterogeneous bubble nucleation, the required supersaturation pressure can be significantly reduced compared to bubble nucleation in a crystal-free homogeneous melt (Hurwitz and Navon, 1994; Toramaru, 1989). Increasing ascent velocities may cause multiple nucleation events due to the change from a diffusion-controlled to a viscosity-controlled regime (Toramaru, 1995). The bubble nucleation record is also influenced by Ostwald ripening and coalescence (Toramaru, 2006). The complex degassing history of natural volcanic rocks often conceals the record of the onset of degassing. Therefore, homogeneous bubble nucleation has already been investigated in experimental studies (e.g. Gondé et al., 2011; Mangan and Sisson, 2000; Mourtada-Bonnefoi and Laporte, 2002).

In many other previous degassing studies glass- or natural volcanic rock powder was used as starting material for decompression experiments (e.g. Gardner et al., 1999; Martel and Iacono-Marziano, 2015; Mastrolorenzo and Pappalardo, 2006; Suzuki et al., 2007). Experiments starting from glass powder and excess H_2O produce numerous small hydration bubbles in the melt prior to decompression. Diffusive growth of such pre-existing hydration bubbles can inhibit nucleation and growth of decompression bubbles in the drainage zone of the hydration bubbles during decompression (Gardner et al., 1999; Larsen and Gardner, 2000). However, pre-existing bubbles in the melt do not exclusively form due to excess H_2O in the capsule. Nominally H_2O-undersaturated starting conditions using glass powder are suggested to produce air (or simplified N_2) bubbles in the melt prior to decompression (Mourtada-Bonnefoi and Laporte, 2002; Simakin et al., 1999) due to the air in the pore space of the powder, which is entrapped during capsule preparation. These bubbles in the melt may then have the same effect on degassing as pre-existing hydration bubbles and facilitate equilibrium degassing

paths during decompression. Thus, it is important to consider the effects of starting material and volatile contents in the experimental samples on degassing.

In this study, the H_2O degassing behavior of two magma compositions (a trachyte from the CI super-eruption and a K-phonolite from the Vesuvius AD 79 plinian eruption) was investigated at constant decompression rates. Decompression experiments starting from glass powder and massive glass cylinders are compared in terms of the onset and extent of degassing. The experimentally derived bubble number densities are used to test the applicability of the vesiculation model of Toramaru (2006), which was developed for homogeneous bubble nucleation at a constant decompression rate. Experimental limitations are outlined and will contribute to improve the investigation of homogeneous bubble nucleation in silicate melts.

Experimental and analytical procedures

Starting material

The starting glasses for all experiments were synthesized by mixing fired oxide (SiO_2, TiO_2, Al_2O_3, FeO, MnO, MgO), dried carbonate ($CaCO_3$, Na_2CO_3, K_2CO_3) and $(NH_4)_2HPO_4$ powders according to the analysis of the CI Triflisco composition (OF17c1-sp) and the Vesuvius "white pumice" composition (VAD79) reported in Civetta et al. (1997) and Iacono Marziano et al. (2007), respectively (Table 1). The powder mixtures were ground and homogenized for 30 min in a zirconia ball mill and fused in a $Pt_{90}Rh_{10}$ crucible for 6 h at 1600 °C. Afterwards, the crucible was rapidly quenched in water. The final homogenization was carried out by grinding the glass batches for 20 min in the ball mill and fusing the glass powders for 1 h at 1600 °C. This step leads to the formation of N_2-rich bubbles (due to entrapped air in the pore space of the glass powders) during melting. Most of these bubbles ascended to the surface of the melt batch during fusing. However, it is possible that some N_2-rich bubbles remained in the melts due to the limited fusing timescale. The amount of residual bubbles is also influenced by bubble size and viscosity of the melt that affect bubble ascent. Instead of a rapid quench in water, the melts were cooled down moderately by an air-fan in order to inhibit tension cracks in the glass. The cooling rate was fast enough to prevent the melt from partial crystallization. 6 - 7 mm long cylinders with 5 mm in diameter were drilled out of the glasses and ground at the edges. For the applied decompression rates in this study, Marxer et al. (2015) showed that 5 mm cylinders provide sufficient space for homogeneous bubble nucleation and growth in the capsule center

that is unaffected by heterogeneous bubble nucleation processes at the capsule-melt interface and the corresponding diffusional loss of H_2O towards the capsule wall.

A calibrated 10 ml pycnometer (±5 µl) was used to determine the porosity of several glass cylinders. The reference densities of the nominally dry, bubble-free glasses were calculated by the model of Appen (1949) modified by Kloess (2000). The resulting density of the CI glass is 2508 $g \cdot l^{-1}$ and 2496 $g \cdot l^{-1}$ for the VAD79 glass. The pycnometer density measurements of the CI glass cylinders (2507±15 $g \cdot l^{-1}$, 4 cylinders measured) matched the calculated density for the CI composition and indicate porosities <1 %. The derived porosity of the VAD79 glass cylinders (2403±48 $g \cdot l^{-1}$, 10 cylinders measured) varies between 1 - 6 %.

After drilling, the residual glasses were crushed and different grain size fractions were separated by sieving. A 1:1 weight fraction mixture of grain sizes from 500 – 200 µm and <200 µm was used as starting material to minimize the porosity during capsule preparation. The loose powder mixture has a porosity of ~46 %. Compaction of the powder with a piston and a hammer in a cylindrical steel container with 5 mm inner diameter resulted in a porosity of ~29 %, which is suggested to be the initial porosity of powder in the filled capsule.

Capsule preparation

Gold-Palladium ($Au_{80}Pd_{20}$) was chosen as capsule material for all experimental runs because of the temperature (*T*) range of the experiments (1300 – 1050 °C) and to inhibit iron loss from the melt into the capsule material (e.g. Kawamoto and Hirose, 1994). $Au_{80}Pd_{20}$ tubes (inner diameter 5 mm, wall thickness 0.2 mm) were cleaned in acetone and annealed at 850 °C under atmospheric conditions over night to soften the material for further processing. All experiments were performed in 13 mm long capsules with a welded lid at the bottom. The capsules were loaded with either glass powder (~220 mg, compacted with a piston) or a glass cylinder (~280 mg) and additional H_2O. The capsule top was crimped with a drill chuck and welded shut. Possible leakage was checked gravimetrically after heating the capsules at 110 °C for at least one hour. Additionally, all capsules were pressurized at room temperature for a few minutes in a cold-seal pressure vessel at 100 MPa with water as pressure medium to ensure the structural integrity of the capsule. A gain of weight due to the infiltration of water into the capsules through microscopic leaks was not observed.

Experimental method

All experiments were conducted in a vertically operated internally heated argon pressure vessel (IHPV) at intrinsic oxygen fugacity (fO_2) conditions. At H_2O-saturated conditions, the fO_2 was determined to be ~3.5 log units above the fO_2 of the quartz-fayalite-magnetite (QFM) solid oxygen buffer (Berndt et al., 2002). The IHPV is equipped with a rapid quench (RQ) device that facilitates a maximum sample cooling rate of approximately 150 $K \cdot s^{-1}$ (Berndt et al., 2002), depending slightly on the mass and the heat conductivity of the capsule. At RQ, the capsule is dropped from the hot spot zone into the cold quench zone of the sample holder. Rapid cooling causes tension cracks in the glassy state. To minimize cracks in the samples, a 55 mm long ceramic filler rod was inserted into the quench zone to slightly reduce the cooling rate during RQ of our experiments. Alternatively, shutting down the furnace while the capsule remains suspended in the hot spot zone quenches a sample with a lower cooling rate of ~150 $K \cdot min^{-1}$ and is referred to as normal quench (NQ) in this study. Both RQ and NQ were performed isobarically.

Isobaric experiments

A set of three isobaric experiments (IB-C-1a/b and IB-C-2, Table 2) starting from CI glass cylinders was performed to check the equilibration time (t_{eq}) for a homogeneous dissolution of H_2O within the melt and to characterize the starting conditions just before decompression. The samples were equilibrated with ~4.7 wt% H_2O at 200 MPa and 1300 °C for a t_{eq} of 96 h. The equilibration temperature (T_{eq}) of 1300 °C was chosen to keep t_{eq} as short as possible, because the total H_2O diffusion in silicate melts increases exponentially with T (e.g. Nowak and Behrens, 1997). After t_{eq}, one sample was quenched rapidly, whereas the T for the other two samples was lowered to the decompression temperature of 1050 °C. After an additional annealing time of 30 min, these two samples were quenched by either RQ or NQ to investigate the influence of the cooling rate on the hydrous melt. Isobaric experiments with the VAD79 composition (REF02-12) are documented in Marxer et al. (2015).

A set of four isobaric experiments with CI glass powder as starting material was conducted at 200 MPa and 1300 °C with increasing H_2O content (Table 2). These powder samples were equilibrated for 24 h and quenched rapidly. The resulting H_2O-bearing glasses (IB-P-1 to 4) were used to verify the near infrared (NIR) absorption coefficients for the trachytic composition (Table 2) given in Fanara et al. (in press). The NIR measurements of the isobaric

samples showed that equilibration times of 96 h for cylinders (IB-C-1a/b, REF12) and 24 h for powder (IB-P-4) are sufficient to dissolve H_2O in the melt homogeneously.

Decompression experiments

Four sets of degassing experiments starting from nominally H_2O-undersaturated conditions using both glass powder and massive cylinders were conducted with identical decompression parameters to investigate the influence of the starting material on melt degassing. CI and VAD79 samples were equilibrated with about 4.7 wt% H_2O at 200 MPa and 1300 °C. Equilibration time was always 96 h for experiments starting from glass cylinders. The powder samples were equilibrated for either 24 or 96 h (Table 3) to investigate the effect of t_{eq} on melt degassing. After t_{eq}, the T was lowered to 1050 °C and the samples were annealed for 30 min. Starting from these super-liquidus conditions (Fanara et al., 2012; Iacono Marziano et al., 2007), isothermal decompression was performed by continuous P release using a high-pressure low-flow metering valve equipped with a piezoelectric nano-positioning system (Marxer et al., 2015; Nowak et al., 2011). The continuous decompression rate was either 0.024 or 0.17 MPa·s^{-1} down to a final pressure (P_{final}) of 100 MPa. Further glass cylinder samples were decompressed to a lower P_{final} of 75 and 60 MPa (Table 3). At P_{final}, all samples were quenched rapidly at isobaric conditions.

Sample preparation

Several pieces of the CI and VAD79 starting glasses from different locations in the melting crucible were embedded in epoxy resin racks for chemical analysis by electron microprobe (EMP). The surfaces of all racks were ground, polished and sputtered. After the experiments, the capsules were checked for weight loss due to possible leakage. The capsules were cut longitudinal along the cylinder axis in two halves. One half was directly embedded in epoxy resin racks for examination with a scanning electron microscope (SEM) to generate high-resolution backscattered electron (BSE) images. The other half of a sample was removed from the capsule, embedded and double-sided ground and polished down to a thickness of 150 - 200 µm for Fourier transform infrared (FTIR) measurements and transmitted light microscopy (TLM).

Analytical methods

EMP analysis

The nominally dry CI and VAD79 starting glasses were analyzed by WDS measurements using a JEOL JXA 8900 R electron microprobe at an accelerating voltage of 15 kV and a beam current of 4 nA. The glasses were analyzed with a defocused beam of 20 µm in diameter to inhibit loss of alkalis. The peak counting times were set to 10 s (Na), 16 s (Si, Al, Fe, Mg, Ca, K) and 30 s (Ti, Mn, P). The results of these WDS analyses are presented in Table 1.

FTIR spectroscopy

The residual total H_2O concentrations of the glasses were determined by NIR measurements with a Bruker Vertex 80v FTIR-spectrometer. A CaF_2 beam splitter and a halogen light source were used. The spectrometer is coupled to a Hyperion 3000 IR-microscope with a motorized sample stage, enabling sequences of spatially resolved measurements. NIR absorption spectra from 4000 to 6000 cm^{-1} of the glasses were recorded in transmission mode using a 15x IR Cassegrain objective and an In-Sb single element detector. The spectra were collected with 32 - 50 scans at a resolution of 4 cm^{-1}. The spectrometer was evacuated and the microscope was flushed continuously with dried air to minimize influence of atmospheric H_2O. The knife-edge aperture was set to 30x30 (VAD79) or 50x50 µm (CI) and reference spectra were taken without a sample in the beam path. The total H_2O content was determined from the peak heights of absorption bands at 5210 cm^{-1} (molecular H_2O) and 4470 cm^{-1} (OH^-) as sum of the species concentrations (e.g. Behrens and Nowak, 2003; Scholze, 1960). Tangential baselines fitting the minima on both sides of each band (Ohlhorst et al., 2001) were used for the trachytic samples. A linear background correction was applied to the phonolitic samples (Iacono Marziano et al., 2007). A Mitutoyo digital micrometer was used to measure the thickness of the samples with an accuracy of 2 - 3 µm. The molar absorption coefficients and the density (ρ) data of the hydrous CI glasses were adopted from Fanara et al. (in press). The absorption coefficients are 0.98(3) and 1.19(2) $l \cdot mol^{-1} \cdot cm^{-1}$ for the 5210 and 4470 cm^{-1} band, respectively. The density was calculated by the equation (ρ [$g \cdot l^{-1}$] = 2457-24·*wt%* H_2O) using the gravimetrically determined initial H_2O contents. The corresponding data for the VAD79 composition are provided in Iacono Marziano et al. (2007). The densities of the hydrous VAD79 glasses were calculated by

(ρ [g·l^{-1}] = 2470-13·*wt%* H_2O) and the molar absorption coefficients are 1.18(11) and 1.14(9) l·mol^{-1}·cm^{-1} for the 5210 and the 4470 cm^{-1} band, respectively.

SEM and 2D image analysis

BSE images of polished sample sections were recorded with a LEO 1450 VP SEM. Each sample was mapped by taking 80 - 130 single images with a resolution of 1024x768 pixels at a magnification of 120 - 300x. Additionally for sample CD-C-5, four different excerpt areas were mapped at a higher magnification of 880 - 1100x. The single images were stitched together and used to determine the bubble number density (N_V) in suitable samples. The bubble number density normalized to pure melt or glass volume (N_V(n)) provides information about nucleation processes during decompression. The bubble intersections were redrawn in a separate image layer and loaded into the ImageJ 1.47 software (Schneider et al., 2012). The bubble intersections were fit with ellipses to determine 2D porosities of the vitrified samples. The axes lengths of the ellipses were imported into the CSDCorrections software (Higgins, 2000) for the calculation of 3D porosities and bubble number densities. A detailed description of this method is provided in Marxer et al. (2015).

The intersection probability of bubbles (or other objects) in a 2D cut plane decreases with the 3D bubble diameter (e.g. Higgins, 2006). The corresponding decrease in the 2D intersection diameter (and in depth of the bubble pit in a polished sample) may complicate proper identification and distinction from other surface features of the specimen. Bubble number densities based on direct 3D sample information may therefore be more reliable in case of very small bubbles on a µm scale. For this study, the N_V-values of samples or parts of samples that contain such small bubbles were determined using transmitted light microscopy.

Transmitted light microscopy

The NIR samples were also examined with a Zeiss Axio Imager M2m microscope to obtain 3D information on N_V in samples with bubbles of only several µm diameter. The microscope is equipped with a motorized sample stage. The Fission Track Studio software "Trackworks" (Autoscan Systems) was used to manually count all observable bubbles in selected sample volumes. The analyzed cuboid volume is confined by the field of view and the thickness of the glass section. The field of view was either 87x65 µm or 175x132 µm depending on the used objective (50x and 100x). The bubble counts were used to calculate the number of bubbles per

total unit volume of glass and bubbles per mm^3 (N_V(t)). TLM provides the actual 3D diameters of bubbles (e.g. Gardner et al., 1999). The averaged bubble diameters and the bubble counts were used to estimate the porosities and to calculate the N_V(n) of the samples.

Results

Isobaric experiments

Examination of the CI and VAD79 starting materials using TLM and SEM revealed that the nominally dry glasses (quenched by air fan cooling) are free of crystals and only contain some air bubbles that resulted from glass synthesis. In contrast, the samples of the isobaric CI experiments with ~4.7 wt% H_2O starting from glass cylinders and powder (IB-C-1a/b and IB-P-4, RQ, Table 2) contain numerous, not clearly recognizable objects <1 µm in size. Figure 1a shows small objects in the glass of sample IB-C-1b quenched from 1050 °C. The number density of objects in these RQ samples ranges between $1 \cdot 10^5$ and $4.5 \cdot 10^5$ mm^{-3} (Table 3). The CI sample with ~4.7 wt% H_2O quenched from 1050°C with a cooling rate of about 150 $K \cdot min^{-1}$ (IB-C-2, NQ) shows needle-shaped and radially aggregated quench crystals of up to 13 µm length (Fig. 1b, c) with an aggregate number density of $7 \cdot 10^4$ mm^{-3}. The rapidly quenched, hydrous VAD79 cylinder sample (REF12, Table 2) is homogeneous without quench crystals or other small objects. The same observation can be made for the two CI samples (RQ) with the lowest H_2O contents of about 1 and 2 wt% (IB-P-1 and IB-P-2, Table 2). The samples IB-P-1 to IB-P-4 with increasing H_2O contents were used to verify the NIR absorption coefficients for the trachytic composition given in Fanara et al. (in press). The measured H_2O contents match the gravimetrically obtained values within error (Table 2).

Decompression experiments

The BSE images of the samples decompressed to a P_{final} of 100 MPa with both decompression rates reveal significant differences in degassing behavior between samples starting from massive glass cylinders and glass powder equilibrated for 24 h prior to decompression (Fig. 2, 3). Images of the complete halved capsules are provided in the electronic appendix (eFig. 1-13). The BSE images suggest that cylinder samples are bubble-free, but the TLM images reveal very small bubbles with diameters <4 µm (Fig. 4 a, c). In contrast, the powder samples, which were equilibrated for 24 h (CD-P-1 and CD-P-24 at 0.17 $MPa \cdot s^{-1}$ and CD-P-2a,

CD-P-22 at 0.024 MPa·s^{-1}, Fig. 2), show high porosities up to 14 % and are characterized by low N_V(n) of big bubbles (87 - 215 mm^{-3}, Table 3). Moreover, CD-P-1 shows a heterogeneous distribution of these big bubbles and a belt of much smaller bubbles in the center of the sample (Fig. 3). This results in two different N_V(n)-values of 215 mm^{-3} for the big bubbles and $2 \cdot 10^5$ mm^{-3} for the belt of small bubbles. The corresponding glass cylinder samples (CD-C-1, CD-C-23 at 0.17 MPa·s^{-1} and CD-C-2, CD-C-25 at 0.024 MPa·s^{-1}, Fig. 2) reveal very high N_V(n) of $2 \cdot 10^5$ to $6 \cdot 10^5$ mm^{-3} with bubble diameters of 1 - 4 µm that result in porosities <1 %. These small bubbles are not observable in BSE images (Fig. 2, 3). Transmitted light images of CD-C-1 and CD-C-2 exhibit small objects in the vicinity of bubbles to which the bubble surface is extended by a thin neck (Fig. 5). In contrast to the powder experiments with a t_{eq} of 24 h, the samples CD-P-2b and CD-P-32 that were equilibrated for 96 h (Fig. 2, 4) show the same degassing texture of small bubbles with high N_V(n) of $2 \cdot 10^5$ to $3 \cdot 10^5$ mm^{-3} as the corresponding glass cylinder samples (CD-C-2 and CD-C-25) (Fig. 2, 4).

The CI glass cylinder samples decompressed to a P_{final} of 75 MPa (CD-C-3 at 0.024 MPa·s^{-1} and CD-C-4 at 0.17 MPa·s^{-1}, Fig. 6) are characterized by higher porosities, bigger bubble sizes and slightly lower N_V(n)-values than the cylinder samples quenched at a P_{final} of 100 MPa (Table 3). The BSE image of sample CD-C-4 suggests that bubbles are limited to the lower part of the glass cylinder (Fig. 6, eFig. 3a). However, both specimens (CD-C-3, CD-C-4) also contain homogeneously distributed small bubbles (<4 µm) in the upper part of the cylinder similar to CD-C-2 (Fig. 4a). The bubbles located at the capsule-melt interface in CD-C-3 (Fig. 6, eFig. 2a, b) are more numerous and clearly bigger than the corresponding bubbles in CD-C-4 (Fig. 6, eFig. 3a, b), which was decompressed with the higher decompression rate. The capsule lid at the bottom of CD-C-3 is not decorated with bubbles. Instead, this sample features some big bubbles in the center of the glass cylinder. The sample area around each of these big bubbles is free of the small bubbles (excerpt Fig. 6).

The CI glass cylinder sample CD-C-5 decompressed to a P_{final} of 60 MPa at 0.17 MPa·s^{-1} was removed from the capsule during sample preparation. The bubbles located at the former capsule-melt interface are therefore only partly visible (Fig. 7a, b, eFig. 1a, b). The BSE image suggests a homogeneous distribution of bubbles with an average diameter of 8 µm within the sample, but the TLM image of the whole sample (Fig. 7b) reveals convection patterns, which are suggested to be induced by a density gradient due to massive bubble nucleation. The porosity and the N_V(n)-values were obtained from the BSE images using the CSDCorrections

software (Higgins, 2000). The mean N_V(n)-value of ~$7 \cdot 10^5$ mm^{-3} (average of four different areas containing more than 400 bubble intersections) is in the same order of magnitude as in the cylinder samples decompressed to a P_{final} of 75 and 100 MPa (Table 3). The mean porosity of ~10 % is the highest of all decompressed cylinder samples. The bubble size distribution (BSD) of sample area 4 is characterized by a near-linear trend with a narrow size range from 3 to 13 µm (Fig. 7c).

The equilibrium solubility of H_2O at a P_{final} of 100 MPa and 1050 °C is ~3.5 wt% for both the CI and the VAD79 composition (Fanara et al., in press; Iacono Marziano et al., 2007). The measured H_2O contents of samples originating from glass powder with a t_{eq} of 24 h and a P_{final} of 100 MPa are closer to the equilibrium H_2O content than the cylinder samples (Table 3). NIR measurements of the highly vesiculated glass cylinder and powder samples with a t_{eq} of 96 h result in values close to the initial H_2O concentration prior to decompression. This also applies for the CI cylinder samples decompressed to a P_{final} of 75 MPa (Table 3). In the upper part of the sample CD-C-3 (Fig. 6, eFig. 2a, b), where the homogeneously distributed small bubbles are present, the measured H_2O content (~4.57 wt%) is near the initial H_2O content of 4.78 wt%. One exception is the bubble-depleted area around the big bubbles in this sample (excerpt Fig. 6). The residual H_2O content in the bubble-depleted zone (~3 wt%, Table 3) is close to the extrapolated solubility of the CI melt at 75 MPa (2.89 wt%) as derived from the solubility data of Fanara et al. (in press). The residual H_2O content of sample CD-C-5 decompressed to a P_{final} of 60 MPa could not be determined by NIR measurements due to high N_V(n)-values of ~$7 \cdot 10^5$ mm^{-3}. The calculated residual H_2O content of ~3.2 wt% derived from the corrected melt porosity is still higher than the extrapolated equilibrium solubility at 60 MPa (2.61 wt%).

Discussion

Quench crystal formation

The NQ isobaric experiment resulted in the formation of quench crystal aggregates consisting of ~13 µm long needle-shaped crystals in the CI melt containing ~4.7 wt% H_2O (Fig. 1b). We suggest that the smaller, unidentified objects in the corresponding RQ isobaric experiments with the CI melt (~4.7 wt% H_2O, both powder and cylinder, both quenched from 1050 and 1300 °C) are also crystals that formed during cooling (Fig. 1a). The RQ samples from the two

isobaric CI experiments with the lowest H_2O contents in the melt do not contain any objects. Thus, the effectiveness of quench crystal formation is controlled by the cooling rate and the H_2O content of the melt that influences the glass transition temperature (T_g) (Dingwell and Webb, 1990; Morizet et al., 2007). An increasing cooling rate leads to a higher T_g, whereas a higher H_2O content in the melt reduces T_g. The quench crystals in the RQ samples of isobaric experiments with 4.7 wt% H_2O are smaller than those in the NQ sample, because the time for crystallization is shorter. Furthermore, diffusivity of components required for crystal formation and growth decreases with H_2O content of the melt (Koepke and Behrens, 2001). This explains the absence of any detectable quench crystals in the nominally dry starting material and the two isobaric CI experiments with the lowest H_2O contents in the melt. The VAD79 samples do not contain any detectable quench crystals probably due to the small difference in bulk composition (Table 1). Both the starting glass and other samples of isobaric experiments (REF02-06 and REF12 from Marxer et al., 2015) do not contain any detectable crystals.

The number densities of quench crystals aggregates (N_C) in the samples of the isobaric CI experiments are within the same order of magnitude (~10^5 mm^{-3}) as the N_V of the bubbles in the cylinder samples decompressed to 100 MPa (Table 2, 3). On a first glance, this could be a hint that the bubbles in the decompressed CI cylinders nucleated heterogeneously on the quench crystals and initiated degassing during cooling. However, crystals can also nucleate heterogeneously on the surface of bubbles (Davis and Ihinger, 1998). Some of the decompressed CI samples contain bubbles that are connected to smaller objects by a thin neck (Fig. 5). These objects are suggested to be quench crystals. Similar bubbles connected by a neck to oxide microlites that were already present in the melt during decompression were observed by Hurwitz and Navon (1994). They presumed that this unstable bubble neck forms due to the shrinkage of the H_2O-filled bubble during isobaric RQ that was further investigated by Marxer et al. (2015). A significant volume reduction of a bubble is only expected if the bubble already existed prior to RQ. Considering the size of the bubble in comparison to the crystal, it would be conceivable that the crystals found in the decompressed CI samples formed at a later stage on the surfaces of existing bubbles and did not affect melt degassing. Quench crystals were not observed in sample CD-C-5 decompressed to a P_{final} of 60 MPa. The absence of quench crystals in this sample is further proof that crystals formed after the nucleation of bubbles during quench. However, small quench crystals <1 µm might not be visible by TLM due to high N_V(n) in combination with bigger mean bubble diameters. The N_V(n)-values of the decompressed CI

cylinders are also comparable to those determined in the corresponding VAD79 samples (Table 3), which do not show any evidence of quench crystal formation. Even if heterogeneous bubble nucleation during quench occurred, it does not affect the principal observations and interpretations made for the comparison of the different starting materials glass powder and massive glass cylinders.

The powder problem

Previous studies already indicated that glass powder as starting material might be not appropriate to study bubble nucleation processes in silicate melts (e.g. Gardner et al., 1999; Iacono Marziano et al., 2007; Mourtada-Bonnefoi and Laporte, 2002; Simakin et al., 1999). The degassing process can be influenced by the growth of pre-existing bubbles in the capsule prior to decompression. Hydration bubbles (Gardner et al., 1999) in our samples were avoided by starting from nominally H_2O-undersaturated conditions, but the reduction of additional water in the capsule increases the pore volume in powder samples that is filled with air.

The amount of entrapped air (assumed as 100 % N_2) in the capsules of our experiments can be calculated considering the capsule dimensions, the pure glass volume and the amount of added water. Once sealed, the capsules have a total free volume of about 157 mm^3. The compacted glass powder has a porosity of ~29 %. Assuming that the whole free capsule volume is filled with ~220 mg powder and considering ~11 mm^3 of added water for samples with 4.7 wt% H_2O, the pore volume is at least ~35 mm^3. This corresponds to ~177 ppm N_2 at atmospheric conditions. The calculated amounts of entrapped N_2 are minimum values for optimal powder compaction assuming no free volume in the capsule headspace above the sample. During heating and melting, the H_2O-N_2 fluid mixture (X_{H2O} near 1) in the pore space will form bubbles throughout the whole sample. After preferential dissolution of H_2O, H_2O-N_2 bubbles with slightly decreased X_{H2O} will remain in the melt. The usage of a more fine-grained powder leads to smaller pores and probably smaller H_2O-N_2 bubbles in the melt after equilibration, but the total porosity will not decrease. If pre-hydrated glass powder is used as starting material this problem is even more severe (e.g. Fiege et al., 2014), because the amount of enclosed N_2 is higher due to lacking water in the powder pore space prior to the decompression experiments.

If massive glass cylinders are used, the free volume in the capsule is lower. Cylinders used in this study were 5 mm in diameter and 6.5 mm in height resulting in a volume of

~127 mm^3. To attain H_2O contents of about 4.7 wt% in the melt, ~13 mm^3 H_2O have to be added considering a cylinder weight of ~280 mg. The remaining free volume of at least 17 mm^3 in our capsules contained ~86 ppm N_2. But in contrast to glass powder, the N_2 is enclosed in the headspace of the capsule or free volumes at the sample-capsule interface that will form one or more bigger bubbles if the glass cylinder is free of air bubbles. The amount of N_2 in experiments starting from cylinders increases if the glass contains a residual porosity due to the synthesis from powder at 1600 °C. The amount of entrapped N_2 in porous glass cylinders was estimated from density measurements with the pycnometer. A maximum porosity of 6 % for the VAD79 glass cylinders would result in only ~3 ppm trapped N_2 under atmospheric conditions. This calculation is based on the assumptions, that the bubbles in the synthesized batch contain 100% N_2 and that the bubble sizes are preserved at T_g of 665 °C during a moderate quench at atmospheric conditions. T_g was calculated for a residue of 0.1 wt% H_2O in the melt using the model of Giordano et al. (2008). Further cooling of the porous glass to ambient T reduces P_{N2} in the bubbles of the glass batch to ~30 kPa and the trapped amount of N_2 is correspondingly low. N_2-filled bubbles in the glass cylinders are therefore far less critical than the powder pore space. However, higher porosities in glass cylinders could still lead to problems if the entrapped amount N_2 within the cylinder sample does not completely dissolve in the melt prior to decompression.

To date only few studies about nitrogen solubility in hydrous silicate melts were performed for the applied P-T and fO_2 range (Carroll and Webster, 1994; Libourel et al., 2003; Miyazaki et al., 2004; Roskosz et al., 2013). N_2 and Ar have comparable atomic/molecular dimensions and comparable solubilities (Carroll and Webster, 1994). The similarity in solubility supports the view that nitrogen dissolves physically in silicate melts at QFM+3.5 as non-reactive N_2 molecules (Libourel et al., 2003). The N_2 solubility is reported to be a few ppm at 0.1 MPa (Libourel et al., 2003; Roskosz et al., 2013) and increases up to 150 ppm per 100 MPa (Carroll and Webster, 1994). Due to lacking N_2-H_2O solubility data, a solubility model of H_2O-N_2 fluid mixtures (Fig. 8) was assumed on the basis of the experimentally determined H_2O-CO_2 solubility reported in Fanara et al. (in press) for the CI composition. These data illustrate that the CO_2 solubility in the CI melt is very low near H_2O-saturated conditions at 200 MPa. Applied to our nominally slightly H_2O-undersaturated starting conditions prior to decompression, it is likely that only about 100 ppm of the entrapped N_2 will dissolve in the melt at 200 MPa and 1050 °C (Fig. 8). The few ppm N_2 that are trapped in the bubbles of the glass

cylinders should therefore easily dissolve together with H_2O and not interfere significantly with melt degassing during decompression. In case of glass powder as starting material, the calculated amount of entrapped N_2 (~177 ppm) will lead to H_2O-N_2 bubbles with a high X_{H2O}(fluid) of ~0.9 that are distributed throughout the whole sample. However, bubbles in the TLM images of the isobaric experiments using powder as starting material could not be observed due to possibly small diameters <1 µm. Pre-existing bubbles in the melt of powder samples will grow by volatile diffusion into the bubbles as soon as the melt becomes supersaturated during decompression. At sufficiently high number densities of pre-existing bubbles, this degassing process can inhibit homogeneous nucleation of bubbles in the melt in case of a diffusion-controlled growth regime (Mourtada-Bonnefoi and Laporte, 2002; Toramaru, 1995). It is therefore possible that one of the major controlling factors of previous degassing experiments was the usage of glass powder (e.g. Fiege et al., 2014; Mastrolorenzo and Pappalardo, 2006; Suzuki et al., 2007).

Decompression experiments (P_{final} = 100 MPa)

Although all experiments were performed at nominally H_2O-undersaturated conditions, the comparison between decompressed cylinder samples of both compositions and their powder equivalents equilibrated for 24 h documents that melt degassing is massively influenced by the starting material due to the probable presence of pre-existing bubbles in the powder samples. In case of the cylinder samples, the melt is bubble-free prior to decompression. Thus, the onset of melt degassing is delayed until the energetic barrier for the formation of the new phase boundary is exceeded by reaching the critical supersaturation pressure to trigger homogeneous bubble nucleation (ΔP_{HoN}). This energetic barrier can be expressed as the free energy of formation (ΔF_c) of a bubble nucleus with critical radius:

$$\Delta F_c = \frac{16\pi\sigma^3}{3\Delta P_{ss}{}^2} \quad \textbf{(1)}$$

and is strongly dependent on the surface tension (σ) of the melt as well as ΔP_{ss} (Hirth et al., 1970). In case of heterogeneous nucleation on crystals or the capsule-melt interface, this energy is lowered with the result that degassing is initiated at a lower ΔP_{ss} in the melt (Hurwitz and Navon, 1994). After nucleation, the bubbles can grow by volatile diffusion and expansion. Both

of these growth processes only increase the bubble volumes and do not affect the N_V(n) of the sample.

The equilibrium porosity (using Eq. 5 in Gardner et al., 1999) is ~14 % in the melts (CI and VAD79 composition) for an initial H_2O content of ~4.7 wt% at a P_{final} of 100 MPa and 1050 °C. The equilibrium solubility of H_2O at 100 MPa in both melts is ~3.5 wt% (Fanara et al., in press; Iacono Marziano et al., 2007). At this P_{final}, the cylinder samples only contain very small bubbles (Fig. 4) with high N_V(n)-values of $1 \cdot 10^5$ to $5 \cdot 10^5$ mm^{-3} (Table 3). Within error, the measured H_2O contents in the cylinder samples correspond to the initial contents, because numerous small bubbles in the samples have inhibited the NIR measurements of the residual H_2O dissolved in the glass. However, the low corrected porosities of <2 % in the melts (Table 3) corresponding to <0.15 wt% degassed H_2O are also proof for high residual total H_2O contents. This documents a high supersaturation in the melt prior to quench and confirms delayed, late-stage bubble nucleation. Porosities close to equilibrium conditions are only reached in the decompression experiments using glass powder that were equilibrated for 24 h (Table 3). The NIR measurements of dissolved H_2O in these glasses also confirm that the melt degassed more efficiently than in experiments with cylinders. Degassing of the powder experiments equilibrated for 24 h was facilitated by growth of tiny pre-existing H_2O-N_2 bubbles and started with the onset of decompression. These bubbles grew during decompression to 100 MPa by volatile expansion, H_2O diffusion, Ostwald ripening and coalescence, leading to low bubble number densities in these experiments (Table 3). In comparison to the cylinder specimens, the low residual H_2O contents of the powder samples suggest a near-equilibrium degassing path for both applied decompression rates. Only sample CD-P-1 (Table 3) shows higher H_2O contents in the narrow belt in the middle of the capsule that is occupied by numerous small bubbles (Fig. 3). This feature may be an artifact from powder compaction and H_2O loading leading to the heterogeneous degassing texture. In any case, this texture does not support the usability of powder samples equilibrated for 24 h, because the glass cylinder samples do not show such inhomogeneity. Decompression experiments starting from glass powder with a t_{eq} of 96 h show a degassing behavior of the melt that is comparable to the corresponding glass cylinder samples (Fig. 4). We suggest that this observation is due to growth and ascent of the H_2O-N_2 bubbles during equilibration, resulting in a bubble-free melt prior to decompression. Bubble ascent in the melt is generally facilitated by buoyancy due to differences in density of the volatile phase and the surrounding melt. Additionally, the viscosity of the melt and the

bubble size are the controlling factors of this process. The ascent of a bubble in a melt can be described by Stokes' Law:

$$v_{bubble} = \frac{2r^2 g(\rho_{melt} - \rho_{fluid})}{9\eta} \quad \textbf{(2)}$$

where v_{bubble} is the ascent velocity, r is the bubble radius, ρ_{melt} and ρ_{fluid} are the densities of the melt and the fluid (assumed to be 100 % H_2O), g is 9.81 $m \cdot s^2$ and η is the viscosity of the melt (Berlo et al., 2011). Equation 2 was used to calculate the ascent distance of bubbles as a function of bubble diameter for two temperatures (1050 and 1300 °C) and two equilibration times (24 and 96 h) (Fig. 9). For simplification, we assume instant volatile saturation of the melt at the beginning of the equilibration period in the powder experiments due to small grain sizes. The viscosity of the hydrous CI melt with 4.7 wt% H_2O was calculated after Misiti et al. (2011) to be 77 Pa·s at 1050 °C and 4 Pa·s at 1300 °C. The viscosities of the hydrous VAD79 melt at these temperatures are slightly lower, respectively. The corresponding densities of H_2O were calculated using the model of Duan and Zhang (2006) to be 311 $g \cdot l^{-1}$ (1050 °C) and 254 $g \cdot l^{-1}$ (1300 °C) at 200 MPa. For a calculated melt density of 2255 $g \cdot l^{-1}$ (Ochs and Lange, 1999), a bubble with 1 µm in diameter would rise only ~2 µm in the hydrous CI melt at 1050 °C in 96 h. At 1300 °C the same bubble would already ascent 43 µm in the same time. A pre-existing bubble in our powder experiments has to rise ~6.5 mm from the bottom to the top of the capsule during a t_{eq} of either 24 or 96 h at 1300 °C (Fig. 9). A timescale of 96 h in our low-viscosity melts most likely facilitates extensive growth of the H_2O-N_2 bubbles by Ostwald ripening and coalescence (Gardner, 2007; Gondé et al., 2011; Martel and Iacono-Marziano, 2015; Masotta et al., 2014). A diameter of 12 µm is required for a bubble to ascend from the bottom lid to the capsule top. We suggest that a t_{eq} of 24 h in our powder experiments is not sufficient to cause significant bubble growth by ripening and coalescence to accelerate the ascent of the pre-existing bubbles during equilibration. Small H_2O-N_2 bubbles therefore remain in the melt and cause immediate degassing by growth of these bubbles at the onset of decompression. In case of the powder experiments with a t_{eq} of 96 h, the melt is bubble-free prior to decompression and melt degassing is delayed until supersaturation facilitates the nucleation of new H_2O-rich bubbles. This is supported by the NIR measurements and the porosities of the 96 h powder

samples that document a high residual H_2O content in the melt on the level of the cylinder samples.

Decompression experiments (P_{final} = 75-60 MPa)

The glass cylinder samples decompressed to a P_{final} of 75 MPa are characterized by higher porosities and slightly lower N_V(n)-values than the cylinder samples quenched at a P_{final} of 100 MPa. Decompression to a lower P_{final} increased the available degassing time and therefore enhanced diffusive bubble growth as well as ripening and bubble coalescence. Figure 10 documents the onset of coalescence of two bubbles. The influence of the degassing timescale is also apparent from the size of the bubbles at the capsule-melt interface in the samples decompressed to 75 MPa. The bubbles in sample CD-C-3 (0.024 MPa·s^{-1}, Fig. 6) are clearly bigger than those in CD-C-4 (0.17 MPa·s^{-1}, Fig. 6) due to longer time for growth of heterogeneously nucleated bubbles at the capsule-melt interface by H_2O diffusion during decompression.

The big bubbles (up to 400 µm diameter) in the center of sample CD-C-3 are suggested to have formed heterogeneously at low ΔP_{ss} at the capsule-melt interface on the bottom lid. After detachment due to volume-related buoyancy force, these bubbles ascended during decompression (Fig. 6, eFig. 2a, b). Assuming heterogeneous nucleation at H_2O-saturated conditions (176 MPa for 4.7 wt% H_2O), it can be calculated from Equation 2 that a bubble with 400 µm diameter already needs ~67 of the 69 minutes decompression time (0.024 MPa·s^{-1}) to ascent 4 mm in the melt. Therefore, the ascent of the detached bubbles must have begun prior to homogeneous nucleation. The ascending detached bubbles grew by volatile expansion and H_2O diffusion from the supersaturated melt into the bubbles. The latter leads to depletion of H_2O in a spherical drainage zone around the bubbles. Due to the ascent, the H_2O-depleted zone covers the whole ascent track. This is evidenced by the absence of small homogeneously nucleated bubbles (excerpt Fig. 6, eFig. 2a, b) and lowered residual H_2O contents in the glass throughout the tracks of the big detached bubbles. Homogeneous nucleation of the small bubbles therefore only occurs in regions with higher H_2O supersaturation. Further ascent of the detached bubbles is accelerated by growth due to coalescence and ripening processes. The detached bubbles delete the nucleation history of an existing population by interaction with the smaller bubbles on their ascend tracks and they may initiate the nucleation of a second bubble population during further decompression in the depleted zones.

The BSE image of sample CD-C-4 (Fig. 6, eFig. 3a, b) shows that the lower central part of the capsule contains more numerous and slightly bigger bubbles (~12 µm) than the rest of the sample (only visible and evaluable in TLM images, Fig. 10). In case of homogeneous bubble nucleation, it is conceivable that the first bubbles preferably nucleated in the lower central part of the sample and had more time to grow. Mangan and Sisson (2000) observed a preferred bubble nucleation close to the upper capsule headspace and attributed this effect to melt displacement during opening of the crimped capsule. However, melt displacement at the bottom lid is unlikely for our capsule geometry. There is no evidence that the shape of the capsule influences nucleation in our experiments.

The CI glass cylinder sample CD-C-5 with the lowest P_{final} of 60 MPa (0.17 MPa·s^{-1}) is the most degassed cylinder sample with the highest porosity of ~10 % in the glass. Due to the lowest final pressure and the high N_V(n) with bubble diameters up to 13 µm, the corrected porosity (~25 %) in the melt is closer to the equilibrium porosity (~33 %) than in samples decompressed to higher P_{final} of 75 and 100 MPa (Table 3). The N_V(n)-values of all decompressed cylinder samples range within one order of magnitude ($6 \cdot 10^4$ – $7 \cdot 10^5$ mm^{-3}) assuming an analytical error of half an order of magnitude. The highest N_V(n)-value of the 60 MPa sample is further proof for homogeneous bubble nucleation in all cylinder samples. It is unlikely that bubbles of up to 13 µm diameter grow during the few seconds of rapid quench. The size distribution (Fig. 7c) with a narrow size range of these bubbles documents a single nucleation event within a short time interval as described in Fig. 7b in Toramaru (1989). Considering homogeneous bubble nucleation in the cylinder samples with a P_{final} of 100 MPa, we can estimate a ΔP_{HoN} of <76 MPa for the CI and <70 MPa for the VAD79 melt using the solubility data of Fanara et al. (in press) and Iacono Marziano et al. (2007), respectively.

Integration of results into the model of Toramaru (2006)

Toramaru (2006) reported a model to describe homogeneous nucleation and growth of bubbles at a constant decompression rate. This formulation relates N_V(n) to physico-chemical parameters such as surface tension, diffusivity and concentration of total H_2O (Eq. 3):

$$N_V(\mathrm{n}) = 34 \cdot C \cdot \left(\frac{16\pi\sigma^3}{3\mathrm{k}TP_W^2}\right)^{-2} \cdot \left(\frac{V_m P_W}{\mathrm{k}T}\right)^{-\frac{1}{4}} \cdot \left(\frac{P_W^2 \mathrm{k}TCD}{4\sigma^2(\mathrm{d}P/\mathrm{d}t)}\right)^{-\frac{3}{2}} \quad \textbf{(3)}$$

where N_V(n) is the number of bubbles per unit of bubble-free melt volume (m^{-3}), C is the initial total H_2O concentration expressed as molecular number per cubic meters (m^{-3}), σ is the surface tension at the bubble-melt interface ($N \cdot m^{-1}$), k is the Boltzmann constant ($1.38 \cdot 10^{-23}$ $J \cdot K^{-1}$), T is the temperature (K), P_W is the H_2O saturation pressure (Pa), V_m is the volume of a H_2O molecule in the melt ($3 \cdot 10^{-29}$ m^3; Burnham and Davis, 1971), D is the total H_2O diffusivity in the silicate melt ($m^2 \cdot s^{-1}$) and dP/dt is the decompression rate in $Pa \cdot s^{-1}$. The conversion of N_V(t)- (e.g. provided by the CSDCorrections software) into N_V(n)-values is essential, because only N_V(n)-values are independent of diffusive bubble growth and expansion (Proussevitch et al., 2007; Toramaru, 1989).

This model is valid for homogeneous bubble nucleation in a melt free of pre-existing bubbles during super-liquidus isothermal decompression at a constant rate in the diffusion-controlled regime. The sample size has to be sufficient to guarantee a melt pool that is unaffected by diffusional volatile loss to the capsule-melt interface. The application of this model necessitates a completed single nucleation event as well as the absence of Ostwald ripening and coalescence. The bubble size distribution should display a narrow size range and follow a linear trend in the ln $n(l)$ vs. l plot, where $n(l)$ is the population density of bubbles with diameter l in a certain size interval (Toramaru, 2006). The diffusion-controlled regime is defined by the parameter $\alpha_4 = t_{dec} P_W / 4\eta > 2 \cdot 10^3$ (Toramaru, 1995), where t_{dec} is the time (s) needed for decompression to P_{final}. For both melt compositions, α_4 is about 10^7 for a decompression rate of 0.17 $MPa \cdot s^{-1}$ and even higher for lower decompression rates. However, during fast decompression to low P_{final} with large ΔP, high-viscous melts such as rhyolites become viscosity-controlled, because the H_2O content in the melt decreases due to exsolution while the viscosity steadily increases (cf. Fig. 9a in Toramaru, 1995).

The parameters D, C, σ, α_4 and P_W of Equation 3 are similar for the CI and the VAD79 melt. For exemplary purpose, the data of CI glass cylinder experiments were applied to the model of Toramaru (2006). A surface tension of 0.133 $N \cdot m^{-1}$ was derived from Bagdassarov et al. (2000) considering the dependence of total H_2O content and T on σ. P_W for the H_2O content of 4.7 wt% at 1050 °C was extrapolated from the solubility experiments of Fanara et al. (in press) to be ~176 MPa. The initial total H_2O content C of $3.54 \cdot 10^{27}$ m^{-3} was calculated using the melt density at P_W and T provided by the model of Ochs and Lange (1999). The total H_2O diffusivity (D) of $1.57 \cdot 10^{-10}$ $m^2 \cdot s^{-1}$ was calculated for 1050 °C and 4.7 wt% H_2O by the formulation for trachytic compositions given in Fanara et al. (2013). Application of Equation 3

results in calculated N_V(n)-values that are up to five orders of magnitude lower than in the samples of our glass cylinder experiments decompressed at rates of 0.024 and 0.17 MPa·s^{-1} to 100 - 60 MPa providing N_V(n) of ~10^5 mm^{-3} (Fig. 11). The discrepancies between calculated and observed N_V(n)-values may be attributed to H_2O species-related changes in *C* and *D* as well as the usage of a macroscopic surface tension. The nucleation of bubbles is a process on a molecular scale, where macroscopic physical descriptions are likely to fail (e.g. Bottinga and Javoy, 1990; Gonnermann and Gardner, 2013; Navon and Lyakhovsky, 1998; Ruckenstein and Nowakowski, 1990; Sparks, 1978; Toramaru, 1989). Bubble nucleation prerequisites the aggregation of H_2O molecule clusters with a typical critical radius of 1 – 10 nm (Gonnermann and Gardner, 2013; Toramaru, 1995) that is attributed to local concentration fluctuations in the melt (Hurwitz and Navon, 1994). It is conceivable to refer the coefficient *C* in Equation 3 to the actual concentration of H_2O molecules with respect to the species concentrations of molecular H_2O and OH^- in the silicate melt at *P*-*T* conditions (Nowak and Behrens, 1995; Nowak and Behrens, 2001). At a total H_2O content of 4.7 wt% and 1050 °C, the molecular H_2O content is in the range of 1 wt%. Considering the H_2O speciation, *D* should be substituted by the diffusivity of molecular H_2O (e.g. Toramaru, 1995), which is one order of magnitude higher than the total H_2O diffusivity at experimental conditions (e.g. Behrens and Nowak, 1997). Such an increase of *D* in Equation 3 results in a decrease of predicted N_V(n) by one order of magnitude (Fig. 11). In contrast, the decrease of *C* due to H_2O speciation barely increases N_V(n) by less than half an order of magnitude. In combination, these opposing effects shift N_V(n) to even lower values than necessary to describe our experimental data. In this model, a significant increase of N_V(n) can be achieved by decreasing the surface tension in Equation 3, while using *C* and *D* for total H_2O. The best match of predicted N_V(n) to our experimental results is achieved for a σ of ~0.003 N·m^{-1} (Fig. 11). Lowered surface tensions on the molecular scale of bubble nucleation compared to macroscopic values were already suggested in previous studies (e.g. Bottinga and Javoy, 1990; Gonnermann and Gardner, 2013; Hamada et al., 2010; Kashchiev, 2003; Kashchiev, 2004; Ruckenstein and Nowakowski, 1990; Toramaru, 1990; Toramaru, 1995). This effect may be attributed to a dependence of surface tension on bubble (nucleus) size (Ruckenstein and Nowakowski, 1990; Tolman, 1949), thermal fluctuations supplying the energy of formation of a new surface (Bottinga and Javoy, 1990) or a diffuse interface between nucleus and surrounding melt (Gonnermann and Gardner, 2013; Kashchiev, 2003; Kashchiev, 2004; Kelton and Greer, 2010). Navon and Lyakhovsky (1998) suggested a completely different

approach to explain the discrepancy between experimentally determined and modeled N_V(n). They proposed to consider the diffusivity of silicate network components rather than H_2O diffusivity to form a H_2O nucleus in a hydrous supersaturated melt. This idea is based on the similar distances of neighboring H_2O molecules in the fluid and in the melt, even if the species concentration of 1 wt% molecular H_2O is considered. At a P_{final} of 100 MPa, the calculated mean distances are 0.6 nm in the fluid and 1.1 nm in the melt. The formation of a nucleus may therefore be kinetically controlled by the diffusion of silicate network components to enable clustering of H_2O molecules. In this case, the diffusivity of network forming cations linked to viscosity of the melt becomes a controlling factor (Navon and Lyakhovsky, 1998). This relation can be expressed by the Eyring equation:

$$D = \frac{\mathrm{k}T}{\eta\lambda} \qquad \textbf{(4)}$$

where k is the Boltzmann constant, T the temperature in K, λ the jump distance in m and η the viscosity in Pa·s. A mean jump distance of $3 \cdot 10^{-10}$ m for the chemical diffusivity of high field strength elements like Zr^{4+} in both dry and hydrous melts was determined by Koepke and Behrens (2001) and is suggested to be comparable to Si^{4+} and Al^{3+} diffusion. At 1050 °C and 4.7 wt% H_2O_t a viscosity of 77 Pa·s was calculated using the relation of Misiti et al. (2011) for the CI melt. Insertion into Equation 4 provides a network former diffusivity of $8 \cdot 10^{-13}$ $m^2 \cdot s^{-1}$ that is more than 2 orders of magnitude lower than the total H_2O diffusivity. The corresponding shift of the logN_V(n)/(dP/dt) line in Fig. 11 by 3.5 orders of magnitude is still not sufficient to match the experimentally determined N_V(n). It is therefore conceivable that both surface tension and diffusivity contribute to the discrepancy between modeled and experimental N_V(n)-values.

Our determined N_V(n) can be compared with selected data of previous studies (Gondé et al., 2011; Mangan and Sisson, 2000; Marxer et al., 2015; Mourtada-Bonnefoi and Laporte, 2002) that potentially fulfill the criteria for the application of the vesiculation model of Toramaru (2006). Experiments using glass powder as starting material were not considered, because the observed N_V(n) are mainly controlled by the number of hydration or H_2O-N_2 bubbles in the melt prior to decompression. A reliable experimentally determined N_V(n) of Gondé et al. (2011) for a haplogranitic melt representing the N_V(n) directly after bubble nucleation (sample #45 in Gondé et al., 2011; filled hexagon in Fig. 11) is also three orders of

magnitude higher than the modeled value using the macroscopic σ and is in the range of our determined N_V(n) (Fig. 11). This supports (1) the credibility of our results (2) that N_V(n) is within error independent of composition and (3) the suggestion of a reduced surface tension and effect of diffusivity for the nucleation process. Comparable to our study, Marxer et al. (2015) performed decompression experiments with the VAD79 composition down to a P_{final} of 75 MPa, but with a higher initial H_2O content of ~5.2 wt% in the 5 mm samples (still slightly H_2O-undersaturated). The resulting N_V(n) of the experiments with the same decompression rates as in this study are 2 - 3 orders of magnitude lower than for the experiments with an initial H_2O content of ~4.7 wt%. Ostwald ripening and coalescence can decrease the number of bubbles during decompression. Due to the higher initial H_2O content in the experiments of Marxer et al. (2015), bubble nucleation and growth started at a higher P than in the experiments of this study. However, the total timescales available for degassing by homogeneous bubble nucleation and growth is e.g. very similar for the CI experiment decompressed to 60 MPa (CD-C-5) with ~4.7 wt% H_2O at a decompression rate of 0.17 MPa·s^{-1} and the corresponding VAD79 experiment with ~5.2 wt% H_2O and a P_{final} of 75 MPa (CD18 reported in Marxer et al., 2015). Nevertheless, the observed N_V(n) in CD-C-5 are orders of magnitude higher. It is conceivable that this sample was quenched just before the onset of extensive bubble coalescence. The recent in situ observation of Masotta et al. (2014) have shown that massive bubble coalescence can occur within minutes in nominally H_2O-free, highly viscous rhyodacitic melts at 1100 °C. This time interval for extensive bubble interaction is expected to be shortened down to a scale of seconds in case of less silicic, hydrous melts.

The N_V(n) of the 5 mm samples in Marxer et al. (2015) are over the whole range of applied decompression rates close to the values predicted by the model of Toramaru (2006), which does not apply to our newly determined data. Among other studies, Toramaru (2006) used some N_V(n) of decompression experiments reported e.g. in Mangan and Sisson (2000) and Mourtada-Bonnefoi and Laporte (2002) to adjust the model parameters. If such parameters are based on experiments that were already subject to Ostwald ripening and/or coalescence, the predicted N_V(n) will generally be too low. Early bubble coalescence during decompression was observed by Mourtada-Bonnefoi and Laporte (2002) and in situ in HDAC experiments by Gondé et al. (2011). Some of these experiments are also characterized by a high total P decrease (ΔP up to >300 MPa) in combination with high porosities of up to 68 % in the glass, which are even higher in the melt due to bubble shrinkage during quench (Marxer et al., 2015). Both

factors enhance the occurrence of bubble interactions that reduce N_V(n) due to the increased degassing timescale and decreasing bubble spacing. This effect is evident from the range of determined N_V(n) reported in Gondé et al. (2011), Mangan and Sisson (2000) and Mourtada-Bonnefoi and Laporte (2002) for samples of experimental sets with similar decompression rate but different degassing timescales (time from onset of homogeneous bubble nucleation to P_{final}). The N_V(n) of samples from experiments with the shortest decompression timescale are the highest within a set (filled symbols in Fig. 11). These bubble populations are presumably unaffected by Ostwald ripening or coalescence. Further decompression leads to bubble interaction and significantly lowered N_V(n) (empty symbols in Fig. 11). It may therefore be necessary to improve current models for homogeneous bubble nucleation with data from new experiments that are not affected by Ostwald ripening and/or bubble coalescence.

Implications and limitations for future studies of homogeneous bubble nucleation in silicate melts

The prerequisite to study homogeneous bubble nucleation is a single-phase melt. As documented in this study and in Marxer et al. (2015) this can be ensured by using massive glass cylinders as starting material and sufficient equilibration time to guarantee a homogeneous volatile content in the melt prior to decompression. Further parameters such as volatile diffusivity, η and σ that are dependent on melt composition and T should be considered before conducting degassing experiments, because the investigation of homogeneous nucleation and growth of volatile bubbles during isothermal decompression requires an experimental window, where the experimental result is mainly controlled by the decompression path. An important limiting parameter is the decompression timescale that is defined by the decompression rate and P_{final}. The time-dependent diffusional loss of volatiles to heterogeneously nucleated bubbles at the capsule wall defines the minimum sample diameter needed to retain a sufficiently sized unaffected melt pool in the center of the specimen. Furthermore, the decompression duration is limited by the ascent of heterogeneously formed bubbles at the capsule-melt interface that is dependent on melt viscosity. These two limitations require the largest technically possible capsule dimensions. On the other hand, an increasing capsule volume leads to a decrease in cooling rate and therefore to possible quench crystal formation. In order to study a single homogeneous bubble nucleation event, P_{final} has to be as close to the terminus of the event as possible. Unnecessary low P_{final} increase the decompression timescale and enable bubble

growth by Ostwald ripening and coalescence that both lead to a reduction of N_V(n). Increasing porosities in the samples decrease the inter-bubble distances and aggravate the interaction of bubbles. Additionally, high porosities cause massive shrinkage of bubbles due to the significant decrease in molar volume of the fluid during isobaric quench. This reduction of bubble volumes necessitates the correction of bubble sizes and porosities that are determined from the vitrified samples in order to match the conditions prior to quench (Marxer et al., 2015).

Considering these experimental limitations, future experiments will improve the investigation of homogeneous bubble nucleation in silicate melts. This will contribute to a better understanding of melt degassing triggering volcanic eruptions at the interface of the molecular to the macroscopic world during magma ascent.

Acknowledgements

This project was funded by the German Science Foundation (DFG NO378/8-1/2) in the frame of the ICDP SPP1006. Several experiments were conducted within the framework of the DFG project NO378/5-1, 2. We thank Simone Schafflick and Indra Gill-Kopp for careful sample preparation, Annette Flicker for FTIR measurements and Thomas Wenzel for support at the EMP. Special thanks to Barbara Maier and Marco Kahlfuss from our workshop for all kind of support concerning the decompression valve and the production of supplies for sample preparation.

References

Appen, A.A. (1949). Berechnung der optischen Eigenschaften, der Dichte und des Ausdehnungskoeffizienten von Silikatgläsern aus ihrer Zusammensetzung. Berichte der Akademischen Wissenschaften, UdSSR, 69, 841-844.

Bagdassarov, N., Dorfman, A., and Dingwell, D.B. (2000). Effect of alkalis, phosphorus, and water on the surface tension of haplogranite melt. American Mineralogist, 85(1), 33-40.

Behrens, H., and Nowak, M. (1997): The mechanisms of water diffusion in polymerized silicate melts. Contributions to Mineralogy and Petrology, 126(4), 377-385.

-. (2003). Quantification of H_2O speciation in silicate glasses and melts by IR spectroscopy: In situ versus quench techniques. Phase Transitions, 76(1-2), 45-61.

Berlo, K., Gardner, J.E., and Blundy, J.D. (2011). Timescales of magma degassing. Timescales of magmatic processes: From core to atmosphere, p. 231-255. John Wiley & Sons, Ltd.

Berndt, J., Liebske, C., Holtz, F., Freise, M., Nowak, M., Ziegenbein, D., Hurkuck, W., and Koepke, J. (2002). A combined rapid-quench and H_2-membrane setup for internally heated pressure vessels: Description and application for water solubility in basaltic melts. American Mineralogist, 87(11-12), 1717-1726.

Bottinga, Y., and Javoy, M. (1990). Mid-ocean ridge basalt degassing: Bubble nucleation. Journal of Geophysical Research, 95, 5125–5131.

Burnham, C.W., and Davis, N.F. (1971). The role of H_2O in silicate melts. 1. P-V-T relations in the system $NaAlSi_3O_8$-H_2O to 10 kilobars and 1000 °C. American Journal of Science, 270, 54-79.

Carroll, M.R., and Webster, J.D. (1994). Solubilities of sulfur, noble gases, nitrogen, chlorine, and fluorine in magmas. In P.H. Ribbe (Ed.), Volatiles in Magmas, 30, p. 231-279. Reviews in Mineralogy, Washington, DC.

Civetta, L., Orsi, G., Pappalardo, L., Fisher, R.V., Heiken, G., and Ort, M. (1997). Geochemical zoning, mingling, eruptive dynamics and depositional processes: The Campanian Ignimbrite, Campi Flegrei caldera, Italy. Journal of Volcanology and Geothermal Research, 75(3-4), 183-219.

Davis, M.J., and Ihinger, P.D. (1998). Heterogeneous crystal nucleation on bubbles in silicate melt. American Mineralogist, 83(9-10), 1008-1015.

De Vivo, B., Petrosino, P., Lima, A., Rolandi, G., and Belkin, H.E. (2010). Research progress in volcanology in the Neapolitan area, southern Italy: A review and some alternative views. Mineralogy and Petrology, 99(1-2), 1-28.

Dingwell, D.B., and Webb, S.L. (1990). Relaxation in Silicate Melts. European Journal of Mineralogy, 2(4), 427-449.

Duan, Z., and Zhang, Z. (2006). Equation of state of the H_2O-CO_2 system up to 10 GPa and 2573 K: Molecular dynamics simulations with ab initio potential surface. Geochimica et Cosmochimica Acta, 70(9), 2311-2324.

Fanara, S., Behrens, H., and Zhang, Y.X. (2013). Water diffusion in potassium-rich phonolitic and trachytic melts. Chemical Geology, 346, 149-161.

Fanara, S., Botcharnikov, R.E., Husen, A., Buddensieck, J., and Behrens, H. (2012). Pre-eruptive conditions of the Campanian Ignimbrite eruption: Experimental constraints from phase equilibria and volatile solubility studies. Proceedings of IODP-ICDP Colloquium, p. 41-43, Kiel, Germany.

Fanara, S., Botcharnikov, R.E., Palladino, D.M., Adams, F., Buddensieck, J., Mulch, A., and Behrens, H. (in press). Volatiles in magmas related to the Campanian Ignimbrite eruption: Experiments vs. natural findings. American Mineralogist.

Fiege, A., Holtz, F., and Cichy, S.B. (2014). Bubble formation during decompression of andesitic melts. American Mineralogist, 99(5-6), 1052-1062.

Gardner, J.E. (2007). Heterogeneous bubble nucleation in highly viscous silicate melts during instantaneous decompression from high pressure. Chemical Geology, 236(1-2), 1-12.

Gardner, J.E., Hilton, M., and Carroll, M.R. (1999). Experimental constraints on degassing of magma: Isothermal bubble growth during continuous decompression from high pressure. Earth and Planetary Science Letters, 168(1-2), 201-218.

Giordano, D., Russell, J.K., and Dingwell, D.B. (2008). Viscosity of magmatic liquids: A model. Earth and Planetary Science Letters, 271, 123-134.

Gondé, C., Martel, C., Pichavant, M., and Bureau, H. (2011). In situ bubble vesiculation in silicic magmas. American Mineralogist, 96(1), 111-124.

Gonnermann, H.M., and Gardner, J.E. (2013). Homogeneous bubble nucleation in rhyolitic melt: Experiments and nonclassical theory. Geochemistry Geophysics Geosystems, 14(11), 4758-4773.

Gonnermann, H.M., and Manga, M. (2007). The fluid mechanics inside a volcano. Annual Review of Fluid Mechanics, 39(1), 321-356.

Hamada, M., Laporte, D., Cluzel, N., Koga, K.T., and Kawamoto, T. (2010). Simulating bubble number density of rhyolitic pumices from Plinian eruptions: Constraints from fast decompression experiments. Bulletin of Volcanology, 72(6), 735-746.

Higgins, M.D. (2000). Measurement of crystal size distributions. American Mineralogist, 85(9), 1105-1116.

-. (2006). Verification of ideal semi-logarithmic, lognormal or fractal crystal size distributions from 2D datasets. Journal of Volcanology and Geothermal Research, 154(1-2), 8-16.

Hirth, J.P., Pound, G.M., and Stpierre, G.R. (1970). Bubble Nucleation. Metallurgical Transactions, 1(4), 939-945.

Hurwitz, S., and Navon, O. (1994). Bubble nucleation in rhyolitic melts: Experiments at high-pressure, temperature and water-content. Earth and Planetary Science Letters, 122(3-4), 267-280.

Iacono Marziano, G., Schmidt, B.C., and Dolfi, D. (2007). Equilibrium and disequilibrium degassing of a phonolitic melt (Vesuvius AD 79 "white pumice") simulated by decompression experiments. Journal of Volcanology and Geothermal Research, 161(3), 151-164.

Kashchiev, D. (2003). Thermodynamically consistent description of the work to form a nucleus of any size. Journal of Chemical Physics, 118(4), 1837-1851.

-. (2004). Multicomponent nucleation: Thermodynamically consistent description of the nucleation work. Journal of Chemical Physics, 120(8), 3749-58.

Kawamoto, T., and Hirose, K. (1994). Au-Pd sample containers for melting experiments on iron and water-bearing systems. European Journal of Mineralogy, 6(3), 381-385.

Kelton, K.F., and Greer, A.L. (2010). Nucleation in condensed matter: Applications in materials and biology, 15, p. 726. Pergamon Materials Series, Oxford, UK.

Kloess, G.H. (2000). Dichtefluktuationen natürlicher Gläser. Habilitation thesis. University of Jena.

Koepke, J., and Behrens, H. (2001). Trace element diffusion in andesitic melts: An application of synchrotron X-ray fluorescence analysis. Geochimica et Cosmochimica Acta, 65(9), 1481-1498.

Larsen, J.F., and Gardner, J.E. (2000). Experimental constraints on bubble interactions in rhyolite melts: Implications for vesicle size distributions. Earth and Planetary Science Letters, 180(1-2), 201-214.

Libourel, G., Marty, B., and Humbert, F. (2003). Nitrogen solubility in basaltic melt. Part I. Effect of oxygen fugacity. Geochimica et Cosmochimica Acta, 67(21), 4123-4135.

Mangan, M., and Sisson, T. (2000). Delayed, disequilibrium degassing in rhyolite magma: Decompression experiments and implications for explosive volcanism. Earth and Planetary Science Letters, 183(3-4), 441-455.

Martel, C., and Iacono-Marziano, G. (2015). Timescales of bubble coalescence, outgassing, and foam collapse in decompressed rhyolitic melts. Earth and Planetary Science Letters, 412, 173-185.

Marxer, H., Bellucci, P., and Nowak, M. (2015). Degassing of H_2O in a phonolitic melt: A closer look at decompression experiments. Journal of Volcanology and Geothermal Research, 297, 109-124.

Masotta, M., Ni, H., and Keppler, H. (2014). In situ observations of bubble growth in basaltic, andesitic and rhyodacitic melts. Contributions to Mineralogy and Petrology, 167(2).

Mastrolorenzo, G., and Pappalardo, L. (2006). Magma degassing and crystallization processes during eruptions of high-risk Neapolitan-volcanoes: Evidence of common equilibrium rising processes in alkaline magmas. Earth and Planetary Science Letters, 250(1-2), 164-181.

Misiti, V., Vetere, F., Freda, C., Scarlato, P., Behrens, H., Mangiacapra, A., and Dingwell, D.B. (2011). A general viscosity model of Campi Flegrei (Italy) melts. Chemical Geology, 290(1-2), 50-59.

Miyazaki, A., Hiyagon, H., Sugiura, N., Hirose, K., and Takahashi, E. (2004). Solubilities of nitrogen and noble gases in silicate melts under various oxygen fugacities: Implications for the origin and degassing history of nitrogen and noble gases in the earth. Geochimica et Cosmochimica Acta, 68(2), 387-401.

Morizet, Y., Nichols, A.R.L., Kohn, S.C., Brooker, R.A., and Dingwell, D.B. (2007). The influence of H_2O and CO_2 on the glass transition temperature: Insights into the effects of volatiles on magma viscosity. European Journal of Mineralogy, 19(5), 657-669.

Mourtada-Bonnefoi, C.C., and Laporte, D. (2002). Homogeneous bubble nucleation in rhyolitic magmas: An experimental study of the effect of H_2O and CO_2. Journal of Geophysical Research-Solid Earth, 107(B4).

Navon, O., and Lyakhovsky, V. (1998). Vesiculation processes in silicic magmas. Geological Society, London, Special Publications, 145(1), 27-50.

Nowak, M., and Behrens, H. (1995). The speciation of water in haplogranitic glasses and melts determined by in situ near-infrared spectroscopy. Geochimica et Cosmochimica Acta, 59(16), 3445-3450.

-. (1997). An experimental investigation on diffusion of water in haplogranitic melts. Contributions to Mineralogy and Petrology, 126(4), 365-376.

-. (2001). Water in rhyolitic magmas: Getting a grip on a slippery problem. Earth and Planetary Science Letters, 184(2), 515-522.

Nowak, M., Cichy, S.B., Botcharnikov, R.E., Walker, N., and Hurkuck, W. (2011). A new type of high-pressure low-flow metering valve for continuous decompression: First experimental results on degassing of rhyodacitic melts. American Mineralogist, 96, 1373-1380.

Ochs, F.A., and Lange, R.A. (1999). The density of hydrous magmatic liquids. Science, 283(5406), 1314-1317.

Ohlhorst, S., Behrens, H., and Holtz, F. (2001). Compositional dependence of molar absorptivities of near-infrared OH^- and H_2O bands in rhyolitic to basaltic glasses. Chemical Geology, 174(1-3), 5-20.

Orsi, G., Dantonio, M., Devita, S., and Gallo, G. (1992). The Neapolitan Yellow Tuff, a large-magnitude trachytic phreatoplinian eruption: Eruptive dynamics, magma withdrawal and caldera collapse. Journal of Volcanology and Geothermal Research, 53(1-4), 275-287.

Pappalardo, L., and Mastrolorenzo, G. (2012). Rapid differentiation in a sill-like magma reservoir: A case study from the Campi Flegrei caldera. Scientific Reports, 2, 712.

Proussevitch, A.A., Sahagian, D.L., and Tsentalovich, E.P. (2007). Statistical analysis of bubble and crystal size distributions: Formulations and procedures. Journal of Volcanology and Geothermal Research, 164(3), 95-111.

Rolandi, G., Bellucci, F., Heizler, M.T., Belkin, H.E., and De Vivo, B. (2003). Tectonic controls on the genesis of ignimbrites from the Campanian Volcanic Zone, southern Italy. Mineralogy and Petrology, 79(1-2), 3-31.

Roskosz, M., Bouhifd, M.A., Jephcoat, A.P., Marty, B., and Mysen, B.O. (2013). Nitrogen solubility in molten metal and silicate at high pressure and temperature. Geochimica et Cosmochimica Acta, 121, 15-28.

Ruckenstein, E., and Nowakowski, B. (1990). A kinetic theory of nucleation in liquids. Journal of Colloid and Interface Science, 137(2), 583-592.

Schneider, C.A., Rasband, W.S., and Eliceiri, K.W. (2012). NIH Image to ImageJ: 25 years of image analysis. Nature Methods, 9(7), 671-675.

Scholze, H. (1960). Zur Frage der Unterscheidung zwischen H_2O-Molekülen und OH-Gruppen in Gläsern und Mineralen. Naturwissenschaften, 47, 226 (in German).

Simakin, A.G., Armienti, P., and Epel'baum, M.B. (1999). Coupled degassing and crystallization: Experimental study at continuous pressure drop, with application to volcanic bombs. Bulletin of Volcanology, 61(5), 275-287.

Sparks, R.S.J. (1978). The dynamics of bubble formation and growth in magmas: A review and analysis. Journal of Volcanology and Geothermal Research, 3(1–2), 1-37.

Suzuki, Y., Gardner, J.E., and Larsen, J.F. (2007). Experimental constraints on syneruptive magma ascent related to the phreatomagmatic phase of the 2000 AD eruption of Usu volcano, Japan. Bulletin of Volcanology, 69(4), 423-444.

Tolman, R.C. (1949). The effect of droplet size on surface tension. Journal of Chemical Physics, 17(3), 333-337.

Toramaru, A. (1989). Vesiculation process and bubble size distributions in ascending magmas with constant velocities. Journal of Geophysical Research: Solid Earth, 94(B12), 17523-17542.

-. (1990). Measurement of bubble-size distributions in vesiculated rocks with implications for quantitative estimation of eruption processes. Journal of Volcanology and Geothermal Research, 43(1-4), 71-90.

-. (1995). Numerical study of nucleation and growth of bubbles in viscous magmas. Journal of Geophysical Research-Solid Earth, 100(B2), 1913-1931.

-. (2006). BND (bubble number density) decompression rate meter for explosive volcanic eruptions. Journal of Volcanology and Geothermal Research, 154(3-4), 303-316.

Tables

Table 1: Chemical compositions (normalized to 100 wt%) of the synthesized starting glasses based on analyses of natural CF Triflisco OP17c1-sp by XRF in Civetta et al. (1997) and natural VAD79 in Iacono Marziano et al. (2007).

	CI Civetta XRF Data	CI this study n = 27	VAD79 Iacono Marziano n = 12	VAD79 this study n = 17
SiO_2	58.52	58.87 (34)	57.15 (39)	57.53 (63)
TiO_2	0.45	0.44 (2)	0.30 (5)	0.29 (2)
Al_2O_3	18.81	18.53 (23)	21.34 (25)	20.52 (18)
FeO[a]	4.36	4.41 (25)	2.70 (17)	2.71 (19)
MnO	0.08	0.08 (3)	0.14 (6)	0.14 (3)
MgO	1.48	1.42 (7)	0.39 (5)	0.38 (3)
CaO	4.13	4.09 (15)	3.26 (12)	3.32 (11)
Na_2O	2.92	3.08 (14)	5.16 (15)	5.38 (17)
K_2O	8.98	8.82 (16)	9.46 (15)	9.53 (21)
P_2O_5	0.26	0.25 (4)	0.09 (4)	0.10 (3)

Notes: Errors are provided in parentheses.

Standard deviation (1σ) based on EMPA analysis.

[a]: Total Fe concentration in the glass given as FeO.

Table 2: Run conditions and H_2O contents of isobaric experiments.

exp. #	starting material	t_{eq}	quench method	T prior quench	weighed portion of H_2O in capsule	total H_2O content in glass by FTIR	number of analyzed objects	average object size	N_C(t) (glass)[d]
		[h]		[°C]	[wt%][a]	[wt%][b]		[µm]	[mm^{-3}]
IB-C-1a	cylinder	96	RQ	1050	4.75(0.05)	4.87(0.10)	82	0.3 - 1	1.17E+05
IB-C-1b	cylinder	96	RQ	1300	4.73(0.05)	4.93(0.10)	84	0.7	1.11E+05
IB-C-2	cylinder	96	NQ	1050	4.72(0.05)	4.66(0.10)	267	10 - 13	7.01E+04
REF12[c]	cylinder	96	RQ	1050	4.86(0.05)	4.89(0.12)			
IB-P-1	powder	24	RQ	1300	0.98(0.05)	1.10(0.05)			
IB-P-2	powder	24	RQ	1300	1.95(0.05)	2.05(0.04)			
IB-P-3	powder	24	RQ	1300	3.87(0.05)	4.01(0.13)			
IB-P-4	powder	24	RQ	1300	4.76(0.05)	4.84(0.17)	280	0.3 - 1	4.42E+05

Equilibration temperature was 1300 °C and equilibration pressure was 200 MPa.

[a]: Weighing error in brackets.

[b]: Means of at least 10 individual measurements over the whole sample (±1σ in brackets), molar absorption coefficients and densities are provided in the text. Thickness of the samples ranges between 120 and 160 µm.

[c]: VAD79 composition, equilibrated at 1050°C, for details see Tab. 1 in Marxer et al. (2015).

[d]: N_C(t) is the number of quench crystal aggregates per total unit volume derived from TLM.

Table 3: Synopsis of the decompression experiments and the main results (continued on the next page).

exp. #	compo-sition	starting material	t_{eq} [h]	P_{final} [MPa]	$dP \cdot dt^{-1}$ [MPa·s^{-1}]	total H_2O content dissolved in melt at P_{start} [wt%][a]	residual total H_2O content in glass by FTIR [wt%][b]	counting method	number of analyzed objects	average object size [µm]
CD-C-5	CI	cylinder	96	60	0.17	4.78(5)	n.d.	BSE	430	7 - 9
								BSE	453	7 - 9
								BSE	441	7 - 9
								BSE	438	7 - 9
								BSE	440	7 - 9
CD-C-3	CI	cylinder	96	75	0.024	4.78 (5)	4.57 (6)[j]	BSE	645	-
								TLM	143	11.5 (2.0)
CD-C-4	CI	cylinder	96	75	0.17	4.75 (5)	4.88 (13)[j]	BSE	507	-
								TLM	182	~ 4
CD-C-1	CI	cylinder	96	100	0.17	4.62 (5)	4.64 (10)[j]	TLM	529	4 - 5
CD-P-1	CI	powder	24	100	0.17	4.67 (5)	4.06 (10)	BSE	123	-
								TLM	213	5 - 7
CD-C-2	CI	cylinder	96	100	0.024	4.68 (5)	4.58 (6)[j]	TLM	901	4 - 5
CD-P-2a	CI	powder	24	100	0.024	4.74 (5)	3.81(8)	BSE	84	130
CD-P-2b	CI	powder	96	100	0.024	4.64 (5)	4.73 (14)	TLM	218	1 - 2
CD-P-22	VAD79	powder	24	100	0.024	4.73 (5)	3.71 (9)	BSE	229	-
CD-C-23	VAD79	cylinder	96	100	0.17	4.76 (5)	4.83 (6)[j]	TLM	362	1 - 2
CD-P-24	VAD79	powder	24	100	0.17	4.73 (5)	3.86 (4)	BSE	134	-
CD-C-25	VAD79	cylinder	96	100	0.024	4.66 (5)	4.68 (5)[j]	TLM	493	1 - 2
CD-P-32	VAD79	powder	96	100	0.024	4.73 (5)	4.60 (8)	TLM	156	1 - 2

Table 3: Synopsis of the decompression experiments and the main results (continued from the previous page).

2D porosity (glass) ImageJ [area%][c]	3D porosity (glass) from BSE or TLM [vol%]	equilibrium porosity (melt) [vol%][d]	expected porosity (melt) [vol%][e]	corrected porosity (melt) [vol%][f]	N_V(t) (glass) [mm^{-3}][g]	N_V(n) (melt) [mm^{-3}][h]	B_s[i]	comments
8.59	8.88	33.6	n.d.	22.6	5.68E+05	6.23E+05	3.00	area 1
10.36	10.5	33.6	n.d.	26.0	7.51E+05	8.39E+05	3.00	area 2
8.66	9.09	33.6	n.d.	23.1	7.06E+05	7.77E+05	3.00	area 3
10.9	10.9	33.6	n.d.	26.8	6.09E+05	6.84E+05	3.00	area 4
9.63	9.84	33.6	n.d.	24.7	6.59E+05	7.30E+05	3.00	average
4.8	5.4	26.5	3.8	15.2	1.87E+05	1.98E+05	3.15	
	1.61	26.5	3.8	4.9	5.53E+04	5.62E+04	3.15	
3.3	3.6 (4)	26.2	0.0	10.5	6.12E+04	6.35E+04	3.15	
	0.27	26.2	0.0	0.9	8.11E+04	7.55E+04	3.15	
	0.54	14.0	0.0	1.6	1.52E+05	1.53E+05	2.98	
4.8	4.9	14.5	8.0	13.3	204	215	2.98	area of big bubbles
	2.9	14.5	1.8	8.2	2.58E+05	2.64E+05	2.98	area of small bubbles
	0.26	14.6	1.4	0.8	4.68E+05	4.69E+05	2.98	
5.6	5.4 (1.5)	15.4	11.9	14.5	73	87	2.98	
	0.1	14.2	0.0	0.3	2.73E+05	3.24E+05	2.98	
4.5	6.1 (1.2)	15.1	12.9	13.6	508	541	2.51	
	0.0	15.4	0.0	0.1	1.01E+05	1.01E+05	2.51	
5.6	5.6 (8)	15.1	11.2	12.6	319	338	2.51	
	0.05	14.4	0.0	0.1	1.29E+05	1.30E+05	2.51	
	0.07	15.1	1.8	0.2	1.77E+05	1.77E+05	2.51	

Table 3: Notes.

Starting pressure (P_{start}) was 200 MPa for all experiments.

[a]: Weighed portions of H_2O (weighing error in brackets).

[b]: Means of individual measurements in the center area of the sample (±1σ in brackets).

[c]: Porosity displayed as 2D phase proportion of bubbles determined from a representative excerpt in the sample center acquired by BSE imaging.

[d]: Calculated from Eq. 5 in Gardner et al. (1999) using solubility data of Fanara et al. (in press) and Iacono-Marziano et al. (2007).

[e]: Calculated from Eq. 5 in Gardner et al. (1999) using the residual H_2O contents.

[f]: Calculated from Eq. 3 in Marxer et al. (2015) using the corresponding shrinkage factor B_s and the 3D porosity.

[g]: N_V(t) is the number of bubbles per total unit volume ($V_{glass} + V_{bubbles}$).

[h]: N_V(n) is the number of bubbles normalized to the bubble-free volume.

[i]: Shrinkage factor calculated from Eq. 2 in Marxer et al. (2015).

[j]: Numerous small objects in the measuring volume.

Figure captions

Fig. 1: TLM and BSE images of two CI isobaric experiments starting from glass cylinders with ~4.7 wt% H_2O, equilibrated for 96 h at 200 MPa and 1300 °C. (a) TLM image of IB-C-1b: RQ starting from 1300 °C. The glass section contains objects ≥1 µm diameter (black dots in focus plane) that are probably quench crystals. Some objects appear to be bigger in diameter due to the optical halo effect. (b) TLM image of IB-C-2: NQ starting from 1050 °C. The glass section contains quench crystal aggregates with radially arranged, needle-shaped crystals with several µm length. The quench crystals are bigger than in sample IB-C-1b due to the lower cooling rate. (c) BSE image of IB-C-2: Single quench crystal aggregate with needle-shaped crystals that are radially arranged around a central microlite of presumable different chemical composition. The crystals were too small for chemical analysis by EMP. The glass-crystal image contrast suggests an oxide microlite as central crystal in the aggregate.

Fig. 2: Comparison of BSE images of selected samples decompressed to a P_{final} of 100 MPa (0.024 MPa·s^{-1}) using massive glass cylinders and glass powder with the CI and VAD79 composition as starting material. Despite identical and homogeneous initial H_2O content in the melt prior to decompression, the glass powder samples that were equilibrated for a t_{eq} of 24 h (central row) are clearly more degassed than the samples starting from massive glass cylinders (top row) and glass powder with a t_{eq} of 96 h (bottom row). The glass powder samples with a t_{eq} of 24 h are characterized by bigger bubbles, higher porosities and lower bubble number densities. The bubbles in the samples with a t_{eq} of 96 h are only few µm in diameter, more numerous and homogeneously distributed in the glass. These small bubbles are not visible at this magnification.

Fig. 3: Comparison of BSE images of selected samples decompressed to a P_{final} of 100 MPa (0.17 MPa·s^{-1}) using a massive CI glass cylinder (t_{eq} = 96 h) and powder (t_{eq} = 24 h) as starting material. In correspondence to the samples of the experiments with a lower decompression rate (shown in Fig. 2), the glass powder sample (CD-P-1, bottom image) is more degassed than the glass cylinder sample (CD-C-1, top image). The glass cylinder sample contains numerous small bubbles on a micrometer scale that are not visible at this magnification. The glass powder

sample also features a belt of small bubbles in the central part of the capsule (right image excerpt).

Fig. 4: TLM images of CI (two left images) and VAD79 (two right images) samples decompressed with 0.024 MPa·s^{-1} to a P_{final} of 100 MPa. All images have the same scale. The samples CD-C-2 (a) and CD-C-25 (c) started from glass cylinders and samples CF-P-2b (b) and CD-P-32 (d) from glass powder. All experiments were equilibrated for 96 h prior to decompression. All samples contain homogeneously distributed bubbles with few µm diameter. The N_V(n) and porosities of the samples are comparable for corresponding experiments with the same melt composition (see Table 3). In contrast to decompressed glass powder samples with a t_{eq} of 24 h, the degassing behavior of samples with a t_{eq} of 96 h is identical to the glass cylinder samples.

Fig. 5: TLM image of CD-C-1 decompressed to a P_{final} of 100 MPa (0.17 MPa·s^{-1}) using a massive CI glass cylinder with different magnifications. The sample contains homogeneously distributed bubbles with several µm diameter. The image reveals that these bubbles are often in close vicinity to a crystal and connected by a thin neck to the crystal surface. The formation of a thin neck towards a microlite is also described in Hurwitz and Navon (1994) and attributed to bubble shrinkage during quench.

Fig. 6: BSE images of CI glass cylinder samples (CD-C-3, CD-C-4) decompressed to a P_{final} of 75 MPa with 0.024 MPa·s^{-1} (top image) and 0.17 MPa·s^{-1} (bottom image). The area around each of the big bubbles in sample CD-C-3 is free of the elsewhere homogeneously distributed small bubbles with several µm diameter (right image excerpt). For details see text.

Fig. 7: BSE (a) and a mapped TLM image (b) of sample CD-C-5 decompressed to a P_{final} of 60 MPa with 0.17 MPa·s^{-1}. The TLM image reveals extensive convection patterns within the capsule. The bubbles in the BSE image were big enough to be analyzed with CSDCorrections. (c) Exemplary BSD plot derived from sample area 4 in (a) shows the logarithmic population density ln $n(l)$ as a function of the diameter (l) of the bubbles in the quenched sample. The diameter corresponds to the major axis of the bubble-ellipsoid. The BSD is characterized by a narrow size range and a near-linear trend.

Fig. 8: H_2O-N_2 solubility model on the basis of the experimentally determined H_2O-CO_2 solubility reported in Fanara et al. (in press) for the CI composition at the decompression *T* of 1050 °C. The amounts of dissolved N_2 are maximum values as suggested by Carroll and Webster (1994). Isobars are adopted from Fanara et al. (in press) and are marked with the corresponding *P*. The dashed isopleth represents the fluid composition in equilibrium with the melt. At 200 MPa and an initial H_2O content of 4.7 wt% in the melt prior to decompression, the solubility of N_2 is correspondingly low. A significant amount of the N_2 in the capsule of glass powder samples remains in the H_2O-dominated fluid phase.

Fig. 9: Ascent distance of bubbles as a function of bubble diameter for the equilibration and decompression *T* (1300 and 1050 °C) and the two equilibration times (24 and 96 h). Instant volatile saturation of the melt at the beginning of the equilibration period in the glass powder experiments is assumed. Increasing *T* accelerates bubble ascent due to the lowered viscosity of the melt and decreased density of the super-critical fluid (see text, Eq. 2).

Fig. 10: The TLM image of sample CD-C-4 decompressed to a P_{final} of 75 MPa with 0.17 MPa·s^{-1} shows two neighbored bubbles that extend towards each other by a small bulge. These bubbles were quenched just at the beginning of coalescence.

Fig. 11: Logarithmic N_V(n)-values of this study (error about ±0.5 log units) and of selected previous experimental studies as a function of decompression rate in comparison to the calculated N_V(n)-values for the CI melt using the model of Toramaru (2006). The trends were calculated for two different surface tensions (σ). Filled symbols represent N_V(n) of samples from experiments where most likely no bubble interaction occurred. Empty symbols represent N_V(n) of samples from experiments that are suggested to be influenced by Ostwald ripening and/or coalescence (indicated by arrows). *Note*: Ma15: CD experiments of Marxer et al. (2015) in 5 mm capsules; VAD79 composition at 1050 °C. Go11: TIHPV experiments of Gondé et al. (2011); haplogranite at 900 °C. ML02: Mourtada-Bonnefoi and Laporte (2002); rhyolite at 800 °C. MS00: Mangan and Sisson (2000); rhyolite at 900 °C.

Figures

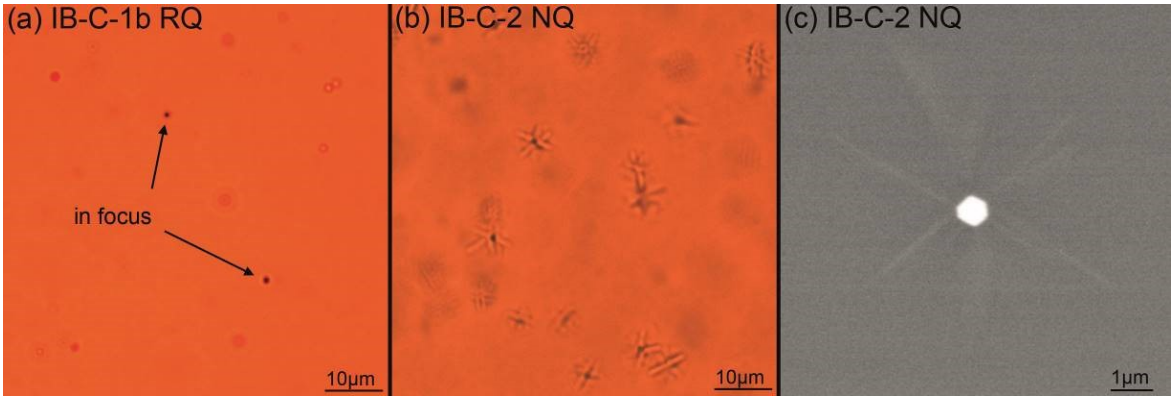

Fig. 1a-c

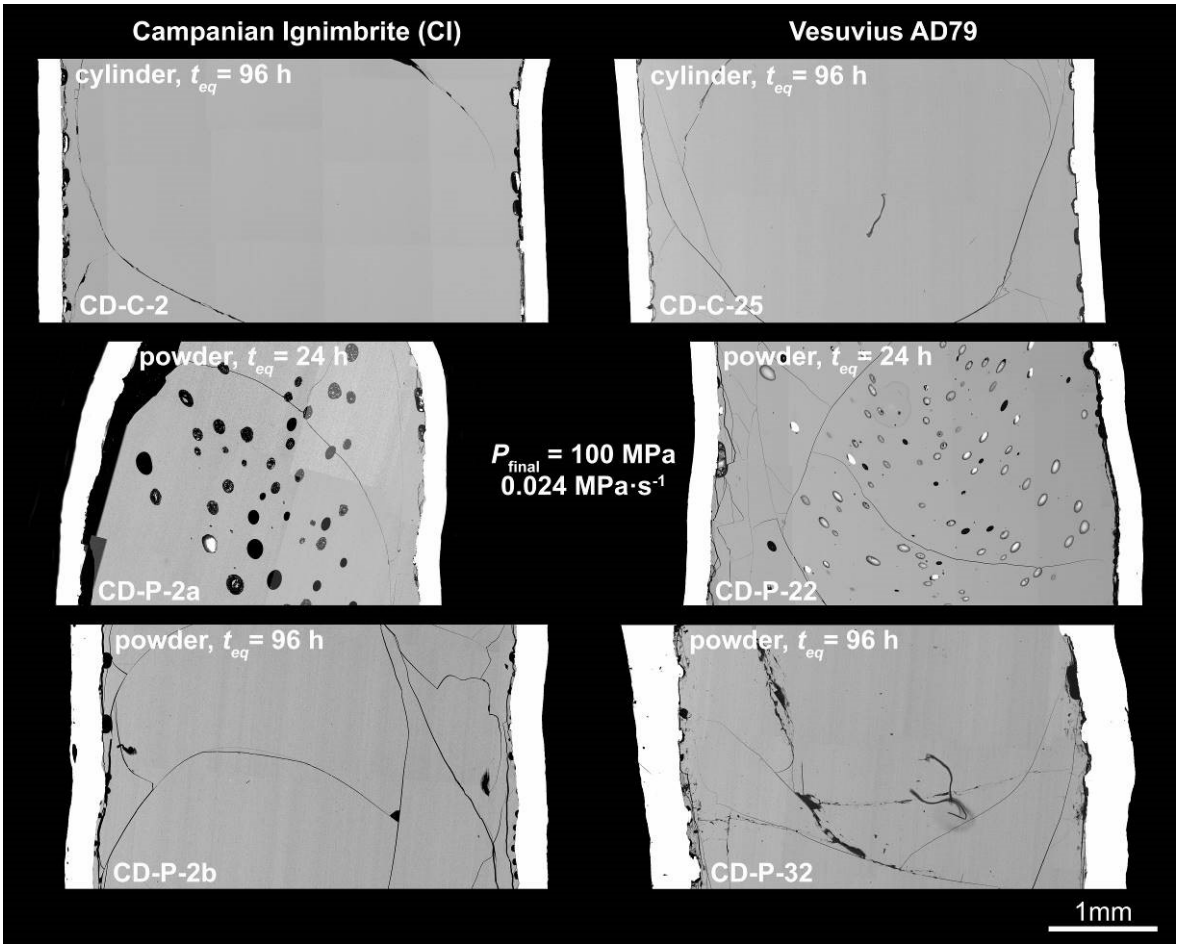

Fig. 2

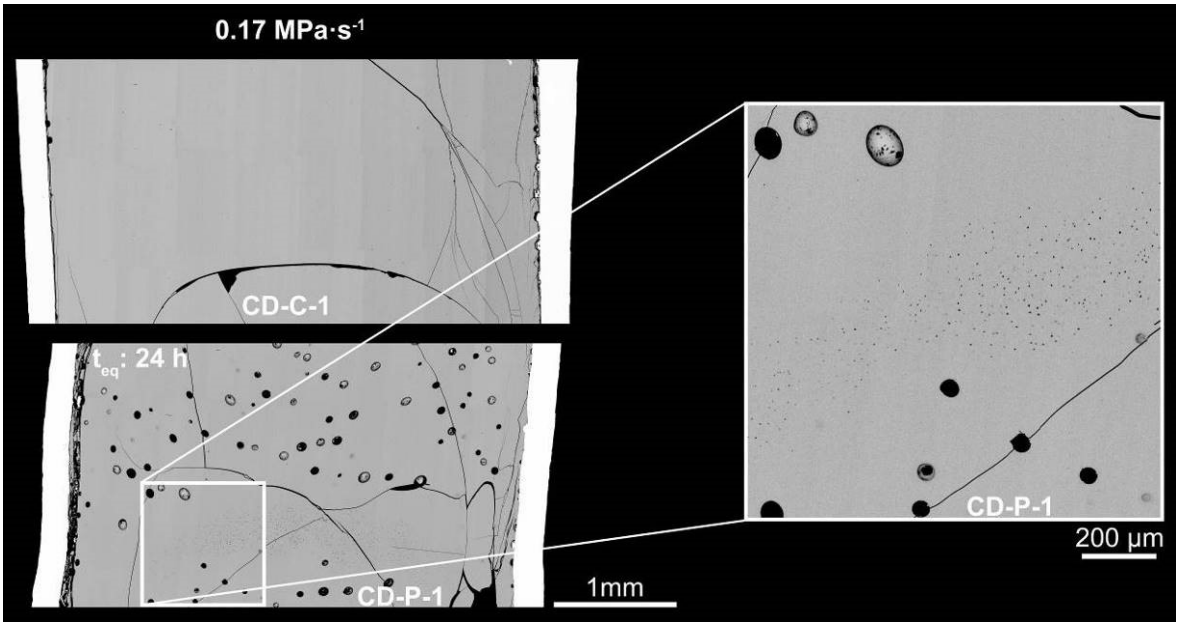
0.17 MPa·s-1
CD-C-1
teq: 24 h
CD-P-1
1mm
CD-P-1
200 µm

Fig. 3

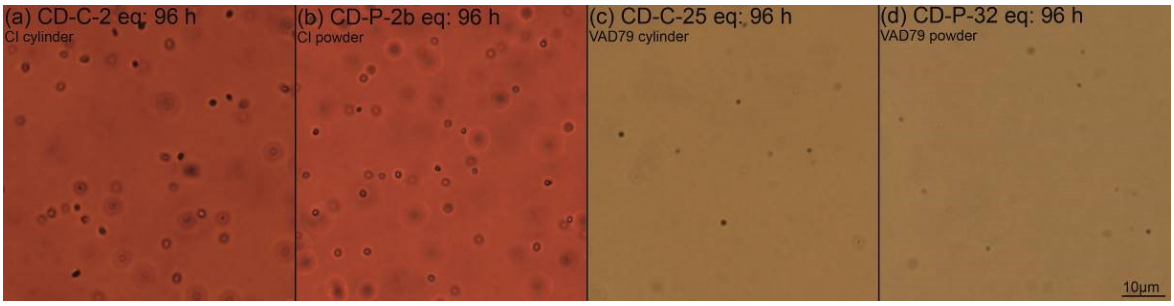
(a) CD-C-2 eq: 96 h
CI cylinder
(b) CD-P-2b eq: 96 h
CI powder
(c) CD-C-25 eq: 96 h
VAD79 cylinder
(d) CD-P-32 eq: 96 h
VAD79 powder
10µm

Fig. 4a-d

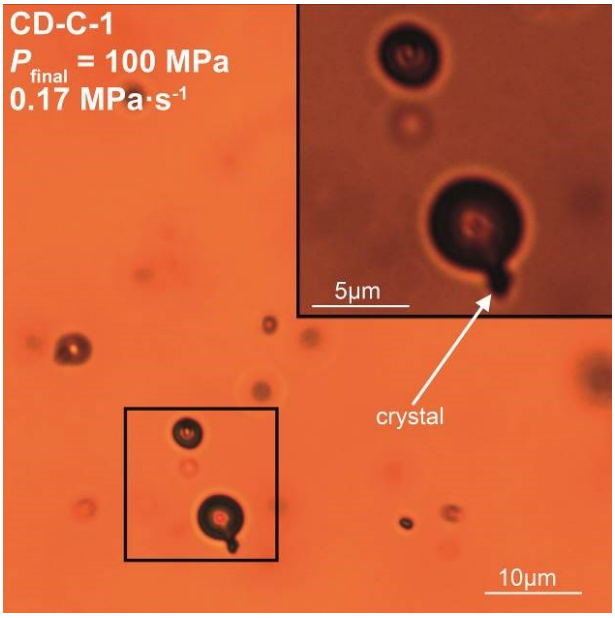
CD-C-1
P_{final} = 100 MPa
0.17 MPa·s^{-1}
5µm
crystal
10µm

Fig. 5

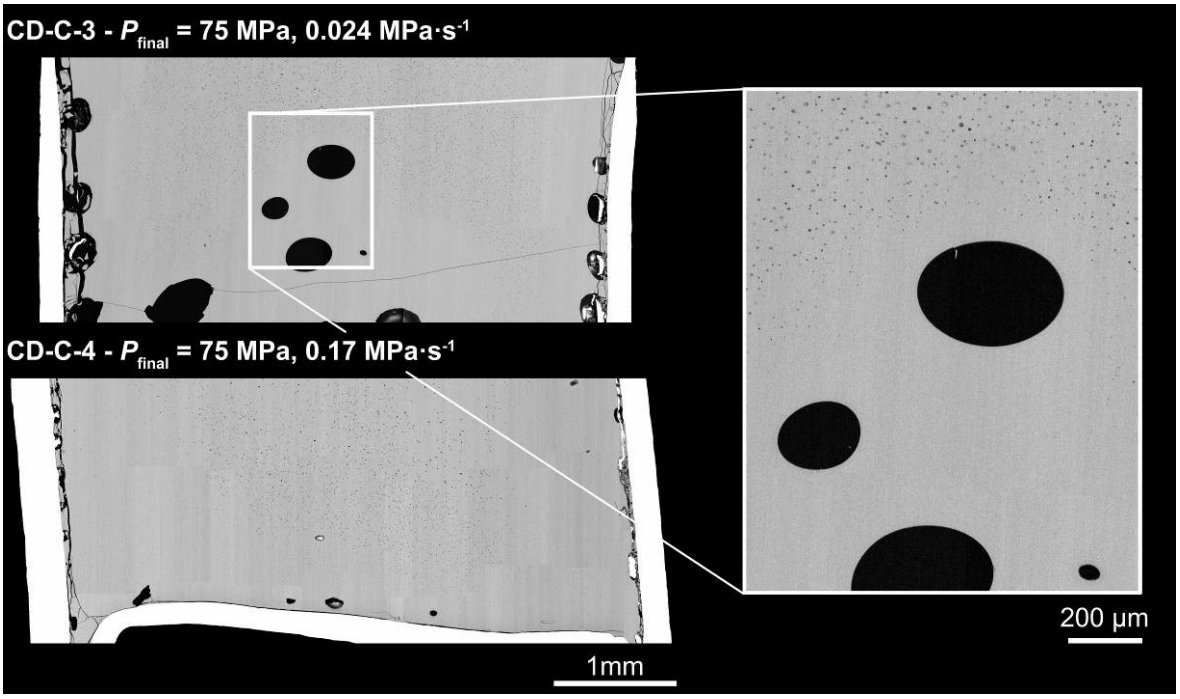
CD-C-3 - P_{final} = 75 MPa, 0.024 MPa·s^{-1}
CD-C-4 - P_{final} = 75 MPa, 0.17 MPa·s^{-1}
200 µm
1mm

Fig. 6

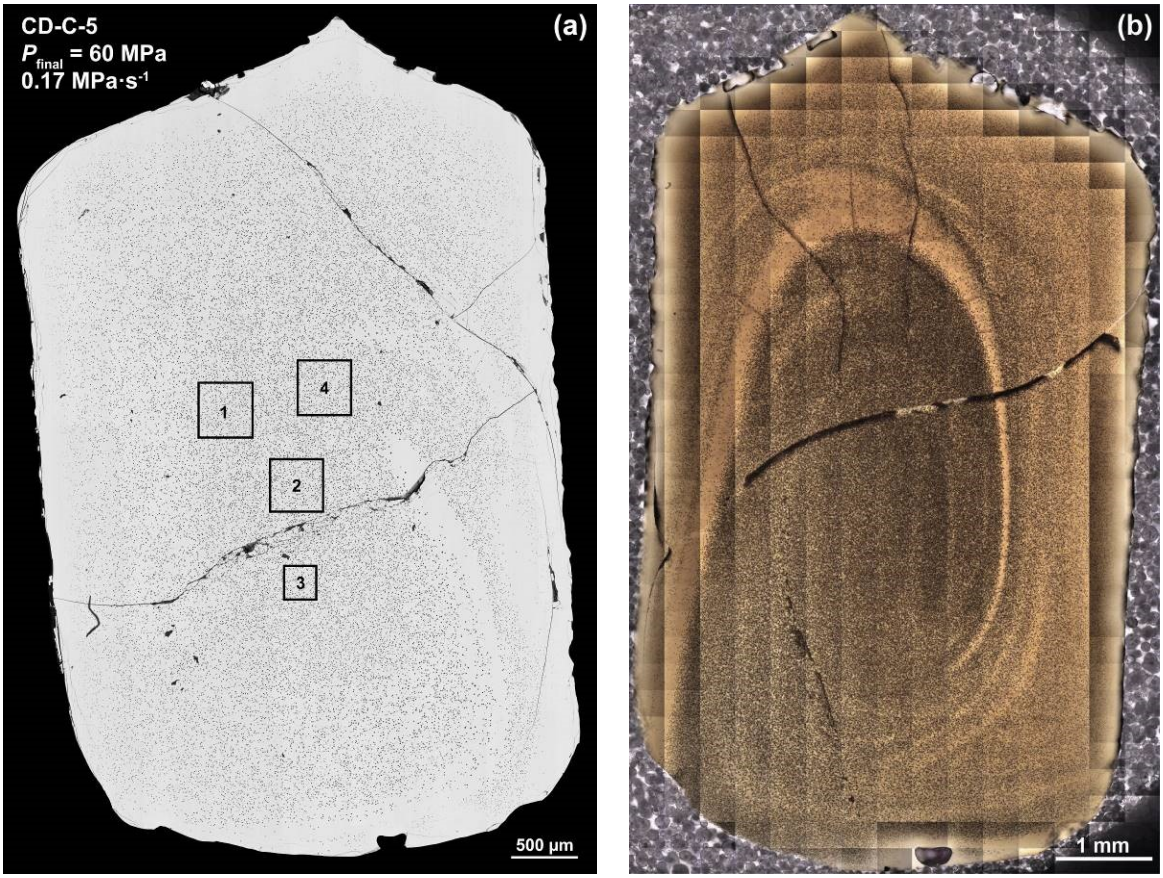
CD-C-5
P_{final} = 60 MPa
0.17 MPa·s^{-1}
(a)
1
2
3
4
500 µm
(b)
1 mm

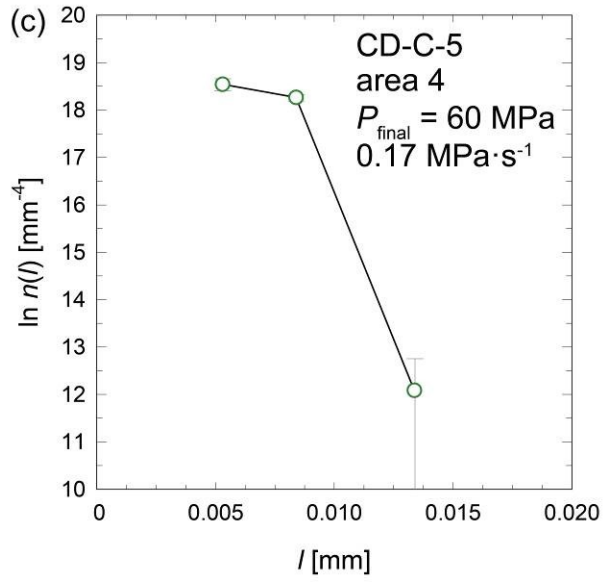
(c)
CD-C-5
area 4
P_{final} = 60 MPa
0.17 MPa·s^{-1}
ln $n(l)$ [mm^{-4}]
l [mm]
20
19
18
17
16
15
14
13
12
11
10
0
0.005
0.010
0.015
0.020

Fig. 7a-c

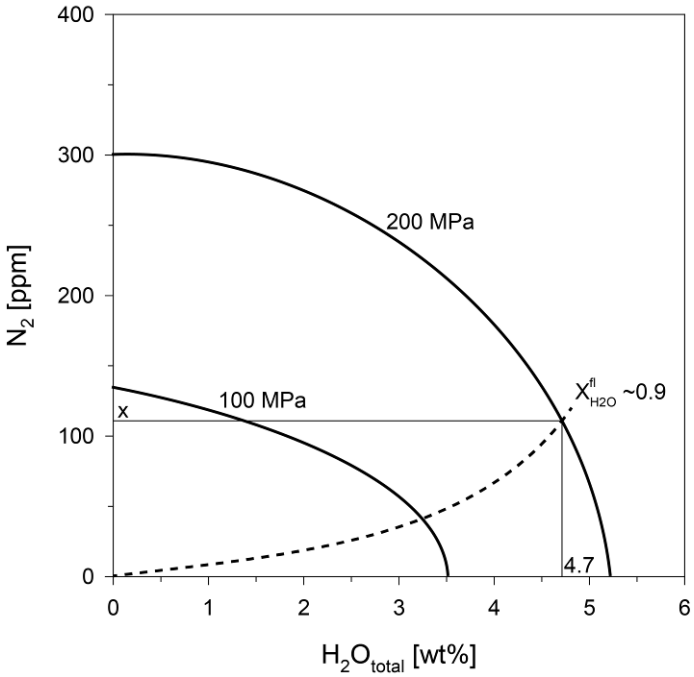
400
300
200
100
0
N2 [ppm]
200 MPa
100 MPa
x
X^fl_H2O ~0.9
4.7
0
1
2
3
4
5
6
H2Ototal [wt%]

Fig. 8

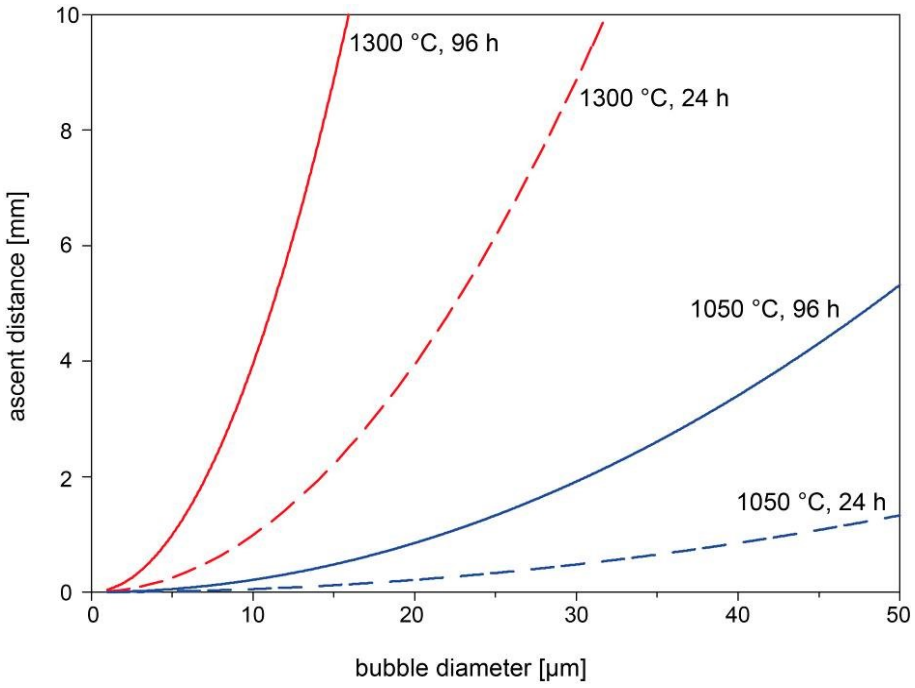
10
8
6
4
2
0
ascent distance [mm]
1300 °C, 96 h
1300 °C, 24 h
1050 °C, 96 h
1050 °C, 24 h
0
10
20
30
40
50
bubble diameter [µm]

Fig. 9

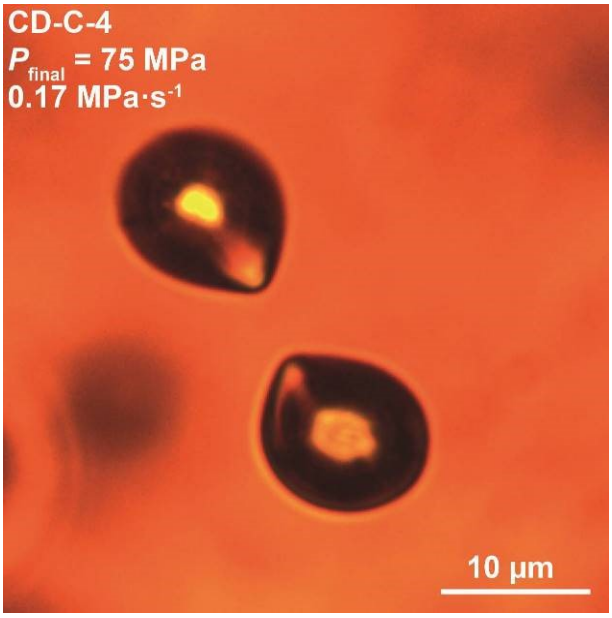

Fig. 10

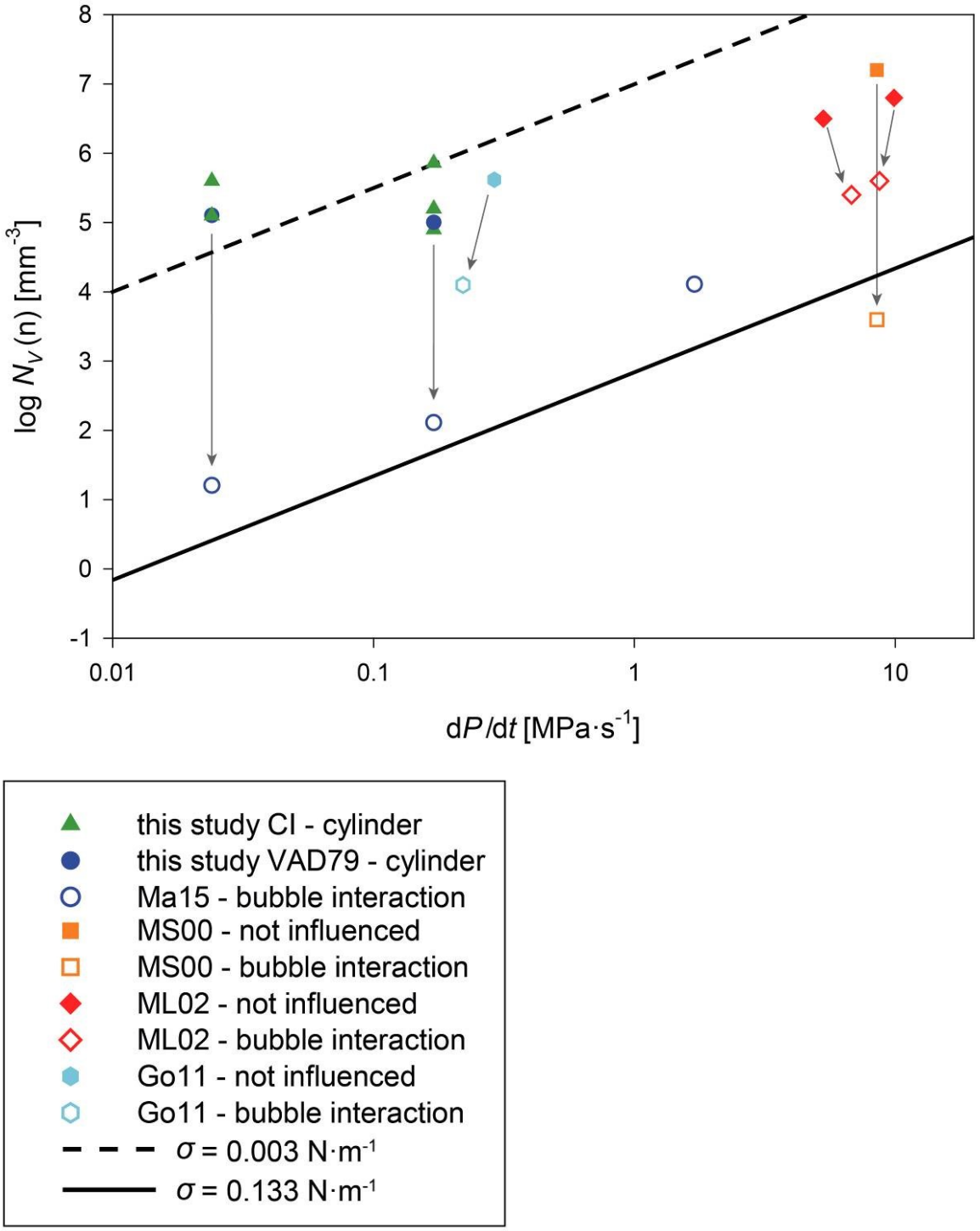
8
7
6
5
4
3
2
1
0
-1
log N_V(n) [mm^{-3}]
0.01
0.1
1
10
dP/dt [MPa·s^{-1}]
this study CI - cylinder
this study VAD79 - cylinder
Ma15 - bubble interaction
MS00 - not influenced
MS00 - bubble interaction
ML02 - not influenced
ML02 - bubble interaction
Go11 - not influenced
Go11 - bubble interaction
σ = 0.003 N·m^{-1}
σ = 0.133 N·m^{-1}

Fig. 11

eFigure captions

eFig. 1a: BSE image of the CI glass cylinder sample CD-C-5 decompressed to a P_{final} of 60 MPa with 0.17 MPa·s^{-1}, t_{eq}: 96 h. The 4 black frames mark the sample areas used for ImageJ analysis.

eFig. 1b: Mapped TLM image of the CI glass cylinder sample CD-C-5 decompressed to a P_{final} of 60 MPa with 0.17 MPa·s^{-1}, t_{eq}: 96 h. Dark spherical objects in the

eFig. 2a: BSE image of the CI glass cylinder sample CD-C-3 decompressed to a P_{final} of 75 MPa with 0.024 MPa·s^{-1}, t_{eq}: 96 h. The black frame marks the sample area used for ImageJ analysis.

eFig. 2b: Mapped TLM image of the CI glass cylinder sample CD-C-3 decompressed to a P_{final} of 75 MPa with 0.024 MPa·s^{-1}, t_{eq}: 96 h.

eFig. 3a: BSE image of the CI glass cylinder sample CD-C-4 decompressed to a P_{final} of 75 MPa with 0.17 MPa·s^{-1}, t_{eq}: 96 h. The black frame marks the sample area used for ImageJ analysis.

eFig. 3b: Mapped TLM image of the CI glass cylinder sample CD-C-4 decompressed to a P_{final} of 75 MPa with 0.17 MPa·s^{-1}, t_{eq}: 96 h.

eFig. 4: BSE image of the CI glass cylinder sample CD-C-1 decompressed to a P_{final} of 100 MPa with 0.17 MPa·s^{-1}, t_{eq}: 96 h.

eFig. 5a: BSE image of the CI glass powder sample CD-P-1 decompressed to a P_{final} of 100 MPa with 0.17 MPa·s^{-1}, t_{eq}: 24 h. The 2 black frames mark the sample areas used for ImageJ analysis.

eFig. 5b: Mapped TLM image of the CI glass powder sample CD-P-1 decompressed to a P_{final} of 100 MPa with 0.17 MPa·s^{-1}, t_{eq}: 24 h.

eFig. 6: BSE image of the CI glass cylinder sample CD-C-2 decompressed to a P_{final} of 100 MPa with 0.024 MPa·s^{-1}, t_{eq}: 96 h.

eFig. 7a: BSE image of the CI glass powder sample CD-P-2a decompressed to a P_{final} of 100 MPa with 0.024 MPa·s^{-1}, t_{eq}: 24 h. The black frame marks the sample area used for ImageJ analysis.

eFig. 7b: Mapped TLM image of the CI glass powder sample CD-P-2a decompressed to a P_{final} of 100 MPa with 0.024 MPa·s^{-1}, t_{eq}: 24 h.

eFig. 8: BSE image of the CI glass powder sample CD-P-2b decompressed to a P_{final} of 100 MPa with 0.024 MPa·s^{-1}, t_{eq}: 96 h.

eFig. 9a: BSE image of the VAD79 glass powder sample CD-P-22 decompressed to a P_{final} of 100 MPa with 0.024 MPa·s^{-1}, t_{eq}: 24 h. The black frame marks the sample area used for ImageJ analysis.

eFig. 9b: Mapped TLM image of the VAD79 glass powder sample CD-P-22 decompressed to a P_{final} of 100 MPa with 0.024 MPa·s^{-1}, t_{eq}: 24 h.

eFig. 10: BSE image of the VAD79 glass cylinder sample CD-C-23 decompressed to a P_{final} of 100 MPa with 0.17 MPa·s^{-1}, t_{eq}: 96 h.

eFig. 11a: BSE image of the VAD79 glass powder sample CD-P-24 decompressed to a P_{final} of 100 MPa with 0.17 MPa·s^{-1}, t_{eq}: 24 h. The black frame marks the sample area used for ImageJ analysis.

eFig. 11b: Mapped TLM image of the VAD79 glass powder sample CD-P-24 decompressed to a P_{final} of 100 MPa with 0.17 MPa·s^{-1}, t_{eq}: 24 h.

eFig. 12: BSE image of the VAD79 glass cylinder sample CD-C-25 decompressed to a P_{final} of 100 MPa with 0.024 MPa·s^{-1}, t_{eq}: 96 h.

eFig. 13: BSE image of the VAD79 glass powder sample CD-P-32 decompressed to a P_{final} of 75 MPa with 0.024 MPa·s^{-1}, t_{eq}: 96 h.

eFigures

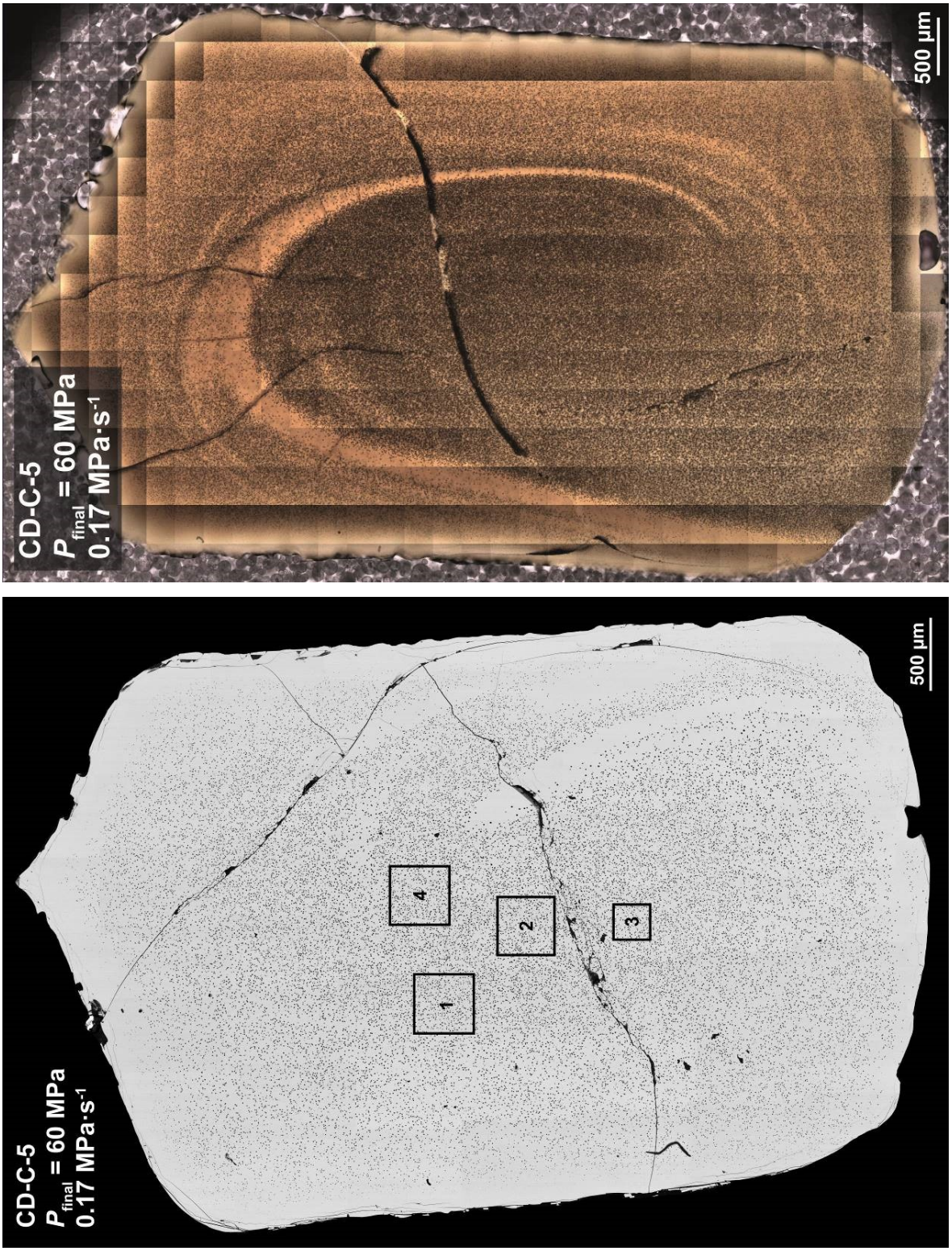

eFig. 1a (bottom), 1b (top)

glass cylinder, t_{eq} = 96 h

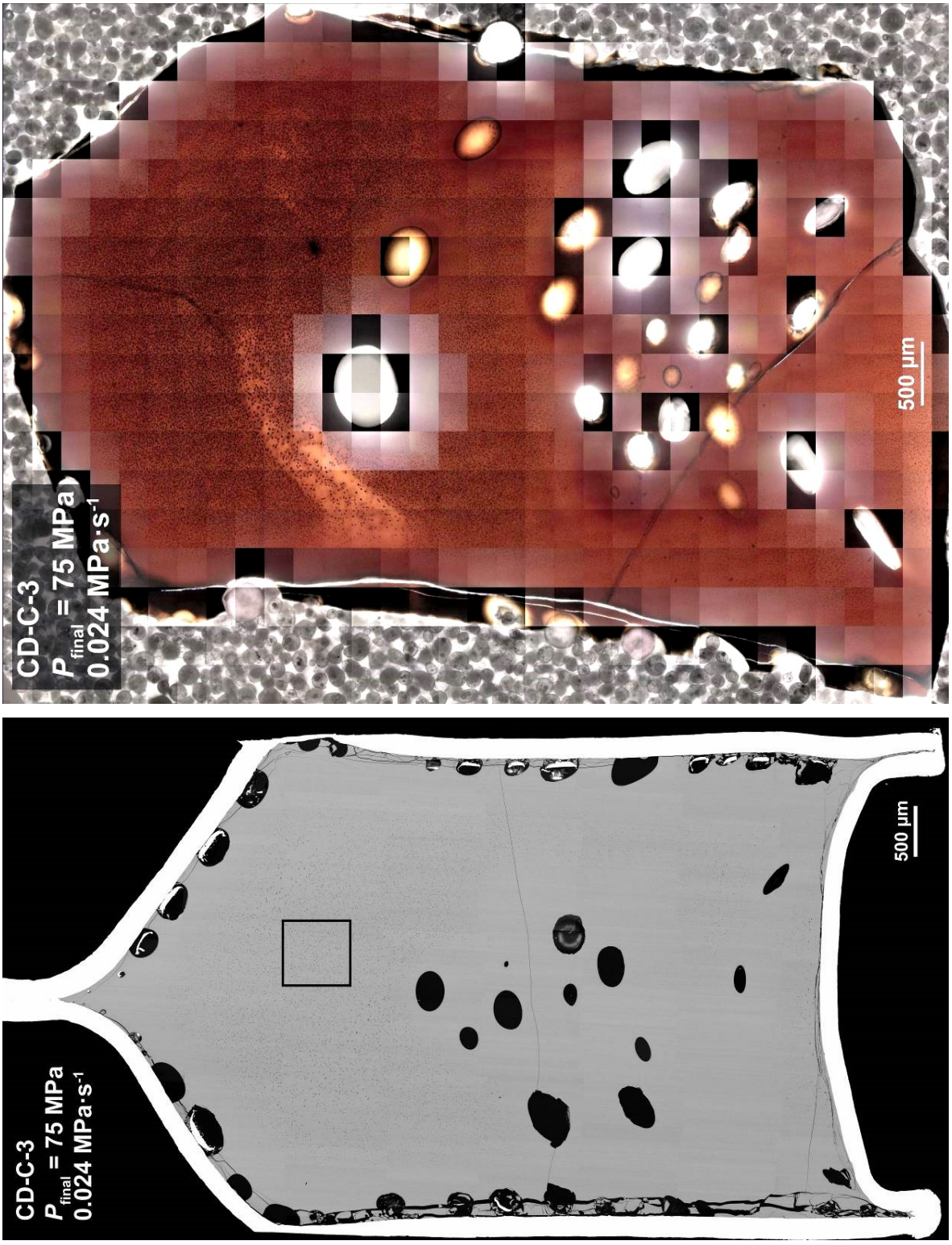

eFig. 2a (bottom), 2b (top)

glass cylinder, t_{eq} = 96 h

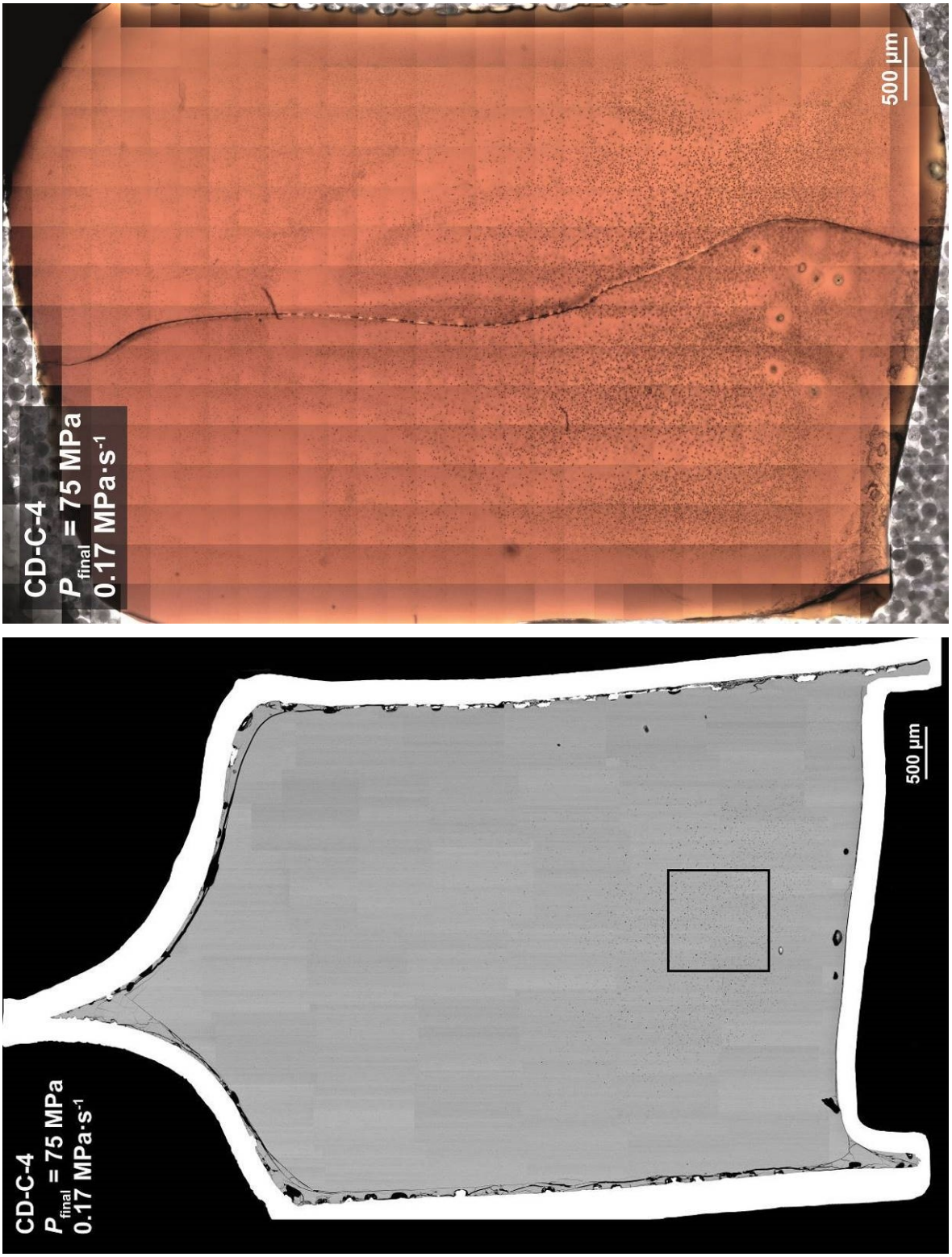

eFig. 3a (bottom), 3b (top)

glass cylinder, t_{eq} = 96 h

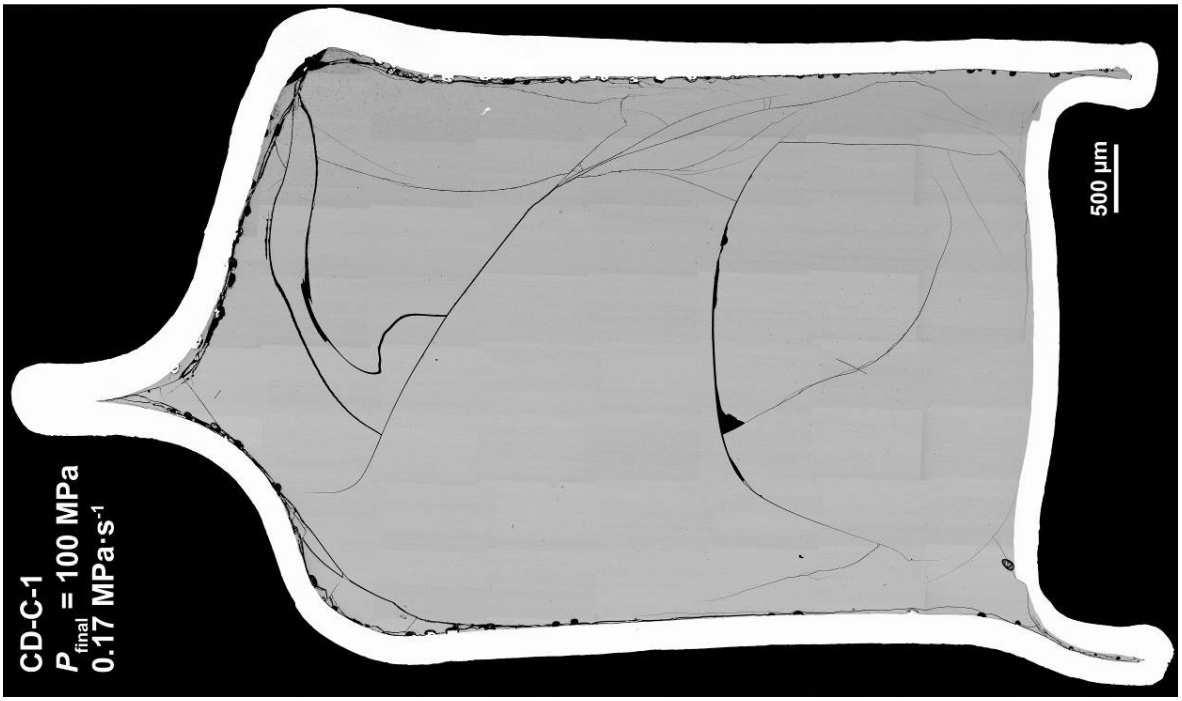

eFig. 4

glass cylinder, t_{eq} = 96 h

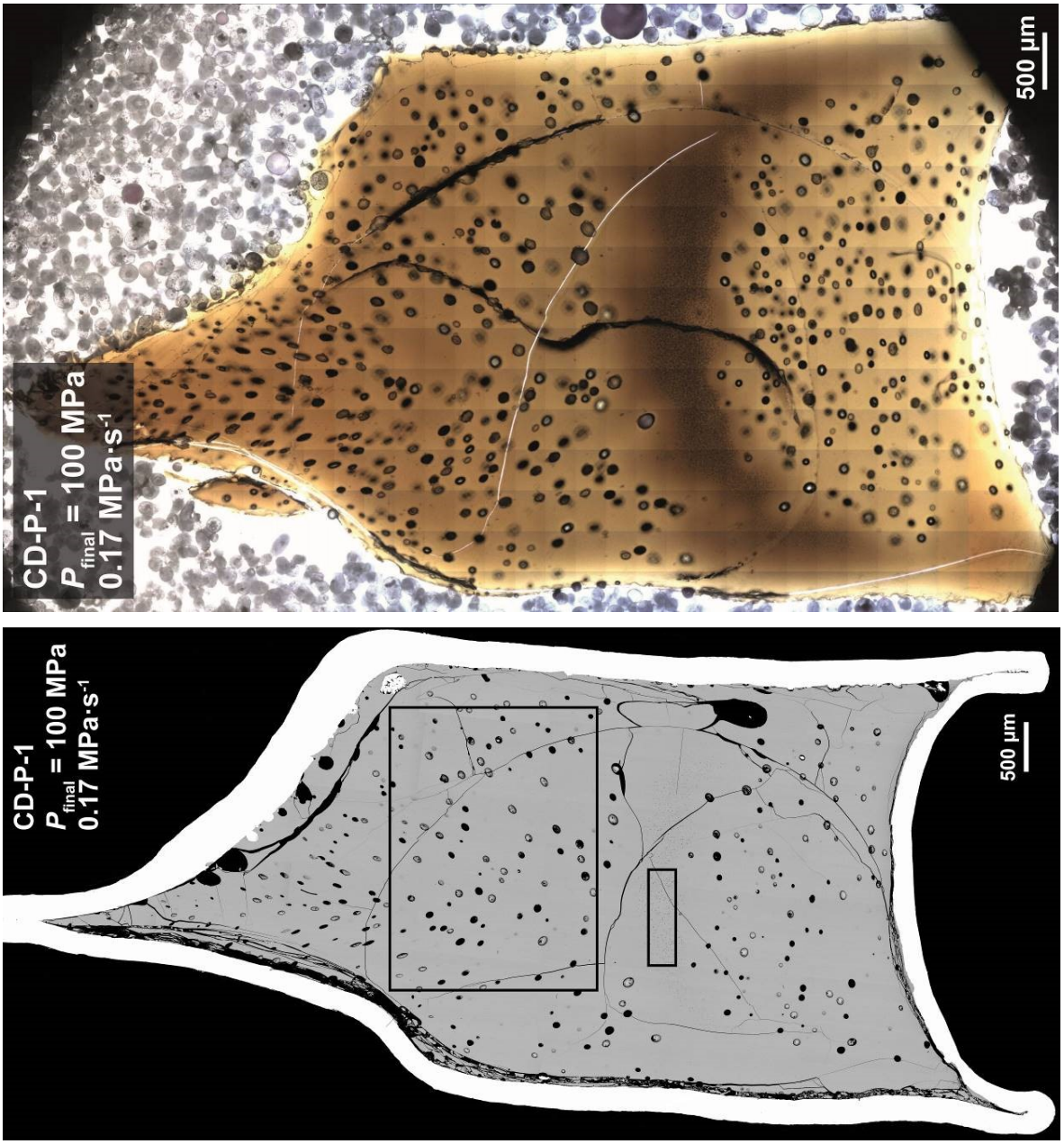

eFig. 5a (bottom), 5b (top)

glass powder, t_{eq} = 24 h

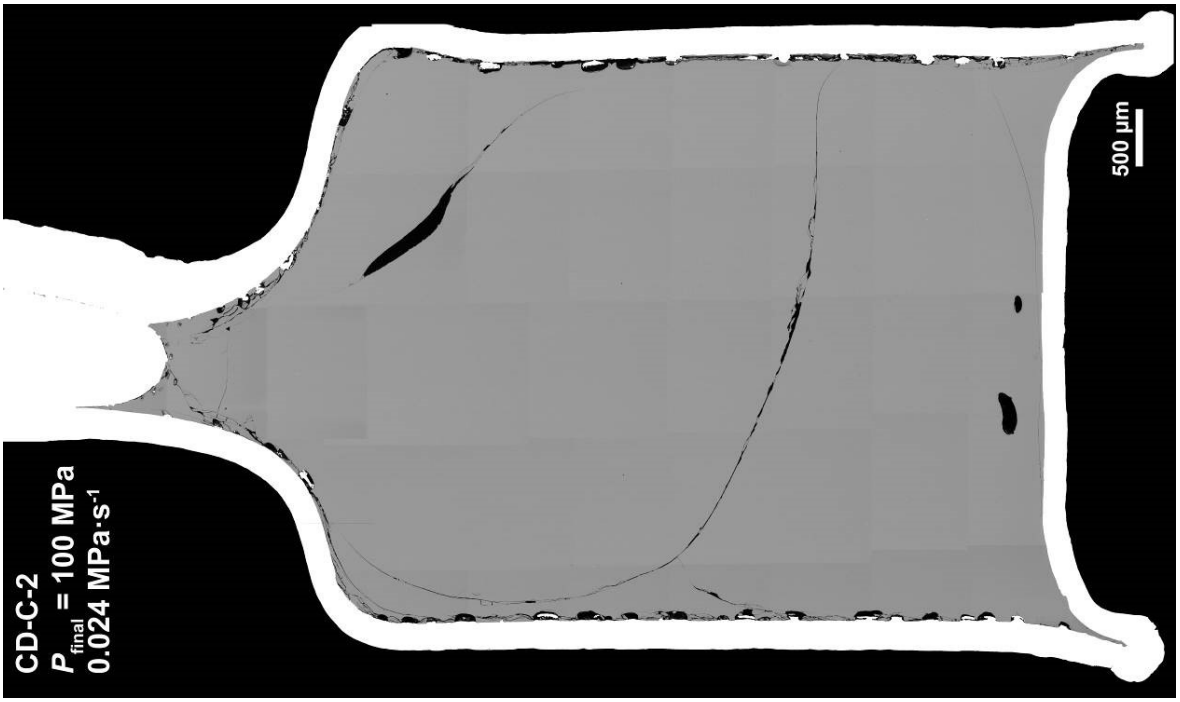

eFig. 6

glass cylinder, t_{eq} = 96 h

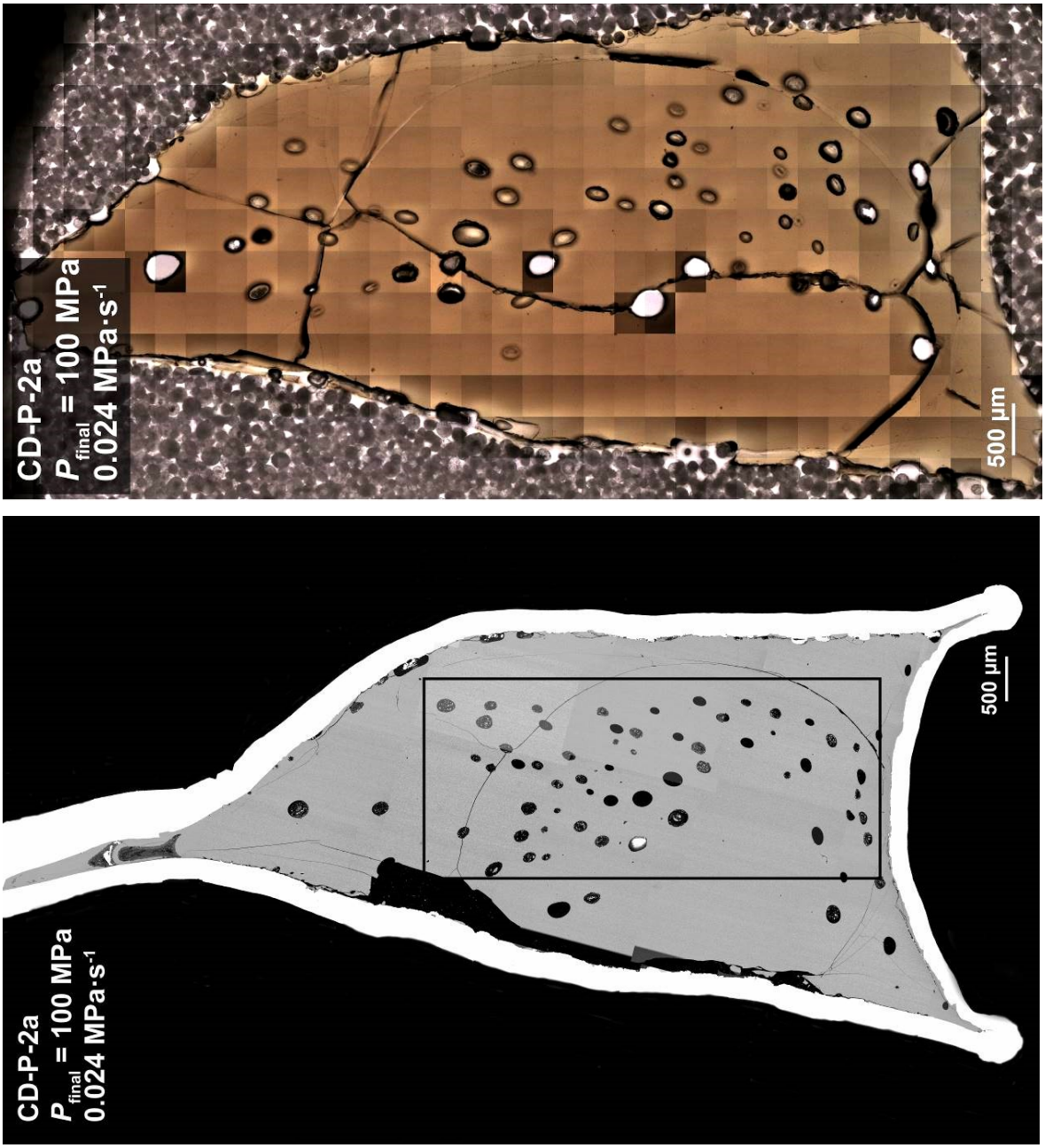

eFig. 7a (bottom), 7b (top)

glass powder, t_{eq} = 24 h

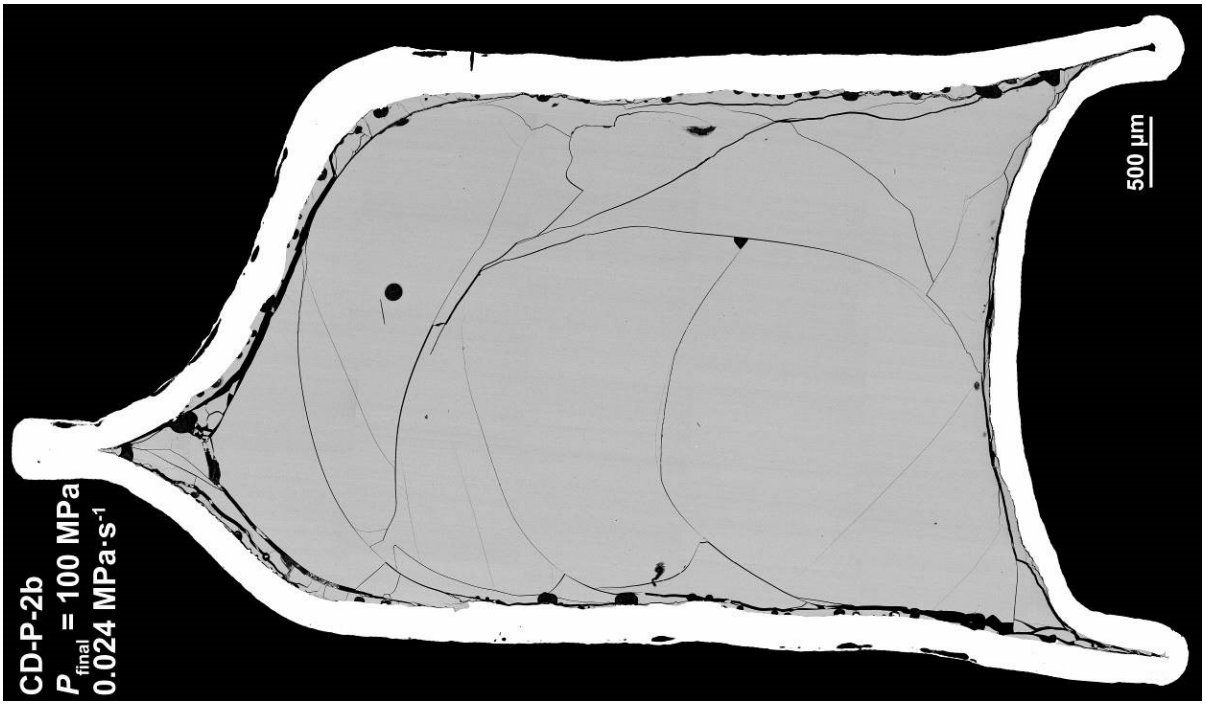

eFig. 8

glass powder, t_{eq} = 96 h

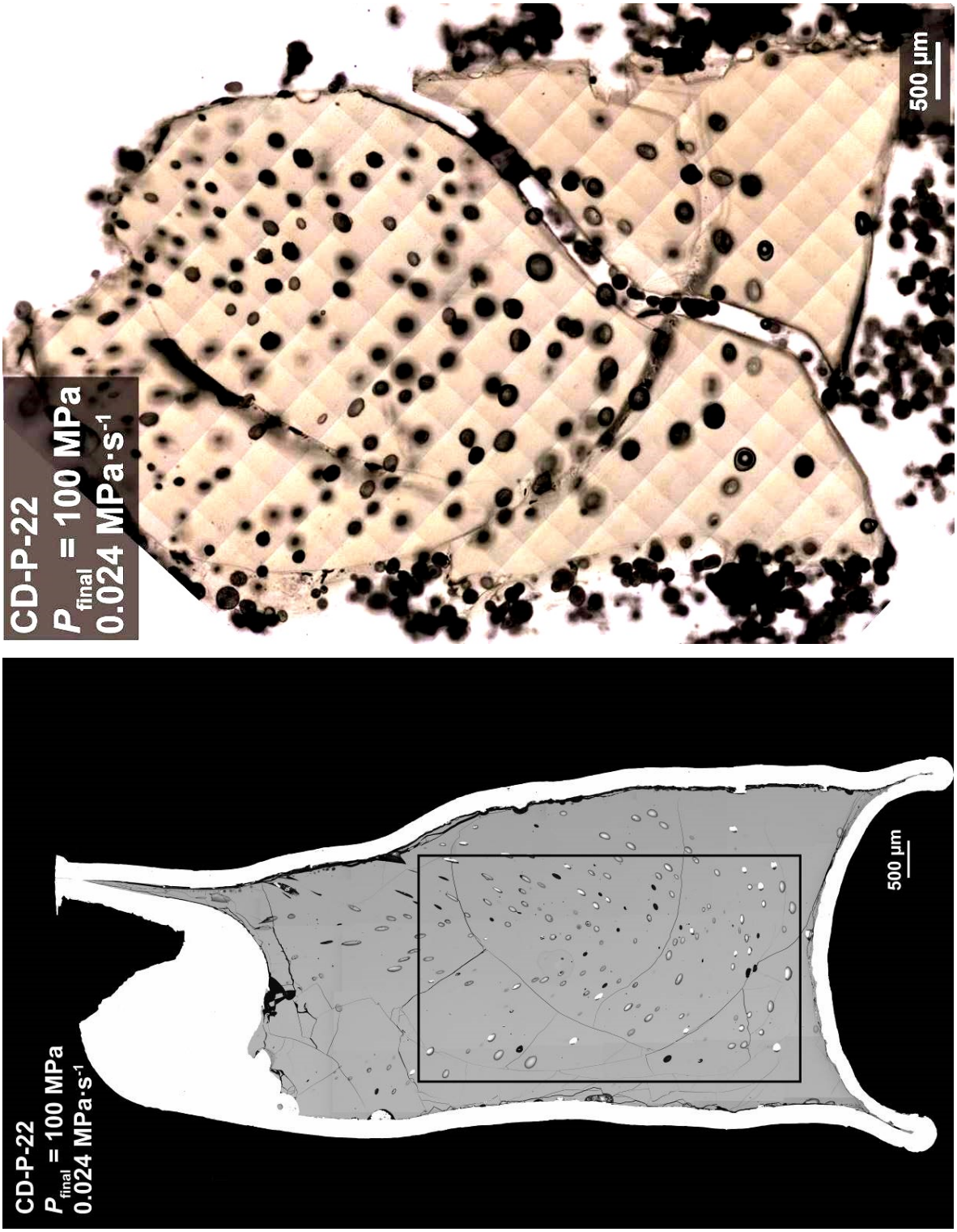

eFig. 9a (bottom), 9b (top)

glass powder, t_{eq} = 24 h

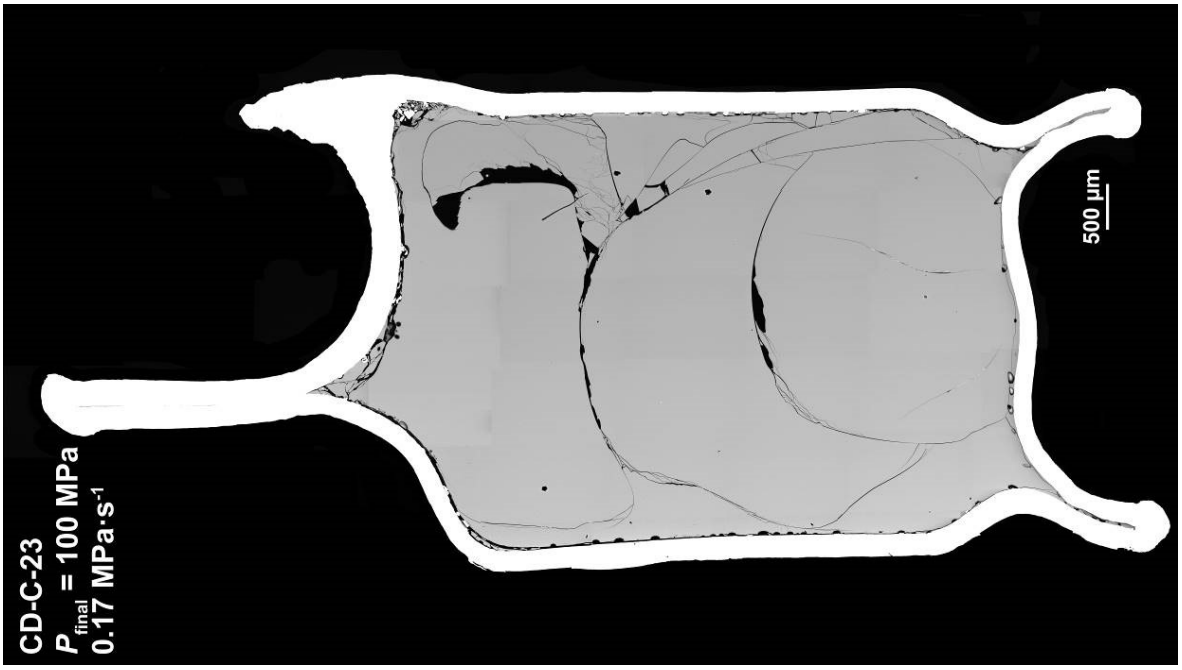

eFig. 10

glass cylinder, t_{eq} = 96 h

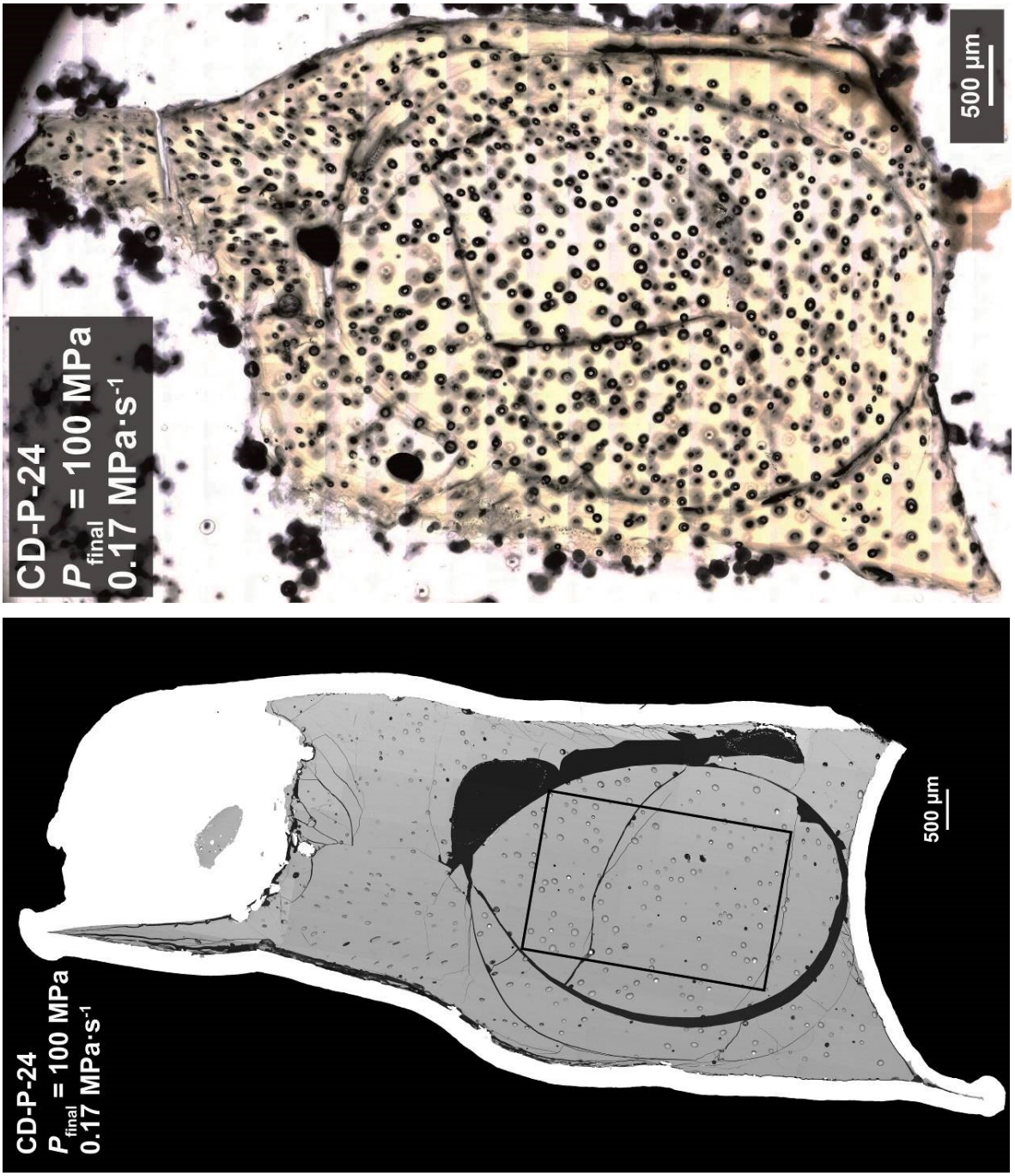

eFig. 11a (bottom), 11b (top)

glass powder, t_{eq} = 24 h

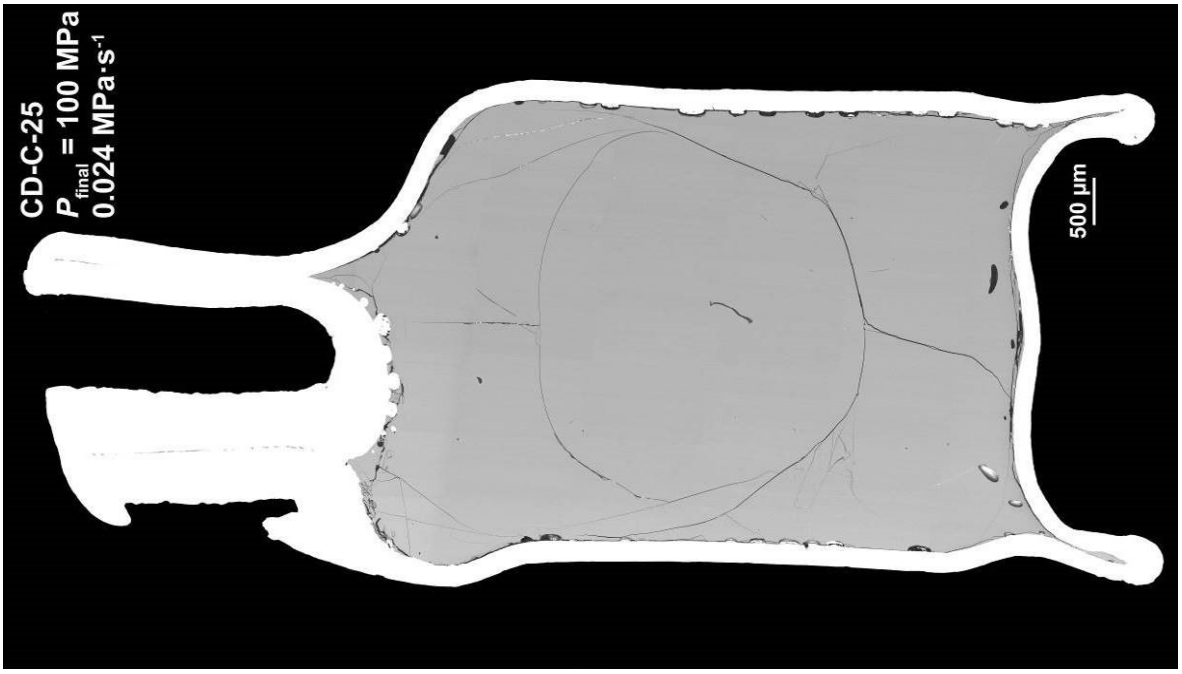

eFig. 12

glass cylinder, t_{eq} = 96 h

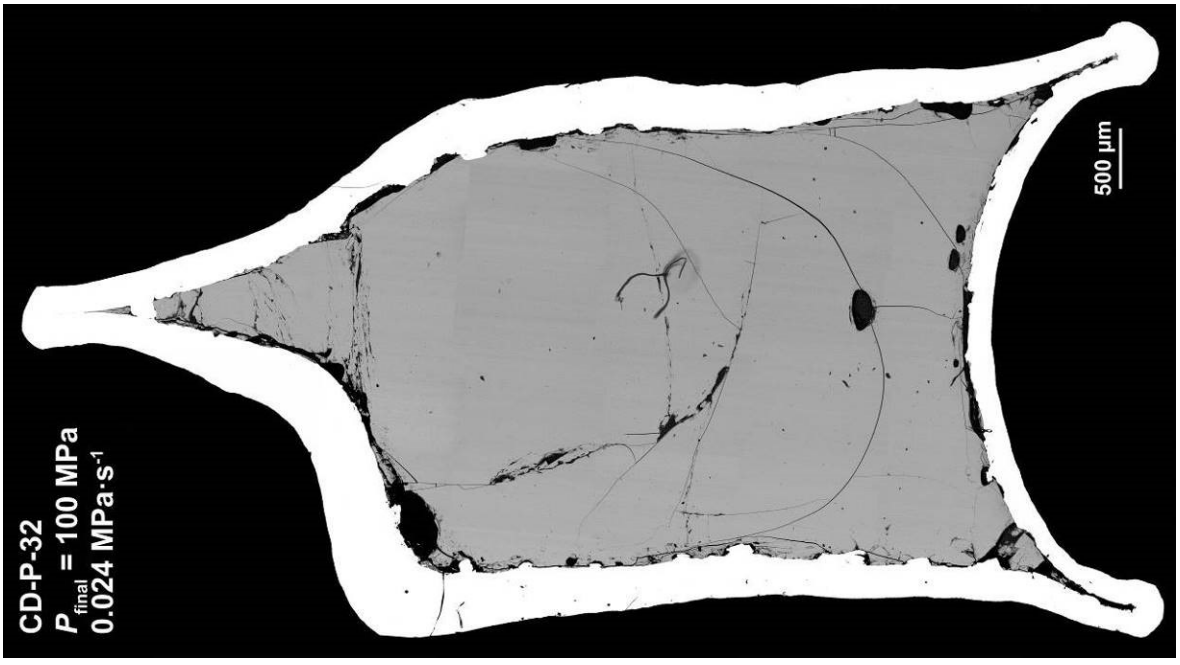

eFig. 13

glass powder, t_{eq} = 96 h